SLAC-R-590
UC-414

Hadron Production in Quark, Antiquark, and Gluon Jets from Electron-Positron Interactions at the Z0 Pole*

Hyejoo Kang

Stanford Linear Accelerator Center
Stanford University
Stanford, CA 94309

SLAC-Report-590
January 2002

Prepared for the Department of Energy
under contract number DE-AC03-76SF00515

*Ph.D. thesis, Rutgers University

ABSTRACT

We present production measurements of the charged hadrons $\pi^{\pm}$, $K^{\pm}$ and p/p̄ in $e^{+}e^{-}$ interactions at the Z^{0} pole. The excellent particle identification capability of the SLC Large Detector (SLD) at the Stanford Linear Collider (SLC) are used. In addition to studies over a wide momentum range in hadronic Z^{0} events of all five flavors, we have made the most precise measurements in light (uds), c and b flavor events separately. Unambiguous flavor dependencies have been observed, and the results have been compared with the predictions of several QCD fragmentation models. We have also exploited the unique feature of electron beam polarization in our experiment to compare hadron production separately in quark and antiquark jets. Direct evidence that higher momentum hadrons are more likely to contain the primary quark and antiquark is seen, with precision sufficient to provide new model tests. Finally, we have studied hard gluon jets in detail. We have confirmed that gluon jets have a higher multiplicity of softer particles than light quark jets, and found this enhancement to be the same for $\pi^{\pm}$, $K^{\pm}$ and p/p̄ at the few percent level at all momenta. Any overall difference in the hadron fractions is limited to 0.018 at the 95% confidence level, indicating that there are no differences at the hadronization stage in jet formation between gluons and quarks.

Acknowledgements

There are many people who encouraged and supported me throughout my graduate school years. It would be impossible for me to enjoy doing physics and to finish my research without them. First of all, I would like to thank my advisor Mohan Kalelkar for his constant support academically and personally. I was fortunate to have such a wise and generous advisor.

I also thank David Muller for his endless advice on my analysis and for proof-reading this dissertation. Also, many thanks to Philip Burrows for his keen advice in many areas and to Gary Bower for many hours of talking about all the issues in life including Physics.

I am grateful to all the SLD people who inspired me to be interested in particle physics, and gave me great answers everytime I asked, especially, David Jackson, Kenneth Baird, Takashi Maruyama, Hidemi Akimoto and Toshinori Abe.

I appreciate that Thomas Wright gave me better ideas for doing things when I came up with new ideas. He has also been a pleasant drinking buddy.

I thank my fellow graduate students at SLD, Danning Dong, Cheng-Ju Lin, Gavin Nesom, Hermann Stangle, Julia Thom, Jodi Wittlin and Giulia Bellodi, for being great collaborators and friends. There are also people who gave me tremendous help in getting started working on particle physics: Homer Neal, Thomas Junk, Hwan-Bae Park and Chul-Hi Park. I owe them a lot.

My greatest thanks to my father and mother, Kwi-Hyun Kang and Mi-Ja Yoo. They have been the biggest supporters in my life in good and tough times. Endless thanks for their love and courage. I give love from my heart to my late brother Se-Goo Kang and my sister Jin-Ha Kang. Finally, my best friend and husband Aaron S Chou for his constant support.

Dedication

For my brother, Se-Goo Kang (1972–1992),

whom I will always love and miss

and

for my family.

Table of Contents

Chapter 1

Introduction

The Standard Model (SM) of particle physics is a well-tested theory of the electroweak and strong interactions of fermions. The component of the SM which describes the strong interactions is called Quantum Chromodynamics (QCD) [1],[2],[3]. Perturbative QCD can quantitatively describe the process of gluon radiation from the high energy initial quark and antiquark in $e^+e^- \rightarrow Z^0/\gamma \rightarrow q\bar{q}$. This gluon radiation process continues until the energy scale of the partons (gluons and quarks) approaches the hadron mass scale and color singlet bound states are produced. The hadronization process by which hadrons are produced from the radiated partons occurs at low energies where perturbative QCD calculations are not possible. Understanding the hadronization process is a big challenge for particle physicists. There have been a lot of effort to construct theories to explain the process. Several phenomenological models (JETSET [4], HERWIG [5] and UCLA [6]) of the hadronization process have been tuned to reproduce data from e^+e^- annihilation.

In order to understand better the hadronization process, observables such as the event topology, the total number of particles produced, and the momentum distribution of charged particles [7],[8],[9],[10],[11],[12] have been measured in many experiments.

More recently, detailed studies of the production of hadrons have been done with the hope to provide new information about the hadronization process. Various measurements of the observables listed above have been performed for different initial quark types in events. There are also measurements of the total number of particles produced and the momentum spectrum of the particles for different hadron types.

The hadronization models predict the momentum spectrum of the produced hadrons of each type. To test the predictions from the models, we present measurements of the production fractions of $\pi^\pm$, $K^\pm$, p/$\bar{\text{p}}$ as a function of hadron momentum in Z^0 decay events at the SLD. Approximately 350,000 hadronic Z^0 decays were produced by the SLAC Linear Collider (SLC) and collected by the SLC Large Detector (SLD) during the 1997–98 run period. For the present analysis, about 223,000 hadronic Z^0 decay events are selected by requiring that they are contained within the acceptance of the SLD, and that they are logged during the run period when the Cherenkov Ring Imaging Detector (CRID) is operating properly. The CRID provides an excellent measurement of the velocities of charged hadrons by measuring the opening angle of the cone of Cherenkov photons emitted as a charged track passes through the liquid and gas radiators. The SLD Central Drift Chamber (CDC) provides a good measurement of the charged hadron momenta. By combining the measured velocity and momentum of a charged hadron, the mass of the hadron can be determined. Particle identification is performed over a broad hadron momentum range using the calculated mass of each hadron.

The production fractions of $\pi^{\pm}$, $K^{\pm}$, p/$\bar{\text{p}}$ are investigated more deeply by repeating the analysis on sub-samples of the data in which the Z^0 decay initial quark type is tagged. The properties of the produced hadron spectra from uds, c, and b quarks are expected to be different due to the larger mass of the c and b quarks compared to the uds quarks. Furthermore, the hadronization models use the assumption of light quarks. Therefore measurements in uds quark event tagged samples allow more accurate tests of these models. By using the SLD silicon CCD based Vertex Detector (VXD3) which precisely measures the position of hadrons, and the stable and small SLC beam overlap region at the e^+e^- collision, charged hadrons (tracks) and secondary vertices displaced from the e^+e^- beam Interaction Point (IP) can be found. Since c and b hadrons have millimeter decay lengths, selection of light (uds), c and b quark event is possible by finding these tracks and vertices.

Because of parity violation of Z^0 bosons in the weak interation, the decays of the longitudinally polarized Z^0's produced by the SLC exhibit a large asymmetry in the distribution of the polar angle of the quark axis. This asymmetry allows us to separate quark and antiquark jets, and to measure differences in hadron production in these jets. Also, leading particles which contain the initial quark and carry a large fraction of the initial quark energy can be studied using high momentum hadrons.

Finally, a comparison of particle production in quark and gluon jets is done to study the jet fragmentation and to test the universality of the hadronization process. High purity gluon jets are tagged in three-jet events and compared with quark jets. Heavy quark (c,b) jets are rejected from our quark jet samples in order to compare only gluon jets and massless quark jets. Differences in inclusive properties in high energy gluon jets and light quark jets are predicted from perturbative QCD. Gluons are expected to radiate more gluons than quarks do at the same energy. Other experiments have observed that gluons have a higher multiplicity and a softer energy spectrum (Sect. 6.4). The differences in hadron production fractions between massless quarks and gluons are expected to be independent of hadron types, apart from kinematic effects.

This thesis is organized as follows. In Chapter 2, a review of the Standard Model including the electroweak theory and QCD is presented. Also the phenomenological hadronization models are briefly discussed. Chapter 3 contains an overview of the SLC accelerator and the SLD detector facilities. The description of event and track selections are included in Chapter 4, followed by a discussion of the event flavor tags and quark and gluon jet tagging methods. In Chapter 5, the particle identification efficiencies using the Cherenkov Ring Imaging Detector (CRID) as well as the particle identification achieved by the CRID are presented. Detailed descriptions of particle production rates of $\pi^{\pm}$, $K^{\pm}$, p/$\bar{\mathrm{p}}$ for different analyses are discussed in Chapter 6. Comparisons are made with previous experiments and with the predictions of fragmentation models. Chapter 7 summarizes the results of the analyses.

Chapter 2

Theory

2.1 The Standard Model

The Standard Model is a Lagrangian field theory which describes fermions and their electroweak and strong interactions. These interactions are gauge fields resulting from requiring local gauge invariance. The framework of the Standard Model(SM) [13] is based on the gauge symmetry group describing the interactions of the fields and the invariance of the Lagrangian under local symmetry transformations. The Lagrangian of the Model is composed of kinetic energy terms and all possible interaction terms of the fields which are gauge invariant. The SM has the gauge symmetry group SU(3)$\bigotimes$SU(2)$\bigotimes$U(1). The SU(3) is the color symmetry group which describes the coupling of gluons to quarks. The SU(2)$\bigotimes$U(1) [14],[15],[16] describes the weak isospin and weak hypercharge symmetries of the coupling of $W^{\pm}$, Z^0, and photons to the fermions. The fundamental fermions and gauge bosons of the SM are summerized in Table 2.1 and table 2.2.

The electric charge, Q is a combination of the 3^{rd} component of the weak isospin T^3, and the weak hypercharge Y,

$$Q = T^3 + \frac{Y}{2}. \tag{2.1}$$

At different energies these interactions sample different degrees of freedom from the vacuum so the measured coupling strengths change with the energy scale. The coupling strengths can be renormalized using a cutoff mass μ to eliminate divergences in loop contributions to the couplings.

When using a renormalized coupling constant defined at some scale μ, the loop contribution contains logarithms of order $\ln(E/\mu)$ where E is the typical energy scale of the

Fermion families			Quantum numbers		
1^{st}	2^{nd}	3^{rd}	Q	T^3	Y
$\begin{pmatrix} \nu_e \\ e \end{pmatrix}_L$	$\begin{pmatrix} \nu_\mu \\ \mu \end{pmatrix}_L$	$\begin{pmatrix} \nu_\tau \\ \tau \end{pmatrix}_L$	$\begin{pmatrix} 0 \\ -1 \end{pmatrix}$	$\begin{pmatrix} \frac{1}{2} \\ -\frac{1}{2} \end{pmatrix}$	$\begin{pmatrix} -1 \\ -1 \end{pmatrix}$
$\begin{pmatrix} u \\ d \end{pmatrix}_L$	$\begin{pmatrix} c \\ s \end{pmatrix}_L$	$\begin{pmatrix} t \\ b \end{pmatrix}_L$	$\begin{pmatrix} \frac{2}{3} \\ -\frac{1}{3} \end{pmatrix}$	$\begin{pmatrix} \frac{1}{2} \\ -\frac{1}{2} \end{pmatrix}$	$\begin{pmatrix} \frac{1}{3} \\ -\frac{1}{3} \end{pmatrix}$
e_R	μ_R	τ_R	-1	0	-2
u_R	c_R	t_R	$\frac{2}{3}$	0	$\frac{4}{3}$
d_R	s_R	b_R	$-\frac{1}{3}$	0	$-\frac{2}{3}$

Table 2.1: Properties of the three fundamental fermion families

Name	Charge (e)	Mass (GeV/c^2)	spin	Other
γ	0	$< 2 \times 10^{-25}$	1	Stable
g	0	0	1	SU(3) color octet
$W^\pm$	±1	80.41 ± 0.10	1	$\Gamma = 2.06 \pm 0.06$ GeV
Z	0	91.187 ± 0.007	1	$\Gamma = 2.490 \pm 0.007$ GeV

Table 2.2: The Standard Model spectrum of gauge bosons

process being calculated. In order to ensure quick convergence of the perturbative expansion, the coupling constants must be calculated using a scale μ of the same order of E so that $\ln(E/\mu)$ contribution to the coupling constants stays small. The energy dependence of the couplings can be described by a differential equation and by integrating the differential equation we can relate the coupling constant for the scale that we are interested in to the coupling constants previously measured at a different energy.

2.2 Electroweak Interaction

The electroweak theory is based on $\mathrm{SU}(2)_L \bigotimes \mathrm{U}(1)$ gauge symmetry which represents the unification of the electromagnetic and weak interactions. The electroweak force is mediated by spin 1 gauge bosons. $\mathrm{SU}(2)_L$ denotes that for known matter fields, only left-handed fermions carry SU(2) charge. The left- and right-handed helicity projection operators are defined as

$$
\begin{aligned}
P_L &= \frac{1}{2}(1-\gamma^5) \\
P_R &= \frac{1}{2}(1+\gamma^5)
\end{aligned} \tag{2.2}
$$

where γ^μ are the Dirac matrices and $\gamma^5 = i\gamma^0\gamma^1\gamma^2\gamma^3$.

Quantum electrodymanics (QED) is developed from the interaction term which results from requiring the Lagrangian to be invariant under a local phase change of the matter fields. The interaction term is

$$-ieJ_\mu^{em}A^\mu = -ie(\bar{\psi}\gamma_\mu Q\psi)A^\mu \tag{2.3}$$

where the electromagnetic current J_μ^{em} couples to the photon (A^μ) and $-e$ is the electron charge. Q is the charge operator and ψ is the spinor wavefunction, with its adjoint being $\bar{\psi} = \psi^\dagger\gamma^0$.

The electroweak interaction process consists of an $SU(2)$ isotriplet of vector fields W_μ^i ($i = 1, 2, 3$) coupled with strength g to the weak isospin current, J_μ^i, with a single $U(1)$ vector field B_μ coupled to the weak hypercharge current, J_μ^Y with strength $(g\prime)/2$ [13]. Therefore the interaction is

$$-ig(J^i)^\mu W_\mu^i - i\frac{g\prime}{2}(J^Y)^\mu B_\mu. \tag{2.4}$$

The charged fields for the interaction are defined as :

$$W_\mu^\pm = \frac{1}{\sqrt{2}}(W_\mu^1 \mp iW_\mu^2). \tag{2.5}$$

W_μ^3 and B_μ are neutral fields and these two neutral fields are linearly combined to produce the mass eigenstate fields A_μ and Z_μ:

$$
\begin{aligned}
A_\mu &= B_\mu\cos\theta_W + W_\mu^3\sin\theta_W \\
Z_\mu &= -B_\mu\sin\theta_W + W_\mu^3\cos\theta_W
\end{aligned} \tag{2.6}
$$

where θ_W is called the Weinberg or weak mixing angle. The neutral current interaction term can be expressed as:

$$
\begin{aligned}
&-igJ^3_\mu(W^3)^\mu - i\frac{g\prime}{2}J^Y_\mu B^\mu = \\
&\quad -i(g\sin\theta_W J^3_\mu + g\prime\cos\theta_W\frac{J^Y_\mu}{2})A^\mu \\
&\quad -i(g\cos\theta_W J^3_\mu - g\prime\sin\theta_W\frac{J^Y_\mu}{2})Z^\mu. \qquad (2.7)
\end{aligned}
$$

Comparing the expression in the parenthesis of the first term with the electromagnetic current from equation 2.3:

$$J^{em}_\mu = J^3_\mu + \frac{1}{2}J^Y_\mu \qquad (2.8)$$

we obtain the relation of the mixing angle to the coupling strengths:

$$
\begin{aligned}
g\sin\theta_W &= g'\cos\theta_W = e \\
\tan\theta_W &= g\prime/g \qquad (2.9)
\end{aligned}
$$

The second term of the equation 2.7 can be expressed as weak neutral current, J^{NC}_μ

$$-i\frac{g}{\cos\theta_W}(J^3_\mu - J^{em}_\mu\sin^2\theta_W)Z^\mu = -i\frac{g}{\cos\theta_W}J^{NC}_\mu Z^\mu \qquad (2.10)$$

The weak neutral current can be obtained using the equation as

$$J^{NC}_\mu = J^3_\mu - J^{em}_\mu\sin^2\theta_W \qquad (2.11)$$

The $Zf\bar{f}$ vertex factor can be obtained from the expression of the neutral current in terms of the fermion fields :

$$
\begin{aligned}
-i\frac{g}{\cos\theta_W}J^{NC}_\mu Z^\mu &= -i\frac{g}{\cos\theta_W}\bar{\psi}_f\gamma^\mu\left(\frac{1}{2}(1-\gamma^5)T_3 - Q\sin^2\theta_W\right)\psi_f Z_\mu \\
&= -i\frac{g}{2\cos\theta_W}\gamma^\mu(v_f - a_f\gamma^5) \qquad (2.12)
\end{aligned}
$$

where v_f and a_f are the vector and axial-vector couplings at this vertex respectively, which are determined in SM with the given $\sin^2\theta_W$ value.

$$\begin{aligned} v_f &= T_{3,f} - 2Q_f \sin^2\theta_W \\ a_f &= T_{3,f} \end{aligned} \tag{2.13}$$

The vector and axial-vector couplings of the fermions to the Z^0 are summarized in Table 2.3.

Table 2.3: Vector couplings and axial-vector couplings of the Z^0 to fundamental fermions.

Fermion	a_f	v_f
$\nu_e,\ \nu_\mu,\ \nu_\tau$	$+\frac{1}{2}$	$+\frac{1}{2}$
$e,\ \mu,\ \tau$	$-\frac{1}{2}$	$-\frac{1}{2} + 2\sin^2\theta_W$
$u,\ c,\ t$	$+\frac{1}{2}$	$+\frac{1}{2} - \frac{4}{3}\sin^2\theta_W$
$d,\ s,\ b$	$-\frac{1}{2}$	$-\frac{1}{2} + \frac{2}{3}\sin^2\theta_W$

Particles are believed to acquire mass through the Higgs mechanism [17],[18]. A component of an isospin doublet of scalar Higgs fields condenses in the vacuum as the universe cools down. The SU(2)$\bigotimes$U(1) symmetry is spontaneously broken, by the vacuum state to a single U(1) symmetry. The remaining U(1) describes the electromagnetic interaction through a massless photon field. The vacuum expectation value of the Higgs generates masses for the electroweak gauge bosons through the gauge interaction terms. Through the Yukawa interaction terms of fermions to the Higgs field in the Lagrangian, the fermion masses are generated. The Higgs field has not been directly detected yet.

2.3 Polarized e^+e^- scattering at the Z^0 pole

$e^+e^- \to f\bar{f}$ process occurs through mediating neutral vector gauge bosons, such as the photon γ and the Z^0. The tree level Feynman diagram for the process is depicted in Figure 2.1.

The cross section proportional to the square of the matrix elements from both diagrams is represented as:

$$\frac{d\sigma}{d\Omega} = \frac{1}{64\pi^2 s}\frac{p_f}{p_e}|\mathcal{M}_{Z^0} + \mathcal{M}_\gamma|^2 \tag{2.14}$$

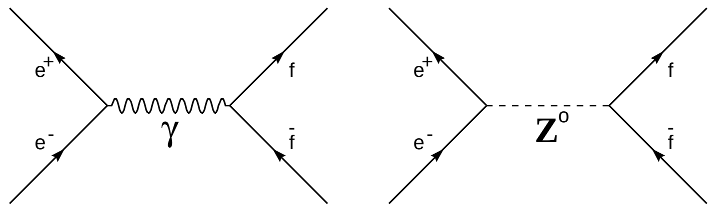

Figure 2.1: The s channel tree level Feynman diagrams for $e^+e^- \to f\bar{f}$

where $\mathcal{M}_{Z^0}$ and $\mathcal{M}_\gamma$ are the matrix elements for Z^0 and γ exchange respectively, and $\sqrt{s}$ is the center of energy, and p_e and p_f are the momenta of the initial electron and final fermion. Figure 2.2 shows the cross section distribution for $e^+e^- \to hadrons$. At Z^0 pole the Z^0 exchange process is predominant and both the electromagnetic contribution and the $\gamma - Z^0$ interference terms are negligible. The ratio of the Z^0 interaction to the γ interaction is ~ 800.

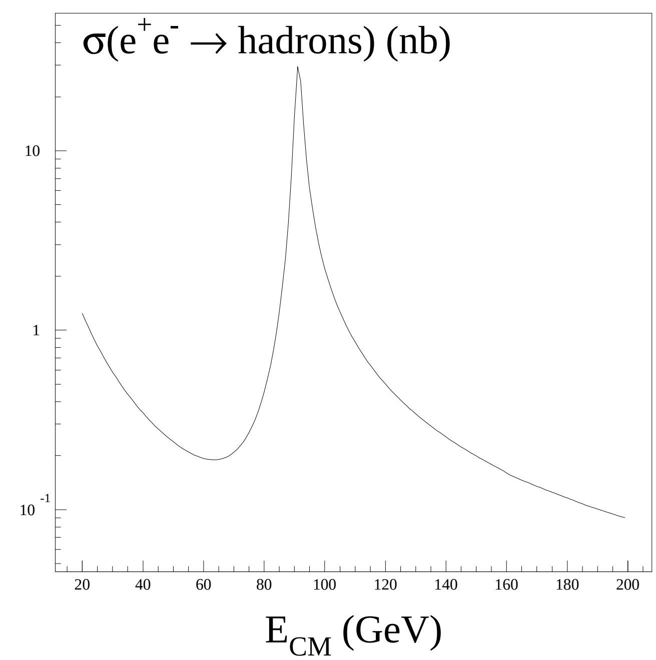

Figure 2.2: The cross section for $e^+e^- \to hadrons$

The amplitude of the Z^0 exchange process calculated using the Feynman rules is

$$\mathcal{M}_{Z^0} = -\frac{g^2}{4\cos^2\theta_W}\left\{\bar{f}\gamma^\nu\left(v_f - a_f\gamma^5\right)f\right\}\frac{g_{\nu\mu} - k_\nu k_\mu/M_{Z^0}^2}{k^2 - M_{Z^0}^2 + iM_{Z^0}\Gamma_{Z^0}}\left\{\bar{e}\gamma^\mu\left(v_e - a_e\gamma^5\right)e\right\}, \tag{2.15}$$

where f and e represent the fermion and electron spinor wavefunctions respectively, M_{Z^0} and Γ_{Z^0} are the mass and width of the Z^0, and k is the 4-momentum of the virtual Z^0.

In order to express $\mathcal{M}_{Z^0}$ explicitly in terms of the left- and right-handed spinor, couplings c_L^f and c_R^f are defined by combinations of v_f and a_f:

$$\begin{aligned} c_L^f &= \frac{1}{2}(v_f + a_f) \\ c_R^f &= \frac{1}{2}(v_f - a_f). \end{aligned} \tag{2.16}$$

Differential cross sections for left- and right-handed electrons can be calculated [19] using c_L^f and c_R^f, summing the final-stage fermion spins:

$$\frac{d\sigma_L}{d\Omega} \propto ({c_R^f}^2 + {c_L^f}^2)(1+x^2) - 2({c_R^f}^2 - {c_L^f}^2)x \tag{2.17}$$

$$\frac{d\sigma_R}{d\Omega} \propto ({c_R^f}^2 + {c_L^f}^2)(1+x^2) + 2({c_R^f}^2 - {c_L^f}^2)x \tag{2.18}$$

where the index L and R denote the helicity of the incoming electron, and $x = \cos\theta$, where θ is the polar angle of the final state fermion f with respect to the electron beam direction. For a partially polarized electron beam and an unpolarized positron beam, the differential production cross section at the Born level can be written as:

$$\frac{d\sigma^f}{d\Omega} \propto (1 - A_e P_e)(1+x^2) + 2A_f(A_e - P_e)x \tag{2.19}$$

where P_e is the longitudinal polarization of the electron beam and the coupling parameter, $A_f(A_e)$ is defined in terms of the left- and right-handed couplings as

$$A_f = \frac{(c_L^f)^2 - (c_R^f)^2}{(c_L^f)^2 + (c_R^f)^2} = \frac{2v_f a_f}{v_f^2 + a_f^2} \tag{2.20}$$

The differential cross sections normalized to the total cross section for three different

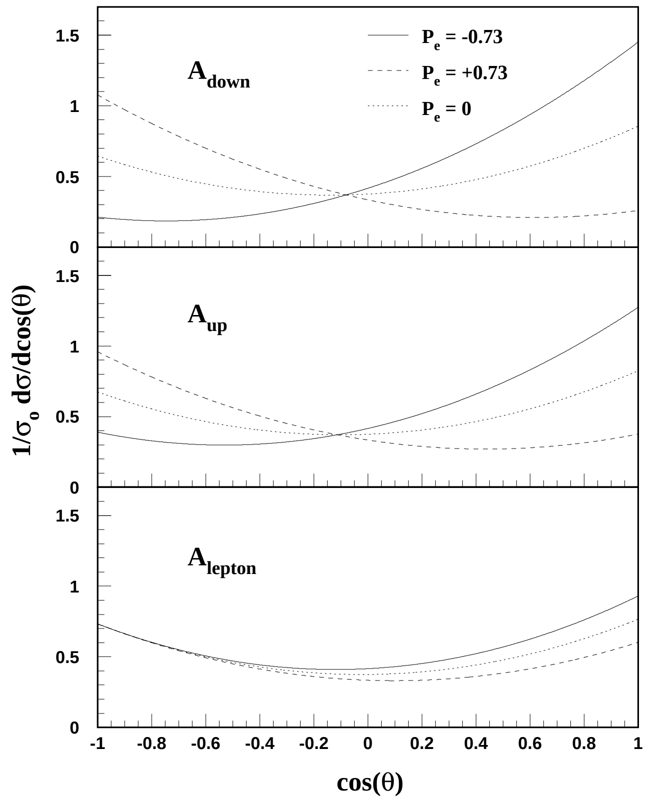

Figure 2.3: Normalized production cross section for different electron polarization

values of P_e, ± 0.73 and 0 (unpolarized) are shown in Figure 2.3. The distributions for u and d quarks and the charged leptons with the assumption of $A_e = 0.15$ are presented in the Figure. It shows the large asymmetry in $\cos\theta$ for non zero P_e. It also shows that negative (left-handed) polarization has a greater cross section than that of positive (right-handed) polarization, which indicates that the coupling of Z^0 is stronger to the left handed fermions.

Asymmetry studies have been done using the polarization of the electron beam at SLD

.

2.4 Quantum Chromodynamics

Quantum Chromodynamics (QCD)[1],[2],[3] is a theory of the strong interaction which uses a non-abelian gauge symmetry group, SU(3)$_{color}$ with eight gauge fields. The QCD gauge bosons are called gluons (g). Gluons have cubic (ggg) and quartic ($gggg$) self-interaction which is a property of non-abelian gauge symmetry groups. Due to self-interactions of virtual and real gluons, the strong coupling $\alpha_s(Q^2)$ decreases as energy increases. So

$\alpha_s(Q^2)$ is small for short distance (high energy) interactions and becomes large in long distance (low energy) interactions. Neither free gluons nor free quarks have been observed, instead only color singlet hadrons formed by quarks have been observed. The QCD running coupling including one-loop contribution in Feynman diagrams can be written:

$$\alpha_s(Q^2) = \frac{\alpha_s(\mu^2)}{1 + \frac{\alpha_s(\mu^2)}{12\pi}(11N_c - 2n_f)\ln(\frac{Q^2}{\mu^2})}, \tag{2.21}$$

where $\alpha_s(\mu^2)$ is the strong coupling constant at an arbitrary renomalization scale μ^2. $N_c = 3$ denotes the number of colors, and n_f is the number of quark flavors with mass less than the energy scale Q. The strong force is *asymptotically free*. This terminology essentially means that as the energy of a process increases, the strength of the strong force decreases and the quarks and gluons become quasi-free. Perturbative QCD can be applied to calculate the strong interaction process at high energy scale by virtue of *asymptotic freedom*. The coupling constant in QCD is close to unity at the proton mass scale. It is conventional to denote the Q^2 scale at which the coupling constant is large by Λ^2_{QCD}, where Λ^2_{QCD} is defined as:

$$\log\Lambda^2_{QCD} = -\frac{4\pi}{\beta_0\alpha_s(\mu^2)} + \ln(\mu^2), \tag{2.22}$$

Where $\beta_0 = 11 - \frac{2}{3}n_f$. Then the coupling constant is expressed as

$$\alpha_s(Q^2) = \frac{4\pi}{\beta_0\ln(Q^2/\Lambda^2_{QCD})}. \tag{2.23}$$

For Q^2 is much bigger than Λ^2_{QCD}, the effective coupling is small and a perturbative description of the strong interaction is applicable, but when Q^2 is comparable to Λ^2_{QCD}, quarks and gluons are strongly bound and form color neutral states whose masses are dominated by the binding energy. These composite particles are called hadrons. Therefore at the hadron mass scale the coupling is too large to apply perturbation theory. Λ_{QCD} is a boundary between quasi-free quarks and gluons and bound hadron states. The value of Λ_{QCD} must be determined from experiment and value is measured in the range 0.1 to 0.5 GeV. At the Z^0 mass pole the strong coupling α_s is about 0.12, and so higher orders in perturbation theory give non-negligible contributions to strong interaction amplitudes.

If the strong coupling α_s is large, the perturbative QCD can not be applied. Therefore more loops must be included to the calculation of a physics quantity. However, there is no exact way to calculate all the loops in this non-perturbative process. There are few theoretical calculations in the non-perturbative regime. Some numerical evaluations of path integrals for non-perturbative process (Lattice QCD [20],[21]) have succeeded in predicting the energy spectrum and decays of hadrons, but there is no real theoretical understanding of quark confinement or chiral symmetry breaking.

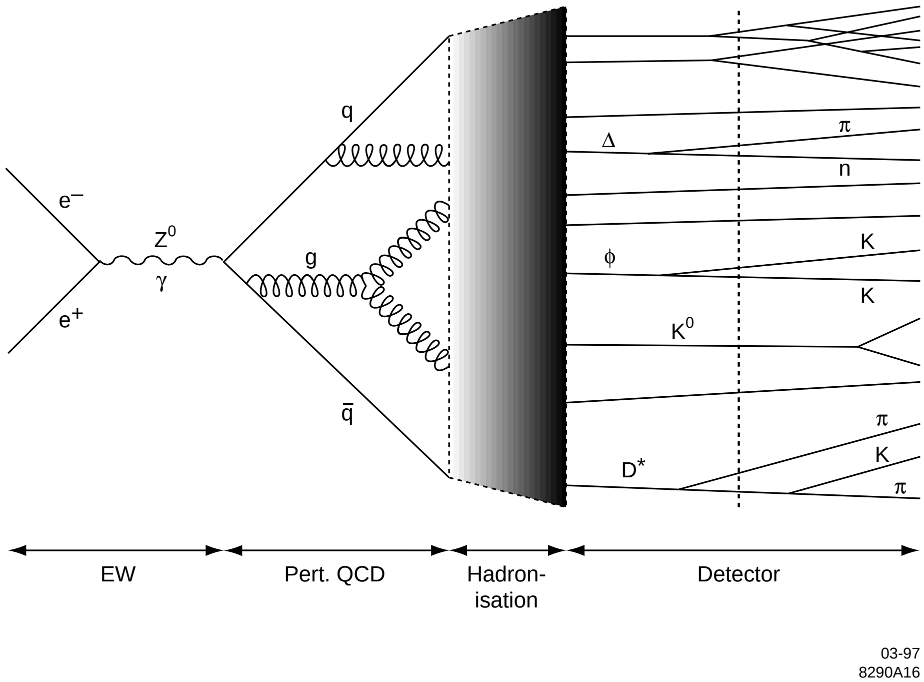

Figure 2.4: $e^+e^- \rightarrow hadrons$ process

2.5 Hadron Production in e^+e^- Collisions

The production of detectable hadrons from high energy partons (quarks and gluons) produced in the process $e^+e^- \rightarrow Z^0/\gamma \rightarrow f\bar{f}$ can be divided into several stages as depicted in Fig. 2.4.

Production of partons: In this early stage, the amplitude for the production of a quark and anti-quark pair is calculated from electroweak interaction.

Perturbative evolution of the partons:

The quark and anti-quark pair has a small α_s because particles are produced with high energy $\sim M_{z^0}/2$. Therefore the quark and anti-quark can evolve according to perturbative QCD as long as α_s stays small. The evolution in this stage can be described by two approaches, the fixed order matrix element method and the parton shower model. The fixed order matrix element is an exact way to calculate the cross sections of q and g production by calculating Feynman diagrams to all orders of α_s. The parton shower approach does not use the full matrix elements but instead simplified approximations for kinematics and the interference of gluons and quarks.

Feynman diagrams of the cross section for $q\bar{q}g$ production in the first order $\mathcal{O}(\alpha_s)$ can be calculated in the fixed order matrix element approach [22]. The different cross section for $q\bar{q}g$ is given by:

$$\frac{d^2\sigma}{dx_1 dx_2} = \sigma_0 \frac{\alpha_s}{2\pi} \frac{x_1^2 + x_2^2}{(1 - x_1)(1 - x_2)}, \tag{2.24}$$

where σ_0 is the tree level cross section for $e^+e^- \rightarrow q\bar{q}$ and $x_i = 2E_i/\sqrt{s}$ are the center of mass energy fractions of the massless quarks. This equation is divergent in the limit of $x_1, x_2 \rightarrow 1$. However the divergence is canceled by the corresponding singularity from one-loop correction in the propagator in the Feynman diagrams with opposite sign so the total cross section is finite. Higher orders of α_s are included in the three jet cross section [23],[24]. The second order perturbative QCD correction in the amplitude for $e^+e^- \rightarrow$ 4-jets is calculated in references [25],[26],[27].

In principle, the matrix element method is the correct approach but calculations for higher order corrections are very complicated due to the large number of Feynman diagrams. As a practical approach, parton evolution can be performed by the parton shower model. The parton shower model is based on the Leading Logarithm Approximation(LLA) [28],[29]. The perturbative expansion of the fixed order matrix element can be rearranged in terms of

$$\sum_{n=1}^{\infty} a_n(\alpha_s(Q^2)\log(Q^2/\Lambda_{QCD}^2))^n + \alpha_s(Q^2)\sum_{n=1}^{\infty} b_n(\alpha_s(Q^2)\log(Q^2/\Lambda_{QCD}^2))^n + \cdots \tag{2.25}$$

The first sum in the above equation represents the LLA contribution. The LLA does not include the gluon interference terms. The LLA contribution is used in a function of parton's energy distribution to describe the evolution of gluons.

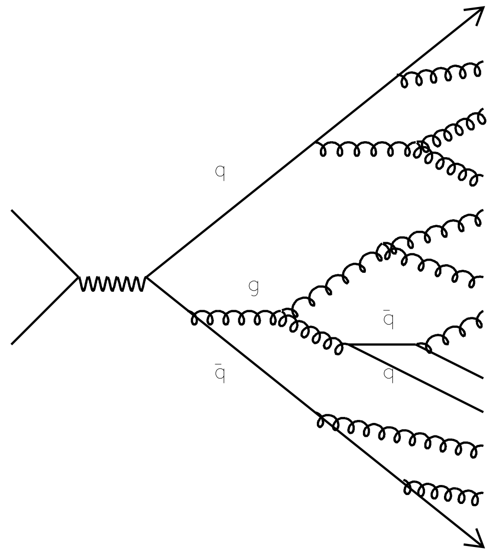

Figure 2.5: Parton shower (fragmentaion)

In the parton shower approach, partons are generated by successive branchings of partons, as shown in Fig. 2.5, according to parton splitting function $P_{a\to bc}(x)$ given as:

$$
\begin{aligned}
P_{q\to qg}(x) &= \frac{4}{3}\left(\frac{1+x^2}{1-x}\right), \\
P_{q\to gq}(x) &= P_{q\to gq}(1-x), \\
P_{g\to gg}(x) &= 6\left(\frac{1-x}{x}+\frac{x}{1-x}+x(1-x)\right) \\
P_{g\to q\bar{q}}(x) &= \frac{1}{2}(x^2+(1-x)^2)
\end{aligned}
\tag{2.26}
$$

where x is the fraction of the 4-momentum of the initial parton that the final parton contains. The probability $\mathcal{P}$, of a branching of partons depends on the strong coupling constant, the 4-momentum fraction x, and $\ln(Q^2/\Lambda^2_{QCD})$ as well as the splitting function. The probability that a branching $a \to bc$ takes place during a small change $dt = dQ^2/Q^2$ of the evolution time parameter $t = \ln(Q^2/\Lambda^2)$ is given by [30]:

$$\frac{d\mathcal{P}_{a\to bc}(t)}{dt} = \int dx \frac{\alpha_s(t)}{2\pi} P_{a\to bc}(x) \tag{2.27}$$

The successive branching is terminated when the process reaches the hadron mass scale.

The parton shower approach is expected to describe the substructure of the initial q and the emitted g's. The parton shower approach using the LLA gives a good prediction of the sub-structure of each jet. However, the parton shower approach cannot predict the absolute value of n-jet event rates.

The Modified-LLA (MLLA) [31] includes the infinite sum of $\alpha_s^n(Q^2)\ln^{2n}(Q^2/\Lambda_{QCD}^2)$ in addition to the LLA contribution with incorporation of angular ordering. The MLLA gives a better description of the topology of gluon emission and the mean gluon multiplicity.

The Next-to-LLA (NLLA) [32] includes sub-leading corrections which is the second term in equation 2.25.

Hadronization: After the partons from the previous stage reach the hadron mass scale, they become bound and form colorless primary hadrons. This process occurs at energies around Λ_{QCD} so the interactions are non-perturbative and not well understood. Several phenomenological models have been adopted as a description. These models are discussed later in detail.

Final state hadrons: Primary hadrons coming from the fragmentation process decay into stable final state particles observable in a detector. Production rates and branching ratios for different particle species are measured in experiments.

2.6 Hadronization

Hadronization is the process in which final partons convert into the primary hadrons. This process happens at a relatively low energy scale compared to parton level and so the strong coupling constant α_s is large and perturbation theory is not applicable. The hadronization process is not fully understood. Some phenomenological models of the hadronizaion process are JETSET [4], HERWIG [5] and UCLA [6].

2.6.1 Cluster hadronization

HERWIG is a cluster hadronization model that the partons at the end of perturbative shower are combined into color singlet clusters. A quark joins with a neighboring anti-quark with opposite color to form a colorless cluster. Remaining gluons at energy of the order of Λ_{QCD} are split into light quark and anti-quark pairs. Once clusters are formed, each cluster locally decays into primary hadrons in phase space: Local parton hadron duality (LPHD), predicts that inclusive distributions of primary hadrons are very similar to those of the final partons except for some correction factors coming from soft gluon emission in the hadronization. A diagram of the cluster hadronization is shown Fig. 2.6.

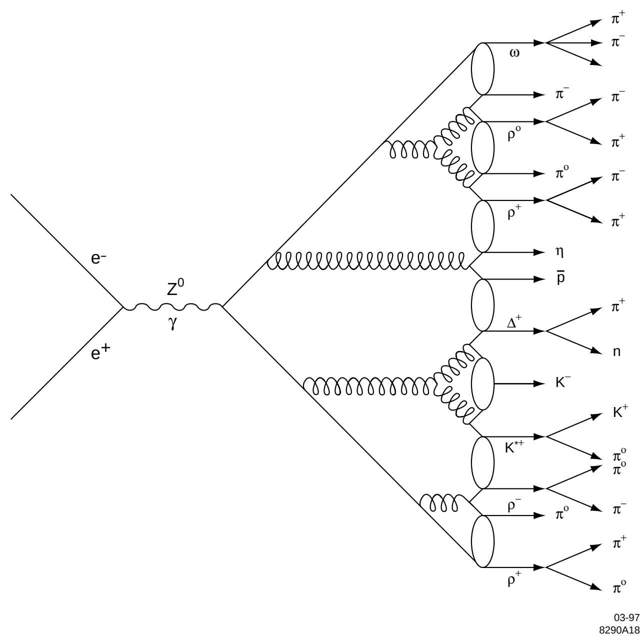

Figure 2.6: HERWIG hadronization

A cluster is characterized by its total mass and total flavor contents. The clusters normally decay into two hadrons, but when a cluster is very heavy it forcibly splits into two lighter clusters first and then decays into hadrons. Occasionally, a light cluster can decay into one hadron. The selection of flavors and spins for the primary hadrons in the cluster decays is based on the amount of phase space available. HERWIG does not describe the production of heavy quark energy spectrum very well.

2.6.2 Independent hadronization

Each parton in the hadronization is treated as a sequence of universal iterative branching based on the excitation of quark pairs. An initial quark with well defined momentum and energy is split into a hadron, qq' and a remaining q'. The momentum and energy of qq' are given by a fragmentation function $f(z)$ where z is the fraction of energy plus longitudinal momentum taken by qq'. The remaining q' produces more hadrons. Flavor and transverse momentum is locally conserved throughout the process. The process of producing hadrons is iterated until the remaining quark's energy is too low to split. The fragmentation function $f(z)$ used is the same in each step.

We do not use this hadronization model for the analyses.

2.6.3 String hadronization

JETSET

String Fragmentation is inspired by the assumption that the strong interaction is linearly confined in QCD at large distances. When a pair of oppositely colored quarks (q and $\bar{q}$) recede from each other they form a color field or color tube called a string which has stored potential energy. The transverse dimensions of the tube are ~ 1 fm. The string is assumed to be uniform without any transverse degrees of freedom. When the string has large enough potential energy, it produces $q\bar{q}$ which form color-singlet systems with the intial $q\bar{q}$-pair and the string breaks into two strings according to a fragmentation function. This process iterates until only on shell hadrons remain. Each primary hadron corresponds to a small piece of string with a q at one end and a $\bar{q}$ at the other end. In order to produce the transverse momentum and mass for the $q\bar{q}$ pair quantum mechanical tunnelling is required. The tunnelling process separates q and $\bar{q}$ generated at a point. The total transverse momentum of a hadron comes from the transverse momentum contributions of the q and $\bar{q}$ which are bound to form the hadron. The tunnelling probability which is the probability of the appearance of the $q\bar{q}$ depends on the transverse mass of the quark, $m_\perp^2 = m^2 + p_\perp^2$. The probability p is given by in terms of the transverse mass $m_\perp^2$

$$p = \exp(-\pi \frac{m_\perp^2}{\kappa}) \tag{2.28}$$

where κ is the string constant which characterizes the amount of stored potential energy per unit length and has a value of $\kappa \approx$1 Gev/fm.

In general, the different string breakings are causally disconnected, therefore the breakings can be described in any suitable order. Hadronization processes which start at the q

end of the system and fragment towards the $\bar{q}$ end must be equivalent to processes which start at the $\bar{q}$. The process is left-right symmetry. The breakings can be modelled using an iterative scheme for the hadronization. Including this statistical left-right symmetry the Lund symmetric fragmentation function (LSFF) can be written as

$$f(z) \propto \frac{1}{z}(1-z)^a \exp\left(-\frac{bm_\perp^2}{z}\right) \tag{2.29}$$

where z is the fraction of energy plus longitudinal momentum of the parent quark that the produced $q\bar{q}$ pair carries away. The coefficient a relates to the parent quark flavor and b to flavor of the q and $\bar{q}$ produced in the string. The LSFF is interpreted as a probability to select the value of z for a hadron, once the choice of the mass and $p_\perp^2$ of the hadron has already been made. Therefore $\exp(-bm_\perp^2/z)$ term is not used for the heavy hadron suppression. Instead, a number of suppressions are controlled by input parameters of the model.

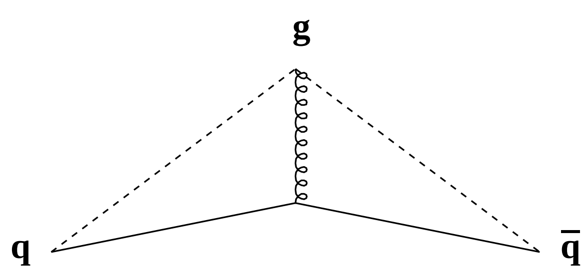

Figure 2.7: A gluon kink in $q\bar{q}g$ case

For $q\bar{q}g$ production a string is stretched from the q end via the g to the $\bar{q}$ end, and as a result the gluon has two string pieces attached (Fig. 2.7). The gluon is a kink on the string carrying energy and momentum. JETSET has a large number of input parameters that control the type of primary hadron produced at each string break. It predicts flavored hadronic production rates and topological event distributions such as the transverse momentum distributions rather well.

UCLA

The UCLA model uses the LSFF summed over all hadrons. The hadronization is performed by an integrated functional form determined by (*i*) four momentum conservation, (*ii*) a phase space with limited transverse momentum, (*iii*) flavor and energy dependent space-time area law, for the area the color string spans for a given hadron, (*iv*) Clebsch-Gordon coefficients for the spin and flavor of a hadron, (*v*) a spatial factor of the hadron wave function (the *knitting factor*). The *knitting factor* is assumed to be comparable for any kind of hadrons.

The UCLA model simply uses the weighted LSFF by the virtual $q\bar{q}$ pair vertex suppression, spatial knitting factor, and Clebsch-Gordon coefficients. The relative probability $P(m^2)$ to produce a hadron with given mass is proportional to the integrated functional form over the allowed values of z and $p_\perp$:

$$P(m^2) \propto \int_0^1 dz \int dp_\perp \frac{1}{z}(1-z)^a \exp\left(\frac{-b(m^2+p_\perp^2)}{z}\right) \tag{2.30}$$

The UCLA model does not need any restriction factors to reproduce certain properties of data such as the suppression of the production of strange hadrons and vector mesons. In this model, heavy hadron suppression comes from the $\exp(-bm^2/z)$ in the fragmentation function with no additional suppression factors for s and vector meson. This model predicts multiplicities, inclusive distributions and meson rates very well.

2.6.4 Heavy quark hadronization

Due to the larger mass of the heavy quarks (c, b), heavy quark hadronization is different from light quark hadronization. Primary hadrons carry most of heavy quark energy and harden the energy spectrum in its direction. A phenomenological heavy quark hadronization is described better by Peterson parameterization [33] than by hadronization models.

The Peterson fragmentation function is

$$f(z) \propto \frac{1}{z(1-\frac{1}{z}-\frac{\epsilon_q}{1-z})^2}, \tag{2.31}$$

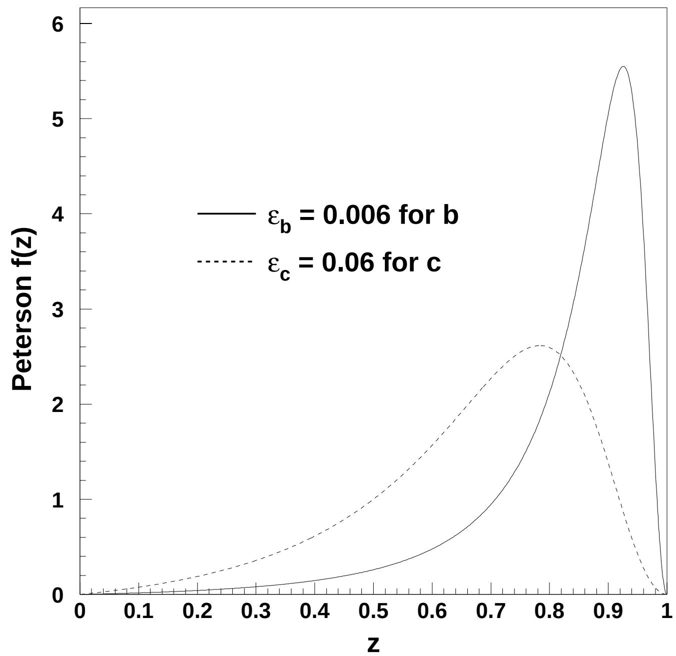

Figure 2.8: Peterson function for b and c quarks

where z is the fraction of the heavy quark momentum carried by the heavy hadron, $z = (E + p_{\|})_{hadron}/(E + p_{\|})_q$. ϵ_q is a free parameter which expected to scale between flavors as $\epsilon_q \propto 1/m_q^2$, where m_q is the mass of heavy quarks. This parameter is determined from experiments.

The Peterson fragmentation function using $\epsilon_b = 0.006$ for b quarks and $\epsilon_c = 0.06$ for c quarks is shown in Fig. 2.8.

The function for b quarks is peaked at high z. There are several more phenomenological models for the heavy quark hadronization and a detailed description can be found in Ref. [34].

Chapter 3

The Experimental Apparatus

The SLAC Linear Collider (SLC) and SLC Large Detector (SLD) are the experimental apparati used to collect the data presented in this thesis. The elements of SLC and SLD are discussed in this chapter.

3.0.5 SLAC Linear Collider

The SLAC Linear Collider(SLC) [35],[36],[37]is a $\sim$ 2 mile long linear electron-positron collider (Fig. 3.1). The SLC produces e^+e^- collisions at a center-of-mass energy of 91.26 GeV at a frequency of 120 Hz. Two longitudinally polarized electron bunches are generated by the source and accelerated to 1.19 GeV. The electron bunches are stored in the North damping ring where the electron spin is rotated into a vertical transverse direction by a spin-rotater magnet near the entrance of the damping ring. The damping ring reduces the transverse emittance of the bunches through synchrotron radiation [38]. Positron bunches are also accelerated to 1.19 GeV and stored in the South damping ring, where they are required to have two machine cycles in the damping ring. The positron bunch and the following two electron bunches then are accelerated through the Linac. The acceleration is supplied by Radio Frequency (RF) pulses from a series of Klystrons. At the end of the Linac, the positron and first electron bunches which have been accelerated up to 46.7 GeV are sent into separate arcs by dipole bending magnets in the Beam Switchyard. Each bunch loses about 1.1 GeV by synchrotron radiation in the 1 km arc when it reaches the Interaction Point (IP). In the arc, the electrons are going through rotations of the electron spin vector and the electrons become longitudinally polarized at the IP [39]. The final focus system makes the bunch size as small as possible to increase the luminosity. The bunches are compressed to $1.6\times0.8\times700$ μm for the 1996-98 run. The small and stable beam size is important to get a high Z^0 production rate. The peak luminosity of SLC was $\sim 3\times\ 10^{30}$ $cm^{-2}s^{-1}$.

The second electron bunch which is accelerated to 30 GeV in the Linac collides with a tungsten target to produce positrons. Positrons filtered from the resulting electromagnetic shower are accelerated and transported back to the front of the Linac.

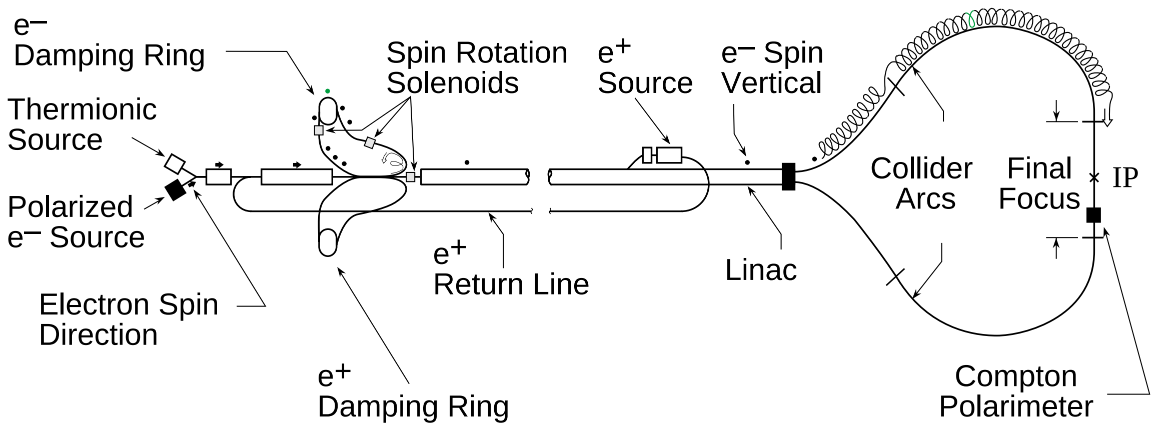

Figure 3.1: The SLC

3.0.6 Polarized Electron Beam Source

The SLC produces polarized Z^0 bosons from the collision of longitudinally polarized electrons with unpolarized positrons. To produce polarized electrons [40], light from a Nd:YAG-pumped Ti:sapphire laser is circularly polarized and brought onto a strained-lattice GaAs photocathode. The light excites electrons into longitudinally polarized states in the conduction band of the photocathode. The conduction band energy level is higher than the vacuum energy level, allowing the excited electrons to escape the photocathode. The energy level diagram of GaAs for the states is shown in Fig. 3.2.

The upper diagram is for bulk GaAs photocathode. The lower diagram is for a strained GaAs lattice which is a layer of GaAs deposited on a GaAsP substrate. The difference in the lattice spacings of the two materials breaks the state degeneracy. The diagram indicates that the maximum polarization achievable with bulk GaAs is 50% and strained GaAs can reach 100% polarization in principle.

In 1992, bulk GaAs photocathode was used to achieve 22% average electron beam

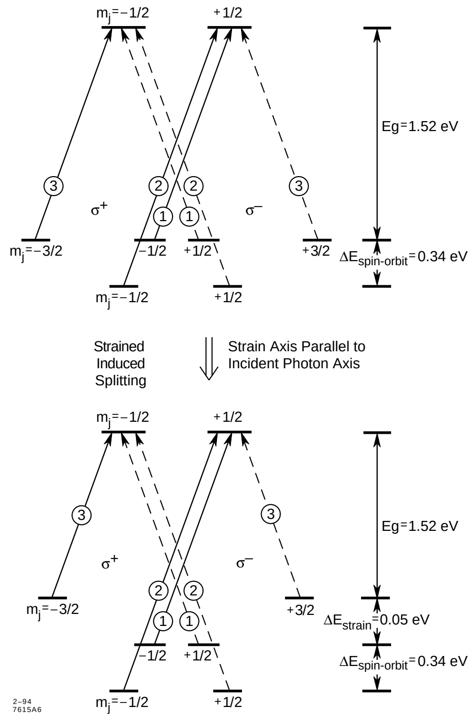

Figure 3.2: Energy level diagram for bulk GaAs (top) and strained GaAs (bottom).

polarization. In 1993, a strained photocathode with a GaAs layer of thickness 300 nm was installed, and more than 60% polarization was attained. Later a thinner layer of 100 nm was used, improving the polarization up to 77% in the 1994-98 run periods.

3.0.7 Compton Polarization

The Compton Polarimeter [41],[42] measures the SLC electron beam polarization using the helicity asymmetry in the Compton scattering cross section. At a point 33 m downstream from the SLC interaction point, circularly polarized photons with 2.33 eV from a frequency-doubled YAG laser collide with the electron beam. The Compton Polarimeter is shown in Fig. 3.3.

The back scattered electrons which lose energy in the photon collision are bent away from the main electron beam by an analyzing bend magnet and directed to a 9 channel Cherenkov detector. The energy spectrum of the scattered electrons is determined by measuring their deflection angles using the device. The Cherenkov detector contains propane gas radiators. The scattered electrons generate Cherenkov photons in the radiators, and the photons

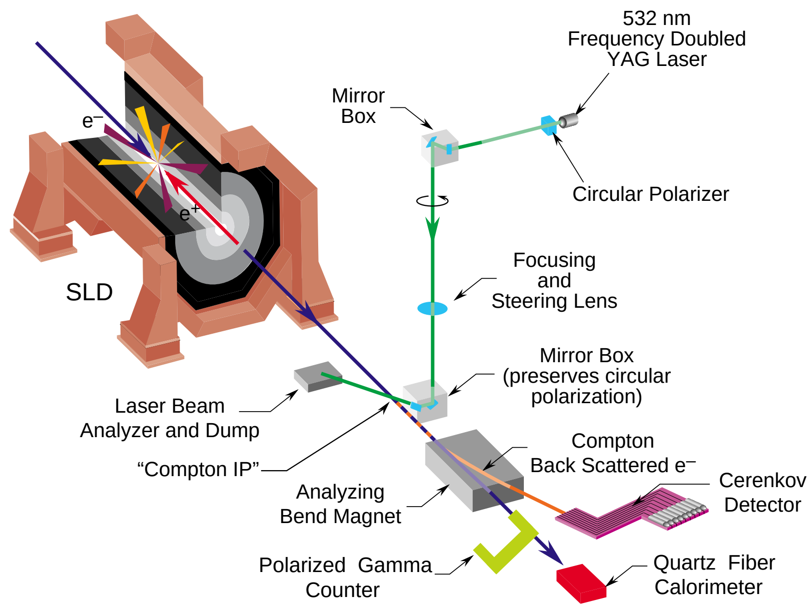

Figure 3.3: The SLC Compton polarimeter.

are detected by photomultiplier tubes arranged transversely to the beam. The differential Compton cross section for the polarized electrons:

$$\frac{d\sigma_C}{dE} = \frac{d\sigma_C^u}{dE}[1 + A_{Compton}(E)] \tag{3.1}$$

where E is the energy of the scattered electron. $\frac{d\sigma_C^u}{dE}$ is the unpolarized differential Compton cross section and $A_{Compton}(E)$ is the measured Compton asymmetry as a function of E. $A_{Compton}(E)$ is measured from the difference of cross sections of parallel ($J_z = \frac{3}{2}$) and antiparallel ($J_z = \frac{1}{2}$) polarizations for the electron and photon for each channel of the detector:

$$A_{Compton}(E) = \frac{\sigma_{J_z=\frac{3}{2}} - \sigma_{J_z=\frac{1}{2}}}{\sigma_{J_z=\frac{3}{2}} + \sigma_{J_z=\frac{1}{2}}} = P_e P_\gamma a_C(E) \tag{3.2}$$

where the analyzing power $a_C(E)$ is the cross section weighted Compton scattering asymmetry calculable in QED, convoluted with the detector response function for each detector channel. The unknown electron beam polarization P_e can be determined from P_γ. P_γ is measured by scanning through voltage and signal in the left and right photodiodes of the Compton Polarimeter.

The average luminosity-weighted polarizations for the various SLD run periods are summarized in Table 3.1.

Table 3.1: Summary of average electron beam polarizations for the different physics run periods.

Run period	Average polarization P_e
1992	0.224 ± 0.006
1993	0.626 ± 0.012
1994-5	0.772 ± 0.005
1996	0.765 ± 0.005
1997	0.733 ± 0.008
1998	0.731 ± 0.008

Two additional detectors measure the electron polarization using the Compton backscattered photons, the polarized gamma counter (PGC) and the quartz fiber calorimeter (QFC). They provide independent cross checks on the polarization measurement from the Compton Polarimeter.

A detailed description of the systematic errors for the polarization result can be found in Ref. [43].

3.0.8 Energy Spectrometer

The Wire Imaging Synchrotron Detectors (WISRD) [44] are installed to measure the energies of the electron and positron beams pulse-by-pulse. The layout of the WISRD is illustrated in Fig. 3.4.

The energy measurement is based on the deflection angle of the beam by a calibrated vertical bend magnet. The deflection angle is inversely proportional to the energy. The vertical bend magnet is located between two horizontal bend magnets which produce the shower of synchrotron radiation. The synchrotron radiation is detected by a multiwire proportional chamber. The deflection angle is induced from the distance between the swaths of radiation. The luminosity-weighted mean center-of-mass collision energy for the 1997-98 run was 91.237±0.029 GeV.

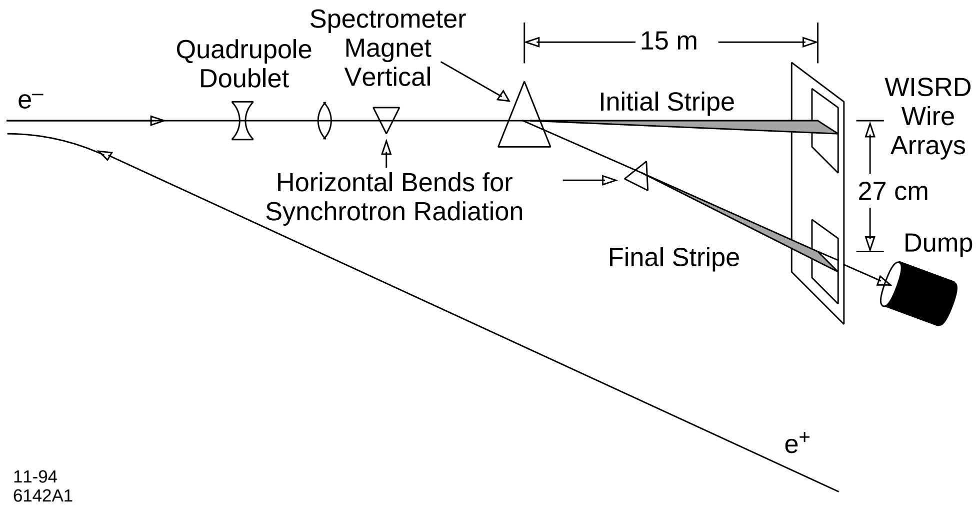

Figure 3.4: Schematic view of the WISRD.

3.1 The SLD

The SLD [45] which surrounds the collision point is degined to observe decay particles from polarized Z^0 generated by the e^+e^- collisions. The section view of the SLD is shown in Fig. 3.5.

3.1.1 Vertex detector

The SLD vertex detector (VXD) is using silicon charge coupled devices (CCD) to measure precise positions on particle trajectories by detection of charge deposition. The reconstructed tracks provide information for hadron decay vertexing. The VXD3 installed for the 1996-98 run period is a pixel-based detector, measuring hit positions in ϕ and z in its cylindrical coordinate system [46]. Each individual CCD covers a 8.0×1.6 cm^2 active area with 4000 × 800 pixels. The pixel size is 20×20 μm^2 and the active region extends to a depth of 20 μm. A minimum-ionizing particle produces about 1200 electron/hole pairs. Structures called ladders each containing two CCDs mounted on a beryllium substrate is shown in Fig. 3.6. These ladders are attached to three layers of beryllium barrels in a shingled arrangement as shown in Fig. 3.7. The first layer has 12 ladders at a mean radius of 2.8 cm and the second layer has 16 ladders at a mean radius of 3.82 cm. The third layer

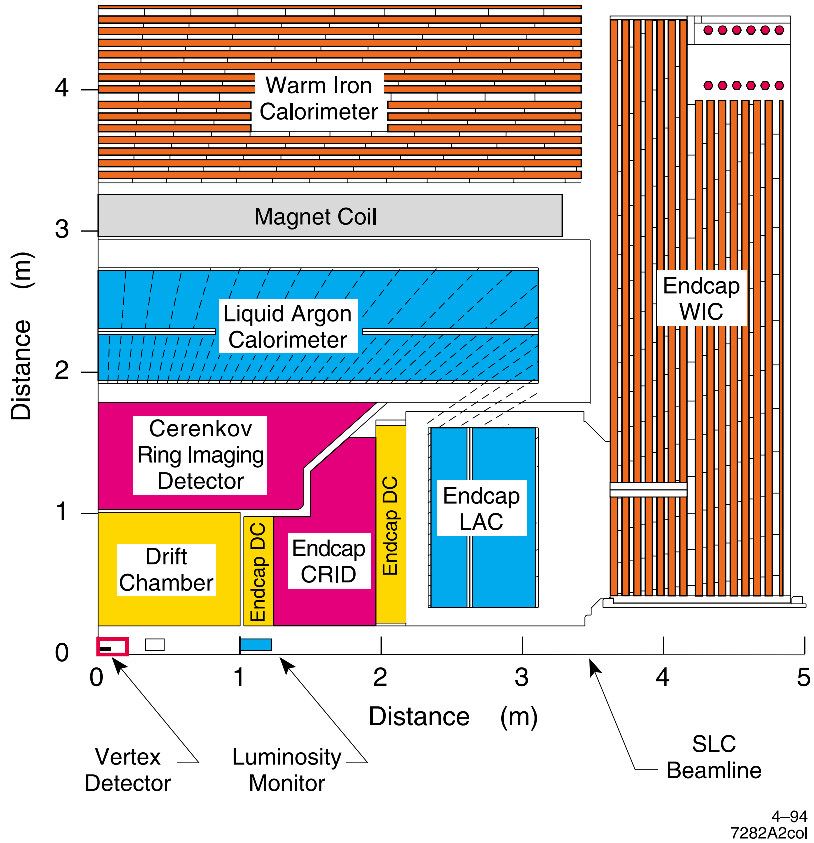

Figure 3.5: Quadrant view of the SLD detector.

has 20 ladders at a mean radius of 4.83 cm. The three-layer angular coverage extends to $|\cos\theta| \leq 0.85$. θ is the polar angle of a track to the beam line. A total of 96 CCDs for 307 million of pixels are used. The total radiation length of the each layer is 0.4%. This low radiation thickness is important for reducing the multiple scattering of tracks. The ladder geometry is shown in figure 3.7.

The VXD3 is operated at a low temperature of about 185K. Low temperature operation is required to reduce charge trapping in the silicon due to lattice defects caused by radiation damage. The readout of charge deposited in each pixel is performed by dividing each CCD into four regions, with one output amplifier in each of the four corners of the CCD. Rows of pixel charges are moved in parallel along the long direction (the I direction) to the readout register. Once a row of pixel charges reaches the readout register, charge is transferred along the edge of the CCD to the output amplifier in the corner (The R direction). The entire read out time for each corner is about 0.2 s or about 26 beam crossings. Since the

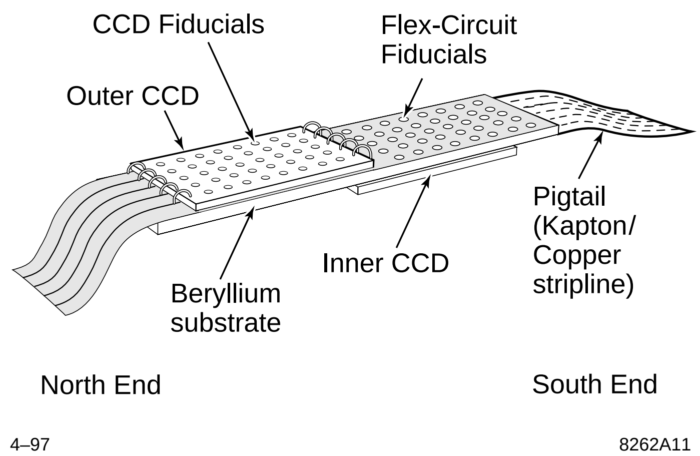

Figure 3.6: VXD3 ladder geometry.

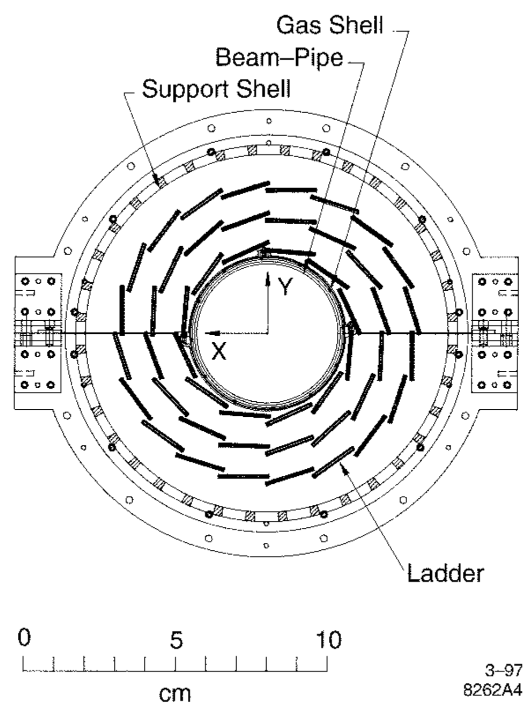

Figure 3.7: Schematic view of VXD3 in the $r\phi$.

Z^0 event rate of about 300 per hour as well as the background rates are both relatively low, the rather slow readout speed is acceptable. The pixel occupancy is $< 10^{-4}$ even with additional hits from background noise.

In order to know the VXD3 geometry and alignment [46],[34], first an optical survey is performed to determine the shape of each CCD, the assembled ladder positions, and estimated gravitational sags of each ladder. Internal alignment of the detector is produced using *i*) charged tracks which traverse the CCD overlap regions, *ii*) tracks that pass through both CCDs on a ladder, and *iii*) tracks with hits in all three layers. After the internal alignment is performed, single-hit resolution is measured to be <4 μm. The single hit resolution is presented in Fig. 3.8.

Further VXD3 alignment is completed with respect to the CDC by comparing the VXD3 hits of tracks with the extrapolated hits of CDC tracks in the VXD3 region.

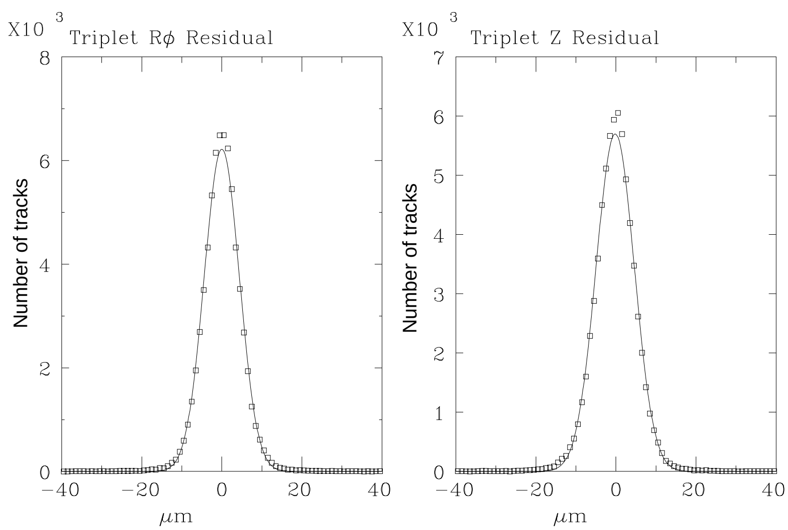

Figure 3.8: The VXD3 single hit resolution in r_ϕ and in z direction.

The high momentum track position resolution at the IP can be measured from the miss distance of the two tracks in $Z \to \mu^+\mu^-$ decays, as shown in Fig. 3.9. The data indicate a single track transverse resolution of 7.7 μm in $r\phi$ μm and 9.6 μm in rz [47].

3.1.2 Drift Chamber

The SLD cylindrical Central Drift Chamber (CDC) is designed to measure the momenta and positions of charged tracks [48],[49]. The CDC extends from 0.2 m to 1.0 m in radius

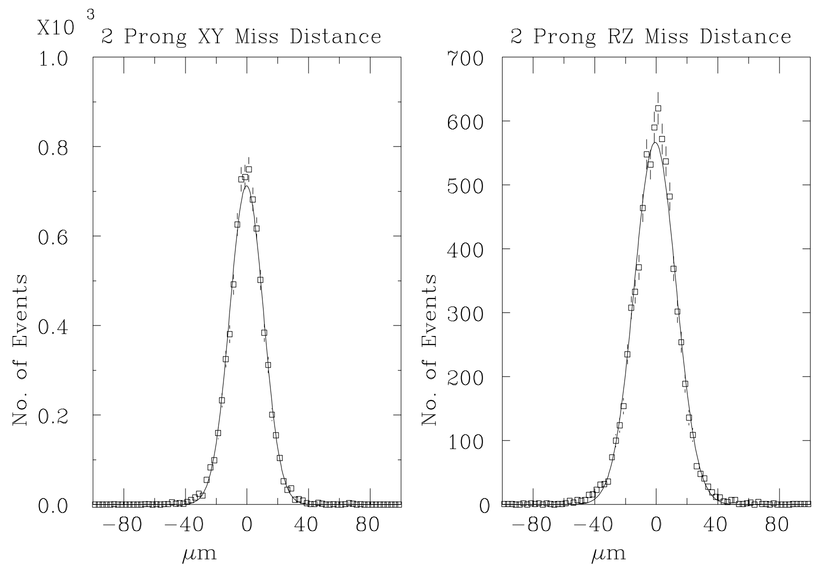

Figure 3.9: Miss distance of tracks in $Z \to \mu^+\mu^-$ events, in $r\phi$ and in rz.

and from -1.0 m to +1.0 m in z, which gives the effective angular coverage for tracks of $|\cos\theta| < 0.71$. The chamber consists of ten superlayers, as shown in Fig. 3.10.

Four axial super layers where wires are in parallel to the beam axis and three pairs of stereo super layers, in which the wires are tilted at angles of ± 41 mrad with respect to the beam axis. Each individual superlayer is composed of independent cells which measure about 6 cm in ϕ and 5 cm in r. Fig. 3.11 shows that each cell is made of 8 sense wires surrounded by 24 guard wires and 27 field wires. The field wires and guard wires which are made of 150 μm gold-coated aluminum are held at high voltage to make ionization electrons drift toward to the sense wires. The guard wires are set at -3027 V to focus the drifting electrons and to produce uniform charge amplification of about 10^5 in the area close to the sense wires. The field wires are held at an average voltage of -5300 V, producing a uniform mean drift field of 0.9 kV/cm. The sense wires are made of 25 μm gold-coated tungsten. They are arranged in 5 mm intervals within the cell.

The chamber is filled with a gas mixture of 75% CO_2, 21% Ar, 4% isobutane, and 0.2% H_2O. CO_2 is chosen due to its low drift velocity, about 7.9 μm/ns at the mean drift field and its low diffusion constant. Low drift velocity allows better position resolution for a given drift time resolution and more accurate separation of multiple hits on a single wire. Ar is added to increase the charge gain and isobutane is included as a quencher. A minimum-ionizing particle traversing through the CDC produces an average of 16 electrons per sense

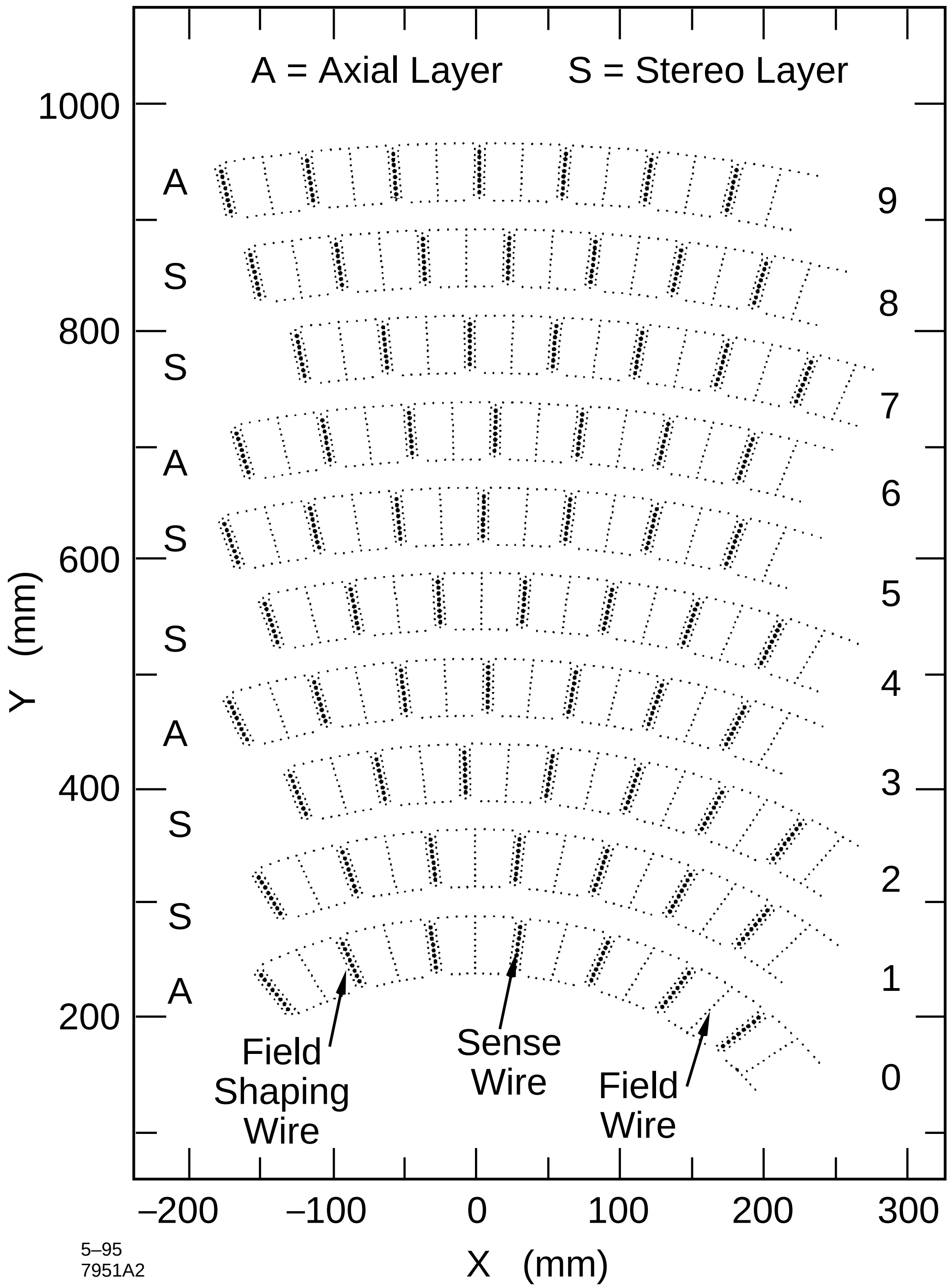

Figure 3.10: Layout of superlayers of the CDC

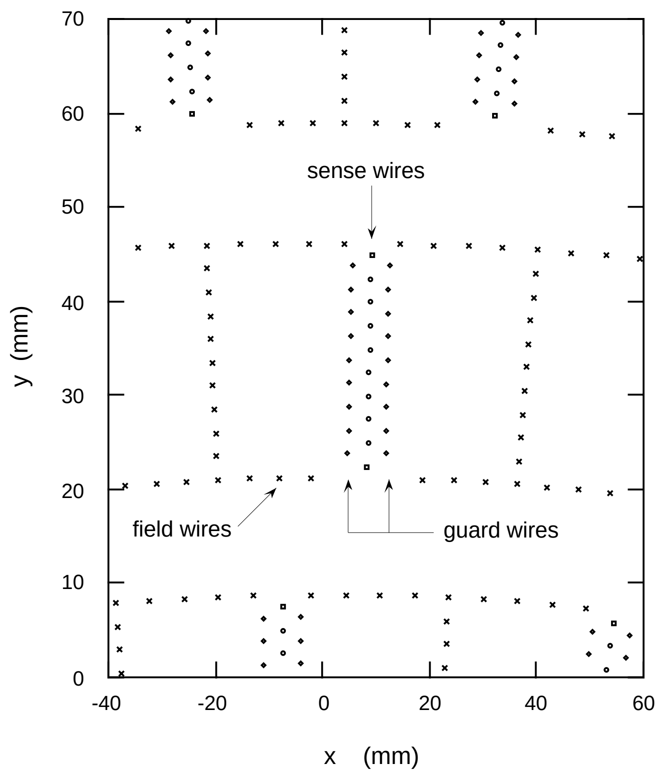

Figure 3.11: Layout of a single cell

wire. A disadvantage of the gas mixture is that the drift velocity depends significantly on the gas density and composition.

The waveforms of the pulses induced by deposited charge on the sense wires are digitized on both ends of the wire. The time of arrival of the leading edge of a pulse is used to measure the distance of the hit position of a particle from the sense wire in ϕ, assuming a model for the drift velocity (which is affected by the drift field configuration) and for the effects of the 0.6 T SLD magnetic field. The drift distance resolution for a single sense wire is $\sim$100 μm, although there are substantial non-Gaussian tails. The position of the trajectory in the z direction is obtained from the ratio of the pulse heights at each end of the sense wire. This charge division method is accurate to about 5 cm. Additional information for the z position is provided by the stereo layers when the tracks are fitted.

Track reconstruction [47] begins with grouping hits from different wires within a superlayer into vector hits (VHs). The track-finding process is performed by finding all combinations of axial VHs which form circles. VHs from the stereo layers with z position information are projected onto the circles. The candidate tracks are processed by a track-fitter which performs a detailed track swim taking into account the effects of magnetic field fluctuation, energy loss and multiple scattering in the detector material. The axial magnetic field makes it possible to measure the transverse momentum of a track to the beam axis from the track curvature. The momentum resolution for the fitted tracks is [50]

$$(\sigma_{p_t}/p_t^2)^2 = 0.0050^2 + (0.010/p_t)^2 \tag{3.3}$$

where p_t is the track momentum transverse to the beam axis measured in GeV/c. The first term comes from the track position measurement uncertainty and the second term is from the effects of multiple scattering [51]. When VXD3 VHs are included in the track-fitter process the resolution improves to [52]

$$(\sigma_{p_t}/p_t^2)^2 = 0.0026^2 + (0.0095/p_t)^2 \tag{3.4}$$

Finally, the CDC-VXD combined impact parameter(the closest distance of an extrapolated track from the IP) resolution in the $r\phi$ and rz are given by

$$\sigma_{r\phi} = 7.7 \oplus \frac{33}{p \sin^{3/2}\theta} \mu\text{m} \tag{3.5}$$

$$\sigma_{r\phi} = 9.6 \oplus \frac{33}{p \sin^{3/2}\theta} \mu\text{m} \tag{3.6}$$

The first term is from the track position measurement error and the second term is coming from multiple scattering.

3.1.3 Cherenkov Ring Imaging Detector

The SLD Cherenkov Ring Imaging Detector (CRID) [53],[54] provides particle identification in a broad momentum range. Particle identification using the CRID makes it possible to do more detailed studies of particle production in q and g jets. For the analyses we use only the Barrel CRID which provides particle identification for around 70% of the solid angle.

When a charged particle traverses a dielectric medium with a velocity higher than the phase velocity of photons, the particle produces Cherenkov radiation. Particles polarize the molecules of the medium and cause the emission of coherent radiation to a large distance. A minimum momentum that a particle starts to radiate Cherenkov photons in a medium is defined as “threshold momentum”. A charged particle with velocity $v = \beta \cdot c$ in a medium with the index of refraction η emits the Cherenkov photons continuously at an opening angle

$$\cos\theta_c = \frac{1}{\beta\eta}, \tag{3.7}$$

where β is the speed of the particle divided by the vacuum speed of light, and η is the index of refraction in the material. The Cherenkov angle calculated from the equation provides the measurement of the velocity of a charged particle. With both the velocity and the measured momentum of a track, the mass of the particle can be deduced. The mass allows the identification of the track as a certain particle type.

With the CRID we reconstruct the Cherenkov radius of each particle using the number of emitted indiviual photons and the position of the photons.

The sectional view of the SLD Barrel CRID is shown in Fig. 3.12. The Barrel CRID had two kinds of radiators, liquid and gas radiators, to cover the low and high momentum regions.

The liquid radiator containing C_6F_{14} is inside of 1 cm thick 40 quartz-windowed trays. The liquid radiator has an index of refraction $\eta = 1.2723$ at $\lambda = 190$ nm [55]. When the momentum of a particle is above its liquid Cherenkov threshold, UV photons are radiated in a cone about the flight direction of the particle. The Cherenkov photons from the liquid radiator is imaged onto one of the 40 quartz-windowed time projection chambers (TPCs). Liquid rings typically span 2−3 TPCs in azimuth and the average liquid Cherenkov angle is 670 mrad.

The TPCs contain C_2H_6 drift gas with 0.1% of tetrakis-dimethylamino-ethylene (TMAE) [56],[54]. Photons with an energy greater than 5.4 eV ionize the TMAE in the TPCs and the resulting photoelectrons are pulled along the SLD magnetic field direction by an electric field of 400 V/cm to multiwire proportional chambers (MWPC) where the position of each photon is measured in three dimensions. A TPC is shown in Fig. 3.13. The inside volume of the TPC is 126.8 cm long and 30.7 cm wide, with a thickness that tapers from

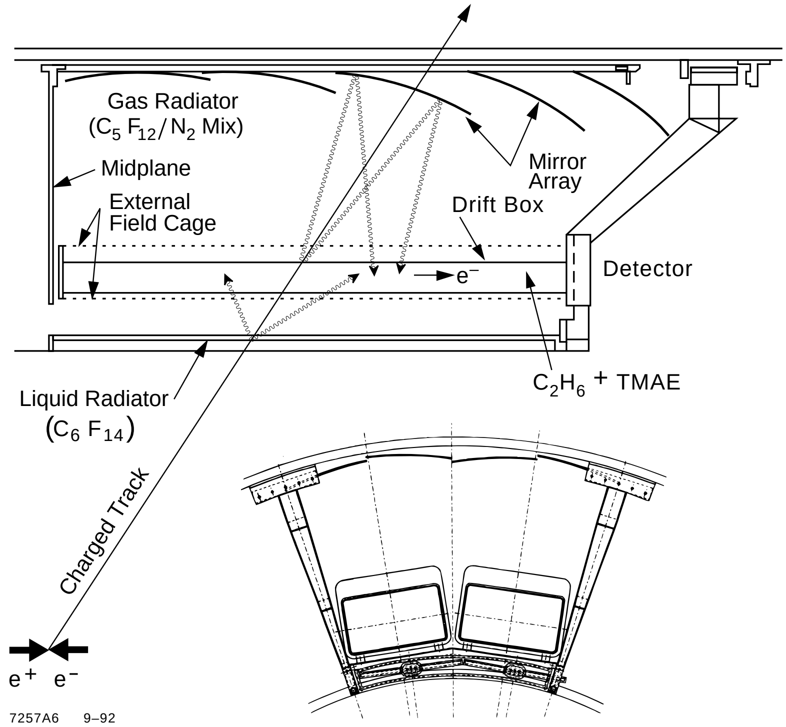

Figure 3.12: The Barrel CRID.

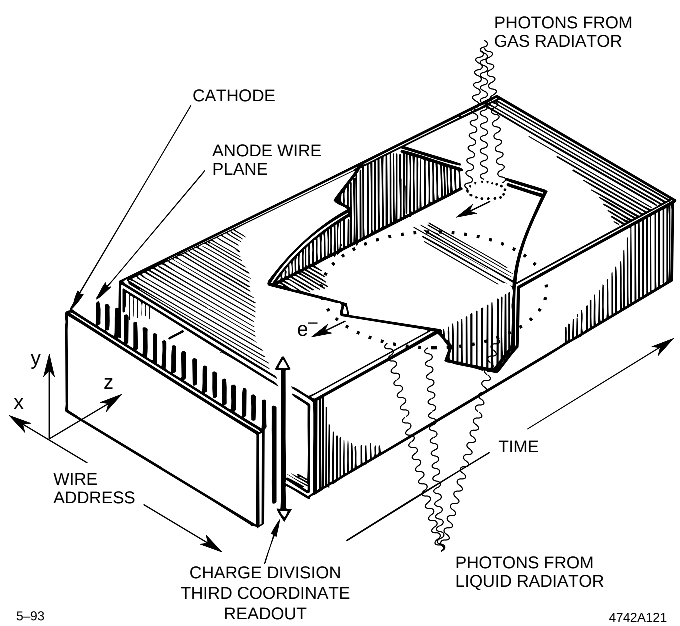

Figure 3.13: A barrel CRID TPC.

9.2 cm at the detector end, where the MWPC are to 5.6 cm at the high voltage end. The detector end and the high voltage end are held to –1.5 kV and –55 kV respectively. The MWPC are composed of 93 of 7 μm carbon wires with 10.35 cm length. The wires are separated by $\sim$ 3.2 mm intervals. The position of the photons are deduced from the wire address, charge division ratios on the wire, and drift time to within 1 mm resolution for each coordinate. These positions are used to reconstruct a Cherenkov angle with respect to the charged track flight direction.

The particle which has passed through a TPC reaches the $\sim$ 40 cm thick gas radiator. The gas radiator contains 85% of C_5F_{12} and 15% of N_2. The gas radiator has 400 UV-reflective spherical mirrors to focus the Cherenkov photons emitted at different times along the trajectory of the particle onto a single point on the TPCs [57]. The mirrors are installed such that rings are not focussed near the edge of a TPC or close to the ionization signal of the original track. The average radius of gas rings is 2.5 cm and the typical gas Cherenkov angle is 50 $m$rad. The exact mixture of two gas types determines the index of refraction which is $\eta = 1.0017$ at $\lambda = 190$ nm.

In order to convert the measured arrival time, charge division and wire number of a hit into spatial coordinates on the TPCs, the velocity and path of photoelectrons drifting in the TPCs, the beam crossing time, and the gain of the electronics at each end of each wire should be measured precisely [58].

The drift velocity is measured every hour with an array of optical fibers which inject UV photons from a Xe flashlamp into the TPCs [59]. There are non-axial drifts of electrons due to small radial components of the SLD magnetic field and due to misalignments of the TPC axes [58],[60].

The relative beam crossing time is determined by the first arrival of hits at the CRID. In order to measure the time shift between the entrance of CRID and the TPC, liquid rings from $e^+e^- \rightarrow \mu^+\mu^-$ and $e^+e^- \rightarrow e^+e^-$ are used. The time shift is measured [58] by requiring the measured average liquid Cherenkov angle to be independent of ϕ, the azimuthal angle of the radiated photon about the track direction. By combining the measured arrival time and time shift, we are able to determine the relative beam crossing time.

To turn these local coordinates into Cherenkov angles, we must know accurately the spatial positions of the TPCs and the liquid radiatior tray and mirror, as well as the trajectory of the charged particle.

The average numbers of detected photons per full liquid and gas ring in a $\beta = 1$ sample from the 1994-5 μ-pair events are 16.1 and 10.0 respectively. The corresponding numbers measured in hadronic events are 12 and 10. The average resolutions for the liquid and gas Cherenkov angles are measured to be 14.0 and 4.0 mrad. Thses resolutions include the effects of residual misalignments and track extrapolation errors [61].

Cherenkov angle curves as a function of momentum are shown in Fig. 3.14. The Fig. also illustrates liquid and gas thresholds for different particle types. The Cherenkov thresholds for a charged e, μ,π, K and p for the liquid and the gas radiator in the Barrel CRIDs are summarized in Table 3.2.

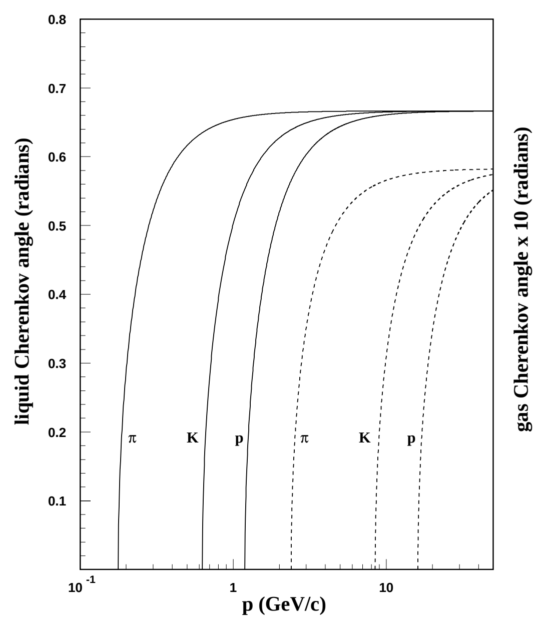

Figure 3.14: The Cherenkov angle for the (solid line) liquid and (dashed line) gas radiators in the barrel CRID.

To identify the charged particles as π, K and p a likelihood $\mathcal{L}$ is calculated for different hypotheses of particle type for a track using (i) the measured Cherenkov angle, (ii) the number of detected photoelectrons at that angle, (iii) the number of expected photons, (iv) the polar angle of the hypothesized particle type, (v) and angle resolutions and a

Table 3.2: Momentum thresholds for the barrel CRID radiators in GeV/c.

Radiator	$e^{\pm}$	$\mu^{\pm}$	$\pi^{\pm}$	$K^{\pm}$	$p/\bar{p}$
C_5F_{12}/N_2	0.009	1.811	2.393	8.463	16.084
C_6F_{14}	0.001	0.134	0.177	0.628	1.193

background term. The background includes the effects due to overlapping of the radiation hits from other tracks and a constant (normalized to the number of hits in the TPC) due to noise which is not associated with any tracks. The differences in log-likelihoods for each hypothesis can be used to identify a track as a certain type of particle. Detailed discussion about the likelihood method can be found in Ref. [54],[58].

3.1.4 Liquid Argon Calorimeter

The SLD liquid argon calorimeter (LAC) [62],[63] makes energy measurements of neutral as well as charged particles. It consists of a cylindrical barrel with 6 m length and radial extension from 1.77 to 2.91 m, extending the polar angle coverage to $|\cos\theta| < 0.84$. The LAC shown in Fig. 3.15 is composed of electromagnetic and hadronic modules.

The individual module consists of alternative layers of grounded lead sheets and segmented lead tiles held at –2 kV, with liquid Ar filling the the gaps between the layers. This way the lead plates serve as electrodes as well as absorbers of high energy particles. A high energy particle interacting with lead plates produces showers of additional particles. The charged particles produced on a shower ionize the Ar, and the drifting charges in the field between two lead plates induce electrical signals on the plates. Several adjacent tiles are linked to form projective towers, and each tower provides roughly equal solid angles to particles from the IP. Each tower is connected to amplifiers to measure the deposited charge.

The calorimeter is radially divided into four separate readout sections, EM1, EM2, HAD1 and HAD2. The thicknesses of the EM1 and EM2 layers are 6 and 15 radiation lengths respectively. The 21 radiation lengths of the two EM layers are sufficient to contain electromagnetic showers from 50 GeV electrons with only 1-2% energy leakage. The towers in EM layers have angular size $\sim$33 mrad in azimuth. In the EM modules, the lead plates

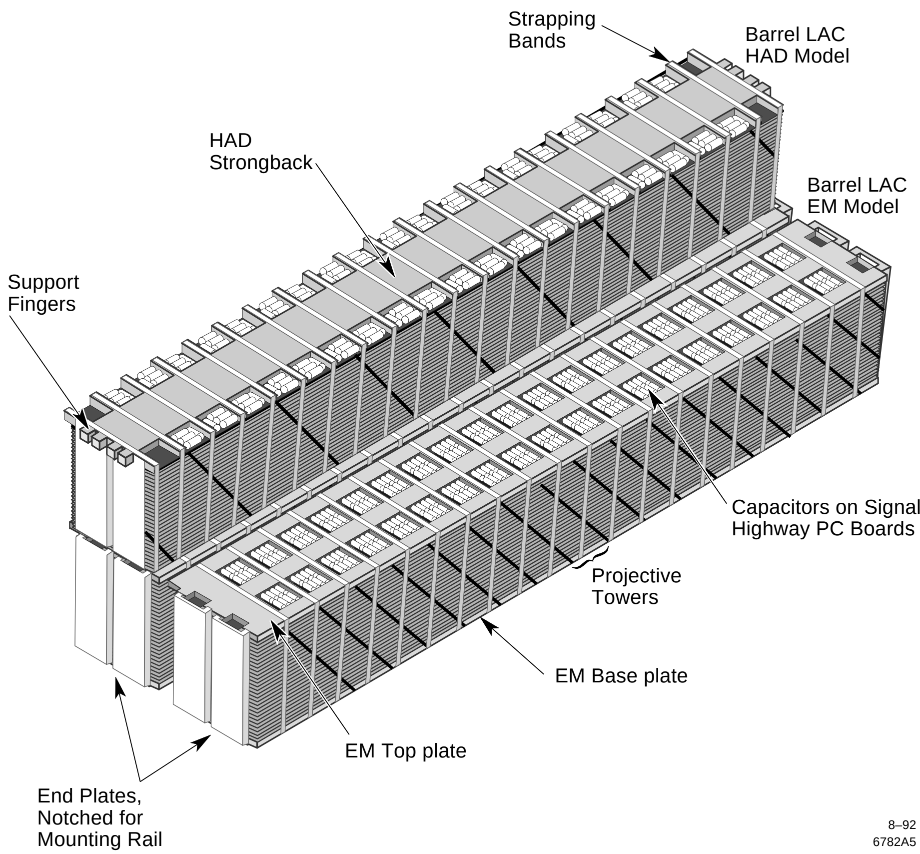

Figure 3.15: LAC barrel modules

are 2 mm thick, separated by 2.75 mm of Ar. The outer two HAD layers are one interaction length each, and are used to measure hadronic showers. In the HAD layers, the lead plate thicknesses are increased to 6 mm with the same 2.75 mm of Ar gaps. The HAD projective towers cover ∼66 mrad in azimuthal angle. The total EM+HAD have 49 radiation lengths and 2.8 interaction lengths, which are sufficient to contain 80-90% of the total energy of a hadronic Z^0 decay. The energy resolution of the LAC is approximately $15\%/\sqrt{E}$ for electromagnetic showers and $60\%/\sqrt{E}$ for hadronic showers, with E measured in GeV.

3.1.5 Warm Iron Calorimeter

The Warm Iron Calorimeter (WIC) [63],[50] is the outermost structure of the SLD. It supports the SLD mechanically and returns the magnetic flux of the solenoid and also absorbs any remaining energy from hadronic showers which escapes the LAC. The WIC also provides muon identification and additional calorimetry information. The WIC consists

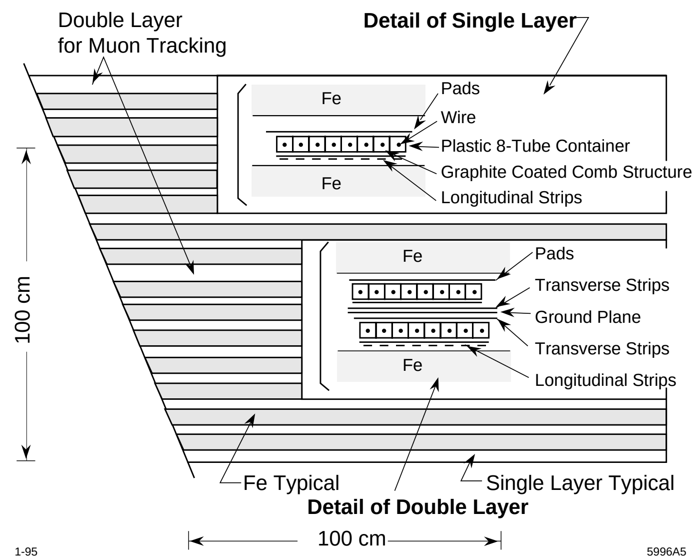

Figure 3.16: The layers and Iarocci streamer tubes in the WIC

of 17 layers of 9 $\times$ 9 mm^2 Iarocci streamer tubes installed within the 5 cm thick steel plates as shown in Fig. 3.16. The Iarocci streamer tubes contain copper-beryllium anode wires and are filled with a gas mixture of 88% CO_2, 9.5% isobutane and 2.5% Ar within plastic rectangles. The tubes have external copper cathode readouts in pad and strip configurations. The rectangluar pads provide calorimetry information. The strip electrodes for muon identification are aligned both longitudinally and transversely to the beamline.

3.1.6 SLD Monte Carlo

Monte Carlo Simulated data allow the estimation of detector acceptances, detector performance, and backgrounds.

The SLD Monte Carlo generates Z^0 decay events using the JETSET 7.4 [4],[64] program. For heavy quarks (c,b), the Peterson fragmentaion function [33] is used. B hadrons are processed using the CLEO B-decay model [65] and the other quarks are modeled using the JETSET 7.4. The SLD detector simulation is done by the GEANT [66] program.

Chapter 4

Hadronic event and jet selection

4.1 Hadronic Z^0 decay event selection

4.1.1 Z^0 event trigger

Since most of the machine cycles do not produce Z^0 events, the SLD applies a set of triggers to read out and record only interesting data on tapes. The main triggers used to identify hadronic Z^0 decays are the energy trigger, the tracking trigger and the hadronic trigger:

- The energy trigger requires the total deposited energy in all LAC towers to be at least 8 GeV, contributing only towers above the threshold of 246 MeV (60 ADC counts) and 1.298 GeV (120 ADC counts) for the EM and HAD sections respectively.
- The tracking trigger requires at least 2 charged tracks separated by at least 120° passing through at least 9 superlayers of the CDC. Furthermore, hits must be reported in > 275 CDC cells. A CDC cell hit is recorded if ≥ 5 of sense wires in the cell are hit.
- The hadronic trigger uses a combination of the energy and tracking information. The trigger requires ≥ 4 Gev and ≥ 1 CDC track.

The SLD also has a random trigger, which occurs every 20 s, for background studies.

Hadronic Z^0 decay events are passed through an off-line filter process to enhance background rejection [67]. The filter uses either the Energy Imbalance Trigger (EIT) or at least one track with $p > 1$ GeV/c in the CDC. The EIT requires that energy deposition in the LAC is greater than minimum energy and should not be from beam-splash background or SLC muon background. More detailed description of the trigger system and the filter can be found in Ref. [67],[68].

The combined selection efficiency for the triggers and the filter is about 92% for hadronic Z^0 decays. Finally, the selected events are processed by detector offline reconstruction algorithms and written out to data summary tapes (DST).

4.1.2 Hadronic event selection

In order to separate hadronic Z^0 decays from leptonic Z^0 events and from the beam background, a further QCD event selection is performed. The event selection is based on well reconstructed tracks and energy, and the requirement that events are well contained within the SLD barrel region. The selection starts with the following QCD quality track selection criteria [58],[69]:

- Charged tracks are required to have a closest transverse distance to the beam axis < 5 cm and < 10 cm from the measured IP z position along the axis. This excludes tracks produced from interactions in the detector material.

- The transverse momentum to the beam axis is required to be greater than 0.15 GeV/c. This removes tracks which multiple scatter and suppresses tracks which spiral back on themselves.

- The polar angle between the track momentum direction and the beam axis satisfies the barrel CDC acceptance limit of $|\cos\theta| < 0.8$.

- The CDC track fit must have $\chi^2/dof < 5$ to remove poorly reconstructed tracks.

Hadronic Z^0 decay event selections require:

- Events must have at least five tracks which satisfy the criteria listed above. This cut mainly removes background events coming from Z^0 decays to $\tau^\pm$ or $\mu^\pm$.

- The polar angle of thrust axis in an event is required to satisfy $|\cos\theta_{thrust}| < 0.71$. The thrust axis indicates the energy flow direction of the event. This thrust axis cut ensures that the event is not near the edge of acceptance of the CDC, where the efficiency of reconstruction of tracks is poor.

- The charged visible energy, E_{vis} is required to be greater than 20 Gev. E_{vis} is calculated as the sum of the energies of all selected tracks assuming the pion mass for each track. The E_{vis} cut is required to suppress events with a significant number of tracks being out of the detector acceptance.

The efficiency for selecting hadronic Z^0 decay events is estimated to be $\sim 96\%$ from the MC study. The relevant subsections of the detector (VXD, CDC and CRID) are required to be properly operating. The total number of the selected events for the 1997–98 run is 223,423. The non-hadronic background rate in this sample is estimated to be $(0.10\pm0.005)\%$ and is dominated by $Z^0 \to \tau^{\pm}$ events.

Finally, additional event selection cuts are applied for vertex finding to ensure to have important VXD information for the tracks and to suppress background and light flavor events.

- Event must pass the EIT filter
- Event should have at least 7 charged tracks.
- At least 3 of the tracks in events must have at least 2 vertex hits for each track.

The total number of selected events after applying the additional vertex cuts for the 1997–98 run is 214,094.

4.2 Flavor Separation

Two different methods are used to select samples of events enriched in light (uds) and heavy (c, b) flavors. The first method is simply to count the number of tracks whose origin is significantly displaced from the IP [70],[60]. The second method is to find secondary vertices using a topological algorithm in each hemisphere or jet [71]. An event is divided into two hemispheres using the thrust axis or multi-jets using the jet axes. The vertexing is performed in each hemisphere or jet using only the tracks in that hemisphere or jet.

These flavor tagging methods are based on the decay kinematics of the heavy B and D hadrons. Heavy hadrons typically have millimeter scale decay lengths. These heavy hadrons decay into numbers of particles and the decaying points can be distinguished from the IP. These decaying points are defined as secondary vertices. The light, c and b events are sufficiently different in topology that pure and efficient flavor tagging is possible.

4.2.1 Interaction Point (IP) Determination

The precise determination of the e^+e^- beam interaction point (IP) at the SLD as well as the accurate position measurements of tracks using the VXD3 are important to separate heavy flavor decay tracks from tracks coming directly from the IP. The SLC interaction region is approximately 1.6 μm $\times$ 0.7 μm in the transverse direction (xy) and 700 μm in the longitudinal direction (z) to the beam. The z position of the IP varies event by event by relatively large amount. Therefore it is measured event by event. The xy position is stable and small enough to average it over many events. The xy position is determined using sets of Z^0 hadronic events which have well defined thrust axes. Each track from the IP can be used to measure the IP in the directions transverse to the track. Normally single event only measures the IP in one dimension, so by using another event with the thrust axis orthogonal to the original event we are able to make measurements in both dimensions transverse to the beam. The typical transverse track error is $\sim$ 50 μm and tracks from 30 consecutive hadronic events are fit to a common vertex to measure the IP. Since the tracks from heavy flavor decays can contaminate the IP determination, these tracks must be excluded from the sets of tracks used to measure the IP. Tracks originating from a heavy flavor decay vertex have large impact parameters with respect to the previously measured IP. In order to reject tracks from heavy flavor decays, only tracks within 5 σ in track errors to the previously measured IP are included in the IP fit.

The beam position resolution is measured on average using μ-pair events. The impact parameter of μ-pair tracks is the convolution of the IP measurement error with the high momentum track errors. The high momentum track errors are measured to be ~ 7.55 μm from the miss distance of μ-pair tracks to each other. With the impact parameter of μ-pairs 8.2 μm and the track error, the IP measurement resolution in the transverse directions is determined to be ~ 3.2 μm.

The z position of the IP is measured for each event using a set of well measured tracks with vertex detector hits. Each track is swum back to its position of the closest approach (POCA) with respect to the beam line. The z position at the POCA (Z_{POCA}) for a track is an estimator for the IP z position measurement. The distribution of Z_{POCA} for all of the tracks in an event can have a long tail caused from mismatched or multiple scattered tracks, or tracks from heavy flavor decays. Therefore the median of the Z_{POCA} position distribution is selected as the best estimator for the IP z position of the event instead of the average of the Z_{POCA} positions. MC studies show that the typical resolution of this IP z position measurement is ~ 20 μm.

4.2.2 Normalized Impact Parameter

The 2D impact parameter δ of a track is defined as the 2 dimension radial distance of closest approach of a track to the IP. The impact parameter is signed according to the crossing position of the track to the jet axis as shown in Fig. 4.1.

Due to long lifetimes, the decays of heavy hadrons produce tracks with large impact parameters. In order to get rid of background tracks coming from poor track reconstruction, detector interactions as well as γ conversions ($\gamma \rightarrow e^- e^+$), and from K_s^0 or $\Lambda^0/\bar{\Lambda}^0$ decays, tracks are required to have following properties:

- Tracks should be inside of the detector acceptance of $|cos_\theta| < 0.8$.
- Tracks must have at least 40 CDC hits and a track fit quality of $\chi^2_{CDC}/dof < 5$.

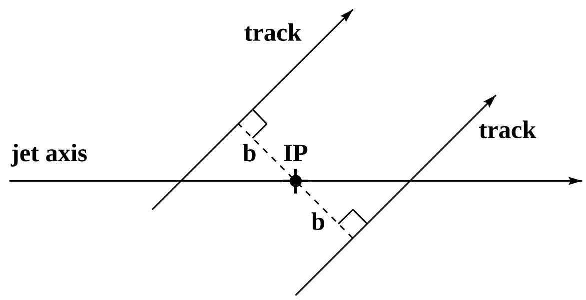

Figure 4.1: The impact parameter is assigned a positive (negative) sign if the charged track crosses the jet axis in front of (behind) the IP.

- Tracks must have a distance of closest approach to the IP of less than 1 cm in xy and 1.5 cm in z to reject tracks not originating from the Z^0 or heavy flavor decays.

- For each track, the first CDC hit of tracks must occur within 39 cm radially from the IP. This cut limits the extrapolation distance from the CDC to the VXD3 when found VXD3 hits are linked to the track. At least one VXD3 hit is required to ensure a good extrapolation of the track back to the IP.

- The combination of the VXD3 and the CDC information must have a track fit quality of $\chi^2_{VXD+CDC}/dof < 5$.

- Pairs of oppositely charged tracks forming a candidate vertex that is consistent in mass with a γ conversion, a K_s^0 or a $\Lambda^0/\bar{\Lambda}^0$ candidate are rejected.

- The impact parameter (δ) of the tracks to the IP has to satisfy $\delta < 3$ mm with the estimated error from measuring the track and IP positions of $\sigma_\delta < 250$ μm.

A significant track is defined as a quality track with impact parameter magnitude greater than three times the impact parameter error, $|\delta| > 3\sigma$ [60].

Fig. 4.2 illustrates the normalized impact parameter δ/σ distributions for the data and MC simulation for each flavor type. For the purpose of the separation of light flavor from heavy flavor event, we count the number of significant tracks N_{sig}, in event. Fig. 4.3 presents a comparison of the N_{sig} distributions for the data and MC.

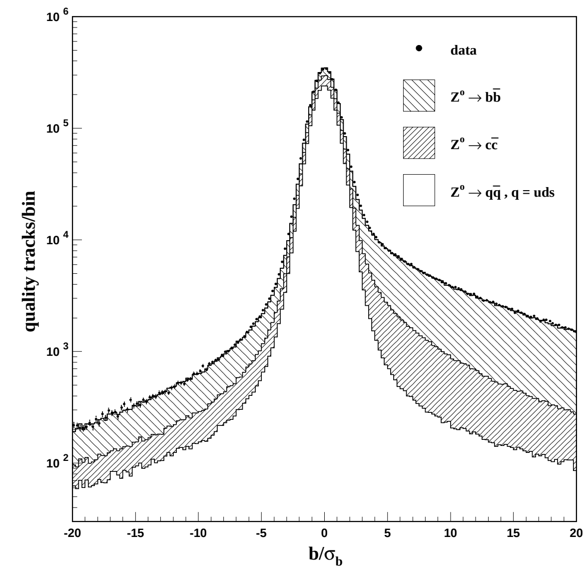

Figure 4.2: The normalized 2D impact parameter

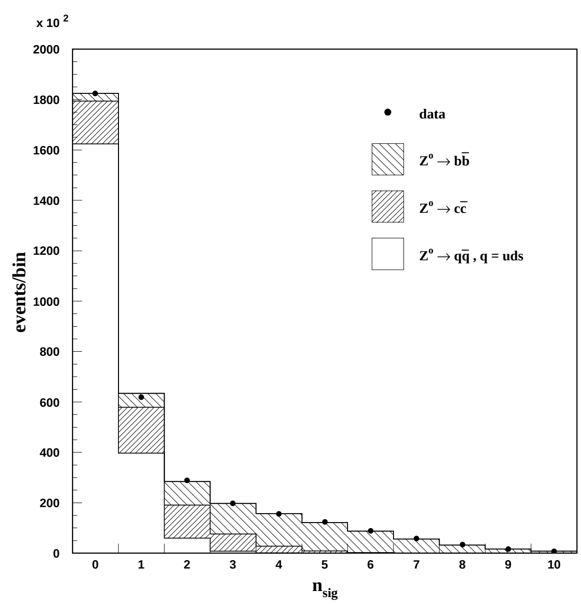

Figure 4.3: The number of significant tracks per event

The figure shows that events with no significant tracks are mostly light flavor, whereas heavy flavor events are characterized by many significant tracks. It also shows that most of b events have more than two significant tracks per event so b and c flavor events are also distinguishable. A better way to tag c and b events is to use topological vertex information.

4.2.3 Secondary Vertex Reconstruction

For the vertex finding method, secondary vertices are constructed from tracks separated from the IP. A topological algorithm [71] searches for vertices in 3 dimensions by overlapping the probability functions of tracks. A Gaussian probability tube for each track is obtained by modelling the measurement uncertainty in the position of the track. The probability function $f(\vec{r})$ is

$$f(\vec{r}) = \exp\left\{-\frac{1}{2}\left[\left(\frac{x' - (x'_0 + y'\kappa)}{\sigma_T}\right)^2 + \left(\frac{z - (z_0 + y'\tan\lambda)}{\sigma_L}\right)^2\right]\right\} \tag{4.1}$$

The x', y' coordinates have been transformed for each track such that the track momentum is oriented in y' direction at the point of closest approach of the track to the IP (POCA) in the xy plane. The first term is a parabolic approximation to the track's circular trajectory in the xy plane and κ is proportional to the curvature of the track. The second term represents the track's roughly linear trajectory in the rz plane. σ_T and σ_L are the measurement errors at the POCA for the $x'y'$ and z directions respectively. All parameters in the function are depicted in Fig. 4.4.

The IP is modelled using a 7×7×20 μm Gaussian ellipsoid centered at the IP position. A vertex occurs where at least two tracks are overlapped. The vertex probability function $V(\vec{r})$ is calculated from the contribution of the probability functions of tracks which form a vertex at a certain point.

$$V(\vec{r}) = \sum_i f_i(\vec{r}) - \frac{\sum_i f_i^2(\vec{r})}{\sum_i f_i(\vec{r})} \tag{4.2}$$

The xy projection of the track function and vertex function are shown in Fig. 4.5. Maxima of $V(\vec{r})$ may be found in several spatial locations by the algorithm. Maxima which are chosen

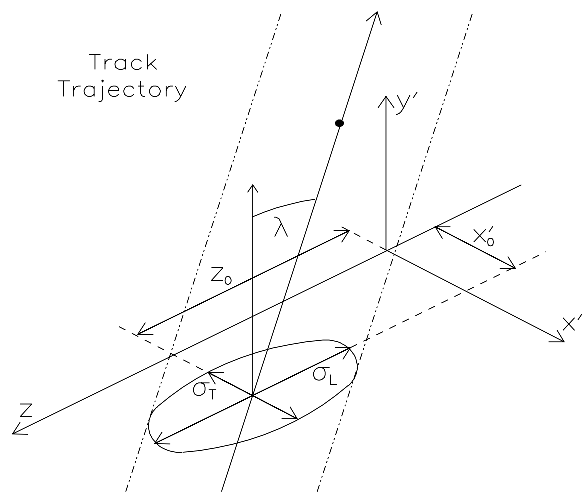

Figure 4.4: The parameters of the Gaussian function $f(\vec{r})$

to be vertices must be well separated from other maxima by valleys of $V(\vec{r})$ deeper than some depth criterion. Maxima which are not well separated are merged. The tracks whose probability density functions contribute to a local maximum are identified as originating from that vertex

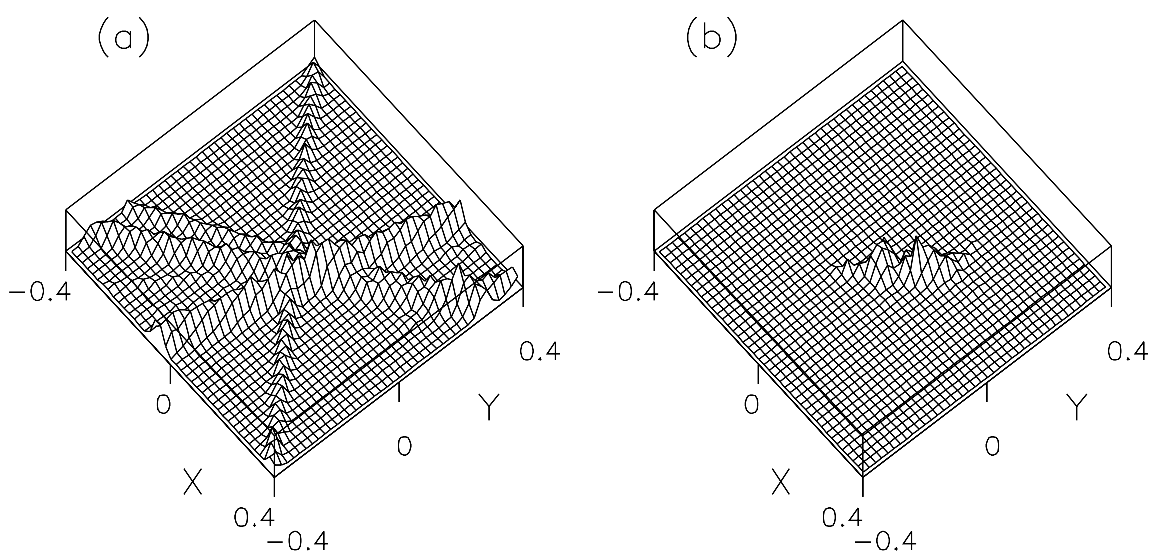

Figure 4.5: (a) is the track probability function and (b) is the vertex function.

A set of track cuts are applied for secondary vertex reconstruction. Tracks are required to have ≥ 3 VXD hits and transverse momentum to be $p_{\perp} > 250$ MeV. Tracks with impact parameter calculated in 3 dimensions δ_3, $\delta_3 > 3$ mm are excluded. Tracks from reconstructed γ, K^0, or Λ^0 decays are also removed. The tagged vertices are required to be within 2.3 cm from the center of the beam pipe to remove false vertices and a mass cut of $|M_{vtx} - M_{K^0}| < 0.015$ is applied to remove any residual K^0 decays. The remaining vertices are passed through a neural network to select the best heavy flavor vertex candidate [72]. After vertices are selected, the next step is to recover the information of tracks which are from heavy hadron decays but do not originate from the same space point of the vertices. The recovered tracks are attached to the candidate vertex.

4.2.4 Flavor Tagging

The heavy flavor events are separated from light flavor events based on cuts on the measured vertex mass and momentum. In addition to the vertex criteria, counting large impact parameter tracks N_{sig} is also used to improve the purity of the light flavor tagging.

The secondary vertex mass is determined using the invariant mass of all charged particles and the vertex momentum transverse to the heavy quark flight direction $\vec{P}_H$. $\vec{P}_H$ is measured using the IP and the vertex position. The vertex momentum P_{vtx} is calculated by summing of the momenta of all charged particles.

The invariant mass M_{ch} of the selected tracks is calculated with the assumption of a charged pion mass for each track.

$$M_{ch} = \sqrt{\left(\sum_i \sqrt{|\vec{p}_i|^2 + m_\pi^2}\right)^2 - \left(\sum_i \vec{p}_i\right)^2} \tag{4.3}$$

Due to conservation of momentum, the Lorentz invariant transverse momentum of neutral particles is equal and opposite to the transverse momentum measured from the charged particles in the secondary vertex. The invariant mass M_{ch} can be corrected for an undetermined contribution from neutral decay particles using the vertex transverse momentum. The minimum possible transverse momentum P_t^{min} is determined by calculating the angle between the charged momentum $\vec{P}_{ch}$ of the vertex and the vertex flight direction $\vec{P}_H$. The vertex flight direction $\vec{P}_H$ is varied within the errors of the IP and the vertex position as shown in Fig. 4.6.

The magnitude of P_t is also constrained to be less than M_{ch} to prevent false vertices from resulting in large masses through the correction. The P_t corrected vertex mass M_{vtx} can

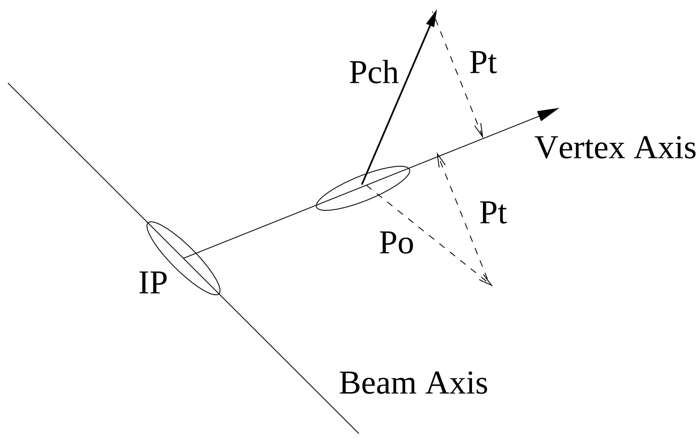

Figure 4.6: The missing P_t measured using the resultant charged momentum P_{ch} and the vertex axis.

then be defined as

$$M_{vtx} = \sqrt{M_{ch}^2 + P_t^2} + |P_t| \tag{4.4}$$

Fig. 4.7 shows the distribution of M_{vtx} in the data and MC for the event with secondary vertices. The clean separation of uds, c and b is shown in the Fig. 4.7.

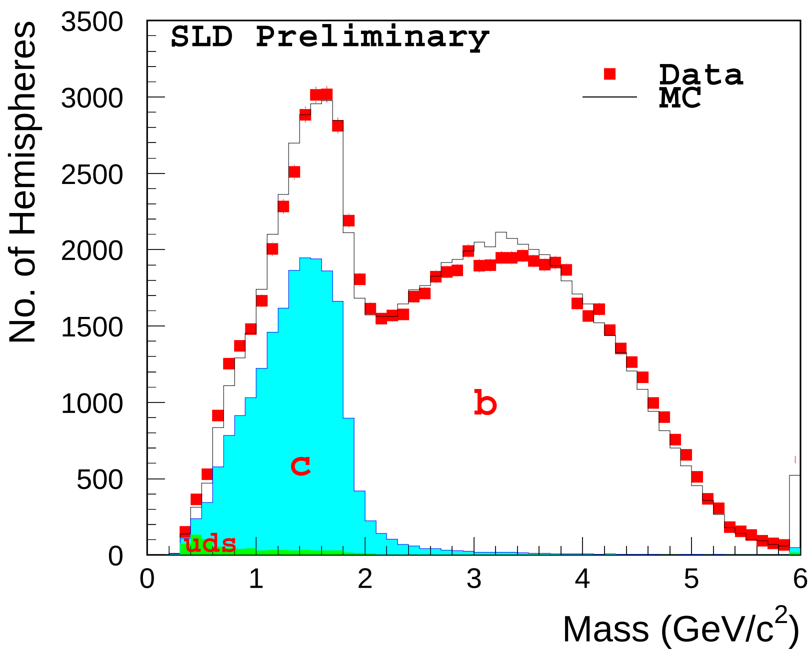

Figure 4.7: The P_t corrected mass M_{vtx} distribution with contribution from each event flavor.

A cutoff on the vertex mass at $\geq$ 2 GeV/c^2 provides high purity b flavor events. For c flavor event selection, we choose a set of selection cuts which give lower purity but higher

	Efficiency for $Z^0 \to$			Purity of $Z^0 \to$		
	$u\bar{u}, d\bar{d}, s\bar{s}$	$c\bar{c}$	$b\bar{b}$	$u\bar{u}, d\bar{d}, s\bar{s}$	$c\bar{c}$	$b\bar{b}$
uds-tag	0.734	0.190	0.010	0.928	0.068	0.004
c-tag	0.049	0.551	0.105	0.203	0.641	0.156
b-tag	0.001	0.024	0.815	0.005	0.023	0.972

Table 4.1: Tagging efficiencies and purities for the MC in the three flavor categories to be tagged as uds, c and b.

efficiency of c flavor event compared to the typical selection criteria [72]. The c flavor event selection criteria used for this thesis are

- $0.5 < M_{vtx} < 2$ GeV/c^2
- $P_{vtx} \geq 2$ GeV/c
- $P_{vtx} - 14 \cdot M_{vtx} > -10$
- $N_{sig} = 2$ or 3 is required for an event without a found secondary vertex.

The primary reason for choosing these c flavor selection cuts is to reduce the momentum dependent bias coming from flavor tagging for different hadron species. This will be discussed in detail later in Chapter 6. Events with no secondary vertex and no N_{sig} are assigned as light flavor events. The light, c and b flavor tagged samples contain 100,926, 33,760 and 39,712 events respectively. The estimated efficiency and purities of the flavor tagged samples from MC studies are listed in Table 4.1.

4.3 Jet Tagging and Separation

4.3.1 Jet Algorithm and Jet Selection

In the hadronic Z^0 decay process, the high energy q and $\bar{q}$ are highly boosted and hadronize into jets of hadrons. These initial q and $\bar{q}$ sometimes radiate hard gluons which generate additional jets. Hadronic jets are the visible record of an event in the detector, and interpreting the hadronic jets in terms of the underlying parton structure makes possible tests of the predictions of perturbative QCD. However, the original parton structure of the events will be obscured by the hadronization proccess. Many different jet reconstruction algorithms have been developed to achieve close resemblance between hadronic and partonic jet structures. Iterative clustering algorithms are employed to reconstruct hadronic jets in an event [73],[74]. The algorithms calculate scaled invariant masses y_{ij}, for all pairs of particles i and j, and the pair with the smallest y_{ij} is combined into a single particle of four-momentum $p_i + p_j$. This procedure is repeated until the y_{ij} of all remaining pairs exceeds a threshold value y_{cut}. The number of jets in the event is then defined as the number of remaining particles. Various schemes have been proposed comprising different y_{ij} definitions and combination procedures; for the results in this thesis the Durham algorithm [75],[76] is used. This algorithm is chosen because it uses angular criteria along with invariant mass, which improves reconstruction of heavy quark jets.

In the Durham method, y_{ij} is defined as:

$$y_{ij} = \frac{2\mathrm{min}(E_i^2, E_j^2)(1 - \cos\theta_{ij})}{E_{vis}^2} \tag{4.5}$$

where E_i and E_i are the energies of particles, i and j, E_{vis} is sum of the energies of all charged particles in an event, and θ_{ij} is the angle between the pair of particles i and j. Hadronic jets are reconstructed from the charged particles in an event using this algorithm with $y_{cut} = 0.005$, which gives the highest three jet event rate. Events with three reconstructed jets are selected. The jet energies are recalculated using the angles between the jet axes:

$$E_{jet,i} = E_{cm}\frac{\sin\theta_i}{\sin\theta_1 + \sin\theta_2 + \sin\theta_3}. \tag{4.6}$$

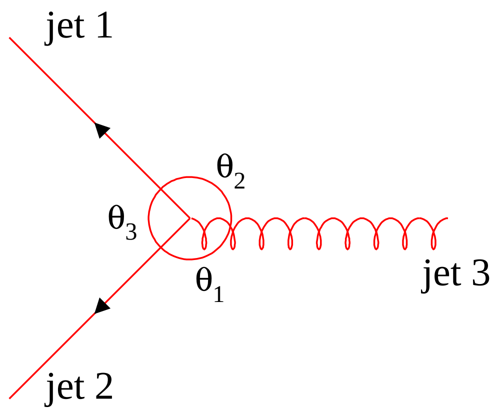

Figure 4.8: The angles between the jet axes in three jet events.

where $E_{cm} = 91.2$ GeV and θ_i are the angle between two jet axes opposite to jet i as shown in Fig. 4.8. These rescaled energy values are close to the parton jet energies compared to the visible energies from the charged particles. A clean sample of well defined three jet events is selected by requiring $|\cos\Theta| < 0.8$, where Θ is the angle between each jet axis and the beam direction, each jet energy is greater than 3 GeV and the sum of all the angles between jet axes $(\theta_1 + \theta_2 + \theta_3)$ is greater than 354°.

4.3.2 Gluon Jet Tagging

In order to tag gluon jets in three jet events, one of the two lower energy jets is required to have a c or b hadron vertex and the other must not have any vertex. Also the polar angle of the jet without vertex must satisfy $|\cos\Theta| < 0.7$. The two lower energy jets must also be separated by at least 18°, to prevent track migration between the jets. If these requirements are satisfied, the jet with no vertex is determined to be a gluon jet. This gluon tagging method assumes that the highest energy jet in a three jet event is a quark or antiquark jet (only 2.5% of the highest energy jets are gluon jets). To find a vertex in a jet the topological vertex finding algorithm described Sect. 4.2 is applied to each jet. Jets containing a vertex with $M_{vtx} > 0.75$ GeV/c^2 and $P_{vtx} > 2$ GeV/c are considered heavy quark jets.

These cuts provide 12,290 gluon tagged jets, with 92% gluon purity estimated by the MC simulation. The dominant background is $b\bar{b}$ quark jets, and concentrate at high jet energy. The peak of the tagged gluon jet energy distribution is $10 < E_{jet} < 15$ GeV as shown in Fig. 4.9.

4.4 Other Mixture Jets Tagging

In order to compare the tagged gluon jets with *uds* quark jets, we select a light mixture sample which is ideally 50% *uds* and 50% gluon jets. Because *uds* quark and gluon jets are indistinguishable, this is an unbiased sample. If no vertex and no large impact parameter tracks are found in the event, the two lower energy jets are put into the light mixture sample with *udsg* purity 94% and *uds* quark purity 46%.

For a cross check and background study we also produce a b mixture and a c mixture sample. The two lower energy jets are included in the b mixture when there is a b vertex in the highest energy jet, the other lower energy jets are included in the b mixture with 98.7% bg purity. If the highest energy jet has a c vertex defined with the conventional c quark selection cuts listed below, the two lower energy jets are included in the c mixture with 92.5% cg purity.

- $0.5 < M_{vtx} < 2$ GeV/c^2
- $P_{vtx} \geq 5$ GeV/c
- $P_{vtx} - 15 \times M_{VTX} > -10$

The energy distributions of these tagged jet mixture samples are also presented in Fig. 4.9.

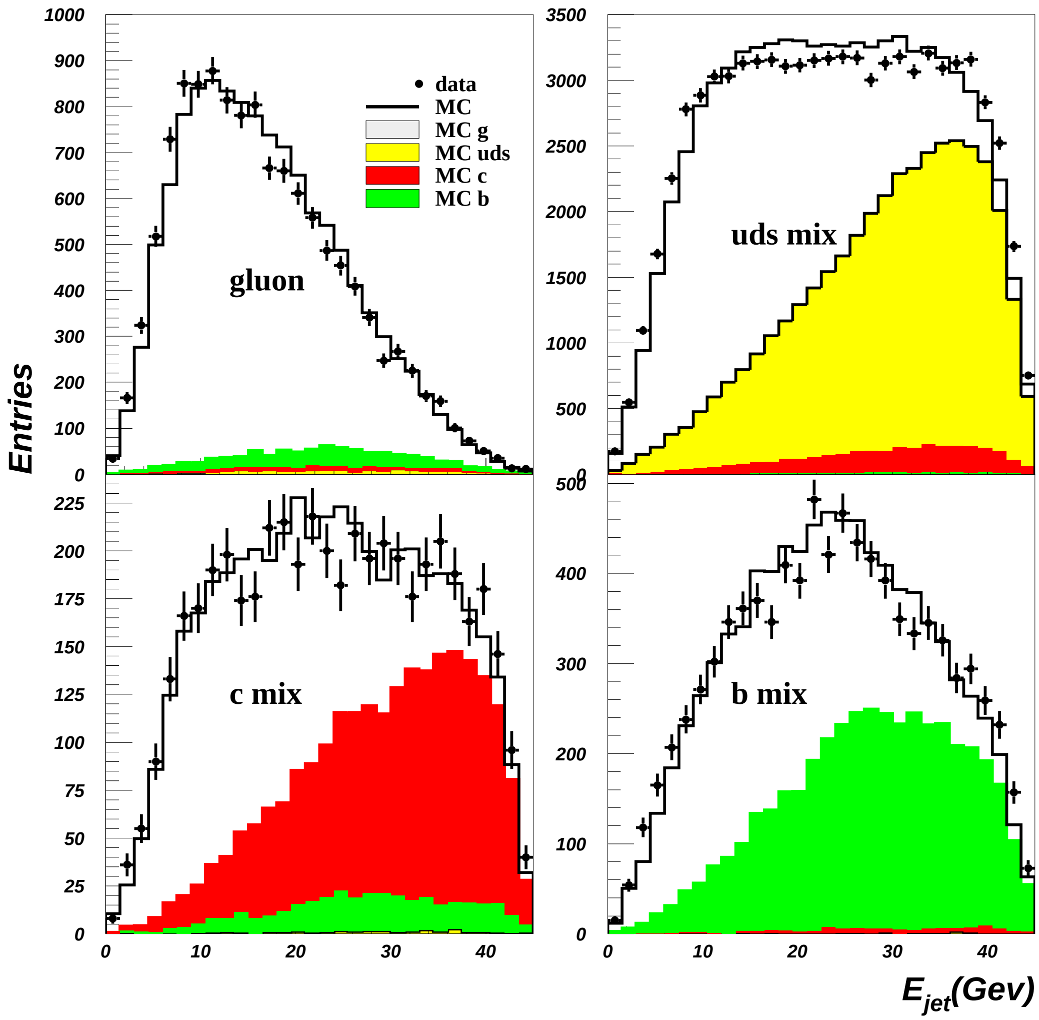

Figure 4.9: Energy distributions of four different jets: gluon tagged jets, $uds-$, $c-$ and $b-$jet mixture samples.

Chapter 5

CRID identification performance

5.1 CRID track selection

Particle identification is performed using the CRID liquid and gas radiators separately: 'liquid' and 'gas' analysis. The identification is also done using combined information from both liquid and gas radiators when both are available: 'combined' analysis.

More track selection criteria are applied to ensure that the tracks are in the barrel CRID acceptance, and that for these tracks, the CRID response is modelled very well by the detector MC simulation. These additional cuts also remove tracks that interact with the detector material or that are multiple scattered away from its trajectory in the CDC or the CRID. When tracks have scattered, they can be mismeasured and ultimately misidentified. When tracks have interacted, they are more likely to give no hits in the CRID, so they look like to have momentum below the CRID thresholds. The track selection cuts related to the detector performance and track reconstruction are

- The momentum p_{tot} of a track must satisfy $0.25 < p_{tot} < 50$ GeV/c. $p_{tot} > 0.25$ GeV/c removes a track missing a large fraction of their expected hits and requires the track to reach the CRID without spiralling back on itself. $p_{tot} < 50$ GeV/c rejects poorly momentum measured tracks which might contain hits from other tracks.

- The cut on the track polar angle with respect to the beam axis is required to be $|\cos\theta| < 0.68$ to ensure that the track is well within the fiducial region of the Barrel CRID. This requires a track to be away from the edge of the liquid ($|\cos\theta| \sim 0.71$) and gas ($|\cos\theta| \sim 0.69$) radiators.

- Tracks must have a minimum of 40 CDC hits, at least one of which is in the outermost superlayer. This condition requires that tracks have enough hits for a precise momentum measurement and ensures that the tracks enter the CRID. Tracks which have scattered or decayed in flight inside the CDC are also rejected by this requirement. Having hits in the outermost superlayer helps to determine the trajectory of the particle in the CRID more precisely.

Additional cuts are required for the liquid and gas radiators separately. The list of CRID track selection cuts for the previous particle identification study are described in reference [58],[77]. These CRID cuts for the previous study were well understood and misidentification was very small but statistical loss was large at 50%. For the current study, fewer CRID cuts are applied, allowing a gain in statistics while the systematic error and misidentification rates are still kept reasonably low. The CRID cuts used for the analysis are the standard CRID reconstruction flag sets:

- **BADID:** BADID is a basic CRID cut. This cut ensures that a track passes through an active region of the liquid or gas radiators. The primary CRID TPC containing the majority of their expected liquid or gas ring images is required to be functional and sensitive. For the gas analysis, this cut requires that the ring image is not reflected from any known bad mirrors, and that no saturated hit must be found within 2.5 cm radius of the ring center.

- **TPCSICK:** The primary TPC must not be the one with a known problem of having a very low photon detection efficiency. Often the '**BADID**' cut already includes this flag.

- **Liquid TPCBAD:** A typical expected liquid ring spans 2–3 TPCs in the azimuthal dimension. This cut requires that the two TPCs containing most of the liquid ring are required to be operating. This requirement is only for the liquid radiators.

- **NOMIP:** This requirement is necessary to remove tracks scattered through large angles before entering the CRID. For the liquid analysis, when a track goes through a TPC, the track is required to be extrapolated within 1 cm of a saturated CRID TPC hit (MIP match). These saturated TPC hits are produced from the passage of minimum-ionizing particles (MIP) in the TPCs. The passage of particles can be detected through large ionization signals which saturate electronics of multiple wires. The geometrical coverage of the TPCs is $\sim 80\%$ for tracks, therefore 'MIP match' cut rejects tracks scattered in the CRID and noise with no signal loss. Previously, there was $\sim 20\%$ statistical loss by discarding signals outside of the TPCs with applying the MIP match cut for all tracks. For the current study, we try to recover the statistical loss by not imposing this cut for the tracks which do not pass through the TPCs. For the gas analysis, we require either a MIP match or the presence of 4 hits consistent with a liquid ring. Since the geometrical coverage of combining the TPCs and liquid radiators is ~ 100, there is no signal loss by applying this cut.

- **GASXISO:** The gas ring images are required to be isolated from saturated TPC hits produced from the passage of the track or of any other tracks. Saturated TPC hits cause signal losses on nearby wires. These losses are not well understood or simulated. This is a problem for tracks above thresholds that can be mis-identified as below the thresholds. The basic '**BADID**' cut described above requires that there are no saturated hits within 2.5 cm radius of the gas ring's center. The value of 2.5 cm is the maximum gas ring radius from the expected gas ring center. This cut still allows some overlap of MIP hits. For $2.5 < p < 20$ GeV/c, this cut is tightened to be 5 cm (GASXISO) to have lower systematic errors, to reduce the misidentification, and to understand the MC simulation very well.

We apply all of the cuts listed above for the combined analysis, but for a CRID cut optimization study, we also use a combined analysis track sample without the '**GASXISO**' cut. For the previous results [58], more CRID cuts were applied and only $\sim 47\%$ of the good tracks which pass the QCD track selection cuts (described in Chapter 4) were accepted. With the current loosened cuts the track acceptance increases from $\sim 47\%$ to $\sim 82\%$ for the liquid analysis. For the gas analysis, it turns out that in $p \geq 20$ GeV/c (above the proton threshold) the misidentification does not become much bigger without the tight ring isolation requirement ('**GASXISO**' cut.). In this momentum region, improvement of the statistics is very important for some analyses in this thesis, and using the loose cut for the ring isolation almost doubles the statistics. The track acceptance for the gas analysis increases from $\sim 40\%$ to $\sim 80\%$ when the '**GASXISO**' cut is removed. The π, K or p identification criteria for a track for each analysis are summarized in Table 5.1. In the low momentum region $0.3 < p < 1.0$ ($2.5 < p < 10.0$) GeV/c, for the liquid (gas) analysis, the kaon and proton hypotheses are indistinguishable since both are below or near their thresholds, so tracks in the low momentum region are identified as either π or not-π, where not-π is a track which does not pass basic identification criteria for pion. In the high momentum region $2.5 < p < 7.0$ ($25.0 < p < 45.0$) GeV/c for the liquid (gas) analysis, π and K hypotheses become indistinguishable within our resolution of ring radius, tracks are identified as either p or not-p, where not-p is a track which does not pass basic identification criteria for p. 2×2 identification efficiency matrices are used for these regions. The identification criteria for the 2×2 efficiency matrices are also summarized in Table 5.1

The minimum log likelihood difference (LLIK) '5' for the liquid analysis is chosen to reduce the misidentification of π's as kaons or protons. For this chosen value, the MC simulation predicts low misidentification rates while maintaining high identification efficiency. The signal to noise ratio at LLIK > 5 in the kaon and proton samples is greater than one for $p < 3$ GeV/c. Due to the lower π fraction, this LLIK value can be reduced to 3 for the gas and the combined analyses.

Fig. 5.1 shows the 2×2 efficiency matrices, π/not-π, and p/not-p by the liquid analysis.

For the gas analysis, the π/not-π 2×2 efficiency matrix shown in Fig. 5.2 is applied in low momentum region ($2.5 < p < 10$ GeV/c).

The leptonic hypotheses are indistinguishable from the π hypothesis in the SLD CRID for most of the momentum regions. For this reason, leptons are included in the π category and later, the measured π production rate is corrected using the MC predicted leptonic fractions. The leptonic fractions are momentum dependent but small over most of the momentum regions. The leptons predominantly come from γ conversions, and b and c semileptonic decays. Similarly, a very small contribution from the heavier baryons as Σ^- and Ξ^- which decay outside the CDC are included in the proton category. Again, the appropriate correction based on MC studies is applied to the measured proton production rate.

Identification Criteria			
	Liquid Analysis	Combined Analysis	Gas Analysis
π ID	$\ln\mathcal{L}_\pi - \ln\mathcal{L}_K > 5$ & $\ln\mathcal{L}_\pi - \ln\mathcal{L}_p > 5$	$\ln\mathcal{L}_\pi - \ln\mathcal{L}_K > 3$ & $\ln\mathcal{L}_\pi - \ln\mathcal{L}_p > 3$	$\ln\mathcal{L}_\pi - \ln\mathcal{L}_K > 3$ & $\ln\mathcal{L}_\pi - \ln\mathcal{L}_p > 3$
K ID	$\ln\mathcal{L}_K - \ln\mathcal{L}_\pi > 5$ & $\ln\mathcal{L}_K - \ln\mathcal{L}_p > 5$	$\ln\mathcal{L}_K - \ln\mathcal{L}_\pi > 3$ & $\ln\mathcal{L}_K - \ln\mathcal{L}_p > 3$	$\ln\mathcal{L}_K - \ln\mathcal{L}_\pi > 3$ & $\ln\mathcal{L}_K - \ln\mathcal{L}_p > 3$
p ID	$\ln\mathcal{L}_p - \ln\mathcal{L}_\pi > 5$ & $\ln\mathcal{L}_p - \ln\mathcal{L}_K > 5$	$\ln\mathcal{L}_p - \ln\mathcal{L}_\pi > 3$ & $\ln\mathcal{L}_p - \ln\mathcal{L}_K > 3$	$\ln\mathcal{L}_p - \ln\mathcal{L}_\pi > 3$ & $\ln\mathcal{L}_p - \ln\mathcal{L}_K > 3$
not-π ID	$\ln\mathcal{L}_K - \ln\mathcal{L}_\pi > 5$		$\ln\mathcal{L}_K - \ln\mathcal{L}_\pi > 3$
not-p ID	$\ln\mathcal{L}_\pi - \ln\mathcal{L}_p > 5$		$\ln\mathcal{L}_\pi - \ln\mathcal{L}_p > 3$

Table 5.1: The criteria for the particle identification of tracks in the 3×3 matrix and in the 2×2 matrix format for all three analyses.

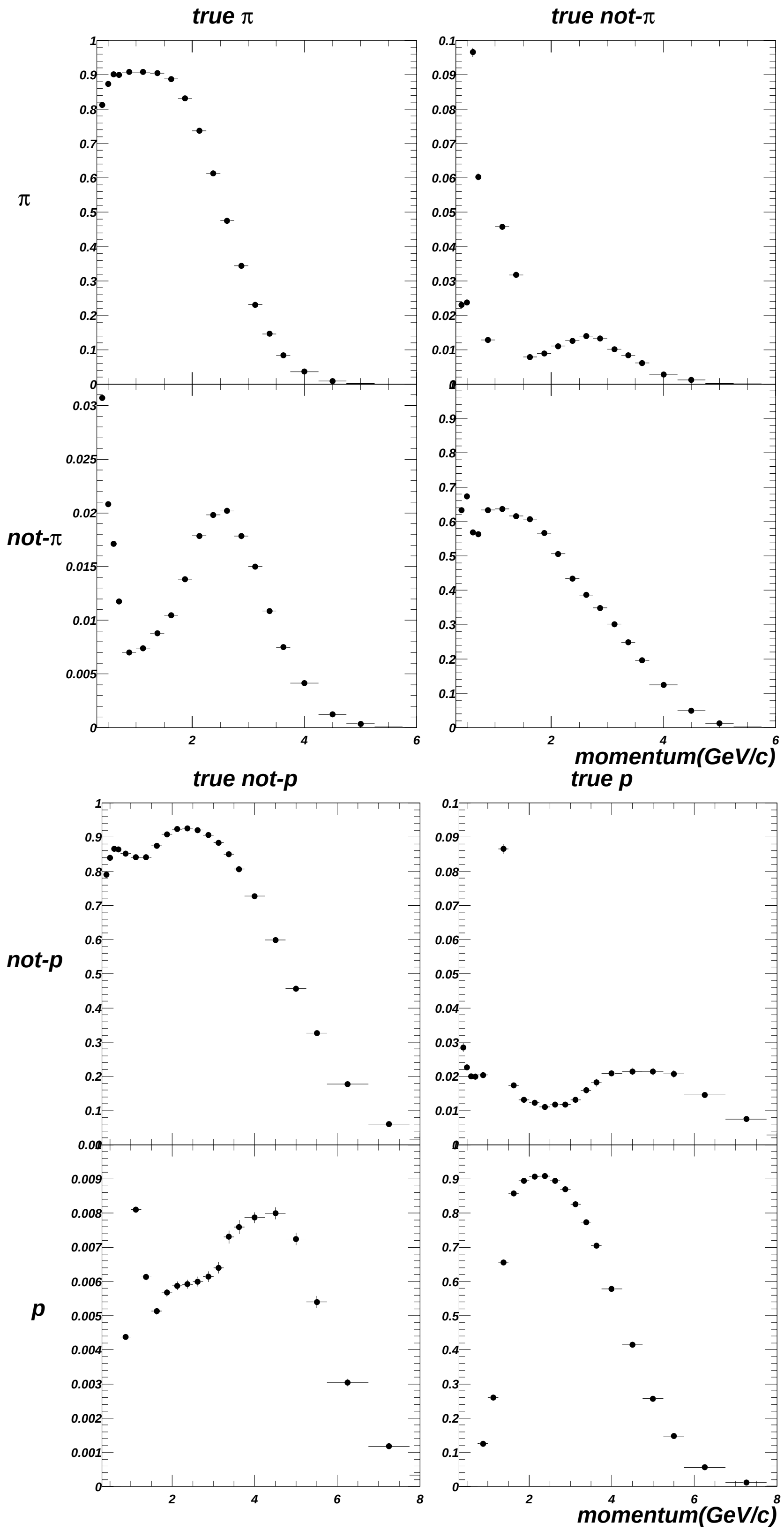

Figure 5.1: Simulated matrix of identification efficiencies of true $\pi^{\pm}$, not-$\pi^{\pm}$ (top) and $p/\bar{p}$,not-$p/\bar{p}$ (liquid) by the liquid analysis

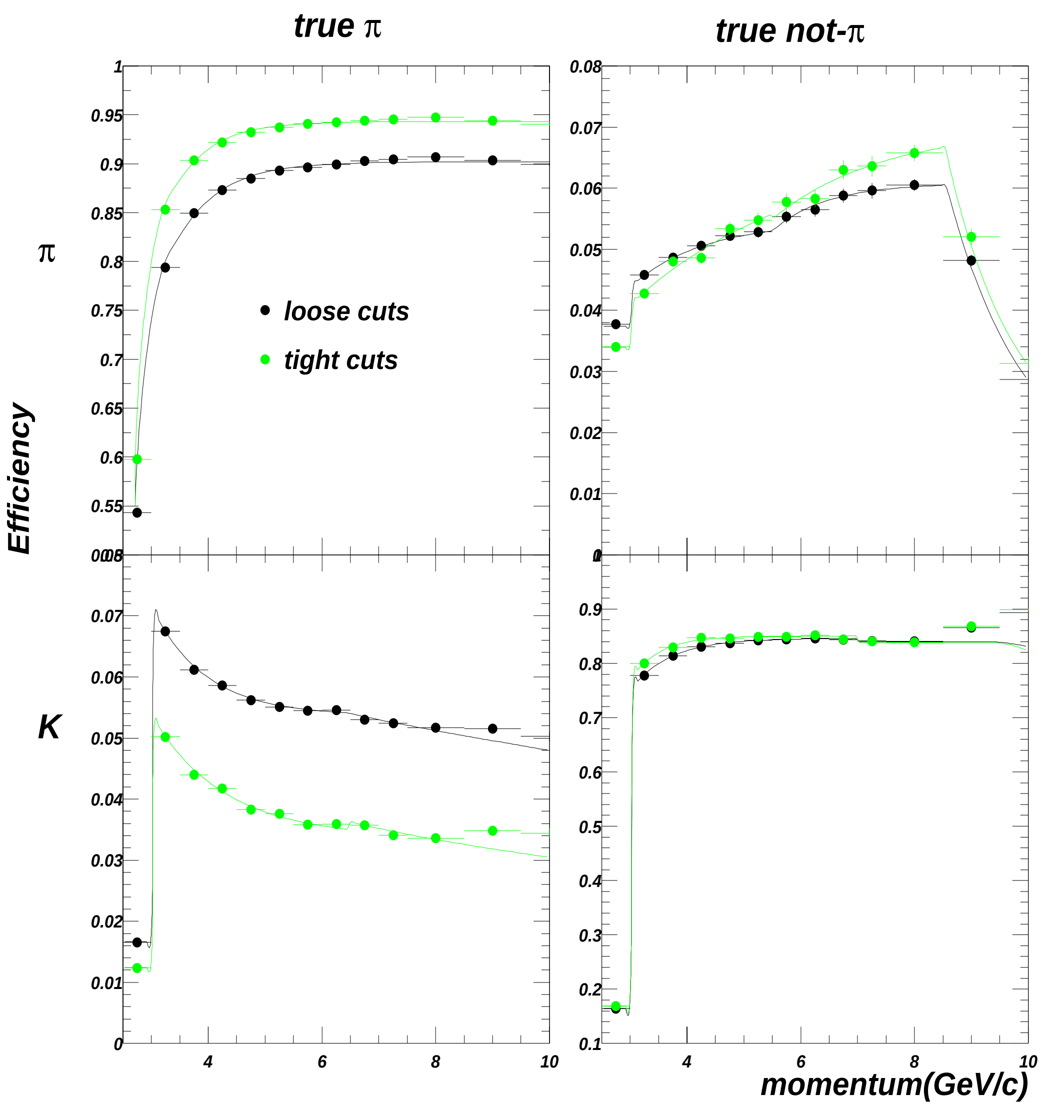

Figure 5.2: Simulated matrix of identification efficiencies of true $\pi^{\pm}$ and not-$\pi^{\pm}$ by the gas analysis with two different CRID cuts described in the text.The points are from the hadronic MC and the curves are the parametrizations described later.

5.2 Particle identification efficiency matrix

The construction of a momentum dependent particle identification efficiency matrix is the main procedure for the particle production analyses. Each element of the efficiency matrix E_{ij} is the probability that a charged hadron of type i which passes all the track selection cuts listed earlier is identified as a hadron of type j. For most momenta, the 3×3 matrix is used. The 2×2 matrices are used where only π/not-π or p/not-p separation is possible as noted in Sect. 5.1, i and j can be $\pi^{\pm}$, $K^{\pm}$ or p/$\bar{p}$. Particle identification efficiencies depend on the selected track sample, and definitions of particle identification are discussed in Sect. 5.1. The $3{\times}3$ gas efficiency matrix is shown in Fig. 5.3 for identifying particles in hadronic events as a function of momentum.

The matrix is generated directly from the CRID simulation for the liquid, combined, and gas analyses. The CRID simulation is tuned to reproduce measured detector resolutions, indices of refraction, and the distributions of numbers of found hits in the data. The tuning is done by smearing Cherenkov angles, the numbers of Cherenkov hits found in different TPCs, and mirror alignments until a satisfactory match to the the data is achieved [58] [60].

The gas analysis is very effective in the momentum ranges of: $2.5{-}35$ GeV/c for π identification, $9{-}35$ GeV/c for K identification, and $10{-}45$ GeV/c for p identification. The liquid analysis is maximally effective in the momentum ranges of: $0.5{-}3$ GeV/c for pions, $0.75{-}3$ GeV/c for kaons, and $0.75{-}5$ GeV/c for protons. The combined analysis extends the range of the liquid kaon and proton coverage up to about $2.5{-}7.5$ GeV/c and also improves the π efficiency in this range.

The gas pion efficiency function $E_{\pi\pi}$ has a rising sharp structure corresponding to the pion Cherenkov threshold ($p \sim 2.5$ GeV/c). A flat plateau continues over the momentum $3.5 < p \leq 12$, and a falloff begins around 15 GeV/c, and the efficiency drops to $\sim 10\%$ at 35 GeV/c. The falloff occurs because the pion and kaon Cherenkov angles become degenerate at high momentum. The gas kaon efficiency function E_{KK} has a structure similar to the gas pion efficiency function except a rising structure begins at the kaon threshold ($p \sim 8.5$ GeV/c). The gas proton efficiency rises slowly above the kaon Cherenkov threshold but the

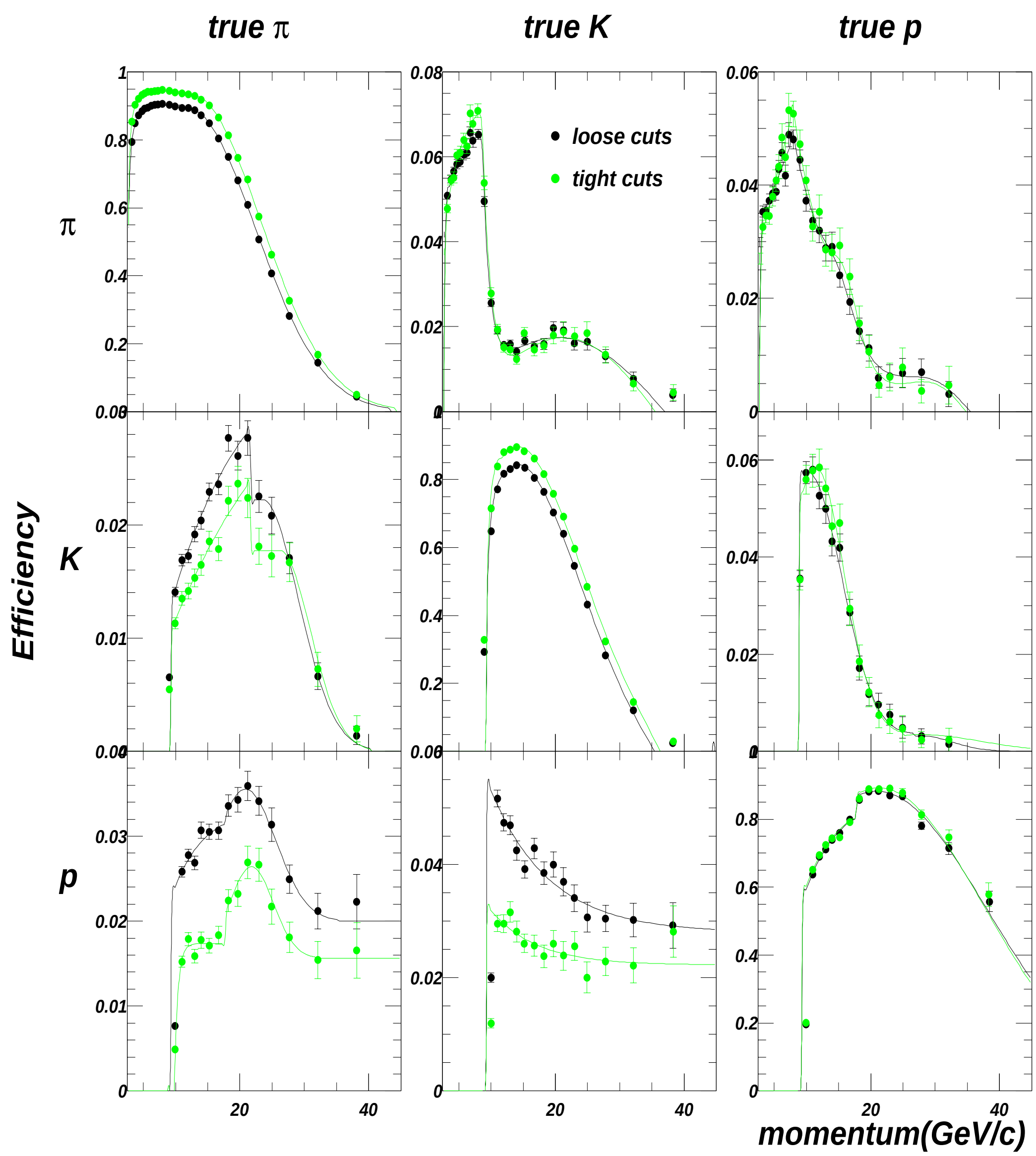

Figure 5.3: Simulated matrix of identification efficiencies for true $\pi^{\pm}$, $K^{\pm}$, and p/$\bar{\text{p}}$ to be identified as each of these three particle types by the gas analysis with two different sets of CRID cuts described in the text. The points are from the hadronic MC and the curves are the parametrizations described later.

rising slope becomes stiff above the proton threshold ($p \sim 17$ GeV/c), and starts to decline at ~ 30 GeV/c. These efficiency structures strongly depend on the Cherenkov thresholds of pions, kaons, and protons and the Cherenkov angle resolution.

Fig. 5.4 shows the 3×3 liquid efficiency matrix. The liquid analysis efficiency functions look very much like those for the gas analysis except that the pion Cherenkov threshold ($p \sim 0.18$ GeV/c) for the liquid analysis is below the momentum cut we applied, so the pion efficiency begins at its maximum.

For the combined analysis, the pion efficiency function is determined predominantly from the gas analysis so the combined pion efficiency function is almost identical to that of the gas analysis. But by combining the gas and liquid information, the misidentification is improved. Hence, the combined pion efficiency is improved compared to that of the gas analysis. The combined proton efficiency is dominantly from the liquid analysis. Combining of the liquid and gas analyses can reduce the misidentification of proton tagged as pion, so again the combined proton efficiency is higher than that of the liquid analysis. The combined kaon efficiency requires both gas not-π and liquid not-p. The combined kaon efficiency is much lower than either the liquid or the gas kaon efficiency. The 3×3 efficiency matrices for the combined analysis with two different sets of the CRID cuts are shown in Fig. 5.5.

The gas misidentification efficiency element $E_{\pi K}$ appears at the kaon threshold since some pions have few hits and backgrounds from noise have hits around the expected kaon radius. The function has a peak at the proton threshold and it starts to decrease like in gas $E_{\pi\pi}$. Gas $E_{\pi p}$ is similar to gas $E_{\pi K}$ for $15 < p < 30$ GeV/c but it becomes flat from ~ 30 GeV/c. Gas E_{Kp} has the same structure as gas $E_{\pi p}$ above the proton threshold. The structure of gas $E_{\pi p}$ and E_{Kp} below the proton threshold is due to the absence of expected hits at the pion and kaon radii. Gas $E_{K\pi}$ and $E_{p\pi}$ have a similar structure around the kaon threshold. Gas $E_{K\pi}$ and $E_{p\pi}$ increase from the pion threshold to the kaon threshold because as momentum increases the pion radius is getting bigger, and therefore there are more chances for the background hits to fall near pion radii and cause the background hits to be identified as pions. Gas $E_{K\pi}$ starts to decrease at the kaon threshold due to the appearance of true hits from kaons. Since the background hits can be identified as either

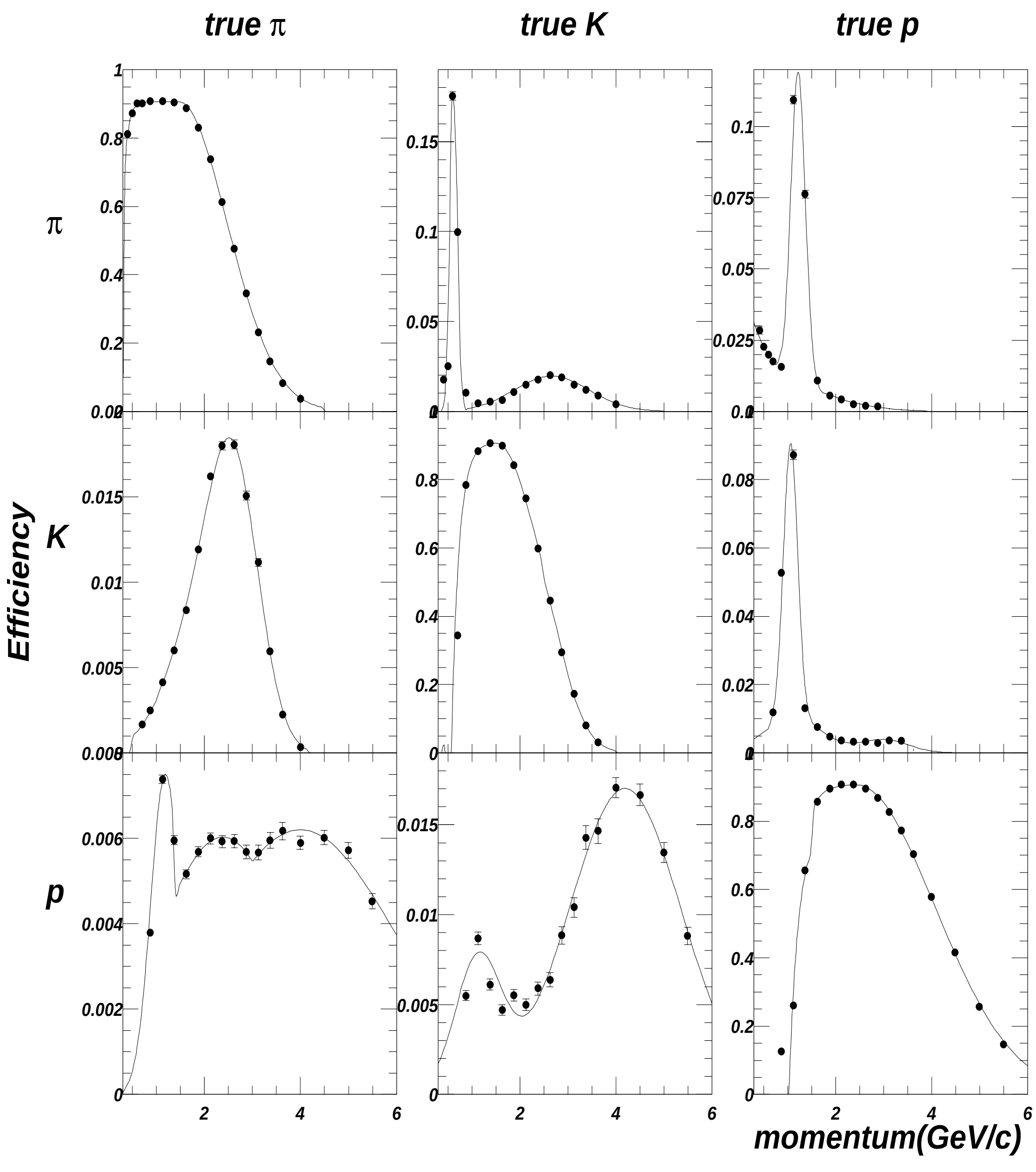

Figure 5.4: Simulated matrix of identification efficiencies for true $\pi^{\pm}$, $K^{\pm}$, and p/$\bar{\rm p}$ to be identified as each of these three particle types by the liquid analysis.

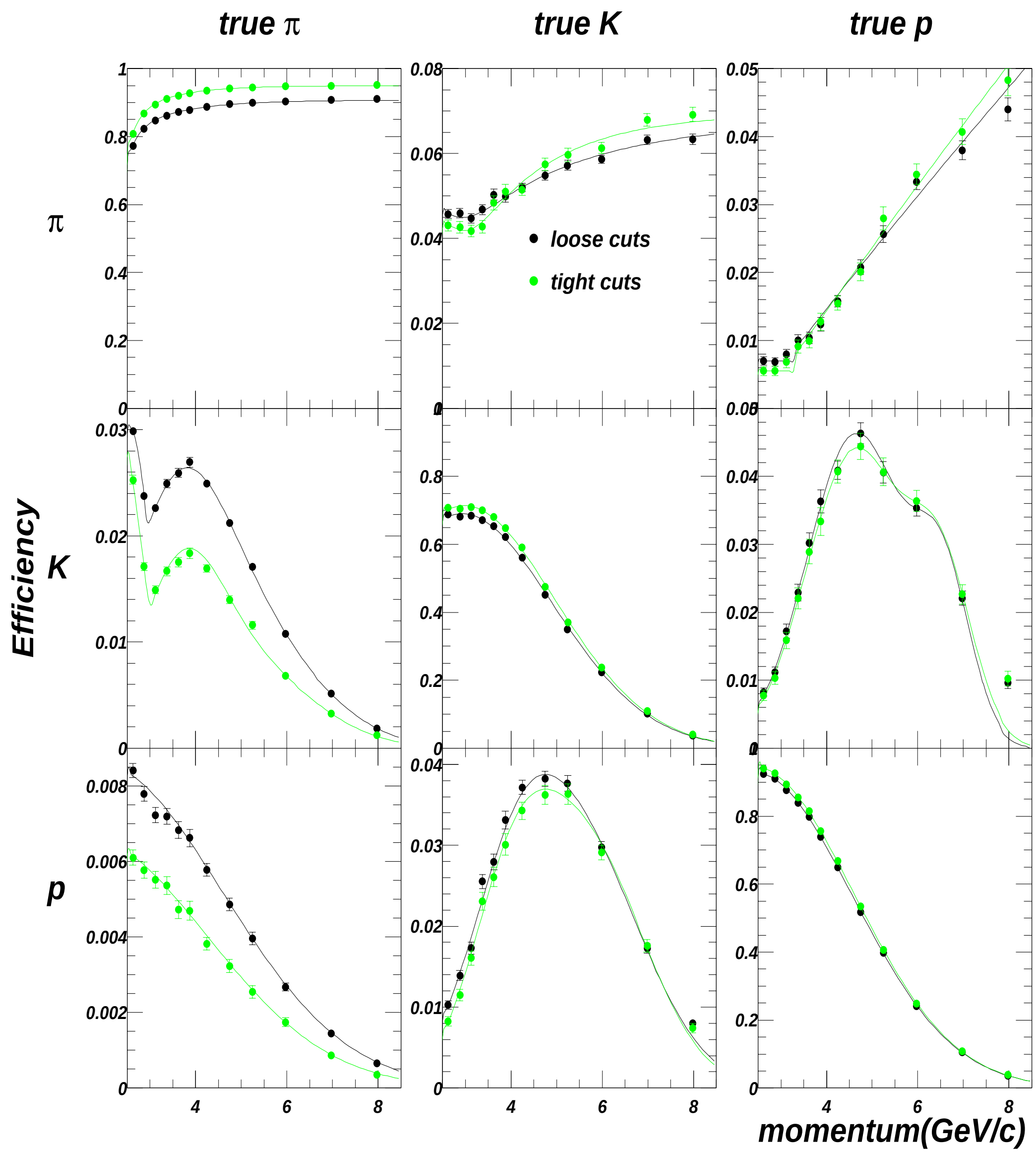

Figure 5.5: Simulated matrix of identification efficiencies by the combined analysis.

pion or kaon, proton misidentification is now divided between gas E_{pK} and $E_{p\pi}$. Gas $E_{K\pi}$ then increases as the kaon and pion radii begin to converge, then decreases as they overlay completely and the proton radius begins to appear. A similar structure in gas $E_{p\pi}$ and E_{pK} exist at higher momentum region.

The MC simulation reproduces the shape of the momentum dependence of the data efficiencies generally well as we will discuss in the next section. Even though the MC is reliably close to the data, we still need to correct the MC efficiency functions by a few percent using the data and the MC K_s and τ decays for the π identification column ($E_{\pi\pi}$, $E_{\pi K}$ and $E_{\pi p}$) and for the proton efficiency function. The rest of the unmeasured efficiency matrix elements are taken from the MC with correction terms deduced from measured efficiencies. The calibration process starts with fitting and parameterizing each element of the hadronic MC efficiency functions with a functional form. This process smooths the statistical fluctuation of the MC and gives a convenient parameterization with a small number of parameters to represent the detector performance and underlying physical effects. The parameterization function forms are not expected to give the true efficiency at every point but to join points at the centers of momentum bins in order to represent the expected structure of the true efficiency curves.

Functions of the identification efficiencies are selected which reflect the momentum dependent structures of the data and the MC. The parameters of the functions can be related to the performance parameters of the CRID. There are several functional forms chosen for the efficiency matrix. For some cases, two or three functions are combined to parameterize an efficiency.

The first functional form used frequently is a rising exponential $R(a, b, c; p) = a(1 - e^{-c(p-b)})$, where p denotes the momentum of a hadron. The amplitude a is sensitive to the average number of detected hits, the edge position b depends mainly on the index of refraction, and the slope c is essentially fixed by the momentum dependence of the average number of expected Cherenkov photons.

The second functional form is a Gaussian $G(A, p_0, \sigma; p) = Ae^{-(p-p_0)^2/2\sigma^2}$. In this case A is sensitive to the average number of detected photons, momentum p_0 depends on the average Cherenkov angle resolution, and σ is essentially fixed by the resolution assumed in the likelihood calculation.

The last functional form is a "half-Gaussian" $H(A, p_0, \sigma; p)$ defined to have a value of A for $p < p_0$ and to equal $G(A, p_0, \sigma; p)$ for $p > p_0$. The determination process of these parameterization functions are described in Ref. [58] in detail. For each function case the important parameters are roughly orthogonal and correspond to the two dominant sources of systematic uncertainties in the CRID simulation, The dominant systematic errors are the number of detected photons and the index of refraction for $R(a, b, c; p)$ function, and the number of detected photons and the average Cherenkov angle resolution for $G(A, p_0, \sigma; p)$ function. For misidentification elements, $R(a, b, c; p)$ and $G(A, p_0, \sigma; p)$ work nicely and have similar physical interpretations. The functions and parameters for the data and the MC hadronic events are summarized in Tables 5.2, 5.3 and 5.4 for the efficiencies, and in Tables 5.5 and 5.6 for the off-diagonal elements of the efficiency matrix.

The calibration procedure is performed by obtaining the efficiency functions in the data and the MC tracks from K_s and τ decays. Differences between the data and the MC efficiencies of the test samples are described in the next section. In order to match the measured hadronic efficiencies, the MC efficiency matrix is modified by the measured differences between the data and the MC K_s and τ decay tracks.

Pion Efficiency Parametrization		
Liquid	Combined	Gas
R(1.004, 0.193, 10.904) $\times$ H(0.893$\pm$0.003, [0.903] 1.207, 1.984) $p < 0.75$	R(0.940, 0.221, 1.043) $\times$ R(1.010, 2.063, 4.688) $p < 3$	R(0.859$\pm$0.005, [0.902] 1.618, 1.315) $p < 11$
R(1.004, 0.193, 10.904) $\times$ H(0.883$\pm$0.003, [0.903] 1.186$\pm$0.013, [1.207] 1.984) $p < 1.75$	R(0.911$\pm$0.007, [0.940] 0.221, 1.043) $\times$ R(1.010, 2.063, 4.688) $p < 5.5$	H(0.897$\pm$0.005, [0.931] 12.651, 1.315) $p < 20$
H(0.853$\pm$0.003, [0.873] 1.551$\pm$0.013, [1.572] 0.980$\pm$0.007) [0.951] $p \geq 1.75$	R(0.907$\pm$0.006, [0.940] 0.221, 1.043) $\times$ R(1.010, 2.063, 4.688) $p \geq 5.5$	H(0.904$\pm$0.007, [0.931] 12.651, 10.539) $p \geq 20$

Table 5.2: Functions ($R(a, b, c)$, $G(A, p_0, \sigma)$ and $H(A, p_0, \sigma)$) used to parametrize the π efficiency of the CRID identification. A parameter value is derived from the calibration (Sect. 5.3), the MC value is given in square brackets.

Kaon Efficiency Parametrization		
Liquid	Combined	Gas
R(1.000, 0.647, 8.870) $\times$ H(0.892$\pm$0.003, [0.902] 1.517$\pm$0.013, [1.538] 0.929) $p < 0.75$ R(1.000, 0.647, 8.870) $\times$ H(0.882$\pm$0.003, [0.902] 1.517$\pm$0.013, [1.538] 0.959$\pm$0.007) [0.929] $p < 2.5$ H(0.562$\pm$0.002, [0.575] 2.160$\pm$0.013, [2.181] 0.624$\pm$0.004) [0.605] $p \geq 2.5$	$E_{pp}\times$ R(1.055, –1.057, 0.334) $2.5 \leq p < 6$	$E_{\pi\pi}$(x – 0.8)$\times$ R(0.999, 5.351, 0.380)$\times$ R(0.991, 35.461, –0.366)$\times$ R(1.000, 9.000, 2.500) $p < 20$ $E_{\pi\pi}$(x – 0.55)$\times$ R(0.999, 5.217, 0.439)$\times$ R(0.988, 36.289, –0.4629)$\times$ R(1.000, 9.000, 2.500) $p \geq 20$

Table 5.3: Functions used to parametrize the kaon efficiency of the CRID identification. A parameter value is derived from the calibration, the MC value is given in square brackets.

Proton Efficiency Parametrization		
Liquid	Combined	Gas
$0.133\times E_{pp}$ $p < 0.75$		R(0.841±0.004, [0.873] 3.701, 0.184) $p < 20$
$0.865\times E_{pp}$ $p < 1.5$	H(0.917±0.002, [0.945] 2.231±0.083, [2.410] 2.273±0.009) [2.183]	
R(1.002, 1.025, 5.066) $\times$ H(0.878±0.002, 2.439, 1.632) $p \geq 1.5$		H(0.866±0.006, [0.892] 22.261, 17.417) $p \geq 20$

Table 5.4: Functions used to parametrize the proton efficiency of the CRID identification. A parameter value is derived from the calibration, the MC value is given in square brackets.

Efficiency Matrix Parametrization			
	Liquid	Combined	Gas
$E_{K\pi}$	$p < 1.5$: G(0.021,2.659,0.777) +G(0.180,0.619,0.074) $p \geq 1.5$: G(0.016,2.659,0.777) +G(0.180,0.619,0.074)	G(0.020,2.219,0.470) +R(0.069,1.662,0.564)	$p < 8.5$: R(0.068,–0.634,0.362) $p < 13.5$: R(0.068,–0.634,0.362) −R(0.120,7.753,0.847) +G(0.069,20.274,21.897) $p < 20$: R(0.077,–0.634,0.362) −R(0.120,7.753,0.847) +G(0.069,20.274,21.897) $p \geq 20$: R(0.075,0.266,0.346) −R(0.129,7.728,0.715) +G(0.071,21.191,19.055)
$E_{p\pi}$	G(0.211,–1.397,0.759) +G(0.014,1.218,1.240) +G(0.110,1.219,0.150)	$p < 3.3$: 0.0055 $p \geq 3.3$: R(0.574,2.486,0.017)	$p < 7.5$: R(0.314,–7.678,0.011) $p < 20$: R(–0.009,25.851,0.101) +G(0.101,0.006,14.831) +G(0.009,30.5,5.593) $p \geq 20$: R(–0.010,24.227,0.112) +G(0.009,15.886,2.060) +G(0.010,30.5,5.367)

Table 5.5: Parametrization functions of $E_{K\pi}$ and $E_{p\pi}$ of the particle identification efficiency matrix.

Efficiency Matrix Parametrization			
	Liquid	Combined	Gas
$E_{\pi K}$	$p < 1.5$: G(0.019,2.632,0.518) +G(0.010,1.903,0.695) $p \geq 1.5$: G(0.012,2.632,0.518) +G(0.006,1.903,0.695)	$p < 3$: G(0.030,2.317,0.525) $p \geq 3$: G(0.017,3.639,1.012) + G(0.009,4.609,1.634)	$p < 13.5$: H(0.031,4.305,0.087) $p < 20$: H(0.041,4.305,0.087) $p \geq 20$: H(0.018,26.201,4.718)
E_{pK}	G(0.011,1.114,0.586) +G(0.080,1.063,0.147) +G(0.004,2.997,0.510)	G(0.044,4.618,1.055) +G(0.024,6.530,0.694) +G(0.020,7.00,1.00)	$9 - 20$: G(0.058,10.138,5.479) +G(0.003,27.82,4.777) $p \geq 20$: G(0.058,11.363,4.532) +G(0.003,27.82,9.196)
$E_{\pi p}$	$p < 1.4$: G(0.008,1.185,0.300) $p < 3$: G(0.008,2.380,1.400) $p \geq 3$: G(0.006,4.000,1.990)	G(0.008,1.354,2.783)	$p < 20$: R(0.077,3.767,0.205) $p \geq 20$: G(0.011,21.803,3.405)
E_{Kp}	G(0.024,4.187,1.165) +G(0.010,1.126,0.485)	G(0.025,4.020,0.931) +G(0.029,5.674,1.293)	$p < 20$: $0.064+0.075e^{-p/9.178}$ $p \geq 20$: $0.035+0.039e^{(}-p/7.116)$

Table 5.6: Parametrization functions of $E_{\pi K}$, E_{pK}, $E_{\pi p}$ and E_{Kp} of the particle identification efficiency matrix.

5.3 Calibration of the efficiencies

5.3.1 Samples for measured data efficiency

Direct tests of the identification efficiencies from the data are required to check the detector performance and calibrate the MC efficiency matrix. For these tests we select track samples that are identified by independent methods from the data as well as the MC and put all the track cuts and identifying criteria on the samples. Tracks from $K_s \to \pi\pi$ and $\tau^{\pm}$ decays are used as π test samples. In order to select $K_s \to \pi\pi$ decays, pairs of oppositely charged tracks are combined if the tracks are consistent within errors with being from a common vertex. Descriptions of the selection criteria of vertex candidates and π's for $K_s \to \pi\pi$ decays, and determination of the candidate positions can be found in reference [70]. The mass difference $|M_{\pi\pi} - M_{K_s^0}|$ between the sum of masses of the π's to form a vertex and K_s's mass ($M_{K_s^0}| = 497.7$ MeV$/c^2$) is shown in Fig. 5.6.

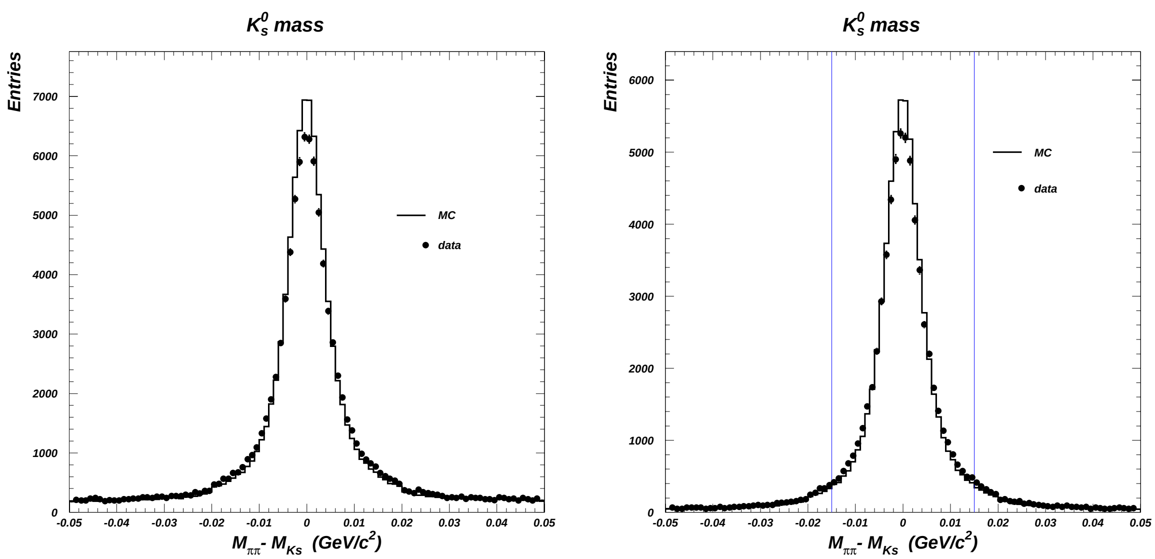

Figure 5.6: $|M_{\pi\pi} - M_{K_s^0}|$ distribution (left) and after the cuts to reject $\Lambda/\bar{\Lambda}$ and $\gamma \to e^-e^+$ (right).

For this analysis, additional cuts are applied to get a purer K_s sample. The mass $M_{\pi\pi}$ of the vertex is required to satisfy $|M_{\pi\pi} - M_{K_s^0}| = 15$ MeV$/c^2$. A cut on the helicity angle θ^*, $|\cos\theta^*| < 0.8$ is applied to remove $\Lambda/\bar{\Lambda}$ and $\gamma \to e^-e^+$ background in the K_s candidate sample [78]. θ^* is the angle between π^+ momentum vector in the K_s rest frame and the K_s flight direction. Fig. 5.6 also presents $|M_{\pi\pi} - M_{K_s^0}|$ with the additional cuts to reject the background.

In the MC, these criteria result in $> 97\%$ purity of K_s in the mass window and $\sim 99.5\%$ π purity for the candidate tracks.

τ-pair events, $Z^0 \to \tau^-\tau^+$ are selected based on low track multiplicity and jet multiplicity. There are also several selection criteria to remove e-pair and μ-pair events from the τ sample. The selection cuts for tagged tau sample are as following:

- There is at least one QCD qualified track (Chapter 4) but not more than nine in the event. This is one of the strongest selection cuts which rejects multi-particle hadronic events.

- Two hemispheres are defined for each event according to the direction of the highest momentum track in the event. There must be at least one track in each hemisphere.

- The momentum of the highest momentum track in the event must be greater than 3 GeV/c. This suppresses events whose thrust axes are out of the detector fiducial region since only soft tracks far from the thrust axis are detected for these events. For one-prong τ decays the charged particle tends to have high momentum. This cut also prevents soft background tracks from interactions with the detector material to be tagged as τ decay tracks. Here, the thrust axes are defined using only tracks.

- The polar angle θ between the track momentum direction and the beam axis is required to satisfy $|\cos\theta| < 0.8$, in order to avoid CDC tracking inefficiencies.

- The total charge of the tracks in one hemisphere is required to be $+e$ and the total charge of the tracks in the other is required to be $-e$. This cut removes random background from beam-pipe interactions or other events.

- The invariant mass calculated by assigning π mass for individual tracks in each hemisphere is required to be smaller than 1.8 GeV/c^2. This cut rejects hadronic Z^0 decay events.

- The angle between the two hemisphere thrust axes determined from tracks in each hemisphere is required to be $\cos\phi < -0.94$. This cut removes wide angle $\mu-$pair events.

The estimated efficiency from the MC simulated τ events is approximately 60% and the estimated hadronic background in the τ sample is negligible ($\sim 0.02\%$). The predominant background is from $\mu-$pair or $e-$pair events but the purity of the selected τ events is over 99%. τ-pair events produce primarily e, μ and π tracks which can be all used for π measurement. The 1.7% kaon content from τ decays is well measured and included in the simulation.

The CDC and CRID track selection cuts for K_s and τ decayed tracks are loose compared with the selection cuts for hadronic events in order to obtain larger statistics. The typical K_s decay particles do not have VXD information and have fewer hits in the CDC since many of the K_s's decay inside of the CDC. The track selection cuts for the calibration samples are loosened to require a minimum 25 hits in the CDC instead of 40. The track to IP impact parameter cuts are also not applied for tracks from K_s and τ decays. The new track selection cuts affect the τ events very little. The independent calibrations of the 'liquid', 'gas' and 'combined' analyses are discussed in the next sections.

Tracks from $\Lambda^0 \to \pi p$ were used as proton samples for the previous particle production study [58]. The selection criteria for $\Lambda^0 \to \pi p$ and proton efficiency study can be found in Ref. [58],[70]. The resulting proton efficiencies for data and MC agreed within 10% except for the momentum region right above the proton threshold. For the current analysis, an alternative method, $\pi \to$ not-p identification, is used to calibrate the proton efficiency. This method will be described in the next sections.

5.3.2 Calibration of Liquid Efficiencies

The liquid π identification efficiency and misidentification rates are calibrated using $\pi^\pm$ from tagged K_s decays. The π efficiency column for the MC and the data are shown in Fig. 5.7.

The parameterizations of the π efficiency of the data and MC K_s are the same as that of hadronic events except for the values of parameters. The parameterization functions for the data and MC K_s decay samples are listed in Table 5.7.

The function $H(A, p_0, \sigma; p)$ is described in Chapter 5. Qualitatively the data and the MC agree well in the shape of the efficiencies. There is a difference in amplitude between the

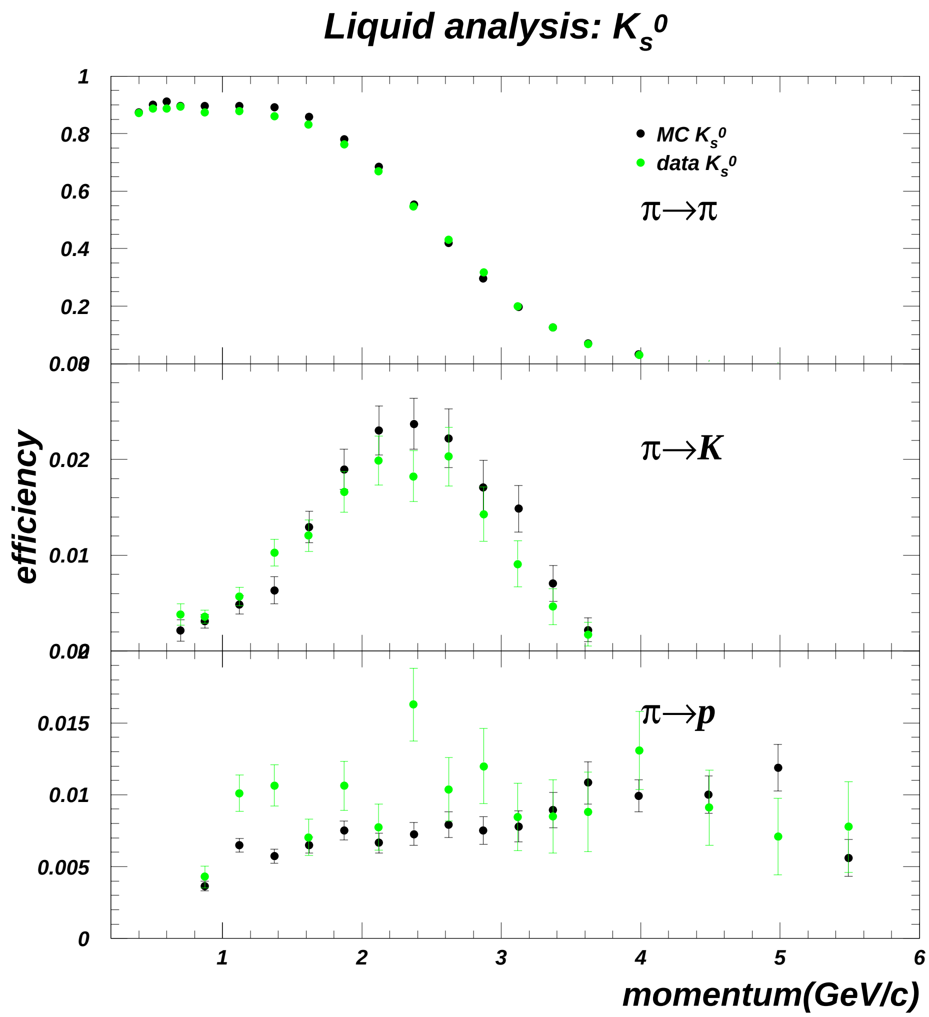

Figure 5.7: Efficiencies for tracks from K_s decays to be identified as each hadron type by the liquid analysis.

Liquid π Efficiency of K_s decays		
	MC K_s	data K_s
$p < 0.75$ GeV/c	$H(0.889, 1.344, 1.029)$	$H(0.879, 1.306, 1.072)$
$p \geq 0.75$ GeV/c	$H(0.875, 1.348, 1.026)$	$H(0.872, 1.335, 1.052)$

Table 5.7: The π parameterization functions for tracks from K_s decays by the liquid analysis.

two efficiencies at the plateau and a shift of the edge position. The K_s MC overestimates the normalization A of the data efficiency by (1.14±0.32)% and (2.61±0.32)% for below (p < 0.75 GeV/c) and above the liquid kaon threshold region respectively. The edge position p_0 of the data π efficiency is shifted by −0.021±0.013 compared to that of the MC π efficiency. There is also a difference between the data and the MC in the slope of the efficiency of about 3%, which implies that a problem with liquid cherenkov angle reconstruction might exist in data. These shift terms are applied to the parametrization of the hadronic MC to yield a measured $E_{\pi\pi}$ in data with a well-defined error.

As a complementary check we also compare the π identification efficiency in MC and data τ events in Fig. 5.8. The π identification efficiency in τ events show the same discrepancy between the data and the MC that we observe in K_s decay particles.

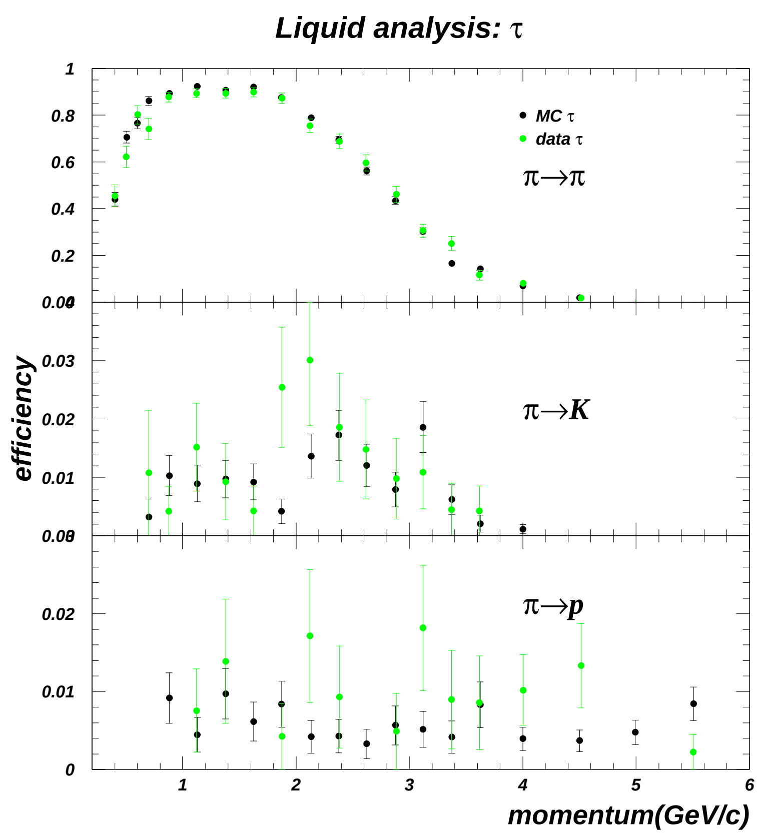

Figure 5.8: Efficiencies for tracks from τ decays to be identified as each hadron type by the liquid analysis.

For $E_{\pi K}$ and $E_{\pi p}$, there are not enough statistics for the τ data to see a structure but the data and MC seem to be consistent. In order to ensure that we can use the correction terms from the K_s sample to calibrate hadronic events, the π efficiency columns of MC K_s and MC hadronic events are compared in Fig. 5.9.

Due to the deteriorating tracking performance and dip angle reconstruction of tracks from long decay length K_s decays, the K_s π sample has a degraded π identification efficiency compared to the MC hadronic events. The amplitude normalization difference is negligible and the discrepancy in the edge shift is statistically significant, but small. Fig. 5.9 also compares the π efficiency columns of the MC τ and the MC hadronic events as a cross check.

For the kaon efficiency E_{KK}, the correction terms measured for the π identification efficiency are applied. This procedure is reasonable because the efficiencies of π and kaon approach each other as momentum increases until the proton radius becomes significantly large compared to the pion or the kaon radius.

For the 2×2 efficiency matrices, K_s decay particles are identified as not-protons if $\mathcal{L}_\pi - \mathcal{L}_p > 5$ or not-π if $\mathcal{L}_K - \mathcal{L}_\pi > 5$. These terms form two different 2×2 efficiency matrices as discussed in Chapter 5. π's identified as not-protons are used for calibration of the proton efficiency in the high momentum regions for the liquid analysis and for the combined analysis. The efficiency for π's identified as not-protons have a similar structure to the efficiency for protons identified as protons at high momenta. This similarity occurs because π's and kaons are indistinguishable at high momenta. The particle identification is from calculating a probability of an observed ring to be the ring of a hypothesized particle. As mentioned earlier, the ring size of hypothesis π and kaon in high momentum region above ~ 2 GeV/c for the liquid analysis are almost indistinguishable compared to the ring size of proton, so particles are identified as either a π/kaon or a proton. In this area the probability of $\pi \to$ not-proton and proton $\to$ not-π are very similar, since particle production rates are determined mainly by the Cherenkov angle resolution. The probability of these two efficiencies are also similar to that of the proton $\to$ proton efficiency except that the falling position of the proton $\to$ proton efficiency is at low momentum. The efficiencies of $\pi \to$ not-proton for the data and the MC K_s decay tracks, and that for the data and MC τ decay track samples are presented in Fig. 5.10 and 5.11, respectively. The $\pi \to$ not-proton efficiencies for true π's in the MC hadronic events, K_s decay track and τ decay track samples

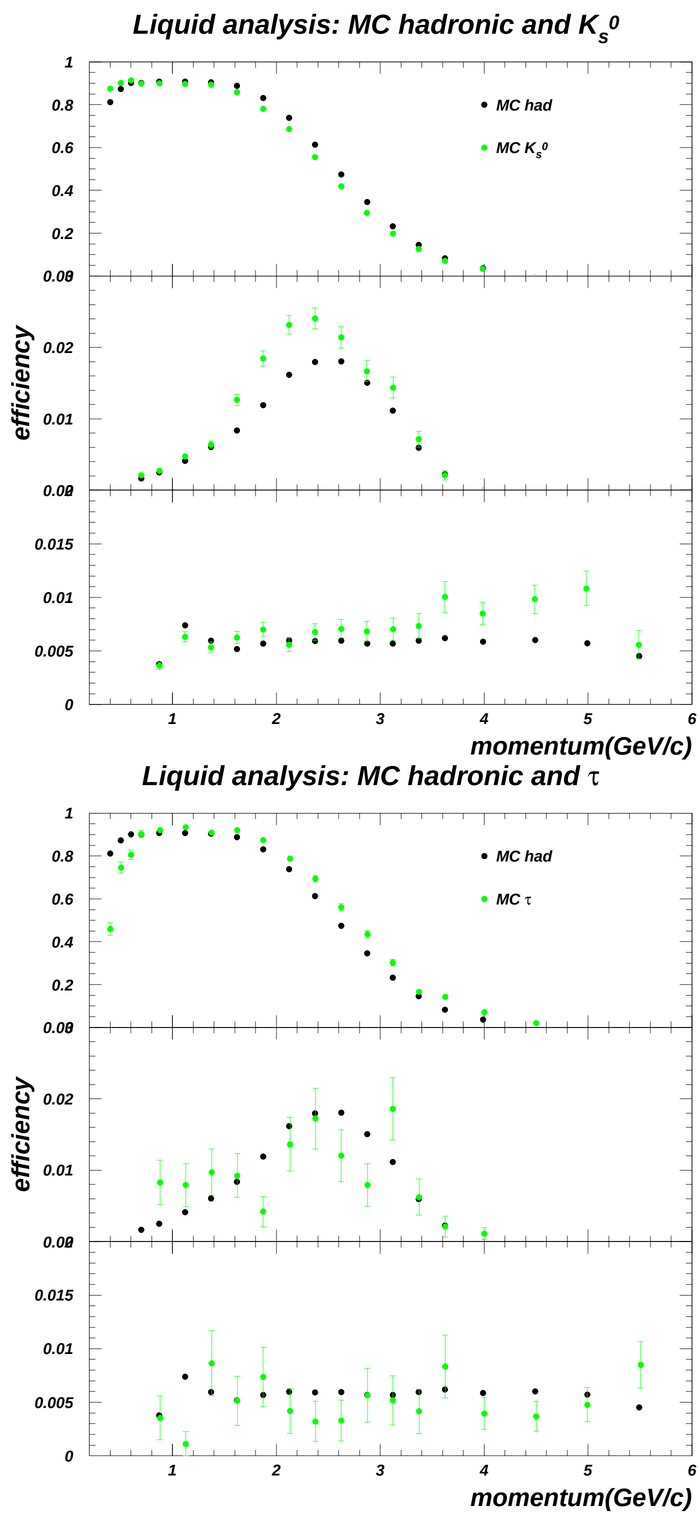

Figure 5.9: π efficiency columns for tracks from MC K_s decays and from MC hadronic events (upper plot), and π efficiency columns for tracks from MC τ decays and from MC hadronic events for the liquid analysis(lower plot).

Liquid not-proton Efficiency of K_s decays	
MC K_s	data K_s
$H(0.890, 2.438, 2.102)$	$H(0.864, 2.259, 2.189)$

Table 5.8: The parameterization functions of $\pi \to$ not-proton for K_s decay tracks for the liquid analysis.

in Fig. 5.12.

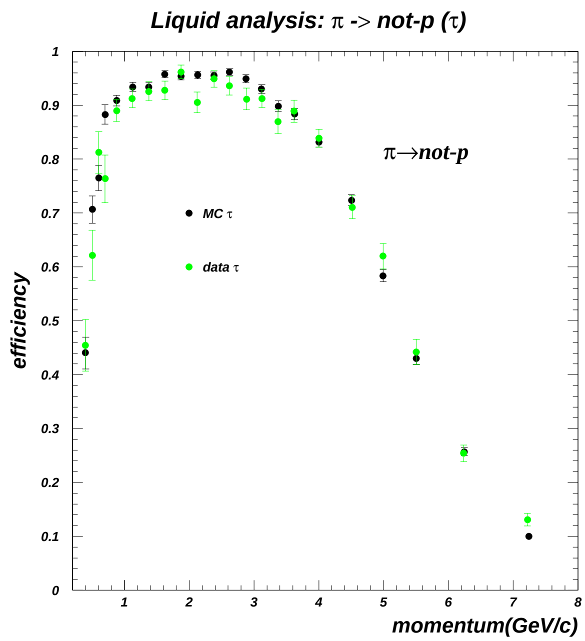

Figure 5.10: The $\pi \to$ not-proton efficiencies for true π's in the MC hadronic events.

The proton efficiency E_{pp} in the 3×3 efficiency matrix has losses due to not only $E_{p\pi}$ but also E_{pK}. The kaon radius is in between the radii of the proton and the π radii, so the proton efficiency in the 3×3 efficiency matrix is further degraded in the high momentum limit. The edge position of the proton efficiency in the 3×3 efficiency matrix begins to fall off at a lower momentum compared to the edge position of 2×2 proton $\to$ not-π efficiency. Since the MC models the shape of an efficiency very well as is shown for the π efficiency, we assume that we can use the correction terms of the detector angle resolution and the average number of detected photons from the π/proton separation to calibrate the kaon/proton separation at high momentum. The parameterization functions of $\pi \to$ not-proton for the data and the MC K_s decay tracks are summarized in Table 5.8

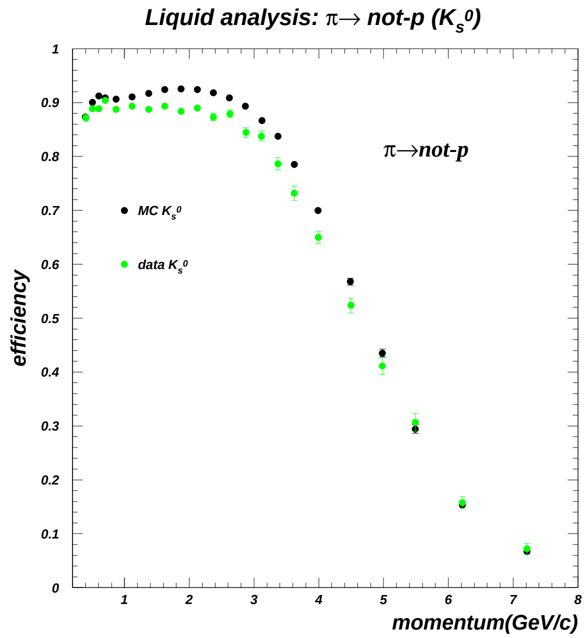

Figure 5.11: The $\pi \rightarrow$ not-proton efficiencies for true π's in the MC K_s decay track sample.

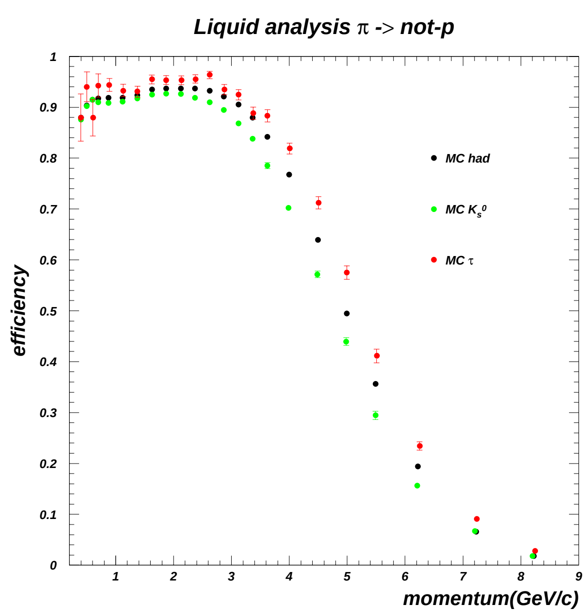

Figure 5.12: The $\pi \rightarrow$ not-proton efficiencies for true π's in the MC τ decay track sample.

For $\pi \rightarrow$ not-proton efficiency, like the π efficiency of 3×3 efficiency matrix, the MC overestimates the amplitude and the edge, and also shows a difference in the slope. An amplitude multiplication factor of 0.971±0.002, an edge shift by −0.179±0.083, and a $\sim 4\%$ slope change are applied to the MC hadronic parameterization functions of the proton efficiency of the 3×3 efficiency matrix.

Among the off-diagonal misidentification terms of the 3×3 efficiency matrix, corrections for $E_{\pi K}$ and $E_{\pi p}$ are also derived using the K_s decay track samples. The shapes of $E_{\pi K}$ and $E_{\pi p}$ of the MC hadronic events are employed to fit the shapes of $E_{\pi K}$ and $E_{\pi p}$ of the data and MC K_s decay tracks. The differences between the data and MC K_s decay tracks are applied to calibrate the MC hadronic $E_{\pi K}$ and $E_{\pi p}$. For $E_{\pi K}$, the MC underestimates the data below the liquid proton threshold ($p < 1.5$ GeV/c) but the MC overestimates the data over the proton threshold. Amplitude multiplication factors for below and above the proton threshold are 1.337±0.120 and 0.840±0.048 respectively. $E_{\pi p}$ of the data K_s decay tracks for $p < 3$ GeV/c is larger than $E_{\pi p}$ of the MC K_s decay tracks, while for $p \geq 3$ GeV/c the two K_s decay tracks samples have the same $E_{\pi p}$. An amplitude multiplication factor for $E_{\pi p}$ is 1.411±0.080. The protons were calibrated using tracks from $\Lambda \rightarrow p\pi^-$ for the previous study. The calibration results from the $\Lambda \rightarrow p\pi^-$ sample were consistent with the calibration result from the $\pi \rightarrow$ not-proton efficiency study.

Since $E_{\pi K}$ has a similar amplitude and shape of $E_{K\pi}$ and $E_{\pi p}$ has a similar feature of $E_{p\pi}$, we can apply the calibration terms of $E_{\pi K}$ to correct $E_{K\pi}$, and the calibration terms of $E_{\pi p}$ to correct $E_{p\pi}$. For the rest of the off-diagonal terms, we do not have any sample used to calibrate the MC hadronic parameterization functions, therefore we assign a systematic error of 25% of the misidentification terms.

5.3.3 Calibration of Gas Efficiencies

The gas calibration is performed with a process similar to the liquid calibration using selected τ events. Since different CRID track selection cuts are employed for $2.5 < p < 20$ GeV/c and $p \geq 20$ GeV/c we calibrate the π efficiency column separately for these momentum regions. Because most of the τ decay tracks are leptons and π's, the π efficiency of τ events is very similar to the π efficiency of hadronic events except for the momentum region below the kaon threshold for the loose cuts as shown in Fig. 5.13.

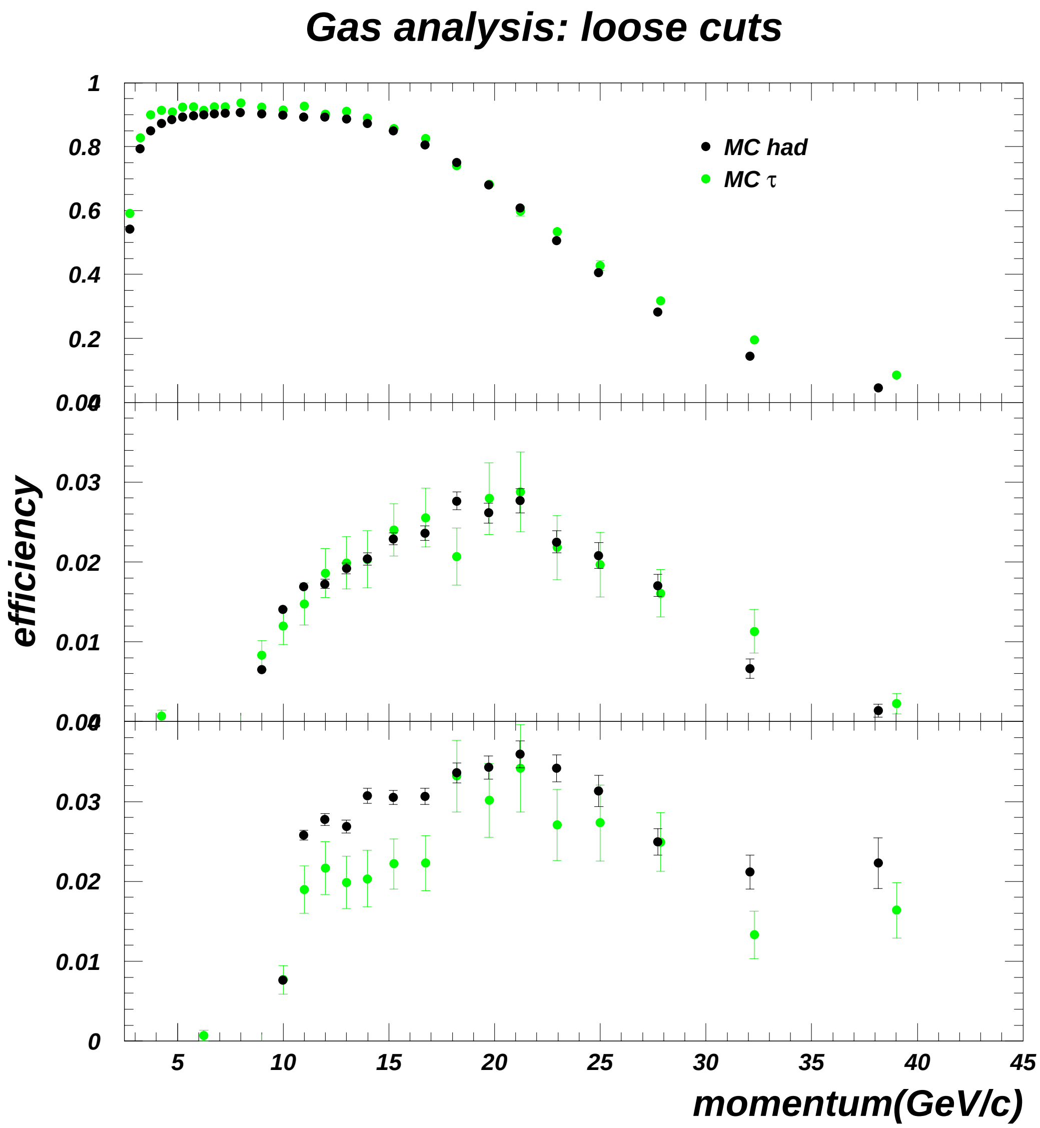

Figure 5.13: Efficiencies for tracks from MC τ decays and MC hadronic events to be identified as each hadron type by the gas analysis with the loose cuts.

The π efficiency with the loose cuts for the τ events is a little higher at low momentum. This difference is predicted due to low multiplicity in the τ events. Low multiplicity of the tracks in the τ events gives much less background coming from overlaps with the signals of other tracks, and from fewer unusable detector areas from saturated wires. But the difference is within 1%. But due to the kaon contents in tracks from τ decays, $E_{\pi K}$ for the MC τ decay track sample is greater than $E_{\pi K}$ for the tracks in the MC hadronic events. For the π efficiency with the tight gas CRID track cuts, differences are negligible in high momentum region. As Fig. 5.14 shows, the tight cuts including the tight ring isolation requirement are very efficient in suppressing such overlap problems in hadronic events.

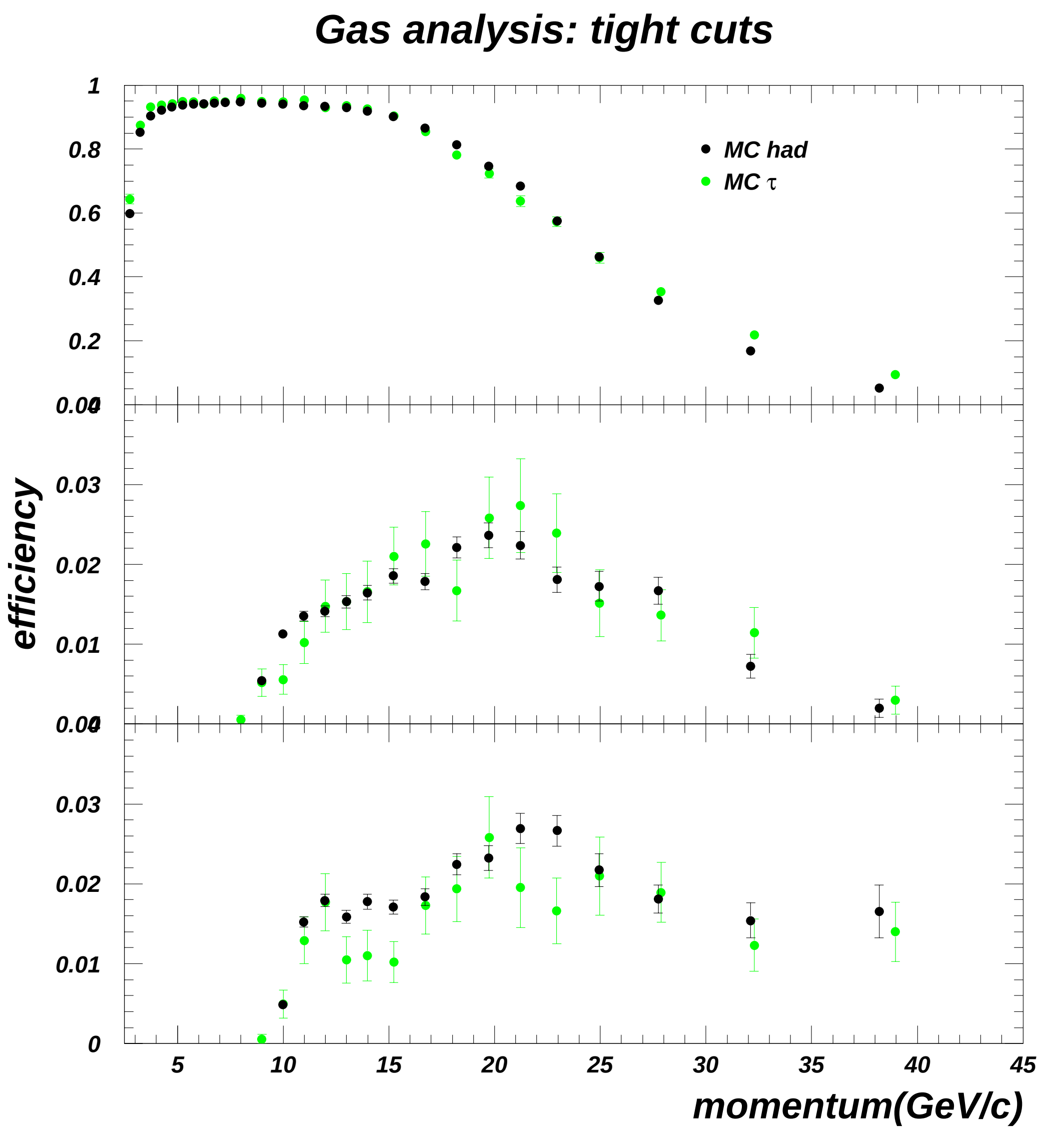

Figure 5.14: Efficiencies for tracks from MC τ decays and MC hadronic events to be identified as each hadron type by the gas analysis with the tight cuts.

The comparison of misidentifications of true π's in MC τ and MC hadronic events shows that $E_{\pi K}$ and $E_{\pi P}$ are consistent except in the momentum region $10 < p < 17$ for $E_{\pi P}$. Below the proton threshold, tracks are identified as protons due to the scarcity of signal hits near the expected pion or kaon radii. $E_{\pi P}$ is higher for π's in the MC hadronic events than that for π's in the MC τ events below the proton threshold as shown in Fig. 5.15. The absence of hits can happen when a π scatteres in the CRID or interactes with the CRID

Gas π Efficiency Parametrization of τ decays		
	MC τ	data τ
$2.5 < p < 11$ GeV/c	$R(0.926, 2.385, 2.414)$	$R(0.881, 2.234, 2.062)$
$11 \geq p < 20$ GeV/c	$H(0.908, 11.041, 11.895)$	$H(0.870, 11.304, 11.850)$
$p \leq 20$ GeV/c	$H(0.932, 11.593, 11.874)$	$H(0.893, 11.302, 12.230)$

Table 5.9: The parameterization functions of the π efficiency for τ decay tracks by the gas analysis.

material, or when a π does not point back to its own gas ring.

Fig. 5.16 and 5.17 show the comparison of the π efficiency column measured in the data τ event sample with the π efficiency column estimated in the MC τ events for the loose and tight CRID cuts.

The parameterization functions of the π efficiency are listed in Table 5.9. The data τ event statistics are sufficient to verify the shape of the momentum dependence of the π efficiency. There is generally a good agreement in the shape of the data and that of the MC.

Below the kaon threshold ($p <$ 10.5 GeV/c), the ratio of the amplitude of the data τ events to the amplitude of the MC τ events is 0.953$\pm$0.005, and in the kaon ring region ($10.5 < p < 20$ GeV/c) the ratio is 0.963$\pm$0.007. In the proton ring region ($p \geq 20$ GeV/c, the amplitude ratio is 0.971$\pm$0.007. The edge positions and slopes of the π efficiencies for the data and MC τ decay track samples are consistent within the statistical uncertainty. In order to get the measured hadronic π efficiency these amplitude ratios are applied to the MC hadronic parameterization functions.

We take the gas kaon efficiency to be equal to the π efficiency parameterization function multiplied by the rising position function from the MC ratio $E_{KK}/E_{\pi\pi}$. The rising position near the kaon threshold corresponds to the rising position of the π efficiency at the π threshold in low momentum regions. At high momentum, the kaon efficiency is not similar to the π efficiency any more because of the appearance of the proton radius. The proton radius approaches the kaon radius as momentum increases, so we model this decrease in the kaon efficiency by multiplying the ratio of the kaon efficiency and the π efficiency estimated from the MC τ decay track sample. For the gas kaon efficiency, like in the liquid analysis,

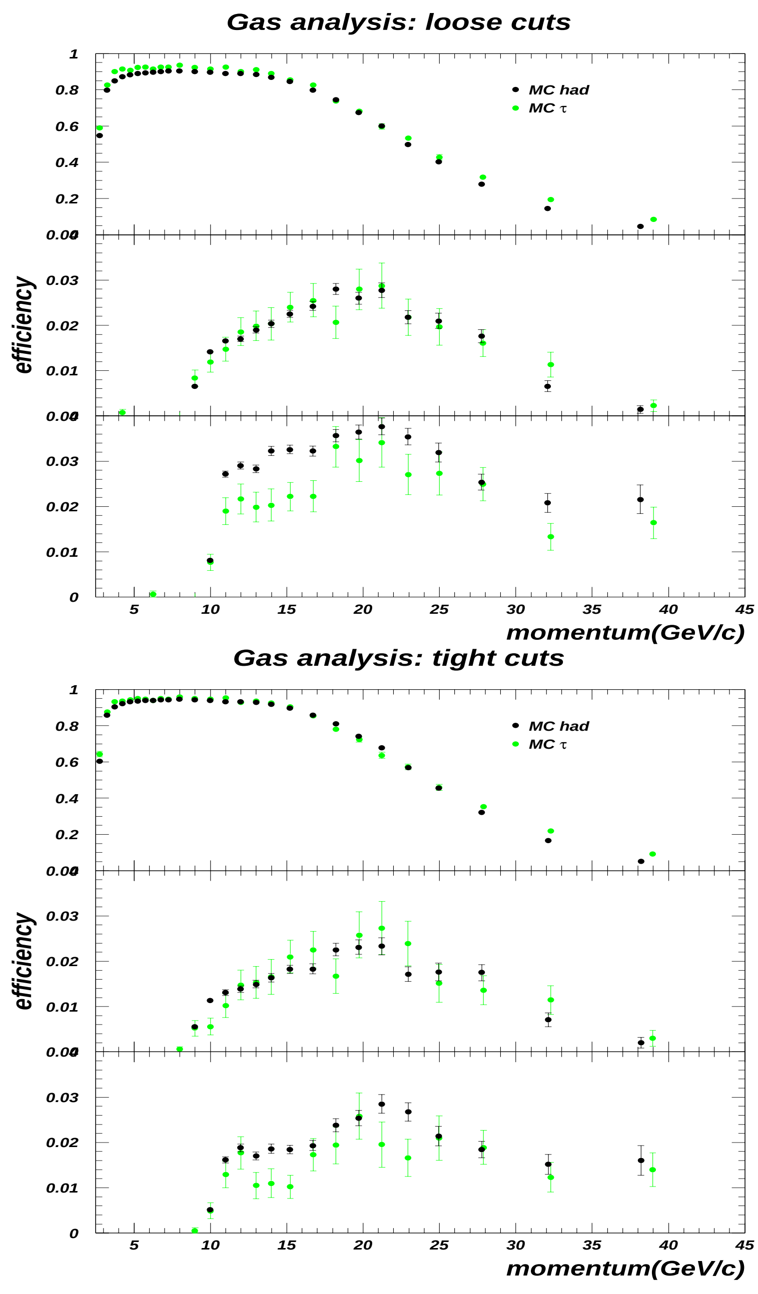

Figure 5.15: Efficiencies for tracks from the MC τ decays and from the MC hadronic events to be identified as each hadron type by the gas analysis for the loose (left) and tight (right) CRID cuts.

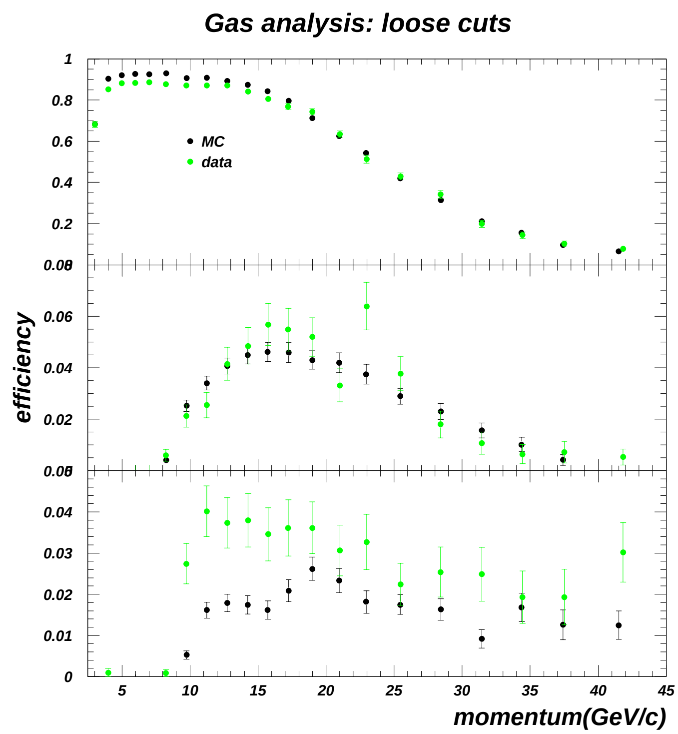

Figure 5.16: Efficiencies for tracks from the data and MC τ decays to be identified as each hadron type by the gas analysis for the loose CRID cuts.

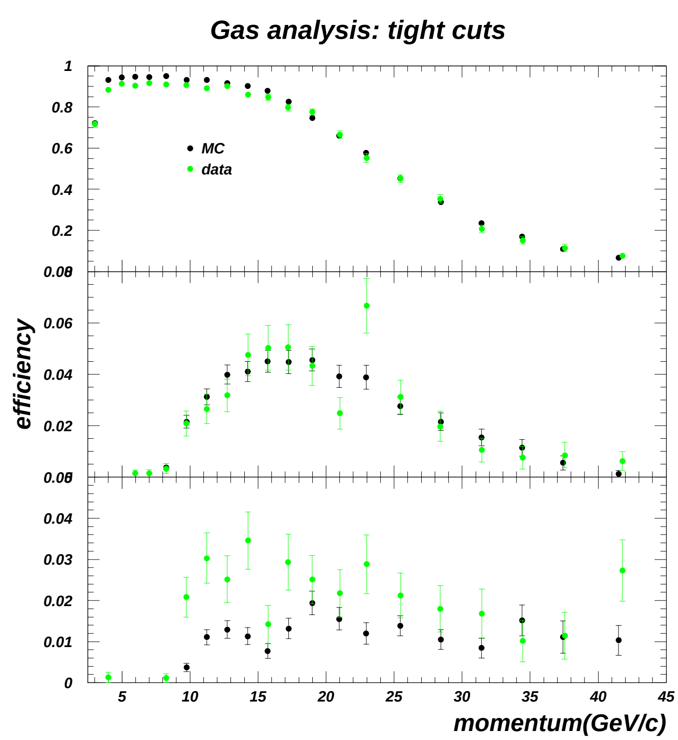

Figure 5.17: Efficiencies for tracks from the data and MC τ decays to be identified as each hadron type by the gas analysis for the tight CRID cuts.

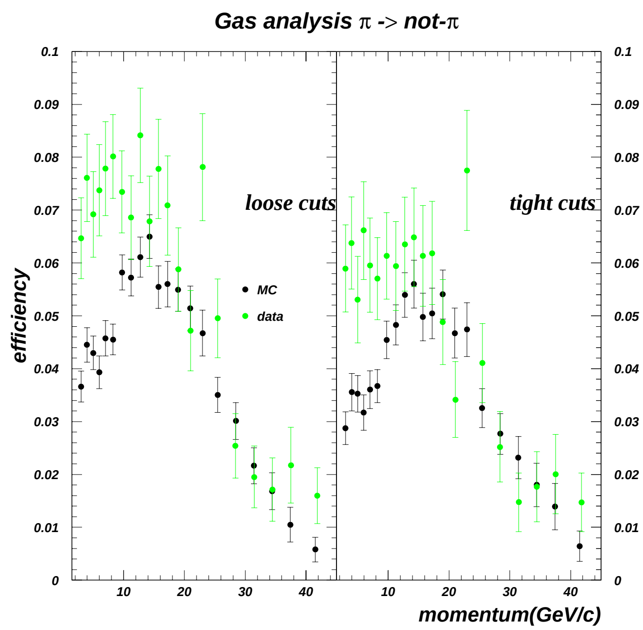

Figure 5.18: Efficiencies for tracks from K_s decays to be identified as not-protons by the gas analysis for the two CRID cuts.

we are confident that we can correct the gas π efficiency for the MC hadronic events by applying the edge shift, amplitude normalization and error driven from the data and the MC τ decay track samples.

The proton efficiency is expected to be similar to the π efficiency above the proton threshold ($p > 18$ GeV/c) except for a shift of the peak position and the wider width of the proton efficiency. These differences in the proton and the π efficiencies are predicted from the Cherenkov angle distribution. Therefore, we are allowed to correct the proton efficiency with the amplitude multiplication factor of the π efficiency for the τ decay tracks. For the further study of the edge shift correction, the MC and data τ decay tracks identified as not-protons ($\mathcal{L}_\pi - \mathcal{L}_p > 3$) are compared in Fig. 5.18.

From this comparison we find that the not-proton efficiency of the MC and the data τ decay tracks are consistent for the edge position within limited statistics . Below the gas kaon threshold ($p < 10$ GeV/c), kaons and protons can not be separated. We parameterize this momentum region with the 2×2 hadronic efficiency matrix, $\pi \to \pi$ and $\pi \to$ not-π if $\mathcal{L}_K - \mathcal{L}_\pi > 3$. The probability that a π is identified as a not-π is supposed to be the same as a not-π is identified as a π. Also, the π efficiency is expected to be the same as the not-π efficiency. Hence we can calibrate all elements in the low momentum 2×2 efficiency matrix with the correction terms taken from a comparison of the π and not-π efficiencies for the data with the MC τ decay track samples. This calibration gives the π efficiency under the gas kaon threshold. For the diagonal elements of the 2×2 efficiency matrix, we can simply apply the amplitude multiplication factor of the π efficiency for the 3×3 efficiency matrix. The misidentification elements of the 2×2 efficiency matrix for the MC τ decay tracks underestimate the data τ decay tracks. The differences between the data and the MC τ decay tracks vary in each threshold region. Below the π threshold ($p <$ 3 GeV/c), an amplitude factor of 2.390 is multiplied to the MC hadronic misidentification elements and below the kaon threshold a factor of 1.461 is multiplied, and 1.728 and 1.174 are multiplied to the MC hadronic misidentification parameterization functions below and above the proton threshold respectively. There are large enough statistics for the data and MC τ events to constrain the shapes of $E^{\tau}_{\pi K}$ and $E^{\tau}_{\pi p}$. The τ decay track samples have almost the same parameterization of the hadronic misidentifications except for higher $E^{\tau}_{\pi K}$ from about 1.7% true kaons in τ events.

For $E^{\tau}_{\pi K}$, there is a good agreement between the data and the MC τ decay tracks above the proton threshold ($p >$ 17 GeV/c) for the loose and the tight CRID track cuts. The MC overestimates the data $E^{\tau}_{\pi K}$ in $p <$ 13 GeV/c, and the MC underestimates the data in $< 13p <$ 17 GeV/c. This is not quite true for $E^{\tau}_{\pi p}$, the MC underestimates the data for the whole momentum regime.

The significant difference between $E_{\pi K}$ and $E_{\pi p}$ of the data and those of the MC can be explained by less material in the detector simulation, residual mis-alignments in the data, and a small deficiency in the background simulation.

To correct $E_{\pi K}$, amplitude multiplication factors of 0.837±0.093 and 1.126±0.689 are applied to the MC hadronic amplitude parameter in $p <$ 13 GeV/c and $13 \geq p <$ 17 Gev/c respectively. Amplitude multiplication factors of 2.292±0.169 and 1.560±0.193 are applied to the amplitude parameter of the MC hadronic $E_{\pi p}$ below and above the proton threshold.

$E_{K\pi}$ and $E_{\pi K}$ have similar structures in $p >$ 17 Gev/c. $E_{p\pi}$ and E_{pK} also have similar structures in $p >$ 25 GeV/c. So the same amplitude multiplication factors from the measured $E^{\tau}_{\pi K}$ and $E^{\tau}_{\pi p}$ are applied to the MC hadronic $E_{K\pi}$ and E_{pK}. Other off-diagonal

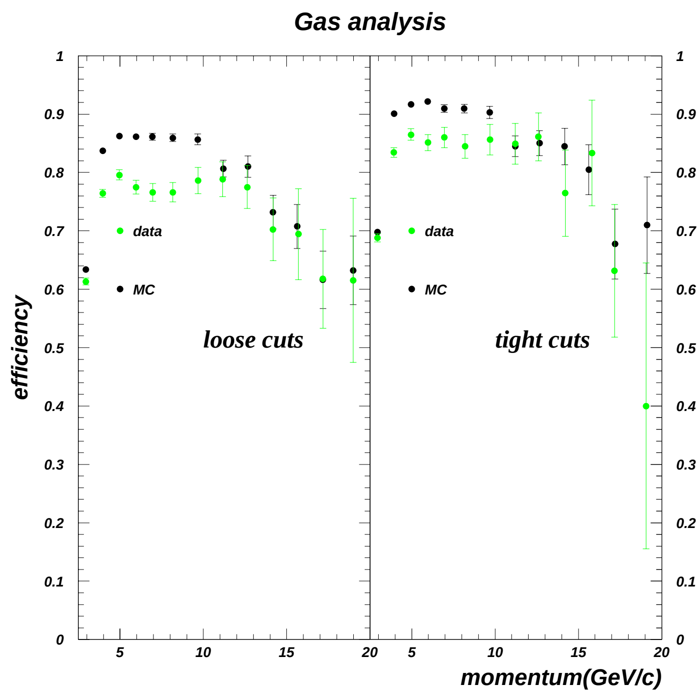

Figure 5.19: The π efficiencies of the data and the MC K_s decay tracks.

elements are assigned the larger of 25% relative or 0.005 as a systematic error at each point to the MC hadronic parameterization functions.

Tracks from $K_s \to \pi^+\pi^-$ are used as a cross-check of the π efficiency calibration at low momentum. Fig. 5.19 shows the π efficiency of the data and the MC K_s decay tracks for the loose and the tight CRID track cuts.

The calibration result for the K_s decay track samples is consistent with the calibration result for the τ event samples. The comparison of the π efficiencies for the MC K_s decay tracks and tracks in the MC hadronic events are shown in Fig. 5.20 for the loose and the tight CRID track cuts.

As explained in the liquid analysis, generally the K_s decay tracks have lower π efficiency compared to the π efficiency for the hadronic events. However, the difference is negligible for the tight cuts.

Λ^0 decay sample was used for the proton efficiency column for the previous study. The amplitude correction for the proton efficiency from the Λ^0 decay sample was consistent with the amplitude correction for the π efficiency correction from the τ and K_s decay track samples.

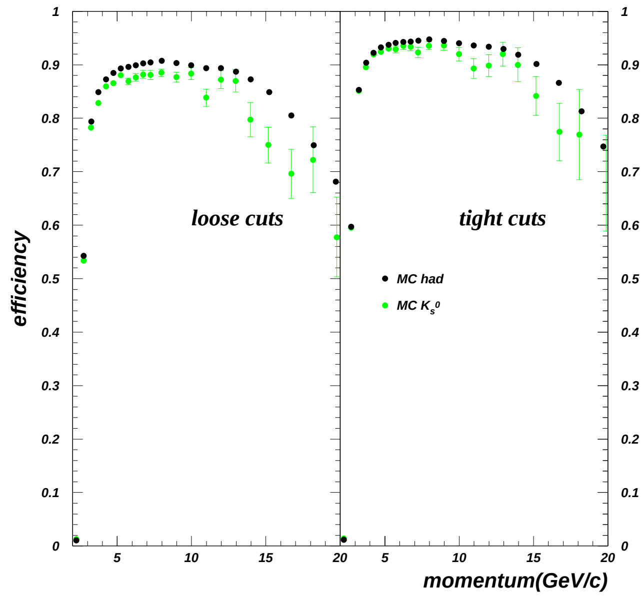

Figure 5.20: Efficiencies for tracks from the MC $K_s$decays and from the MC hadronic events to be identified as each hadron type by the gas analysis for the loose (left) and tight (right) CRID cuts.

5.3.4 Calibration of Combined Efficiencies

For the combined analysis, the momentum range from 2.5 GeV/c to $\sim$ 9 GeV/c is considered. As mentioned in Sect. 5.1, the π/K separation for the combined analysis is essentially performed in the gas system, and the K/p separation is achieved mainly in the liquid system. Therefore, we expect corresponding shifts and amplitude multiplication factors of the gas and the liquid calibrations to be applied to the efficiencies for the combined analysis. We also employ two different CRID track selection cuts for the combined analysis in order to study the optimization of the statistics and systematic errors. We can use both K_s decay tracks and τ decay tracks as calibration samples for the combined analysis. We require the liquid CRID track cuts but do not require the gas 'BADID' (loose cuts) as CRID track cuts. As a second set of CRID track cuts, addition to the loose cuts, the tight gas ring isolation is required (tight cuts).

The data and the MC π efficiency columns are compared in Fig. 5.21 and 5.22 for both K_s and τ decay track samples for the two combined CRID track cuts.

The π efficiencies of the data and the MC are consistent for both calibration samples in $2.5 < p < 3$ GeV/c. The parameterization functions of the π efficiencies of the two

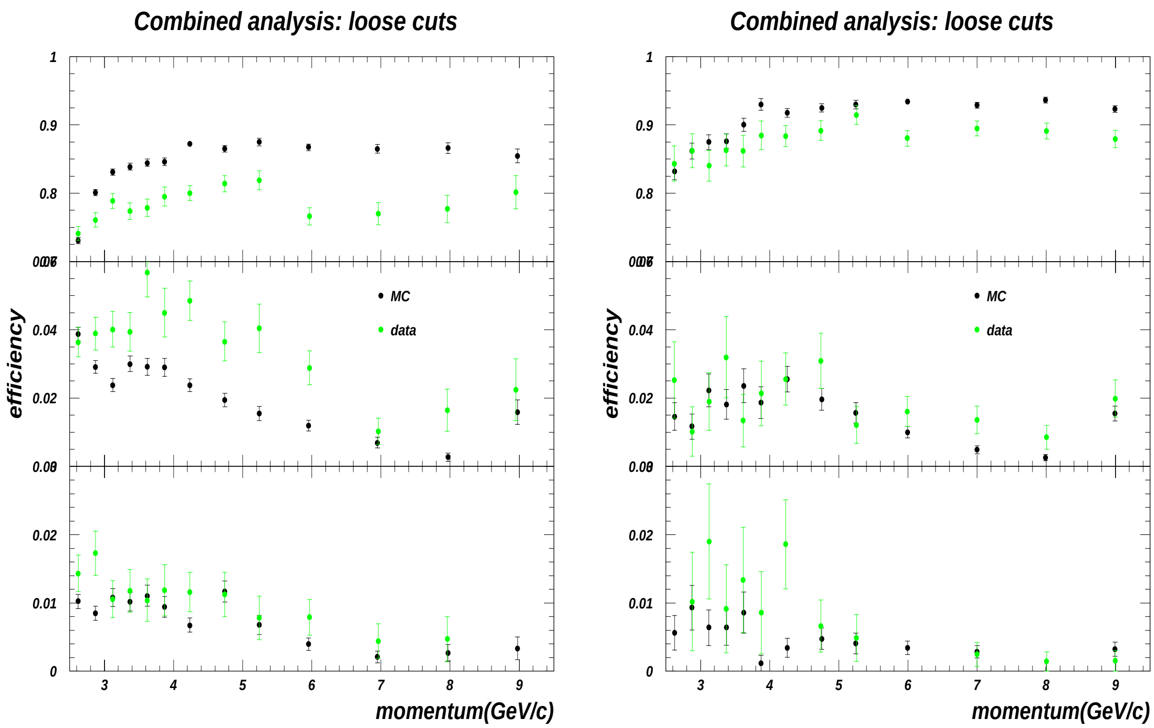

Figure 5.21: Efficiencies for tracks from the data and MC K_s (left) and τ (right) decays to be identified as each hadron type by the combined analysis for the loose CRID cuts.

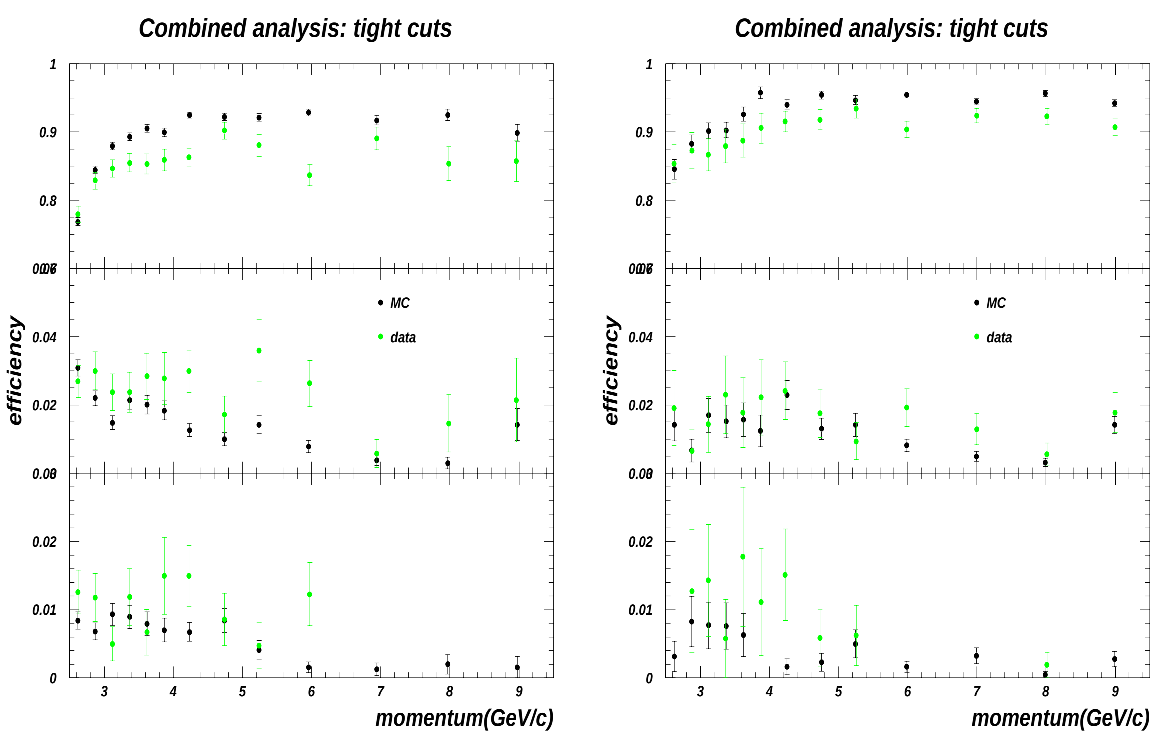

Figure 5.22: Efficiencies for tracks from the data and MC K_s (left) and τ (right) decays to be identified as each hadron type by the combined analysis for the tight CRID cuts.

Combined π Efficiencies of test samples		
	MC	data
K_s	$R(0.810, 2.142, 4.522)$	$R(0.738, 1.953, 6.125)$
τ	$R(0.907, 0.616, 1.193)$	$R(0.860, 0.115, 1.227)$

Table 5.10: Combined π efficiencies of tracks from K_s and τ decays with the loose cuts

calibration samples are listed in Table 5.3.4 and Table 5.3.4 for the loose and tight CRID track cuts respectively. Instead of two $R(a, b, c; p)$ functions used for the π efficiency for the MC hadronic events, only one $R(a, b, c; p)$ function is applied for the calibration samples.

Combined π Efficiencies of test samples		
	MC	data
K_s	$R(0.921, 1.886, 2.470)$	$R(0.885, 1.255, 1.600)$
τ	$R(0.951, 1.366, 1.722)$	$R(0.922, 0.356, 1.106)$

Table 5.11: Combined π efficiencies of tracks from K_s and τ decays with the tight cuts

For the combined analysis, we are using the correction terms for K_s decay tracks, since the tracks from K_s decays have the properties similar to the properties of tracks in hadronic events. However, K_s decay track samples show a statistical fluctuation in high momentum region, therefore we calibrate the high momentum region with the correction terms for τ event samples. Calibration terms for the π efficiency are consistent with the calibration terms for the π efficiency for the gas analysis as we expect. The π efficiency for K_s decay tracks has bigger correction terms than the π efficiency for τ decay tracks. The correction terms from the two CRID track cuts are consistent for the whole momentum region, and the amplitude multiplication factor is 0.969$\pm$0.007.

For $E_{\pi K}$ and $E_{\pi p}$, neither sample has sufficient statistics in the data to show the shape of the functional parameterizations. We take the previously derived parameterization functions from MC hadronic events and try to fit $E_{\pi K}$ and $E_{\pi p}$ for the K_s and τ decay track samples. There is a difference between K_s and τ decay tracks in $E_{\pi K}$. The misidentification rate in the K_s samples displays a discrepancy between the data and the MC, while τ data and MC misidentification rates are consistent. We calibrate the MC hadronic parameterization functions with correction terms derived from the K_s track samples. The amplitude multiplication factor for the calibration is 1.735 and 1.529 for the loose and tight CRID track cuts, respectively. The MC underestimate the data for $E_{\pi p}$ by factors of 1.339 and 1.244 for the loose and tight cuts separatively.

The combined proton efficiency is calibrated using the probabilities that τ and K_s decay tracks are identified as not-protons in the liquid analysis. Since proton identification is done in the liquid system, this is a well defined way to calibrate. The combined kaon efficiency is taken to be the proton efficiency multiplied by a extra inefficiency factor estimated from the MC hadronic sample. The rest of the off-diagonal misidentification terms remain uncalibrated for the MC parameterization and so for the systematic error analysis, these terms are varied by the larger of $\pm 25\%$ (relative) or ± 0.005.

For the previous study [58],[77], the proton efficiency column $E_{\mathrm{p}j}$ was also calibrated using Λ^0 decays. There was no difference in the proton efficiencies in the data and the MC Λ^0 decay track samples. For this reason, Λ^0 decays are not included in the calibration for the current study.

Chapter 6

Hadron Production Analysis

6.1 Measurement of the Hadron Fractions in Flavor Inclusive Events.

The hadronic fraction analysis is straightforward. First, we count the measured total number n_i of tracks identified as π's, K's and p's in each momentum bin. The true fractions f_j are extracted using equation 6.1.

$$n_i = n \sum_j E_{ji} f_j \tag{6.1}$$

where n is the total number of tracks passing the QCD and CRID selection cuts described in Chapter 4, and E_{ji} is the particle identification efficiency matrix. equation 6.1 is used to solve for f_j in each momentum bin. The three true fractions f_j are not constrained to sum to unity in our procedure. Instead we compare the sum to unity as a consistency check.

The fractions f_j are corrected for the contribution of leptons. The leptonic fraction is estimated from MC to be $< 7\%$ of the inclusive track sample for $p > 1$ GeV/c as shown in Fig. 6.1. The leptons come predominantly from D and B hadron decays in $c\bar{c}$ and $b\bar{b}$ events. For low momenta $p < 1$ GeV/c, electron production is dominated by γ conversions which produce up to $\sim$9% of the total track sample.

The fractions are also corrected for the effects of beam related backgrounds and interactions in the detector material. Particles coming from detector interactions are predominantly low momentum protons as shown in Fig. 6.2.

In order to remove the main background effect, only negative charged tracks are used for $p < 2.5$ GeV/c. This remaining non-proton background correction is estimated to be $< 1\%$ for f_π, $\sim 1.7\%$ for f_K and $\sim 1.7\%$ for f_{p^-} for track momenta below 2.5 GeV/c as shown in Fig. 6.3.

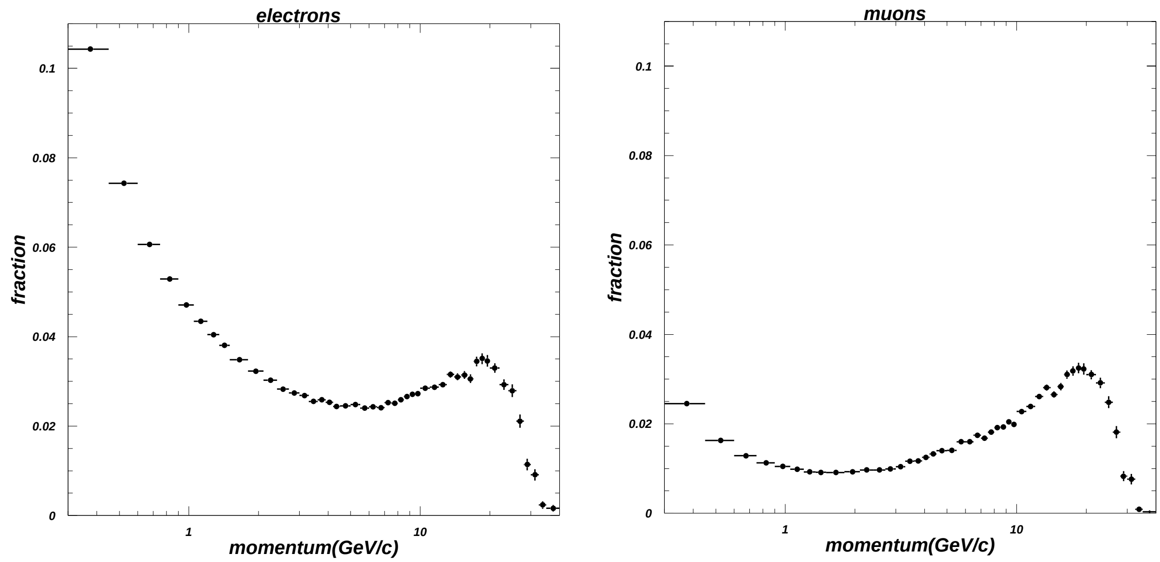

Figure 6.1: The fractions of electrons (left) and μ's (right) in the selected track sample. These leptonic fractions are estimated from the MC.

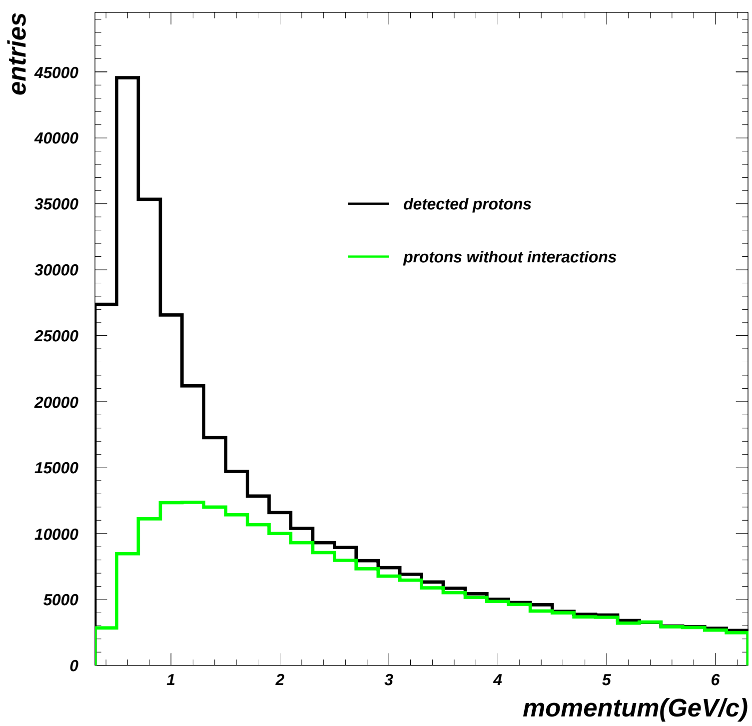

Figure 6.2: Protons coming from detector interactions estimated by the simulation for $p < 5$ GeV/c.

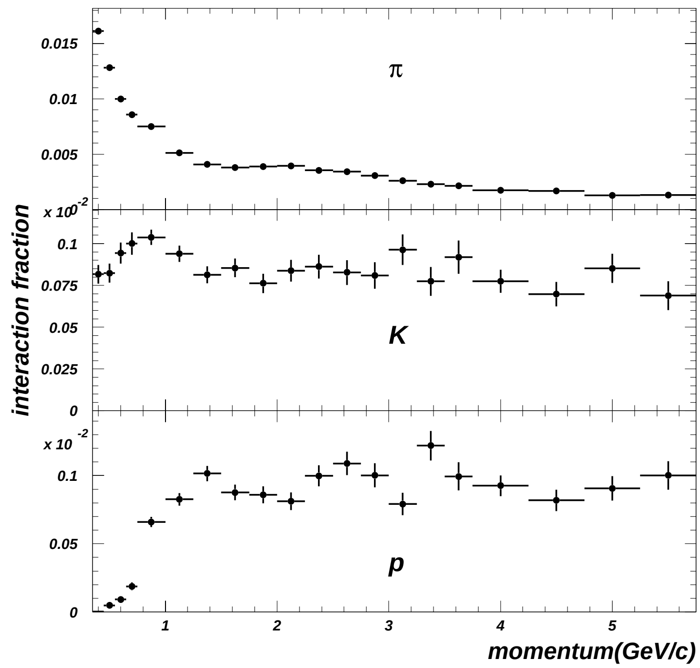

Figure 6.3: The fractions of $\pi^{\pm}$, $K^{\pm}$ and $\bar{\mathrm{p}}$ coming from detector interactions estimated by the simulation.

These background corrections are very small compared to the statistical or systematic errors. The correction for background becomes negligible ($< 0.2\%$) for all three hadron fractions above 2.5 GeV/c, so no correction is used for this momentum region.

For this analysis, we only count the number of hadrons from the primary interaction or from decays of hadrons with lifetime less than $3{\times}10^{-10}$s. Therefore there must be a correction for stable hadrons whose lifetime is longer than $3{\times}10^{-10}$ s (for example, K^0_L, π and K flight decays) but decay in the detector, and for hadrons whose lifetime is shorter (Λ^0, K^0_s) but still decay outside of the detector. This correction is performed using an estimation from the MC simulation. The effect of π and K (stable hadrons) decays in flight is negligible and so only K^0_L decays are included in the correction for long lived hadrons. The correction for contributions of short lifetime hadron decays is less than 1% except that late Λ^0 decays account for as much as 25% of high-momentum protons.

The corrected charged hadron fractions for hadronic Z^0 decays as functions of momentum are shown in Fig. 6.4 for all three analyses (liquid, gas, and combined). The charged hadron fractions are summarized in Tables B.1–B.2 in Appendix B.

The π fraction f_π is measured from $p = 0.3$ to $p = 40$ GeV/c. There is a gap in

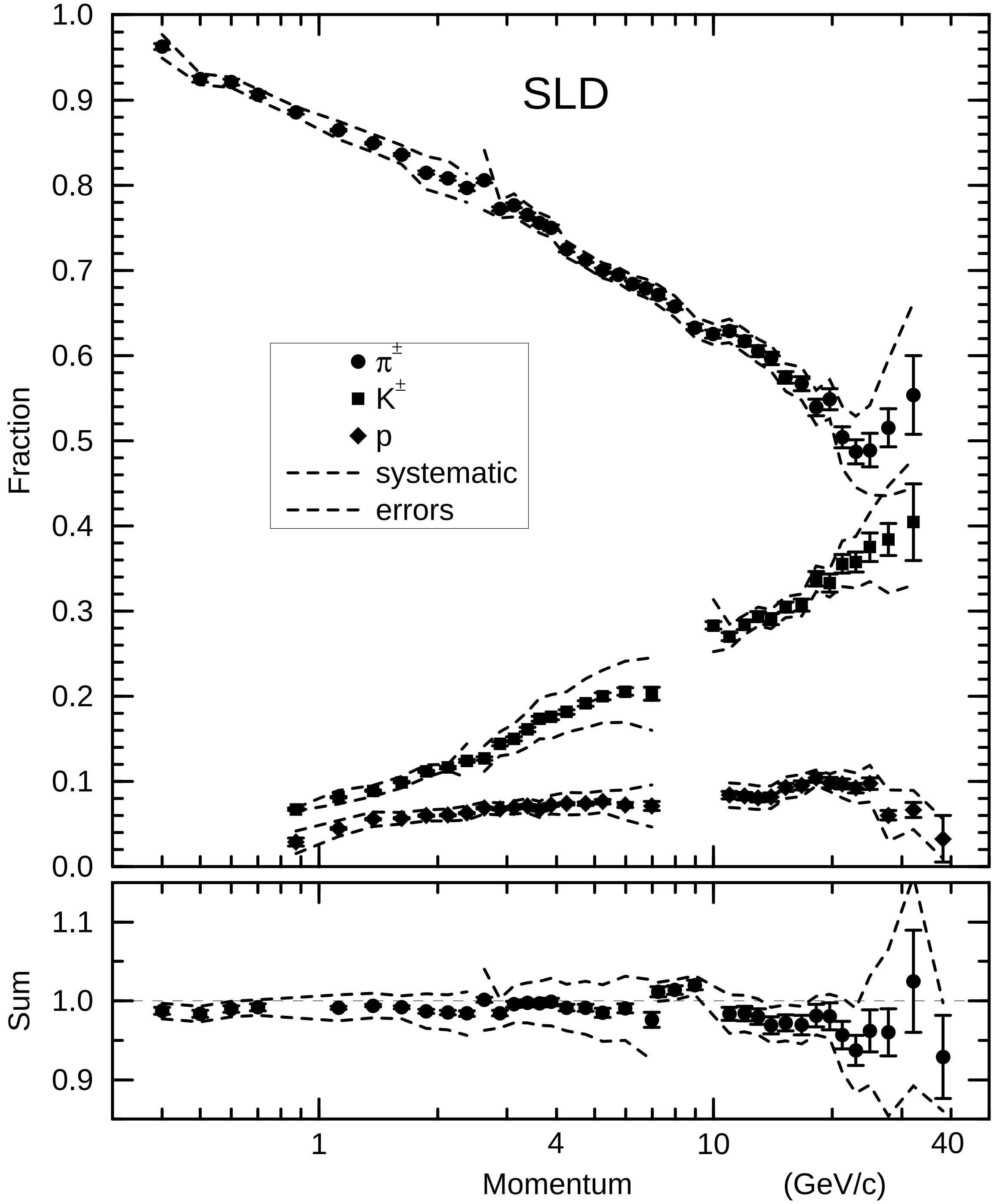

Figure 6.4: Measured fractions of $\pi^{\pm}$ (circles), $K^{\pm}$ (squares) and p/$\bar{\mathrm{p}}$ (diamonds) in hadronic Z^0 decays. The error bars are statistical errors and the dotted lines are systematic errors.

kaon/proton separation for $7 < p < 10$ GeV/c, because neither the liquid radiators nor the gas radiators cover this momentum region. The error bars represent the statistical errors and the dashed bands represent the systematic errors. For each momentum bin, the analysis with the smallest overall error is used, namely the liquid analysis for $p < 2.5$ GeV/c, the combined analysis for $2.5 < p < 7.5$ GeV/c, and the gas analysis for $p > 7.5$ GeV/c. The primary systematic uncertainties come from the calibration of the individual particle identification efficiency matrix element. The systematic uncertainties are dominated by the diagonal elements of the matrix, and bin errors are strongly positively correlated across the momentum range of a given analysis. For the f_π measurement, the systematic errors are dominant in the momentum regions where the π efficiency element for each analysis are falling off quickly, $p > 2$ GeV/c for the liquid and $p > 25$ GeV/c for gas analyses. In other momentum regions the errors have roughly equal statistical and systematic components. For the f_K and f_p measurements, the systematic errors are generally much larger than the statistical errors over the entire momentum region. A general feature of the measured true fractions is that the π fraction is dominant for low momentum regions. It begins higher than 0.9 at low momentum, and steadily decreases as momentum increases, eventually reaching $\sim$0.5 at $p > 20$ GeV/c. The K fraction begins at $\sim$0.06 and constantly increases with increasing momentum and becoming 0.4 at high momentum. Finally, the p fraction increases with increasing momentum up to 0.1 at $p \sim 20$ Gev/c where it then starts to decrease slowly. For low momenta ($p < 1$ GeV/c), the CRID does not have a good enough resolution to distinguish K's and p's. The π fraction is predominant in that momentum region. In high momentum regimes, the mass difference between s and ud quarks becomes negligible compared to the momenta of the quarks, so strangeness suppression is reduced. As expected, for $p \sim 45$ GeV/c, the π and K fractions converge. There is a small bump for the K fraction for $3 < p < 5$ GeV/c.

The sum of all three hadron fractions is also presented in the bottom of Fig. 6.4. The hadron fractions should sum to unity if the particle identification efficiencies are well modelled. Our result for the sum has small fluctuations around unity, indicating that the particle identification efficiency matrix for the data may not be perfectly modelled. However, the sum is found to be consistent with unity within the errors.

The results of the hadron fractions are consistent with the previous SLD results [69],[58]. The new results are also compared with the LEP results (DELPHI,ALEPH,OPAL), and the comparison is shown in Fig. 6.5. The results from other Cherenkov ring imaging detector (DELPHI) are presented as open points and the results from the experiments use dE/dx for particle identification (ALEPH,OPAL) are presented as bands. Our hadron fractions in flavor inclusive events are in good agreement with the measurments from different experiments within the correlated errors [79],[80],[81]. The hadron fractions from ALEPH and OPAL cover very low momentum regions for the $K^{\pm}$, p/$\bar{\mathrm{p}}$ where our experiment can not distinguish K's and p's. Also the hadron fractions from DELPHI, ALEPH and OPAL cover our gap for kaon/proton separation ($7 < p < 10$ GeV/c). When combined, these measurements have good overall momentum coverage and good precision.

We compare the hadron fractions in flavor inclusive events with the predictions of the SLD MC simulation and of three different fragmentation models: JETSET 7.4, UCLA 7.41 and HERWIG 5.8d with default parameters in Fig. 6.6.

The default parameters are determined from tuning to reproduce the charged hadron momentum spectrum and the inclusive event shape as well as the distribution of the number of charged hadrons per event. The SLD MC simulation includes fragmentation parameters tuned to reproduce the momentum distributions of particles and early LEP measurements of hadron productions [82]. The general features of the hadron fractions as functions of momentum are reproduced qualitatively by the SLD MC and by all three fragmentation models, but quantitatively no model describes the data well. The SLD MC simulation is tuned to the p production rate measured in the previous analysis. The SLD MC simulation describes the measured true p fractions very well except for $10 < p < 15$ GeV/c. The p fraction from the SLD MC is a little higher than the p fraction measured in the data for that momentum region. The SLD MC overestimates the π fraction for $p > 4$ GeV/c and underestimates the K fraction for $p > 10$ GeV/c. The predictions of individual models are very different for the π fraction at very high momentum. The predictions of the JETSET and UCLA models overestimate the π fraction for $2 < p < 10$ GeV/c while the HERWIG model describes the data very well in this momentum region. The data do not have sufficient statistics to select the correct model prediction for the π fraction at high momentum.

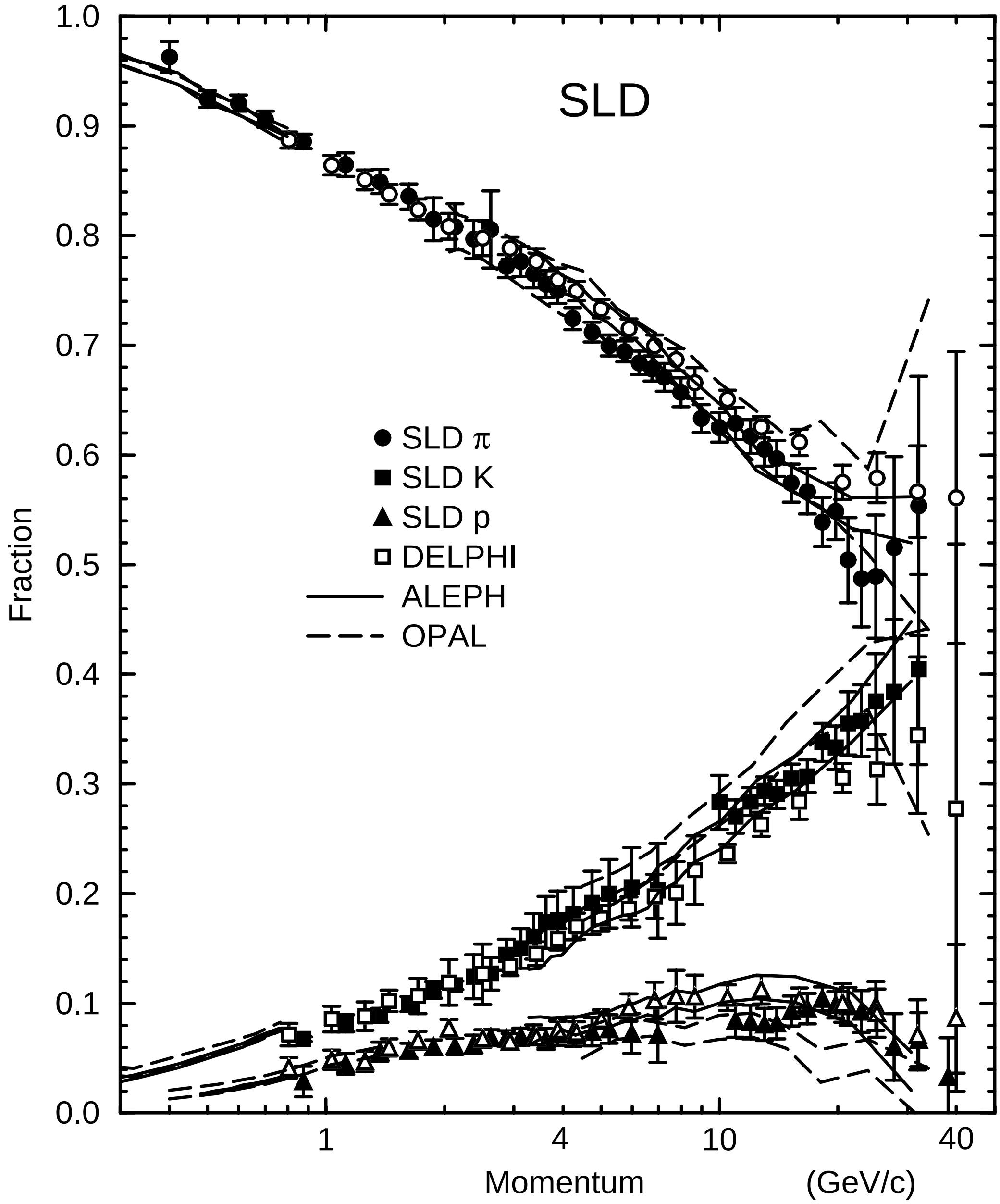

Figure 6.5: Comparison of our measured hadron fractions and measurements from LEP experiments (DELPHI, ALEPH and OPAL)

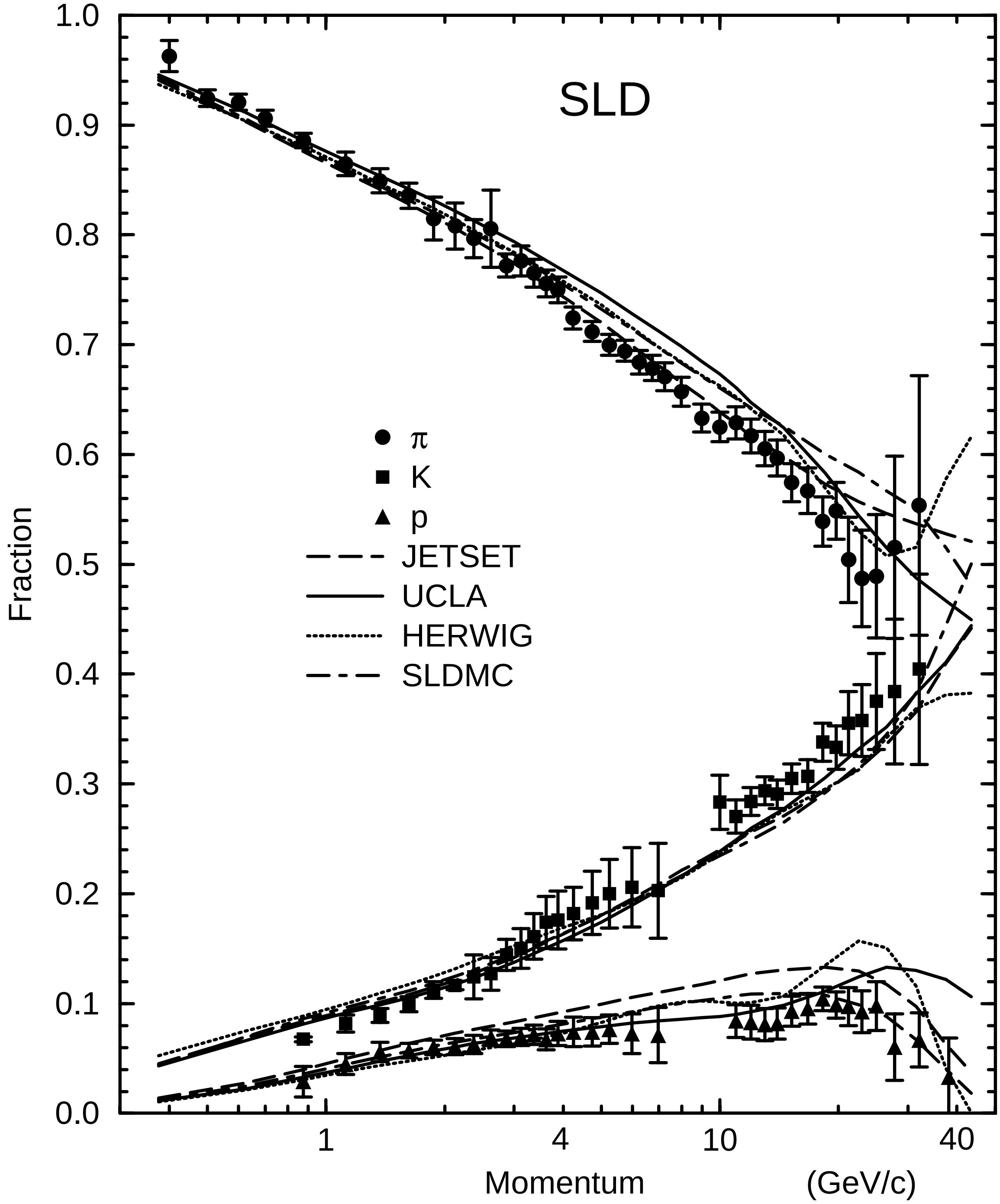

Figure 6.6: Comparion of the measured charged hadron fractions in flavor inclusive events with the predictions of the three models as well as the SLD MC simulation.

All three models overestimate the K fraction in low momentum regions and underestimate it for $p > 3$ GeV/c.

The predictions of individual models are very different for the p fraction for $p > 7$ GeV/c. The JETSET model overestimates the p fraction throughout the entire momentum region. The HERWIG model describes the p fraction very well below $p = 7$ GeV/c. The UCLA model predicts the p fraction well below $p = 20$ GeV/c. However, the HERWIG and UCLA models overestimate the p fraction at high momentum.

6.2 Flavor dependent analysis

The fragmentation models are based on massless quarks, and therefore excluding heavy quark events in our measurements allow more accurate tests of the phenomenological models. The first procedure in the flavor dependent analysis is tagging event flavors. The flavor tagging method and the efficiency and purity for each flavor tag is discussed in Chapter 4.2.

The hadron fraction analysis is repeated on the light$-$, $c-$, and $b-$tagged event samples separately to yield the true hadron fractions $f_h^{i_{tag}}$, where i_{tag} ={light, c and b}, and h ={π, K and p}. Since leptonic fractions in light (uds) and heavy (c,b) flavor events are different, we do not perform the inclusive lepton correction (described in section 6.1) for the flavor dependent analysis but correct the hadron fractions appropriately for each flavor later. After other corrections, we convert the hadron fractions to the hadron production rates. This procedure is for unfolding the flavor tagged samples independent of the simulated multiplicities and the different hadron fractions in each flavor events. In the unfolding procedure, the data charged multiplicities and the data inclusive momentum spectrum for different flavor events are used, instead of the MC prediction. In order to calculate the hadron production rates, we multiply the hadron fractions $f_h^{i_{tag}}$ of the flavor tagged samples by $n^{i_{tag}}$, the average number of tracks that pass the QCD track selection cuts in each momentum bin per i-tagged event. In principle, we also need to apply an overall efficiency factor for the QCD track selection cuts (Sect. 4.1.1) to the hadron production rates in order to obtain the correct production rates per tagged event [83], however we assume that the track selection cuts have no hadron species dependence and no event flavor dependence. Therefore, we are allowed to ignore this overall efficiency factor for this analysis. The converted production rates, $R^{i_{tag}}$ of different hadron species are written as:

$$R_h^{i_{tag}} = n^{i_{tag}} \cdot f_h^{i_{tag}} \tag{6.2}$$

To extract the true hadron production rates, $R_h^{j_{true}}$ in events of the three flavor types j ={uds, c and b}, representing events of $Z^0 \to u\bar{u}, d\bar{d}, s\bar{s}$, $Z^0 \to c\bar{c}$ and $Z^0 \to b\bar{b}$ respectively, we invert the equation for individual species h in each momentum bin:

$$R_h^{i_{tag}} = \frac{\sum_j B_{ji}^h \epsilon_{ji} F_j R_h^{j_{true}}}{\sum_j \epsilon_{ji} F_j}. \tag{6.3}$$

where F_j is the fraction of hadronic Z^0 decays of flavor type j as listed in Table 6.2 [84]. ϵ_{ji} denotes the event flavor tagging efficiency defined as:

$$\epsilon_{ji} = \frac{\mathcal{N}_{j_{true} \to i_{tag}}}{\mathcal{N}_{j_{true}}} \tag{6.4}$$

where $\mathcal{N}_{j_{true}}$ is the total number of simulated true j flavor events which pass the QCD event selection criteria, and $\mathcal{N}_{j_{true} \to i_{tag}}$ is the total number of those events that are tagged as flavor i. ϵ_{ji} is estimated from the MC simulation and given in Table 4.1 in Chapter 4.2.

F_{uds}	0.612
F_c	0.172
F_b	0.216

Table 6.1: The standard model production fractions for $Z^0 \to q\bar{q}$.

The B_{ji}^h terms represent the momentum-dependent flavor tagging bias for hadron species h contained in events of flavor j which are tagged as i flavors. The flavor tagging biases for hadron h are calculated from the MC simulation as:

$$B_{ji}^h = \frac{\frac{N_{j_{true} \to i_{tag}}^h}{\mathcal{N}_{j_{true} \to i_{tag}}}}{\frac{N_{j_{true}}^h}{\mathcal{N}_{j_{true}}}} \tag{6.5}$$

where $N_{j_{true}}^h$ denotes the total number of good tracks of true hadron species h in true j flavor events and $N_{j_{true} \to i_{tag}}^h$ are the total number of good tracks of true hadron species h found in true j flavor events tagged as i flavor. In this flavor tagging bias formulation all bias terms are ideally unity. If flavor tagging biases are unity, the coefficient of the production rates of the hadron species, $R_h^{j_{true}}$ in equation 6.3 is simply the event tagging purity, $\mathcal{P}_{ij}$ defined as:

$$\mathcal{P}_{ji} = \frac{\mathcal{N}_{j_{true} \to i_{tag}}}{\sum_k \mathcal{N}_{k_{true} \to i_{tag}}} = \frac{F_j \epsilon_{ji}}{\sum_k F_k \epsilon_{ki}}. \tag{6.6}$$

The MC estimated $\mathcal{P}_{ij}$ are also listed in Table 4.1 in Chapter 4.

The flavor tagging bias matrices for hadron species h are obtained using the SLD MC simulation as functions of momentum. The bias matrices are presnted in Fig. 6.7 for pions, in Fig. 6.8 for kaons, and in Fig. 6.9 for protons.

The columns denote tracks in events tagged as light, c, b and non-flavor. Non-flavor tagged events do not satisfy any flavor tagging criteria, so we can not identify the flavor of the events. The rows are the tracks in true light, c and b flavor events. The origin of the flavor tagging biases is a feature of our flavor tagging methods. The flavor tag requires precision vertexing, and the vertex finding algorithm tends to be more efficient for higher track multiplicity c and b flavor events due to the requirement of the minimum number of tracks displaced from the IP to form a heavy hadron decay vertex. Tracks in a high multiplicity event have lower average momenta by conservation of energy and most tracks from heavy (D, B) hadron decays are light mass hadrons. Therefore, B^{π}_{cc} and B^{K}_{cc} are greater than unity for $1 < p < 30$ GeV/c, and B^{π}_{bb} and B^{K}_{bb} are also greater than unity for $1 < p < 35$ GeV/c.

Most of the tracks in events are pions so this feature is explicitly visible in the flavor tagging bias for pions. On the other hand, the vertex finding requires a low momentum cut on tracks, and also the selection of c and b vertices rejects vertices with low momentum (Sect. 4.2), so B^{h}_{cc} and B^{h}_{bb} terms for pions and kaons increase as momentum increases, and have peaks around $p = 10$ GeV/c. Secondary vertices of D and B hadron decays have many kaons with momentum $0.5 < p < 15$ GeV/c, therefore the magnitudes of B^{K}_{cc} and B^{K}_{bb} in that momentum regions are larger than the magnitudes of B^{π}_{cc} and B^{π}_{bb} respectively. Since protons in b and c flavor events are mainly from hadronization, b and c flavor events rarely have high momentum protons. Most of the high momentum protons in c flavor events come from c baryon decays, and c baryons have a shorter lifetime compared to charm mesons, therefore it is more difficult to separate the c baryon secondary vertices from the IP. Hence B^{p}_{cc} is lower than unity for the entire momenta. Fig. 6.9 indicates $b-$tagged events do not have substantial bias for protons.

The light flavor event tag requires that no vertex and no tracks with significant impact parameter N_{sig} are found in the event. This flavor tag is more efficient for low multiplicity light flavor events. This is true since more secondary vertices or N_{sig} are found in

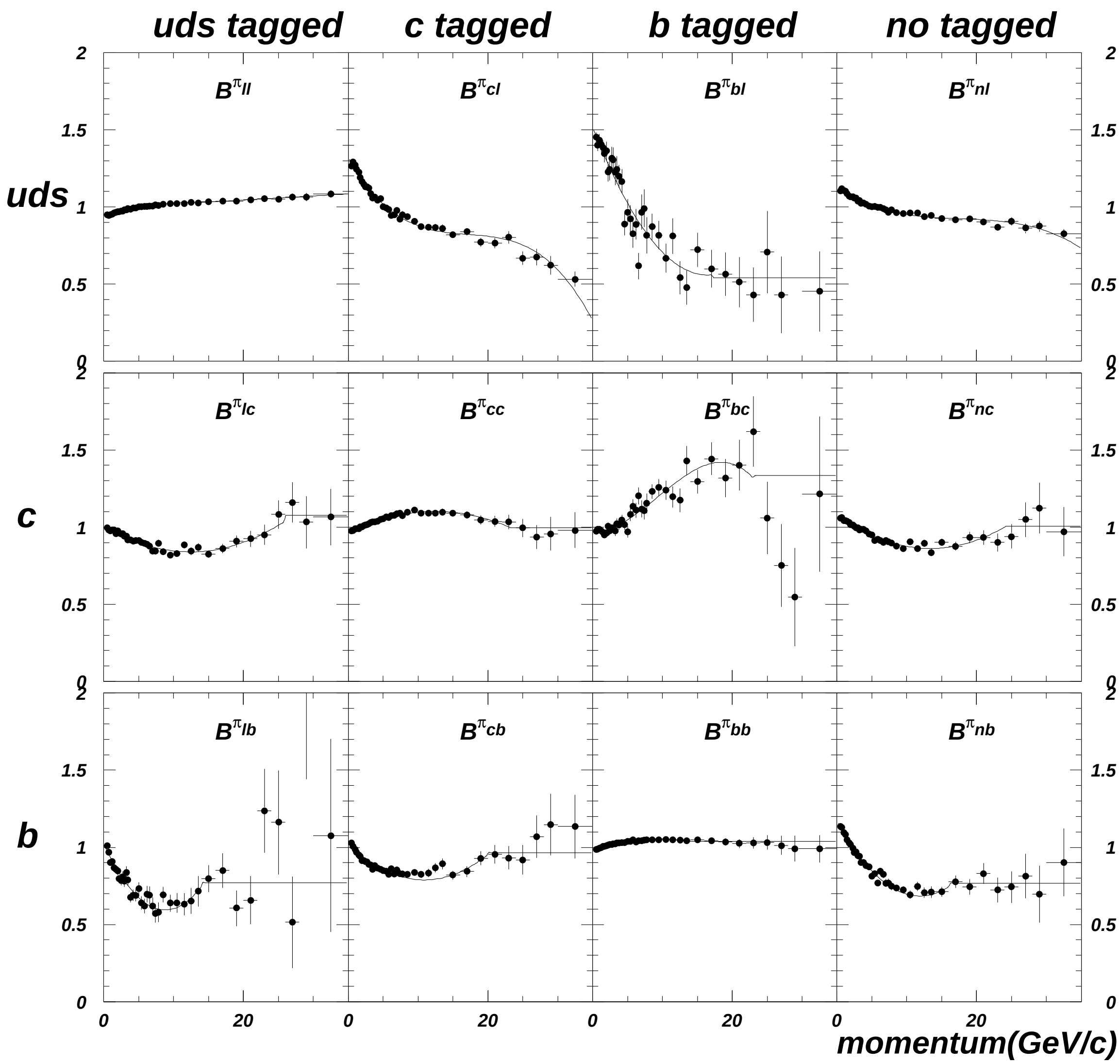

Figure 6.7: Flavor tagging bias matrix for simulated charged pions. Each row represents events of different true flavors and each column represents events tagged as different flavors.

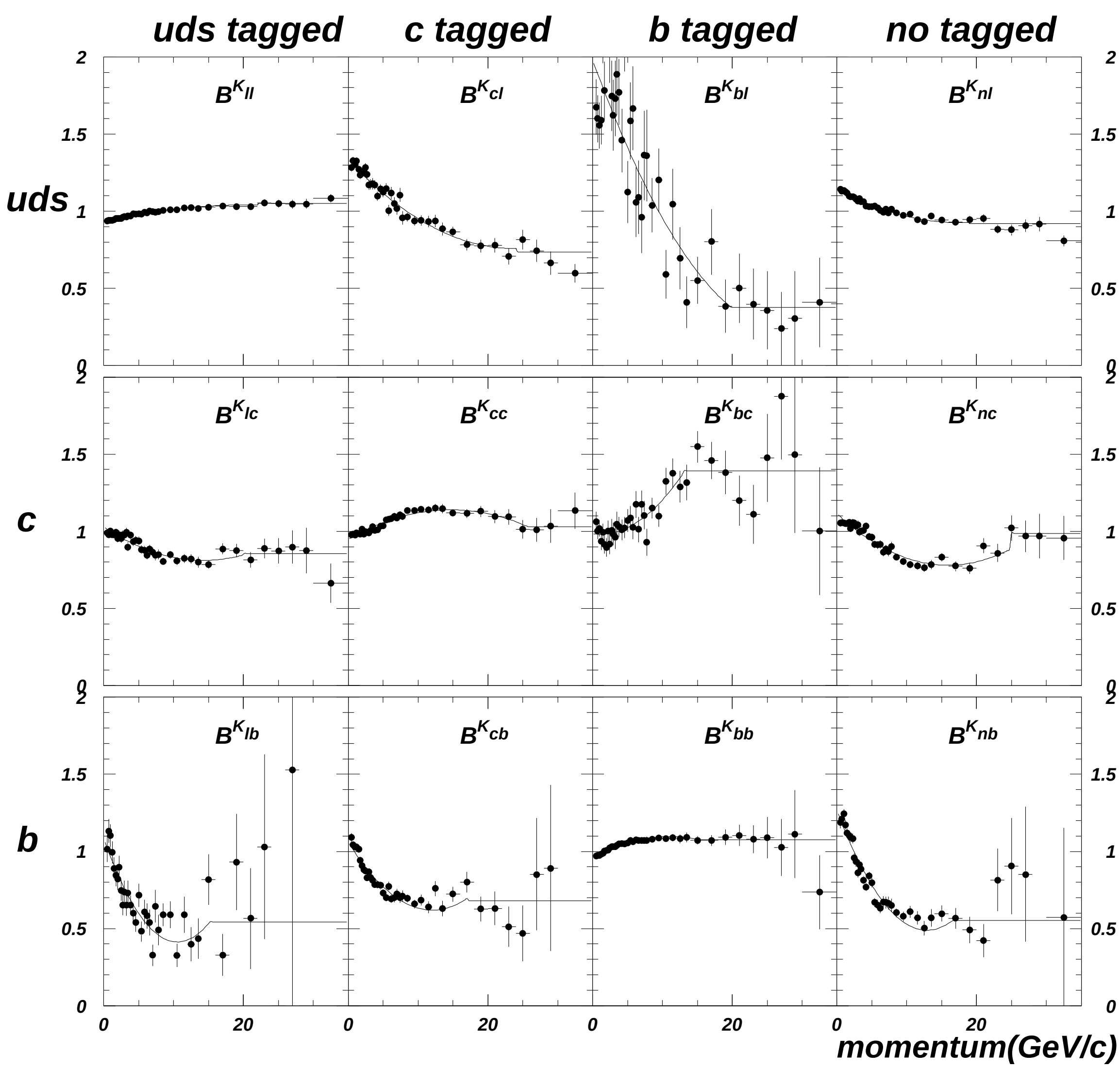

Figure 6.8: Flavor tagging bias matrix for simulated charged kaons. Each row represents events of different true flavors and each column represents events tagged as different flavors.

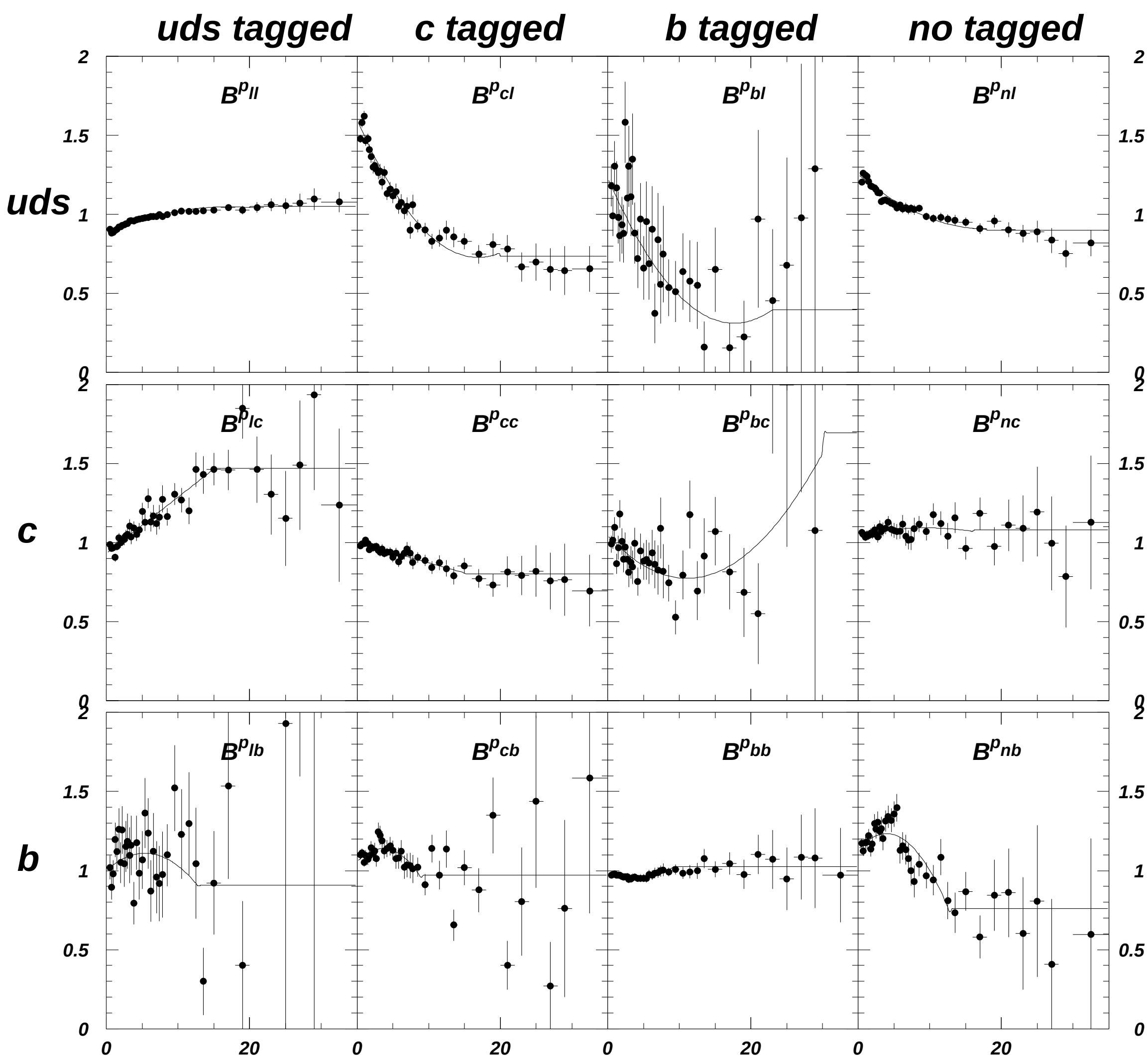

Figure 6.9: Flavor tagging bias matrix for simulated charged protons. Each row represents events of different true flavors and each column represents events tagged as different flavors.

events with high multiplicities. Therefore, events tagged as light flavor tend to have low multiplicities, and tracks in low multiplicity events have higher momentum compared to tracks in high multitplicity events. We can therefore expect that B^h_{ll} is much greater than unity in high momentum regimes. This argument also explains that the bias term is below unity at low momentum. B^K_{ll} is noticeably lower than B^π_{ll} for $p < 5$ GeV/c. Due to the deviation of B^h_{ll}, the other off-diagonal terms are significantly higher than unity at low momentum and lower than unity in the high momentum regions. In intermediate momentum regimes ($5 < p < 15$ GeV/c), the value of B^h_{ll} is greater than unity and the slope of B^h_{ll} becomes smooth. Light flavor events can have tracks from low momentum K_s or $\Lambda^0/\bar{\Lambda}^0$ decays inside the VXD3. The momenta of these tracks might be poorly reconstructed, so the found decay vertex is not tagged as the K_s or $\Lambda^0/\bar{\Lambda}^0$ decay but mistagged as a secondary vertex of a B or D hadron decay. In some cases even though K_s or $\Lambda^0/\bar{\Lambda}^0$ are properly reconstructed, there is a possibility that a track not related with the strange particle decay happens to be attached to the K_s or $\Lambda^0/\bar{\Lambda}^0$ decay vertex, and a false secondary vertex is formed. These false vertices are the main contribution to the c tag and b tag impurity from light flavor events.

The diagonal bias values are typically very close to unity and within ~ 15 % of unity in all cases. Small diagonal bias terms for flavor tagging are the reason that the current flavor tagging method is chosen, especially for c tagged events. Fortunately, the elements with the most deviation from unity for each row are the terms that have the lowest contributing populations, so the product of $\epsilon_{ji}B_{ji}$, where $i =$\{light, c, b and tagged as non-flavor\}, is small and has little effect on the unfolded results.

Parameterizations of the features of each bias element are performed. In principle, $\sum_i \epsilon_{ji}B_{ji}(p)$ must be unity to conserve the total number of tracks. The sum indicates that any event that suffers a flavor tagging bias from a particular tag must enter some other sample category. This can be checked with the definition of B_{ji} and ϵ_{ji} described earlier. The parameterization procedure used for the current analysis does not require $\sum_i \epsilon_{ji}B_{ji}(p) = 1$. Instead the sum is used as a cross check and is found to be unity with very small deviation for all momenta. The parameterization functions are applied for unfolding the flavor tagged events to reduce MC statistical fluctuations.

The unfolded pion rates are corrected for leptonic contamination by subtracting the leptonic rates estimated using the MC for each flavor events. At low momentum, the leptonic rates are dominated by electrons which come from γ conversions. This contribution is a 5% effect at 1 GeV/c then drops rapidly as momentum increases.

For the heavy flavor events, electrons and muons from semi-leptonic decays of heavy hadrons cause the leptonic correction to increase with momentum above 5 GeV/c, reaching 13% and 60% for c and b flavor events respectively for $p > 15$ GeV/c.

By inverting equation 6.3, we can derive the unfolded production rates $R^{j_h^{true}}$. Finally, the unfolded $R^{j_h^{true}}$ are converted to unfolded fractions $f^{j_h^{true}} = R^{j_h^{true}} / \sum_h R^{j_h^{true}}$, which are shown in Fig. 6.10 for each event flavor. The unfolded $f^{j_h^{true}}$ are listed in Tables B.3– B.5 in Appendix B. The general features of the hadron fractions for flavor separated events are similar to those of the hadron fractions for flavor inclusive events at low momentum. For light flavor and c flavor events, the features of the hadron fractions are still very similar to the hadron fractions for the flavor inclusive events at high momentum. For b flavor events, the pion and kaon fractions become constant for $p > 10$ GeV/c instead of decreasing with momentum, and the proton fraction is almost zero for $p > 15$ GeV/c.

In order to see the differences between event flavors more clearly, the fractions of all three flavor events are plotted in Fig. 6.11.

The kaon fractions for heavy flavor events are higher than the kaon fractions for light flavor events because many kaons coming from B hadron decays are concentrated in the $2 < p < 10$ GeV/c region and similarly a lot of kaons from D hadron decays are populated in the $4 < p < 20$ GeV/c region. Correspondingly, the pion fractions for heavy flavor events are lower than the pion fractions for light flavor events for these momentum regions. Due to the smaller statistics for each flavor event samples compared to the statistics for flavor inclusive event sample, fewer bins are used for the flavor dependent analysis than for the inclusive study.

DELPHI is the only other experiment to perform the flavor dependent analysis. DELPHI have studied only uds and b flavor events [85]. Our results of the hadron fractions in uds flavor events are consistent with the result of DELPHI measurement within correlated errors. The top plot in Fig. 6.12 shows the comparion of the hadron fractions in uds events

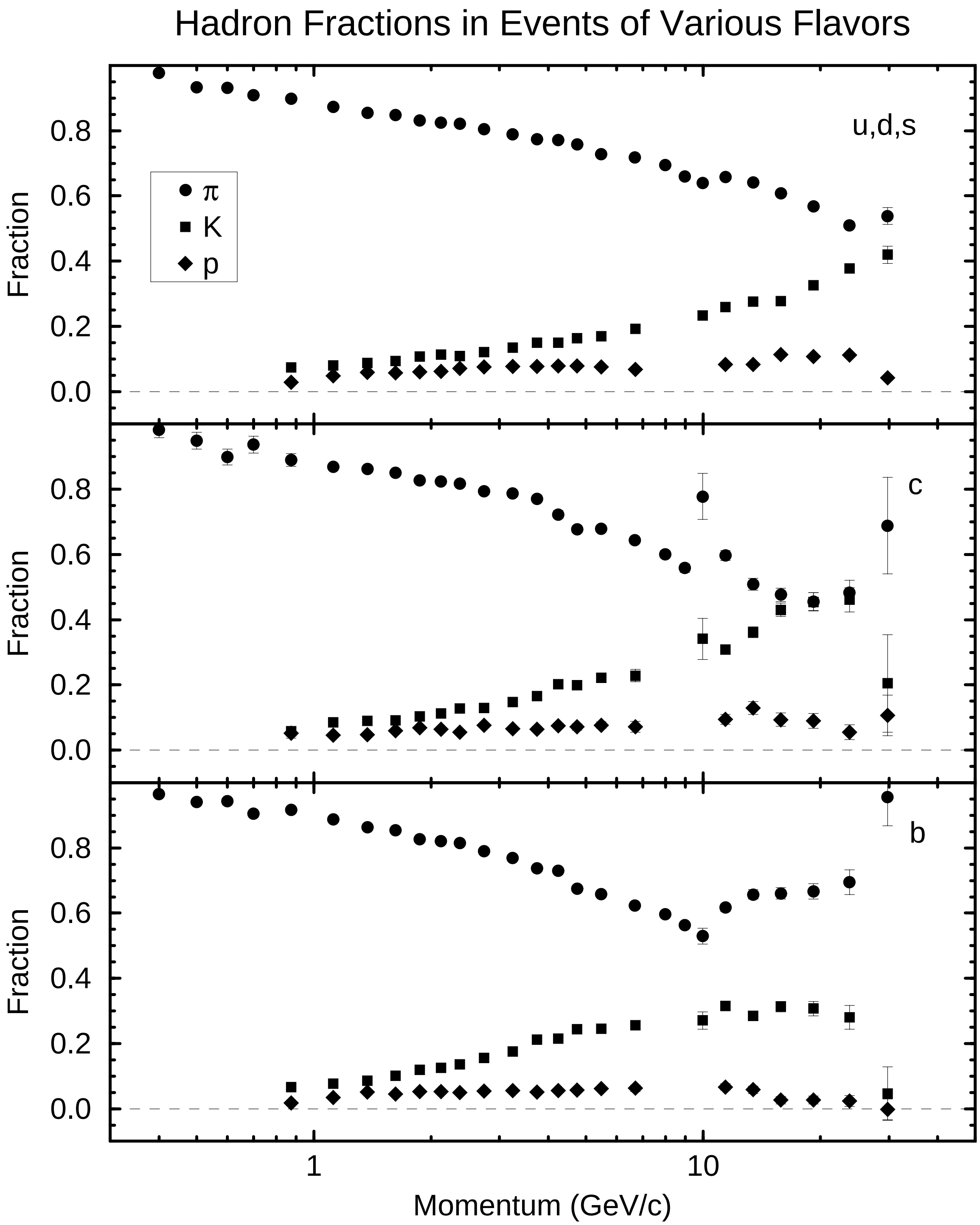

Figure 6.10: Completely corrected production fractions of pions, kaons and protons for different flavor events.

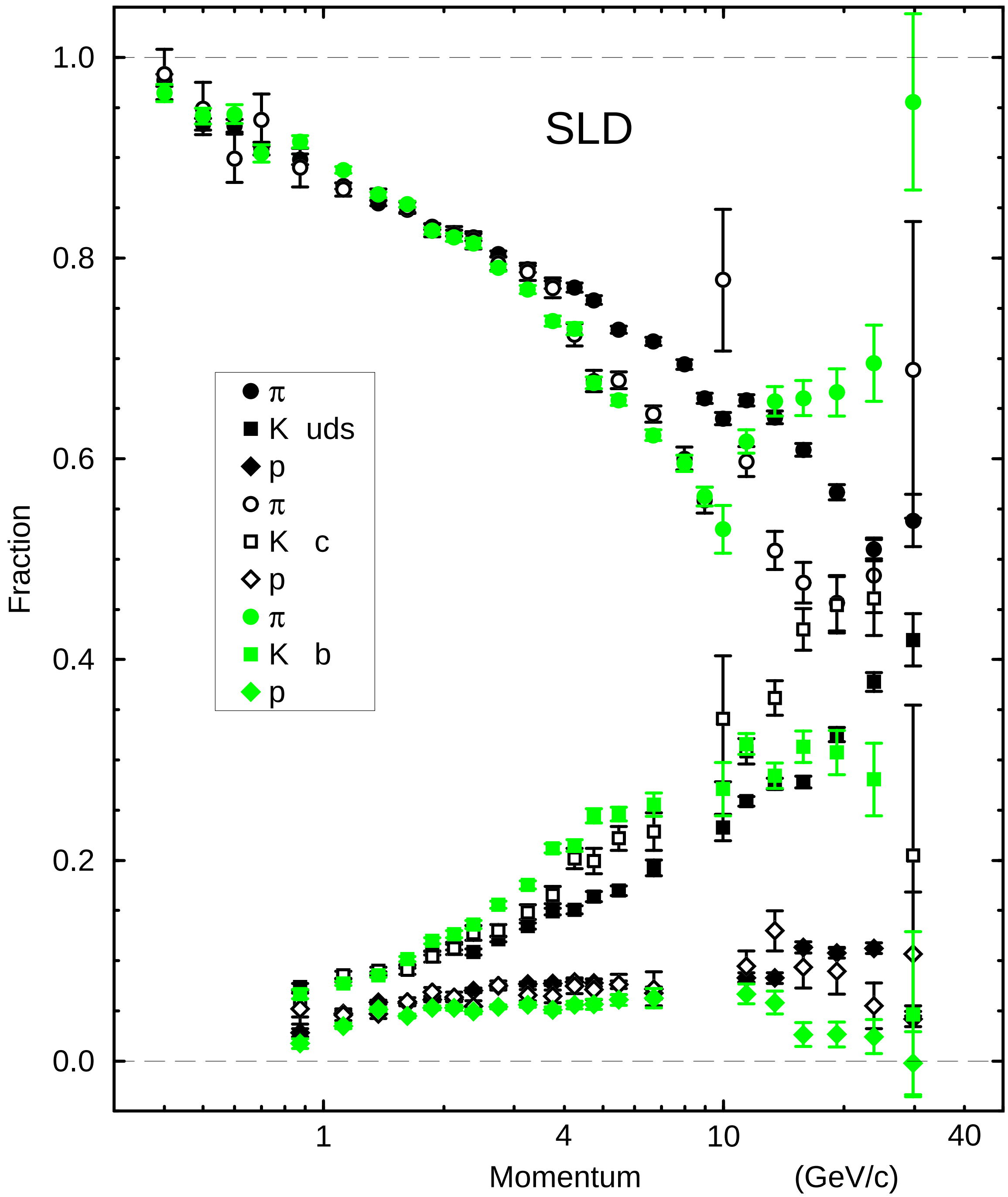

Figure 6.11: The production fractions of pions, kaons and protons in *uds*, *c* and *b* quark events.

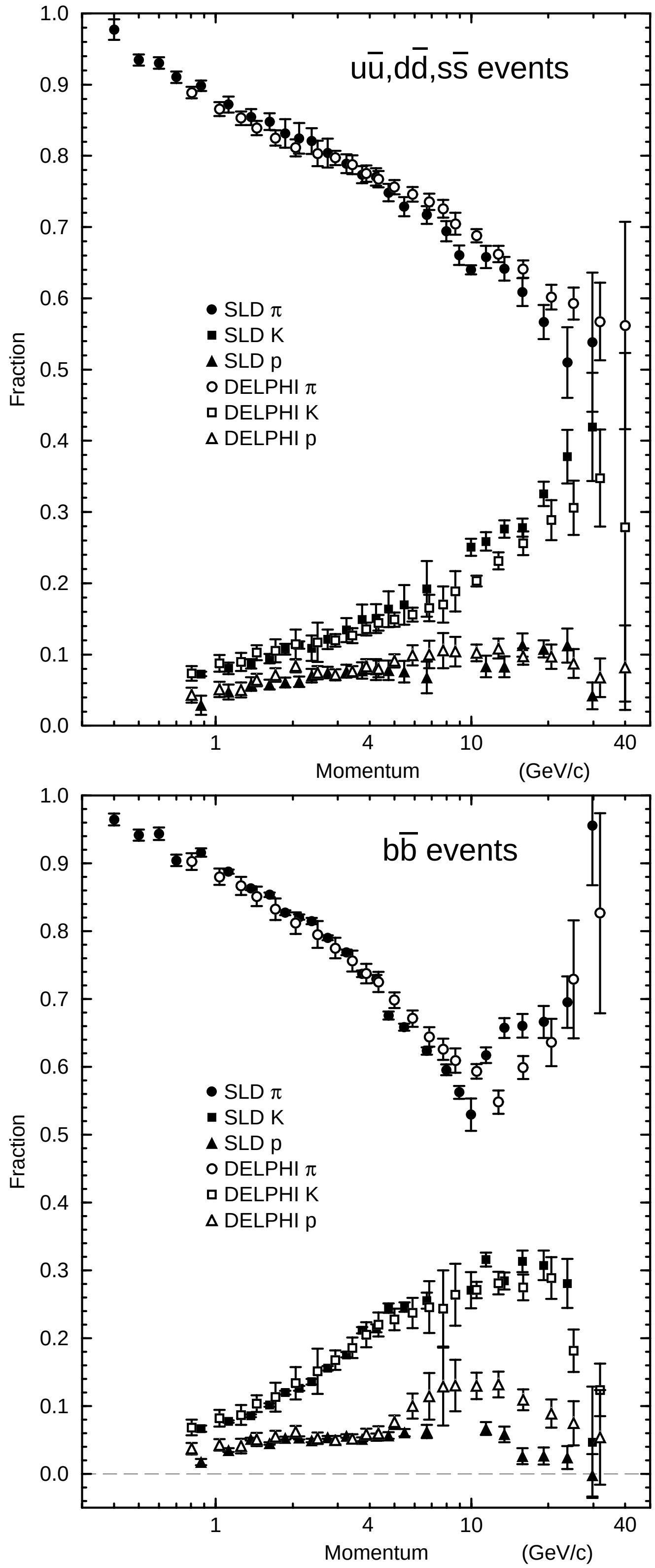

Figure 6.12: Comparison of our measured hadron fractions in uds events and the results of DELPHI measurements (top), and comparison of our hadron fractions in b events and the hadron fractions in b events from DELPHI (bottom).

from SLD and DELPHI. SLD and DELPHI have a similar feature of the pion and kaon fractions in *uds* events except for high momentum regions. DELPHI measures the higher pion fraction, and the lower kaon fraction for $p > 3$ GeV/c compared to our result. Two measurements agree very well for the proton fraction.

The hadron fractions in b events show some differences between the results from SLD and the results from DELPHI. The comparion of the hadron fractions in b events from the two experiments is also shown in the bottom plot of Fig. 6.12. All hadron fractions in b events from SLD and DELPHI agree very well for $p < 7$ GeV/c. The DELPHI proton fraction is substantially higher than the SLD proton fraction for $10 < p < 30$ GeV/c. Correspondingly, the pion fraction from DELPHI is lower than the pion fraction from SLD for that momentum range. The kaon fractions from the both measurements are consistent.

Fig. 6.13 shows the comparison of the measured charged hadron fractions in light flavor events with the prediction of the SLD MC simulation in addition to the predictions of three fragmentation models . The SLD MC simulation describes the proton fractions very well throughout the entire momentum range. The SLD MC is also in good agreement with the data kaon fraction. Qualitatively there is little difference between the light flavor data and the data for the flavor inclusive event sample. However, the light flavor measurements are more relevant for comparison with QCD predictions which use the assumption of massless primary quark production. The same general differences between the predictions of the three models and the data are observed in both the light flavor sample and the flavor inclusive sample.

The light flavor measurements thus indicate that these deficiencies are in the fragmentation or hadronization simulation, and are not simply due to the modelling of heavy hadron production and decay.

The systematic errors calculated in the flavor inclusive analysis are predominantly from the uncertainties of the identification efficiency matrix, and are common to all three event flavor samples. Therefore we do not show these errors for the flavor dependent analysis.

Additional systematic errors related to the comparison of different event flavors come from uncertainties in the unfolding procedure.

Variations of three different parameters: the flavor tagging efficiency, the flavor tagging

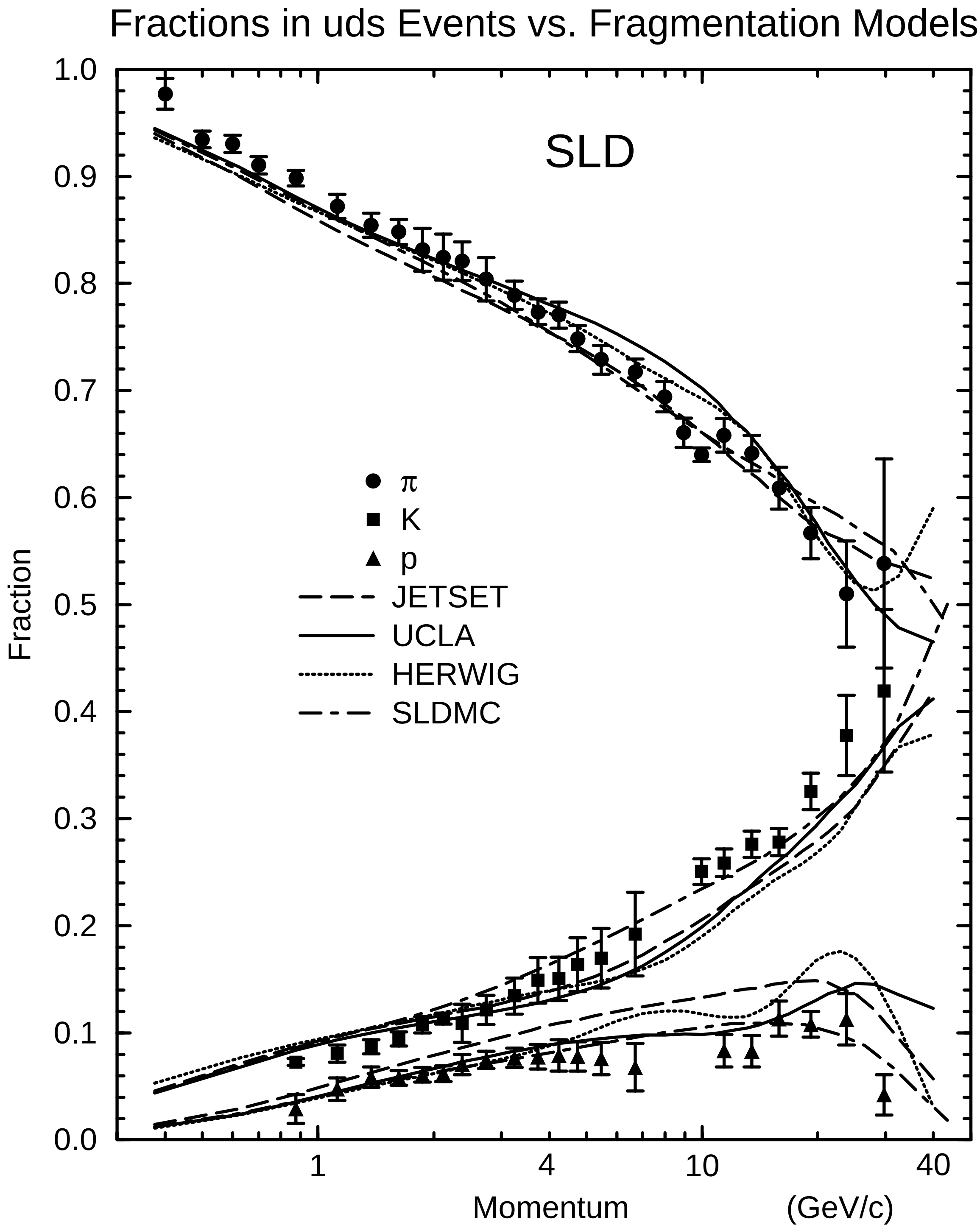

Figure 6.13: The production fractions of charged hadrons in *uds* events and the predictions of the JETSET, HERWIG and UCLA models as well as the SLD MC simulation.

bias and the lepton background are considered for yielding the systematic errors from the flavor dependent analysis. The variations are performed for each parameter so as to conserve the sum of the variations of relevant terms to be zero.

We consider three independent variations of the flavor tagging efficiency matrix, each varying one of the diagonal elements of ϵ_{ii}. For each case, one diagonal element is varied by ± 0.01 and simultaneously one or more elements ϵ_{ik} in the same row is varied by a total of ∓ 0.01.

We also consider three independent variations of the flavor tagging bias matrix, in each case varying the diagonal value B^h_{ii} for a flavor i and for all hadrons h simultaneously by the larger value of ± 0.005 or $\pm 20\%$ of the deviation of B^h_{ii} from unity. The differences from unity of the other elements, $B^h_{ki} - 1$ in the same row are also scaled by the same factor.

The MC γ conversion rate is varied by $\pm 15\%$, and the rates of leptons from other sources in light, c, and b flavor events are varied by $\pm 50\%$, $\pm 10\%$ and $\pm 5\%$ respectively. The variation values in the lepton rates for c and b flavor events correspond to the uncertainties in measured semi-leptonic branching ratios. The uncertainties due to variations in the world average values of the SM fractions F_j [84] are negligible compared with the statistical errors. The unfolding systematic errors are typically small compared with the statistical errors and are dominated by the variations in the flavor tagging bias (B_{ji}).

In Fig. 6.14, the ratios of hadron production rates in b flavor events to light flavor event for the three hadron species are shown. The primary systematic errors in particle identification are cancelled in the ratios, and the statistical errors are dominant. There is greater production of charged π's in b flavor events at low x_p, where $x_p \equiv 2p/E_{cm}$. The ratio of the π production rates rising as x_p increases for $0.01 < x_p < 0.04$. The ratio of the π production rates becomes flat for $0.03 < x_p < 0.05$ with a value of ~ 1.2, and then starts decreasing as x_p increases. The production rates of charged kaons is approximately equal in b and in light flavor events at $x_p \approx 0.02$, but the ratio of the kaon production rates in b flavor to those in light flavor events increases with x_p, peaking at $x_p \approx 0.07$ with a value of ~ 1.7, and then declines rapidly as x_p increases. There is approximately equal proton production rates in b and in light flavor events below $x_p = 0.05$. For $x_p > 0.1$, the proton production rates in b flavor events fall faster with increasing momentum. These features

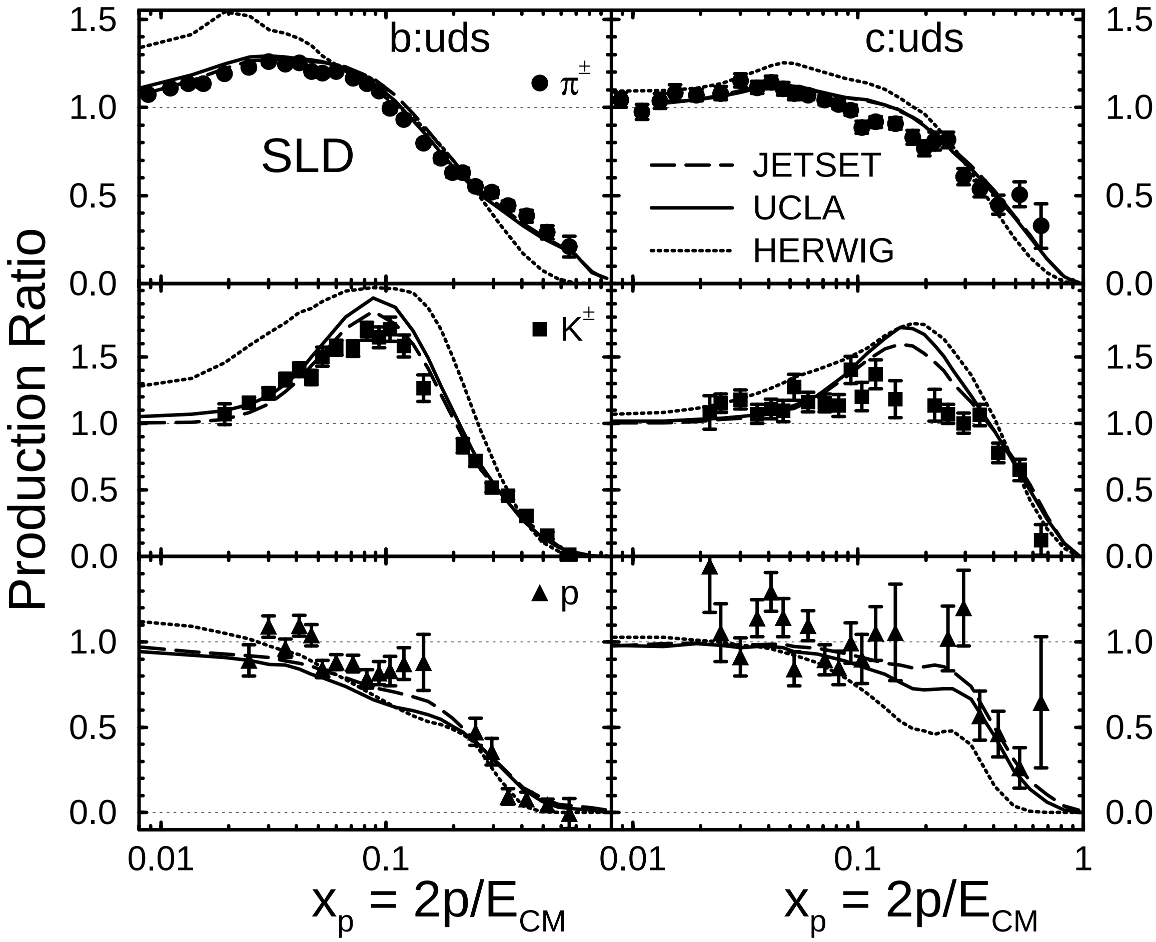

Figure 6.14: The relative ratios of hadron production rates in heavy (c,b) flavor events to those in light (uds) flavor events along with the predictions of three fragmentation models.

are expected because in $b\bar{b}$ events, a large fraction of the event energy is carried by the leading B and $\bar{B}$ hadrons, leaving little phase space to produce high momentum hadrons. The B hadrons decay into a large number of lighter particles (π's and kaons), which are concentrated in the region of $0.02 < x_p < 0.2$. Similar qualitative features are observed for $c\bar{c}$ events. The fragmentation models reproduce these features qualitatively, although the HERWIG model overestimates the π and kaon ratios by a large factor at low x_p. The values of these ratios depend on the B hadron energy spectra and decay properties as well as on the hadron production in the fragmentation models.

Fig. 6.14 also shows the ratios of the three hadron production rates in c flavor events to the production rates in light flavor events. The errors are larger than those in the b:uds comparison. The observed features are qualitatively similar to those observed in the b:uds ratio but quantitative differences are shown. The ratio of the π production rates in the c:uds comparison for $x_p < 0.1$ is smaller than that in the b:uds comparison. For $x_p < 0.12$, the proton production rates in c and in light flavor event are approximately equal.

Since leading D hadrons carry a lower portion of the event energy than leading B hadrons, there is more phase space available for fragmentation hadron production. The D hadron decay products often include a kaon carrying a large fraction of the D hadron momentum, so there are fewer additional charged pions than in B hadron decays. All models are consistent with the data for the c:uds comparison , except that the HERWIG model overestimates the ratio of the π production rates for $0.03 < x_p < 0.15$ and the ratio of the kaon production rates for $0.04 < x_p < 0.1$, and underestimates the ratio of the proton production rates for $x_p > 0.1$.

6.3 Leading Hadron production

The purpose of the leading hadron production study is to understand how the quantum numbers (color, flavor) of quarks can be observed in jets. By understanding this, we hope to observe distinctive properties of each quark type and to separate events initiated by u, d and s quarks. Leading hadrons are hadrons which contain the initial quark or antiquark in an event. b and c quark events are extensively studied and have also been used for other measurements [52],[86]. Because B and D hadrons are mainly produced as leading hadrons in $b\bar{b}$ and $c\bar{c}$ events instead of fragmentation, identification of these hadrons can be used to tag $b\bar{b}$ and $c\bar{c}$ events . The MC simulations and experimental results show that leading heavy hadrons carry a large portion of initial quark/antiquark energy in events [34]. The MC simulation predicts that leading hadrons in light (uds) events have on average higher momenta compared to the average momenta of hadrons from fragmentation. However, many hadrons that come from fragmentation can also have high momentum in uds events, so the identification of leading hadrons is ambiguous. Also the probability of quark and corresponding antiquark production in fragmentation is expected to be equal for all types of quark events.

For the leading hadron analysis, we want to test whether a uds quark jet produces more hadrons that contain a valence uds quark than hadrons that contain $\bar{u}\bar{d}\bar{s}$ quarks. As explained in Appendix A, the longitudinally polarized electron beam of the SLC produces a large electroweak forward-backward asymmetry in the distribution of the polar angle of quark jet directions in Z^0 decays. This asymmetry allows us to separate samples enriched in quark and in antiquark jets, and allows us to measure the differences of hadron production in these jet samples.

The weak interaction of Z^0 bosons predicts that quarks tend to associate with the electron beam direction for left-handed electron beams, and with the positron beam direction for right-handed electron beams (parity violation). According to the asymmetry plots of quark shown in Fig. 2.2 in Chapter 2, this asymmetry is large at high $|\cos\theta|$, where θ is the polar angle of the quark jet direction with respect to the electon beam direction. The event thrust axis is determined with LAC clusters information. The polar angle of the thrust axis to the electron beam direction θ_{th} is used to approximate the initial $q\bar{q}$ jet directions. The z component of thrust axis is assigned such that it points in the positive SLD z direction[1], $\vec{t_z} > 0$. The event is divided into two hemispheres using a plane perpendicular to the thrust axis. When the polarization is left-handed, the hemisphere in the forward region is assigned as the "quark jet" hemisphere. If the polarization is right-handed, the hemisphere in the backward region is assigned as a "quark jet" hemisphere. For both cases, the opposite hemispheres are assigned as "anti-quark jet" hemispheres. A track is included in a quark jet hemisphere if the momentum of track satisfies $\vec{p} \cdot \vec{t} < 0$. Otherwise it is included in an anti-quark hemisphere. In order to improve the jet tagging purity, events in the central region of the detector where the production asymmetry is small are rejected by the requirement $|\cos\theta_{th}| > 0.2$. The number of the remaining light quark events is 72,933 after applying the $|\cos\theta_{th}|$ requirement.

The sign of the electron beam polarization is measured event-by-event and its magnitude is averaged over several events. The luminosity-weighted average magnitude of the polarization listed in Chapter 3 and the Standard Model coupling assumption determine the purity of the quark tagged sample to be ~ 0.73.

For the leading hadron analysis, only *uds* flavor events are used. Heavy flavor events are rejected because they include particles from heavy hadron (D,B) decays which contaminate the fractions of hadrons coming purely from hadronization.

The hadron fraction analysis is performed separately on each of the light quark and antiquark tagged samples. Positively and negatively charged tracks are also distinguished for the leading hadron analysis. The correction for leptons and late Λ^0 decays are not included. With the assumption of CP invariance, we expect that results for the positively charged tracks in the quark$-$tagged sample and the negatively charged tracks in the antiquark$-$tagged sample to be consistent. In order to increase statistics, these two samples are combined and interpreted as being representative of positive hadrons (π^+, K^+ and p) in light quark jets. From these combined distributions, the measured positive hadron fractions of light quark jets $f_{h+}^{q_{tag}}$ are yielded. The positively charged tracks in the antiquark$-$tagged

[1]The positive SLD z is defined along the positron beam direction.

sample and the negatively charged tracks in the quark−tagged sample are also combined to yield the measured negative hadron fractions of light quark jets $f^{q_{tag}}_{h-}$, and interpreted as being representative of negative hadrons (π^-, K^- and $\bar{p}$) in light quark jets.

The measured hadron fractions are converted into hadron production rates, $R^{q_{tag}}_{h\pm}$ using

$$R^{q_{tag}}_{h\pm} = n^{q_{tag}}_{\pm} \cdot f^{q_{tag}}_{h\pm} \tag{6.7}$$

where $n^{q_{tag}}_{\pm}$ is the average number of tracks which pass the QCD track selection cuts in each momentum bin per light quark−tagged hemispheres. $R^{q_{tag}}_{h\pm}$ is corrected for heavy flavor contamination to get the corrected production rates $\tilde{R}^{q_{tag}}_{h\pm}$. A correction for the contributions from heavy flavor contamination is applied for $R^{q_{tag}}_{h\pm}$ using the MC prediction. Fig. 6.15 shows the measured $R^{q_{tag}}_{h\pm}$ along with the MC predicted contribution from heavy flavors where $h = \{\ \pi,\ K$ and $p\ \}$. The contributions show substantial differences between hadrons and antihadrons for charged kaons at high momenta due to decay products of heavy hadrons. The differences between hadrons and antihadrons for charged π's and for charged protons are insignificant. The residual heavy flavor contributions are estimated to be typically $\sim 8\%$ of the total tracks from the MC. The MC simulated heavy flavor background is worst for charged kaons as shown in Fig. 6.15. However, since the *uds* tag is very efficient, the effect of this correction on the results is negligible compared with the statistical errors.

The corrected rates $\tilde{R}^{q_{tag}}_{h\pm}$ can be related to true production rates $R^{q}_{h\pm}$ in terms of the light flavor tagging bias and the effective purity P of the quark jet tag.

$$\begin{aligned}
\tilde{R}^{q_{tag}}_{h+} &= PR^{q}_{h+}B^{h}_{ll} + (1-P)R^{q}_{h-}B^{h}_{ll} \\
\tilde{R}^{q_{tag}}_{h-} &= PR^{q}_{h-}B^{h}_{ll} + (1-P)R^{q}_{h+}B^{h}_{ll}
\end{aligned} \tag{6.8}$$

The unfolded true production rates $R^{q}_{h\pm}$ in light quark jets are extracted by inverting the

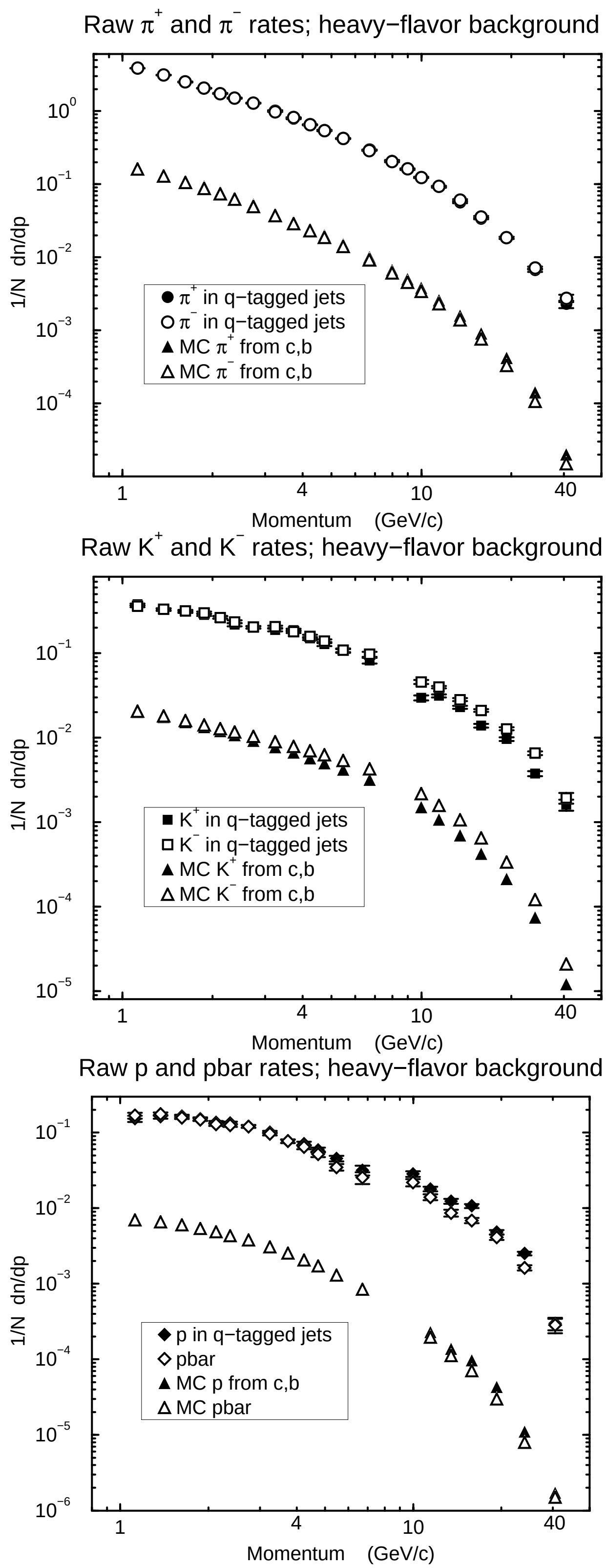

Figure 6.15: The measured h^+ and h^- rates in tagged light quark jets and the $h\pm$ contribution from c and b quark jets estimated in the MC. $h = \{\pi,\ K \text{ and } p\}$.

matrix above.

$$
\begin{aligned}
R^q_{h+} &= \frac{P\tilde{R}^{q_{tag}}_{h+} - (1-P)\tilde{R}^{q_{tag}}_{h-}}{(2P-1)B^h_{ll}} \\
R^q_{h-} &= \frac{P\tilde{R}^{q_{tag}}_{h-} - (1-P)\tilde{R}^{q_{tag}}_{h+}}{(2P-1)B^h_{ll}}
\end{aligned}
\tag{6.9}
$$

The effective purity P including the effect of the cutoff in acceptance of the barrel CRID at $|\cos\theta| = 0.68$ is estimated to be 0.72 from the MC simulation, which is lower than the value of 0.73 from the average electron polarization [78]. The purity P is independent of hadron momentum.

The unfolded measured true production rates $R^q_{h\pm}$ are shown in Fig. 6.16. The unfolded true production rates $R^q_{h\pm}$ are converted to the unfolded fractions $f^q_{h\pm} = R^q_{h\pm}/\sum_h(R^q_{h+} + R^q_{h-})$. The unfolded $f^q_{h\pm}$ are listed in Tables B.6–B.8 in Appendix B. The common systematic errors from particle identification for hadrons and for antihadrons are not included in this Fig.. The hadron production rates and antihadron production rates at low momentum are consistent for all hadron species. This result is expected, since most of low momentum hadrons and antihadrons come from fragmentation. For charged pions, very small difference is seen between π^+ and π^- in high momentum region. There are significant differences between hadrons and antihadrons for kaons and protons in high momentum regions ($p > 10$ GeV/c), and the differences seem to increase as momentum increases.

Systematic errors in the heavy flavor contamination are estimated by varying the elements of the event flavor tagging efficiency matrix (ϵ_{ji}) and by varying the values of the tagging bias matrix (B_{ji}). The systematic errors are the same as those described in the flavor dependent analysis. The variation of F_b, F_c (conventionally written as R_b, R_c), A_b and A_c values by the errors on their world averages are performed to yield an additional systematic for the contribution from heavy quark background [84]. A systematic uncertainty of ± 0.015 is applied to the effective quark purity P to account for uncertainties in the beam polarization and MC statistics. The systematic errors are small compared with the statistical errors, and are dominated by the uncertainty on the effective purity.

The leading particle production analysis is unique at SLD due to the high longitudinal polarization of electron beam. OPAL [87] tried to do this analysis, but obtained limited

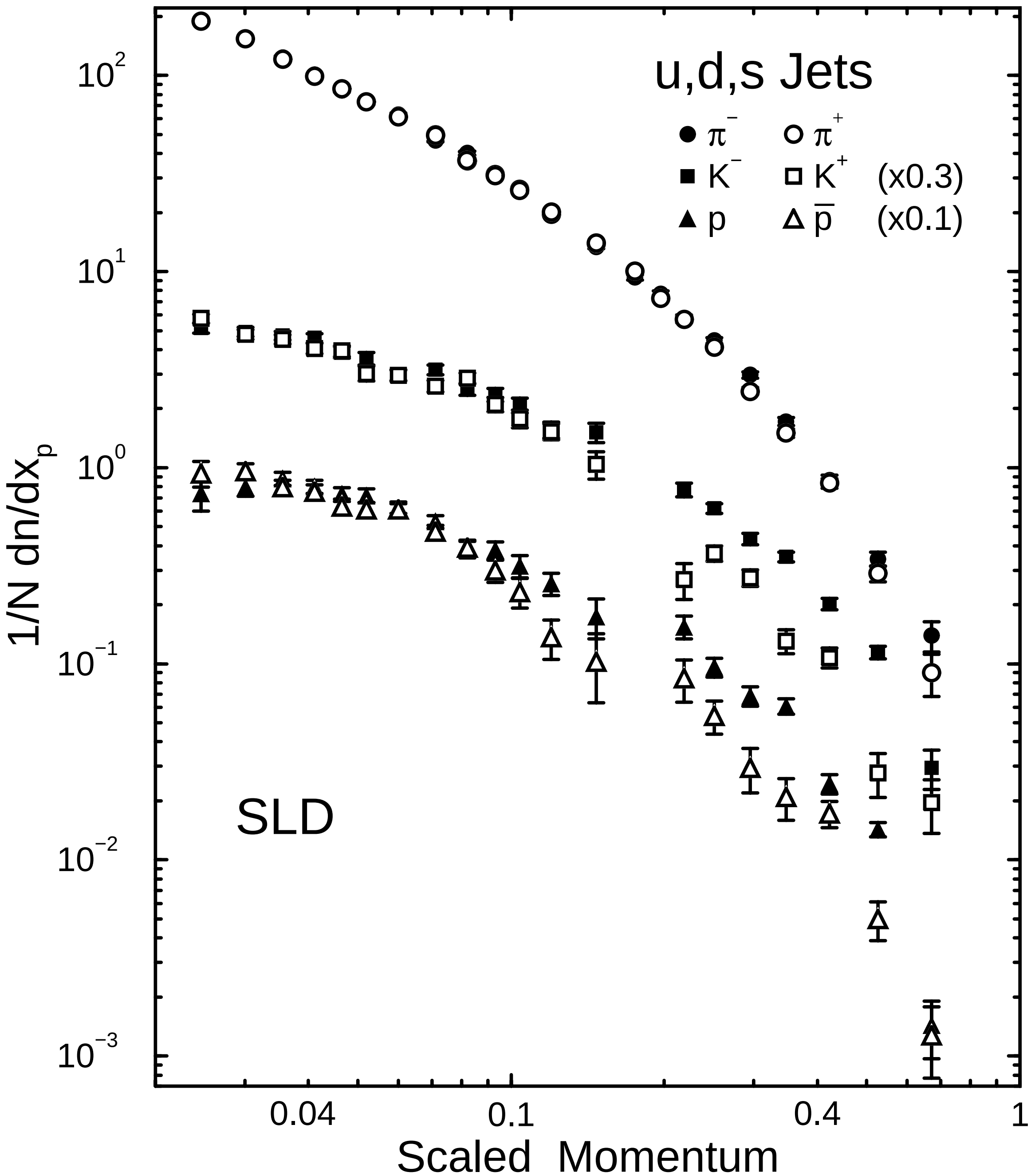

Figure 6.16: The differential production rates of $\pi^{\pm}$, $K^{\pm}$ and $p/\bar{p}$ per light (uds) flavor jet.

results.

In order to investigate leading hadron effects, a discriminating variable is constructed as:

$$D_h = \frac{R_h^q - R_{\overline{h}}^q}{R_h^q + R_{\overline{h}}^q} \tag{6.10}$$

The common systematic errors are cancelled explicitly in this variable. A value of zero corresponds to equal production rates of hadrons and antihadrons. Values of $+1$ and -1 correspond to complete dominance of hadron production and antihadron production respectively. Fig. 6.17 shows the results for D_h for all three charged hadrons, and also shows the results from our previous study for the strange vector meson K^{*0} and Λ^0 baryon [77]. D_h for π's, K and p's in light quark jets are summarized in Table B.9 in Appendix B.

The values of D_h for all hadron species are consistent with zero at low x_p, whereas the values of the variable are significantly positive at high x_p. Since baryons contain quarks instead of antiquarks, the observed excess of both protons and Λ's over their antibaryons in light quark jets for $x_p > 0.2$ provides good evidence for leading baryon production. For $x_p < 0.2$, where the contribution from fragmentation is very high, no excess is observed. Some of the antiprotons are produced in association with leading protons and others are generated from non-leading fragmentation. The production rate of antiprotons from fragmentation at high x_p is supposed to be the same as the production rate of protons from hadronization. The non-zero value of D_h for baryons at $x_p > 0.2$ is a direct indication of the effects of leading hadrons.

The interpretation of the results for mesons is more complicated because mesons contain both a valence quark and a valence antiquark. All down type quarks are predicted to be produced equally and with the same forward-backward asymmetry in SM Z^0 decays, therefore when leading hadron $\bar{K}^{*0}$ $(s\bar{d})$ are produced equally in s and $\bar{d}$ jets, then a measured $D_{\bar{K}^{*0}}$ is expected to be zero. The data points of $D_{\bar{K}^{*0}}$ at high x_p are definitely positive, indicating that more leading $\bar{K}^{*0}$ are produced in s jets than in $\bar{d}$ jets. This is a consequence of strangeness suppression in fragmentation.

For π^- $(d\bar{u})$ and π^+ $(u\bar{d})$, the different Z^0 branching ratios F_u, F_d and parity violating parameters A_u, A_d of up and down type quarks cause a non-zero dilution of leading hadron

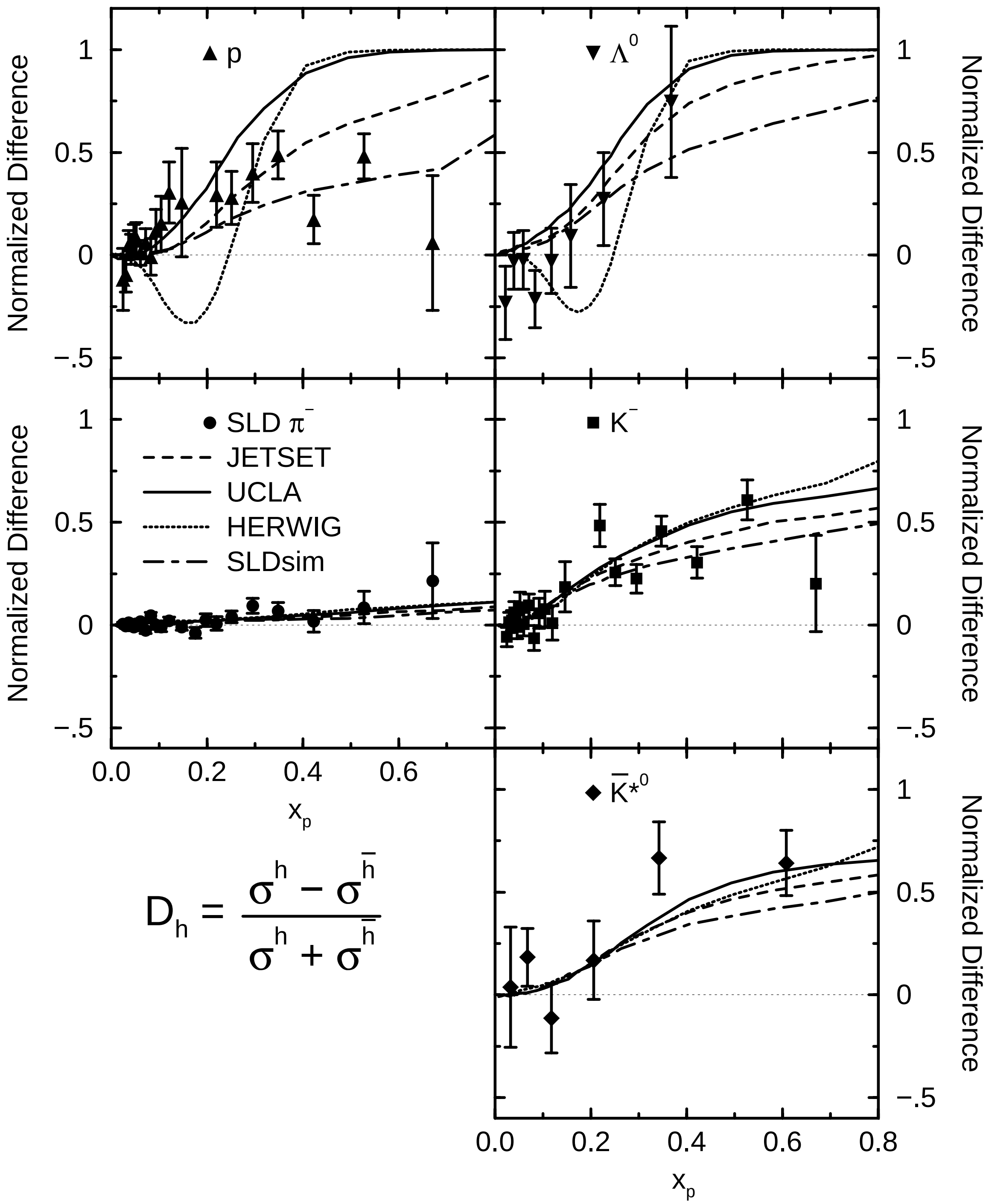

Figure 6.17: Normalized production rate differences (D_h) between hadrons and antihadrons in light quark jets and the predictions of the predictions of three fragmentation models.

signal at high x_p. The measured D_{π^-} is consistently above zero at high x_p. But the data points are consistent with zero within the statistical error, so we have only a suggestion for leading π production.

The measured D_{K^-} is consistently positive for $x_p > 0.2$, and shows production of leading charged kaons at high x_p and substantially more production of leading K^- in s-jets than in $\bar{u}$-jets. The measured D_{K^-} is another indication of the strangeness suppresseion.

Fig. 6.17 also shows the predictions of the three fragmentation models. The fragmentation models reproduce qualitative features of the data for π's, $\bar{K}^{*0}$'s and Λ^0's. The predictions of all three models are consistent with the measured D_{π^-}. The HERWIG model is inconsistent with the data D_{Λ^0}. Unfortunately, there is no data points of Λ^0 at high x_p to confirm the predictions of the models. For the protons, no model describes the data points at high x_p. The data points are much below the predictions of the models. The JETSET model is consistent with the data protons for $x_p < 0.4$. The HERWIG and UCLA predictions are inconsistent with the data points, and rise sharply to unity at $x_p \approx 0.4$. The HERWIG prediction drops below zero in the range in which we have no proton coverage. The measured D_{K^-} fluctuates statistically at high x_p. The data points are scattered about the predictions at high x_p.

6.4 Particle production in light quark and gluon jets

6.4.1 Motivation and other experiments

Many general properties of the jet fragmentation can be predicted from first principles in perturbative QCD, for example the scaling of jet observables with energy and the differences in inclusive properties of jets initiated by high energy gluons and those initiated by massless quarks. The differences of properties in jets between quarks and gluons are due to the Casimir factors (color charges) $C_F = (N_c^2 - 1)/2N_c = 4/3$ and $C_A = N_c = 3$. These color charges give a higher hadron multiplicity [88],[89], lower average hadron energy and wider average jet angle [90] in gluon jets than in quark jets with the same energy and under the same condition. The ratio of the emitted gluon multiplicity in gluon jets to that of quark jets at a parton shower stage is expected to be asymptotically equal to the ratio of the color charges, $r_0 = C_A/C_F = 9/4$ at infinite energy and time. This ratio r_0 is influenced by effects from finite energy scales and kinematics, which cut off gluon emission well before the asymptotic limit in quark and gluon jets. This termination of gluon emission happens in gluon jets at an earlier stage in a parton shower than in quark jets, and results in less hadron production in gluon jets [91],[92],[93],[94]. In jet fragmentation, the effects from gluon interference on gluon and quark jets are considered (MLLA). As a consequence of gluon interference, a depletion of gluon emission in the volume between the q and $\bar{q}$ jets in $q\bar{q}g$ events, and suppression of soft gluon emission within each jet in a parton shower are predicted. Therefore we expect that the multiplicity ratio of hadrons in gluon and quark jets to be lower than r_0. The reduction of r_0 can be calculated directly in perturbative QCD at some scale or can be predicted by Monte Carlo simulation.

Also the properties of heavy (c, b) quark jets are expected to be different from (Sect. 6.3) those of light(uds) quark jets due to the presence of massive leading heavy hadrons which carry most of the primary quark energy. The leading heavy hadrons decay into a large number of particles, hence the multiplicity in heavy quark jets is higher than that of light quark jets. The discrepancy in jet properties amongst quark types confused early measurements of the differences of inclusive properties in quark and gluon jets from several experiments [95]. The results from these experiments were inconsistent. Some of them (HRS [96], MARK

II [97], UA2 [98], UA1 [99], PLUTO [100], AMY [101]) showed small differences between quark and gluon jets, and some of them (TASSO [102], JADE [103], CELLO [104]) did not show any difference, so the interpretation of the results was inconclusive.

Light and heavy quark jet separation was performed to explicitly compare the inclusive properties in massless quark and gluon jets [105]. Many recent measurements from Z^0 decay experiments tagged event flavors separately to search for precise properties of the inclusive charged track distributions (OPAL [106], [107], [108], DELPHI [109], ALEPH [110]). These experiments selected geometrically symmetric three jet events to compare gluon jets and quark jets at a common energy. Gluon jets were anti-tagged when two jets are tagged as b quark jets. These gluon jets were compared to jets in uds three jet events.

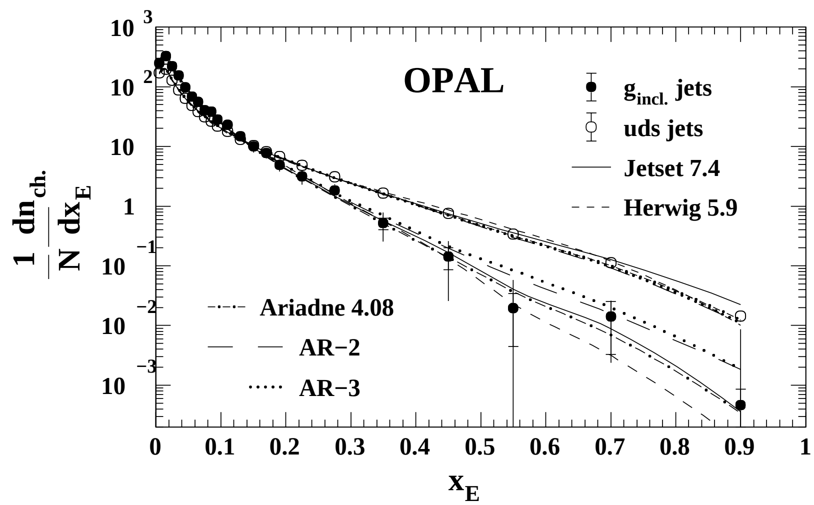

Figure 6.18: Corrected production rate distributions of charged particles for scaled energy $x \equiv E/E_{jet}$, for 40.1 GeV gluon jets and 45.6 GeV uds quark jets.

There has been a huge improvement in experimental measurements of the inclusive properties of uds quark and gluon jets as well as in theoretical calculations with higher precision. OPAL's result on the ratio of the charged particles (multiplicity) in gluon jets with mean energy of 41.8 GeV/c to that in uds jets at 45.6 GeV/c is shown in Fig. 6.18 as a function of the scaled particle energy $x \equiv E/E_{jet}$ [111] [112]. They select gluon jets as gluon hemispheres opposite to collinear quark and antiquark hemispheres in three jet $b\bar{b}$ events. uds jets are taken from two jet uds events. The measured ratio of the average

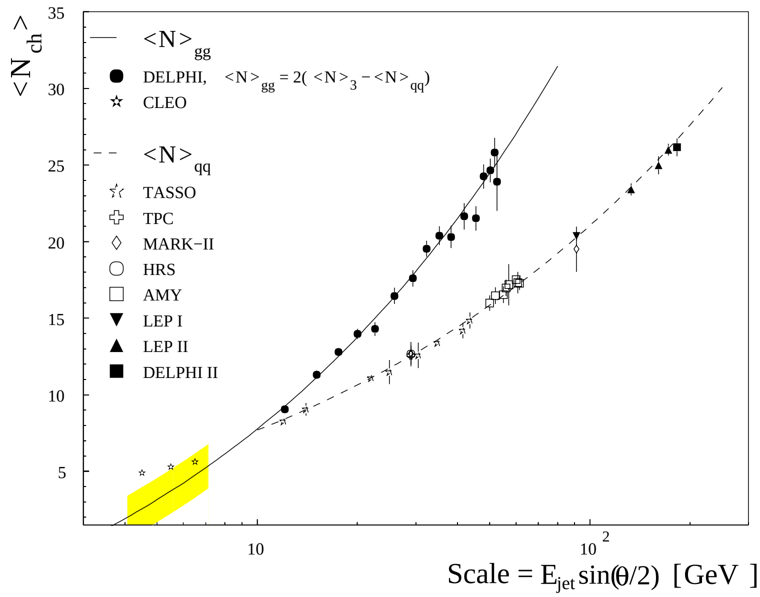

Figure 6.19: Charged particle multiplicity for $q\bar{q}$ and gg pairs as function of energy for several experiments.

multiplicity between gluon and uds quark jets is [112]

$$r_{ch} \equiv \frac{< n_{ch} >_{g}^{41.8GeV}}{< n_{ch} >_{uds-hemi}^{45.6GeV}} = 1.509 \pm 0.022(stat.) \pm 0.046(syst.) \tag{6.11}$$

Theoretical calculations have also improved by including higher orders in perturbative QCD [113], [114]. Theoretical predictions of the momentum and flavor dependent ratio of multiplicities in gluon jets and in uds quark jets are in the range $r_{theory} = 1.6 - 1.8$. These new theoretical values have come closer to the experimental value.

DELPHI has compared the gluon and quark fragmentation functions as a function of a jet energy-like variable $\kappa = E_{jet} \sin\frac{\theta}{2}$ [115],[116],[117]. E_{jet} is the energy of a jet and θ is the angle between this jet and the closest other jet in the event. The two lower energy jets in three jet events without a b quark tag are selected to represent quark jets. When one of the two lower energy jets is tagged as a heavy quark jet in a three jet event, then the other lower energy jet is anti-tagged as a gluon jet. The gluon and quark fragmentation functions are parameterized in order to determine the ratio of the color factor of quarks to the color factor of gluons. The slopes of jet multiplicities in gluon and quark jets as a function of κ are compared in Fig. 6.19 [118]. In Fig. 6.19, the data points from many other experiments are included. The figure shows that the average multiplicities in quark jets and in gluon jets are the same at ~ 10 GeV, and above this energy, the average multiplicity in gluon jets increases faster than in quark jets. The lines in the figure are fits to the multiplicities in quark jets and in gluon jets, and the ratio of the fits is approximately $r_0 = C_A/C_F = 9/4$.

OPAL has considered only soft particles with large transverse momenta relative to the jet axis because soft particle multiplicities are insensitive to higher order corrections and to the effects of energy conservation [119]. Therefore by selecting only these particles, most of the kinematic effects are removed. Assuming Local Parton Hadron Duality (LPHD), the ratio of soft multiplicity in gluon jets to that in quark jets is a direct measurement of the color charge ratio. The measured value is consistent with the expected ratio [120]. These results exhibit differences between gluon and quark jets, and confirm an important element of the structure of QCD, namely the color octet of non-abelian gauge bosons.

It is interesting to check whether differences between gluon and quark jets are the same for all hadron species. The differences in hadron production between gluon and quark jets are expected to be independent of hadron species since QCD effects in gluon and quark jets are the same. However, differences in production at high energy might be expected due to leading particle production. Because most of the leading particles are expected to have high energy (Sect. 6.3) and gluon jets contain no leading particles, the ratio of particle production in gluon and quark jets can be affected by leading particle effects. In addition, differences in the production rates for different hadron types in quark and gluon jets are predicted by some of the fragmentation models [121]. The comparison of the hadron type dependence of particle production in quark and gluon jets is in progress for both charged and neutral hadrons. OPAL has studied the production of charged hadrons $\pi^{\pm}$, $K^{\pm}$ and $p/\bar{p}$ [122], and neutral hadrons, π^0, η, K_s and Λ^0 [123, 124]. ALEPH has studied the production of $\pi^{\pm}$, $K^{\pm}$ and $p/\bar{p}$ [110], and π^0, η, $\eta'(958)$, K_s and Λ^0 [125]. DELPHI has measured the relative rates for $\pi^{\pm}$, $K^{\pm}$ and $p/\bar{p}$ [126]. L3 has studied η [127], K_s and Λ^0 [128].

DELPHI and OPAL have seen that the enhancement of proton production in gluon jets is greater than the enhancement averaged over all charged particle types. L3 and ALEPH have observed a similar enhancement in the production of η mesons, but OPAL has observed that the production enhancement in gluon jets is independent of whether the particles are π^0, η, or K_sḢowever, the interpretation of the measurements is inconclusive due to limited statistics, a small energy coverage, and biases from gluon and quark jet selection.

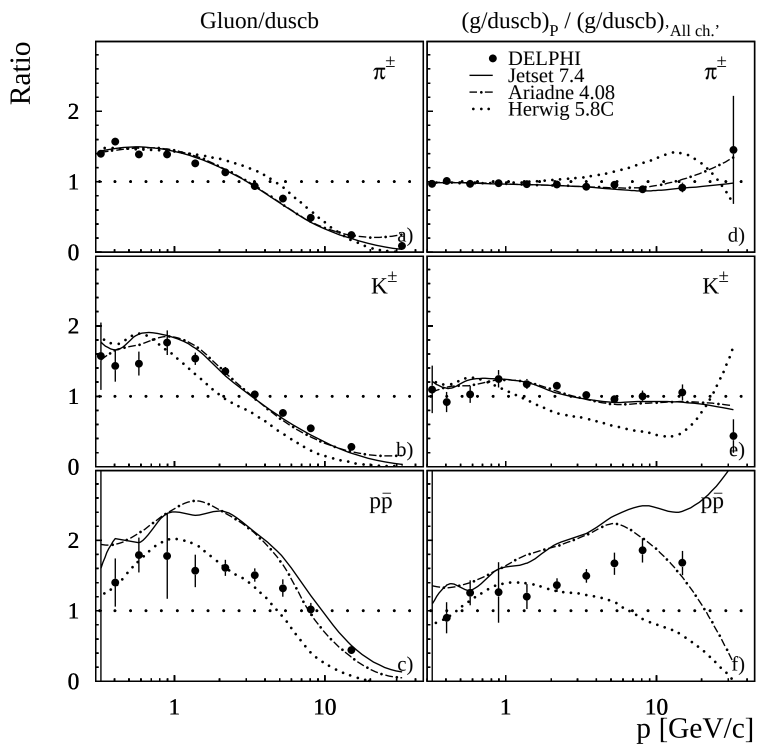

Figure 6.20: (a)–(c) The ratios of (a) $\pi^{\pm}$ (b) $K^{\pm}$, and (c) $p/\bar{p}$ in gluon to those in quark jets. (d)–(f) those ratios normalized to the ratio of multiplicities in gluon and quark jets.

The best measurement comparing charged particle production rates so far is from DELPHI [126]. DELPHI has used geometrically symmetric three jet events including all quark types. Fig. 6.20 shows the gluon jet and flavor inclusive quark jet comparison from DELPHI. In Fig. 6.20, plots (a)–(c) are the ratios of the numbers of (a) $\pi^{\pm}$ (b) $K^{\pm}$, and (c) $p/\bar{p}$ in gluon jets to the numbers found in quark ($udscb$) jets. Plots (d)–(f) are the same ratios normalized to the charged particle production ratio averaged over the distribution of all particle types. This measurement indicates a sustantial enhancement in the proton production fractions in gluon jets. Fig. 6.20 also shows that the predictions of several different fragmentation models are inconsistent with the data, and with each other. In principle, the data can discriminate among the models, but since the data do not agree with any predictions from the models, the measurement cannot be easily interpreted to give information on actual differences between gluon and quark hadronization. This type of measurement can in principle be improved by rejecting heavy flavor jets in order to remove many $K^{\pm}$ and $\pi^{\pm}$ originating from D and B hadron decays.

6.4.2 Quark and gluon jet comparison

As described in Chapter 4.3, four different jet samples: pure g jets as well as $uds-$, $c-$ and $b-$jet mixtures, are selected using vertices and N_{sig} in the three jets in three-jet events.

The inclusive properties of gluon and quark jets are compared using the four selected jet samples. As expected, differences between the gluon tagged jets and the $uds-$jet mixture sample are confirmed. Fig. 6.21 shows the average number of charged hadrons in the two jet samples. The multiplicity of charged hadrons in the gluon tagged jets is observed to be higher than in the $uds-$jet mixture.

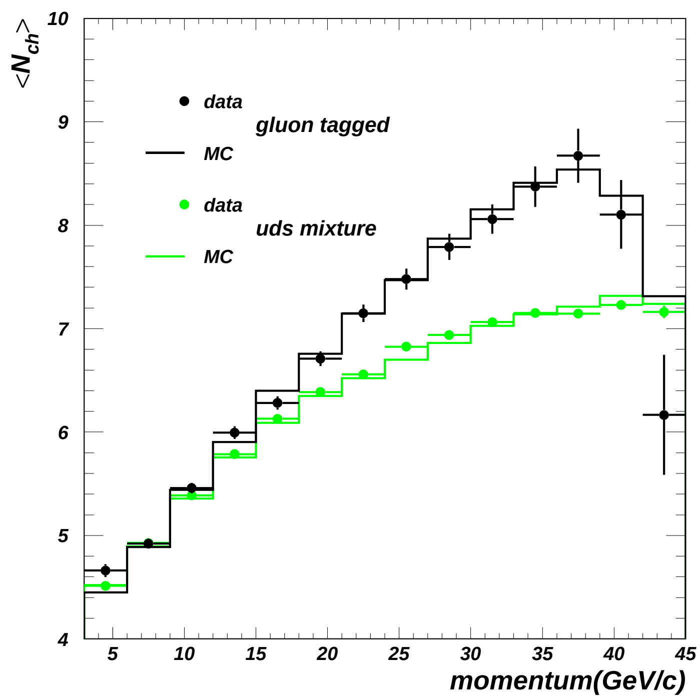

Figure 6.21: Average multiplicities of charged hadrons in the gluon tagged jet and in the $uds-$jet mixture samples.

The hadron fractions analysis is performed on all four jet samples without corrections for leptons and late decays of Λ^0's.

Once the charged hadron fractions analysis is repeated, the hadron fractions measured in gluon tagged jets and in the $uds-$jet mixture are corrected using leptonic fractions estimated from the MC. Fig. 6.22 compares the measured charged hadron fractions for hadronic Z^0 decays as a function of momentum in the gluon tagged jet and $uds-$jet mixture samples.

Due to the scarceness of tracks in the gluon jets at high momentum ($p > 15$ GeV/c) the measured hadron fractions cover only the range $1 < p \leq 15$ GeV/c. Furthermore, the bin size used for this analysis is larger than the bin size used for the other analyses presented in this thesis. The systematic errors shown in the plots are from particle identification as described in the hadron fraction analysis. For the gluon tagged jets, the statistical errors are comparable to the systematic errors for the π fraction. The statistical errors are dominant for the kaon and proton fractions. The measured hadron fractions in the gluon tagged jet sample and in the $uds-$jet mixture sample along with their statistical and systematic errors are listed in Tables B.10–B.12 in Appendix B. Fig. 6.22 shows the sums of the three measured hadron fractions for the gluon tagged jet and for the $uds-$jet mixture samples. The sum of the hadron fractions for both jet samples is consistent with unity within the errors throughout the entire momentum range. The sum for the gluon tagged jet sample is higher by $\sim$1% on average, thus limiting any differences between particle identification in the gluon tagged jets and that in general hadronic events to this level. This systematic error is much smaller than the statistical error. The features of the hadron fractions in the gluon tagged jet sample and those in the $uds-$jet mixture sample are qualitatively the same as the features of the flavor inclusive and flavor dependent event hadron fractions. The π fraction in the $uds-$jet mixture is higher than the π fraction in the gluon tagged jet sample throughout the entire momentum range. Correspondingly, the K and p fractions in the $uds-$jet mixture are lower than those in the gluon tagged jet sample.

The uncorrected charged hadron fractions for the $c-$ and $b-$jet mixtures, and the SLD MC predictions for the hadron fractions are shown in Fig. 6.23. The SLD MC describes the hadron fractions for both mixture samples very well.

In order to see the difference between the gluon tagged jet and the $uds-$jet mixture samples explicitly for each of the hadron species $h = \{\pi^{\pm},\ K^{\pm},\ \mathrm{p}\bar{\mathrm{p}}\}$, the ratios $r^h_f = f^h_{g-tag}/f^h_{uds-mix}$ of each hadron fraction in the gluon tagged jets f^h_{g-tag} to the fraction in

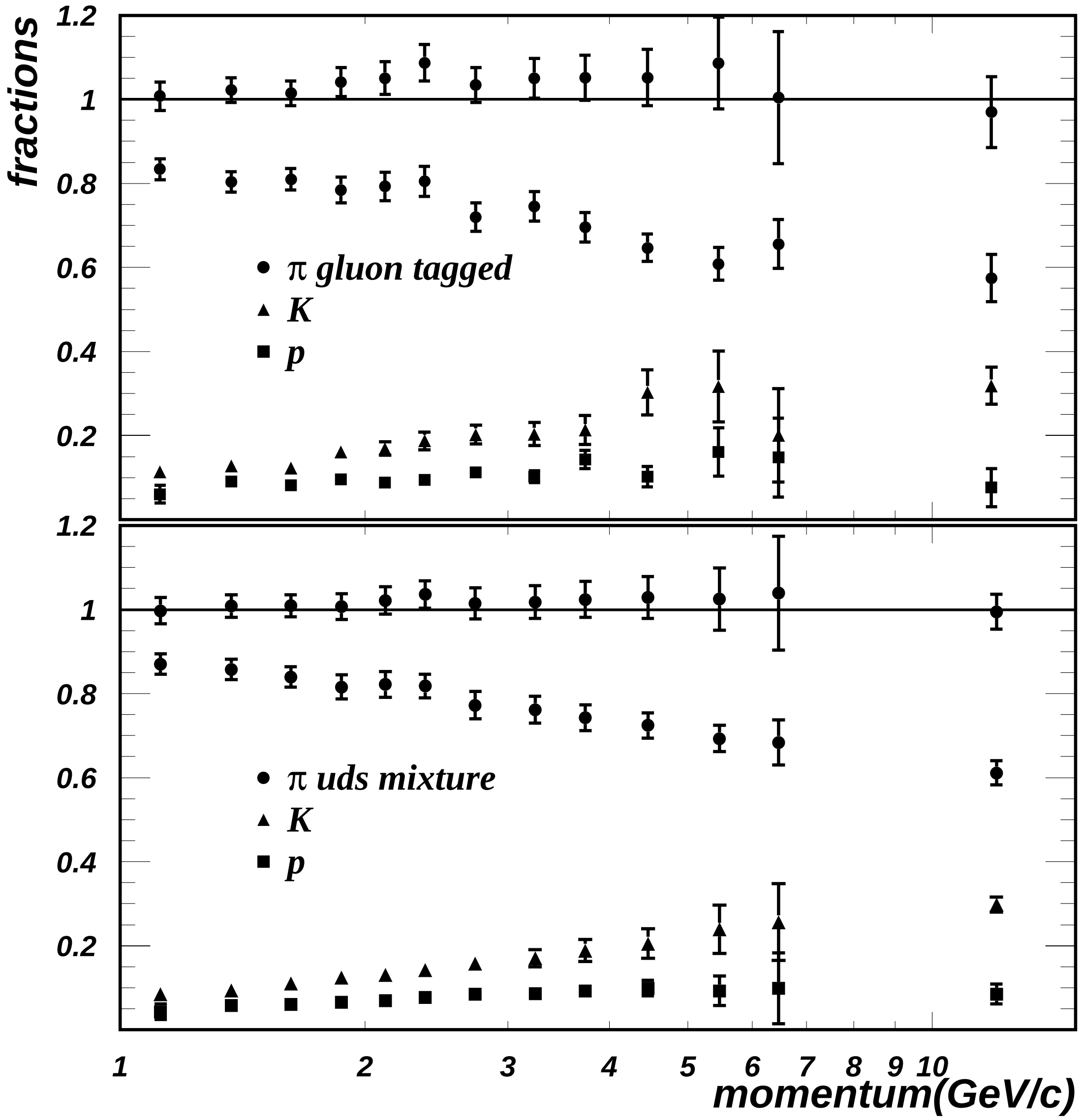

Figure 6.22: Measured charged hadron fractions for hadronic Z^0 decays for the gluon tagged jet sample and the $uds-$jet mixture sample. The error bars include both the statistical errors and the systematic errors.

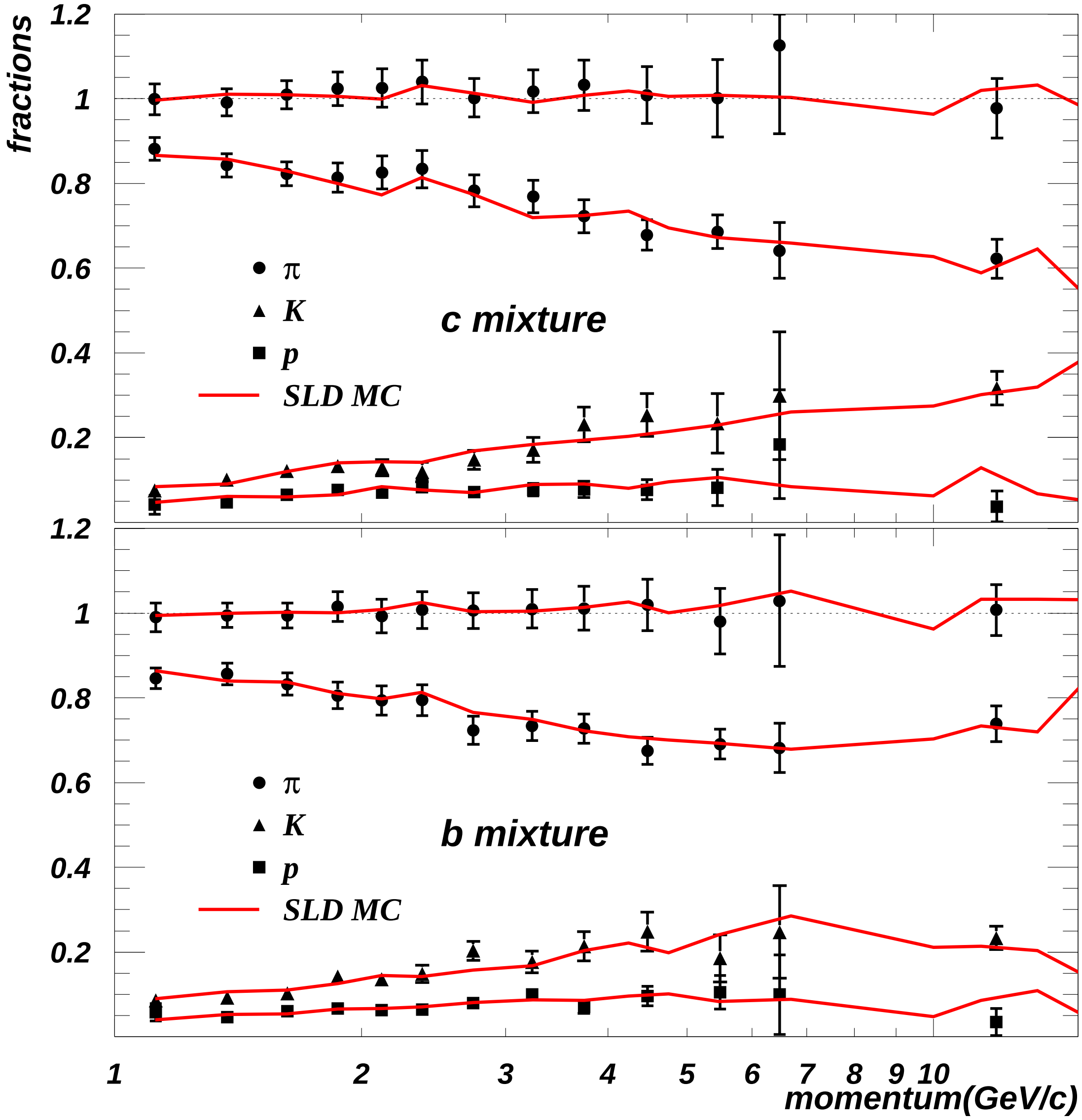

Figure 6.23: Measured charged hadron fractions for hadronic Z^0 decays for the $c-$jet mixture sample and the $b-$jet mixture sample. Leptons are included in the π catagory. The error bars include both the statistical errors and the systematic errors.

the $uds-$jet mixture sample $f^h_{uds-mix}$ are determined. The ratios r^h_f for $\pi^\pm$, $K^\pm$ and $\mathrm{p}\bar{\mathrm{p}}$ are shown in Fig. 6.24.

Since most of the common systematic errors coming from particle identification cancel in these ratios, only the statistical errors are shown for the data fractions. The statistical errors for the MC fractions are smaller by a factor of ∼2 than those for the data fractions in any momentum region. The ratios for the data and the SLD MC as a function of momentum and their errors are summarized in Tables B.13–B.15 in Appendix B. These ratios deviate significantly from unity. r^π_f is lower than unity and correspondingly, r^K_f and r^{p}_f are visibly higher than unity. These deviations of the relative ratios are qualitatively similar to the deviations of the relative ratios seen in the DELPHI measurement for $1 < p < 15$ GeV/c. The average values of the relative ratios of the hadron fractions over the momentum region $1 < p < 15$ GeV/c are determined and listed in Table 6.2

Average ratio of fractions in gluon and light quark jets		
	data	MC
$< r^\pi_f >$	0.9452±0.0089(stat.)±0.0012(syst.)	0.9549±0.0045(stat.)
$< r^K_f >$	1.2307±0.0375(stat.)±0.0066(syst.)	1.1554±0.0185(stat.)
$< r^{\mathrm{p}}_f >$	1.3478±0.0747(stat.)±0.0460syst.)	1.3195±0.0302(stat.)

Table 6.2: The average ratios of the hadron fractions in the gluon tagged jets to the hadron fractions in the $uds-$jet mixture sample in data and in the SLD MC.

The average value of the relative ratio of the K fractions from SLD is higher than unity, whereas the average values of the relative ratios of the K fractions from three other experiments DELPHI [126], OPAL [129],ARGUS [130] are lower than unity. The difference in the relative K fractions might be due to K's from heavy hadron decays in heavy quark jets that the other experiments include in their quark jet samples. Also the gluon jet selection and the momentum coverage for the fractions are different for different experiments. Therefore, it is difficult to directly compare the results from SLD and the results from other experiments.

The MC simulation reproduces the features of the SLD measured ratios. Therefore,

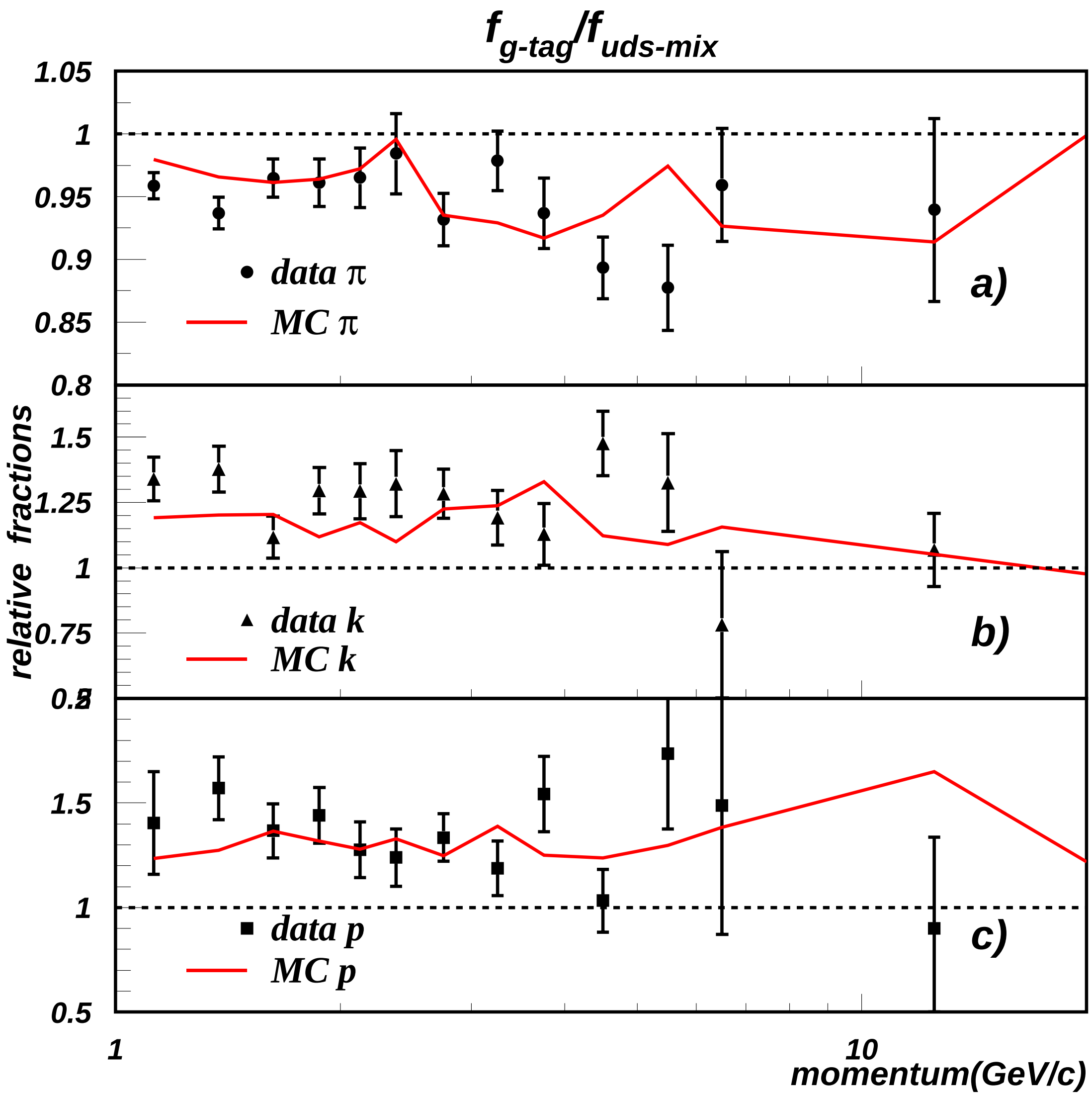

Figure 6.24: Measured relative ratios of charged hadron fractions in the gluon tagged jet sample to those in the $uds-$jet mixture sample along with the predictions of the SLD simulation. The error bars for the data fractions represent only the statistical errors. The statistical errors for the MC fractions are not shown but they are smaller than half of the statistical errors for the data fractions in any momentum region.

the deviations are considered to be consistent with those caused by kinematic effects or jet tagging biases. For example, the two different jet samples have different jet energy distributions and different particle tagging biases coming from the jet selection cuts used to create the samples. The average values of the relative ratios of the hadron fractions from the SLD MC are also summarized in Table 6.2. The ratios of the average values $< r_f^h >$ in the data to those in the SLD MC are

$$\begin{aligned}
\frac{< r_f^{\pi} >_{data}}{< r_f^{\pi} >_{MC}} &= 0.9898 \pm 0.0105 \\
\frac{< r_f^{K} >_{data}}{< r_f^{K} >_{MC}} &= 1.0652 \pm 0.0371 \\
\frac{< r_f^{\mathrm{p}} >_{data}}{< r_f^{\mathrm{p}} >_{MC}} &= 1.0214 \pm 0.0705
\end{aligned}$$

These ratios show that the average values of $< r_f^h >$ for the SLD MC are consistent with the average values of $< r_f^h >$ for the data within the errors. We conclude that the relative production rates of $\pi^{\pm}$, $K^{\pm}$ and $\mathrm{p}\bar{\mathrm{p}}$ are the same within our uncertainties of a few percent.

The light quark and gluon analysis can be improved in the future by correcting for the heavy quark background rates in the jet samples.

Chapter 7

Conclusions

New detailed studies of the production of the charged hadrons $\pi^{\pm}$, $K^{\pm}$, p/$\bar{\text{p}}$ have been made over a broad momentum range using approximately 223,000 hadronic Z^0 decays collected by the SLD in 1997–1998.

The charged hadron production fractions in flavor-inclusive (*udscb*) events have been measured using particle identified track samples. The excellent particle identification is achieved by using the SLD Cherenkov Ring Imaging Detector (CRID) and the SLD Central Drift Chamber (CDC).

The results of the flavor inclusive fraction analysis are consistent with previous SLD results [69] which used data from a different run period (93–95) and sets of tighter CRID track selection cuts. The precision of this result is improved by a factor of $\sim$4 in statistics. For the previous result, the statistical errors are comparable to the systematic errors for the π and p fractions, and are almost twice as big as the systematic errors for the K fraction. However, for our new result, the systematic error is dominant for all hadron fractions.

A feature of the hadron fractions (Fig. 6.4) is that the measured π fraction is dominant at low momentum, and decreases with increasing momentum. The K fraction begins at less than 0.1 and steadily increases as momentum increases, and eventually becomes comparable with the π fraction at high momentum. The p fraction increases as momentum increases up to 0.1 at $p \sim 20$ Gev/c and then the fraction starts to decrease slowly. These features are also seen by three LEP experiments at the Z^0 pole. One of the LEP experiments also has a Ring Imaging detector (DELPHI). These four measurements are consistent with one another, and are complimentary in their momentum coverage and systematic errors, making these fractions a very precisely measured feature of hadronic Z^0 decays.

The fragmentation models JETSET, HERWIG and UCLA which are tuned to the data of experiments at lower E_{CM} describe the hadron fractions qualitatively well as shown in Fig.6.6 but there are still discrepancies in the fractions for each particle type. Generally, the predictions for the π fraction from all models are higher than the measured π fraction for $5 < p < 10$ GeV/c and the predictions for the K fraction from the models are lower than the measured K fraction for $p > 5$ GeV/c. The p fractions from the models are inconsistent with the data in any momentum region, and are different from each other at high momentum. The JETSET model overestimates the π fraction for $2 < p < 10$ GeV/c and overestimates the p fraction throughout the entire momentum range. The UCLA model also overestimates the π fraction for $2 < p < 10$ GeV/c and overestimates the p fraction at high momentum. The HERWIG model describes the data very well except for the p fraction at high momentum. The SLD MC simulation is a version of JETSET with several parameters tuned to improve agreement with LEP and SLC data. The p fraction from the SLD MC simulation is much closer to the measured p fraction for $10 < p < 15$ GeV/c than any other models, including JETSET. The SLD MC simulation describes the momentum dependence of the p fraction very well. However, the SLD MC simulation overestimates π fraction for $p > 4$ GeV/c and underestimates the K fraction for $p > 10$ GeV/c.

High purity light (uds), c and b quark event samples are selected by using topological vertex finding and by counting tracks with significant impact parameter. The precise position measurement of tracks by using the SLD VXD3 provides highly efficient and pure event flavor tagging. Charged hadron production rates are measured independently in light, c and b quark events. The general features of the hadron fractions in flavor separated events (Fig. 6.11) are similar at low momentum. At intermediate momentum, c and b flavor events have enhanced K fractions. At high momentum, b flavor events have a reduced K fraction and the p fraction decreases almost zero for $p > 15$ GeV/c

DELPHI is the only other experiment to perform the flavor dependent analysis and they have studied only uds and b flavor events. The SLD results of the hadron fractions in uds flavor events are consistent with the result of DELPHI measurement, while the hadron fractions in b events from the two experiments show differences in the p fractions at high momentum.

The light quark events provide a more suitable test of hadronization models, as they are based on massless quarks. The features of the hadron fractions in light quark events that are not described well by the hadronization models are the same features described above for flavor inclusive events as shown in Fig. 6.13. Some of these features are more pronounced in light quark events. For example, the structure of the p fraction at high momentum. This similarity of the features of the hadron fractions in flavor inclusive events and in light quark events indicates that these deficiencies of the models are in the simulation of the hadronization process and not simply artfacts of the modeling of heavy hadron decays.

Differences in the hadron fractions between light quark and heavy (c,b) quark events are observed. The main difference is in the K fractions which are higher in heavy quark events than light quark events because many K's coming from B hadron decays are concentrated in the $2 < p < 10$ GeV/c region and similarly many Ks from D hadron decays populate in the $4 < p < 20$ GeV/c region. By comparing the hadron production rates as a function of scaled hadron momentum $x_p \equiv 2p/E_{cm}$ in heavy quark events and in light quark events as shown in Fig. 6.14, heavy (B and D) hadron production and decay modeling problems can be isolated. The π production rate at low x_p is higher in heavy quark events than in light quark events because many π's coming from heavy hadron decays are concentrated in low momentum region. Since heavy hadrons carry most of the energy of initial quarks in events, leaving little phase space to produce high momentum hadrons, the hadron production rates in light quark are higher at high x_p than in heavy quark events. The JETSET and UCLA models describe qualitatively well the features of the ratios of the hadron production rates in heavy quark events to those in light quark events. However, the prediction from the HERWIG model are inconsistent with the measurement, and imply that the HERWIG model has additional model discrepancies in heavy hadron decays.

A unique study of light leading particles containing an initial quark or antiquark has been performed by exploiting a large electroweak forward-backward production asymmetry which is allowed by the highly polarized SLC electron beam Heavy (D,B) hadrons are almost all leading particles and have been studied in detail. However, little is known about the leading particles in u, d and s quark jets since these quarks are much lighter and indistinguishable from one another. By separating quark jets from antiquark jets in light flavor (uds) event sample, hadrons containing the initial quarks and their antihadrons are compared.

The difference in production rates between hadrons and antihadrons normalized with the sum of the hadron and antihadron production rates as shown in Fig. 6.17 is not only a variable to see the leading particle effects explicitly but also a very good way to test the fragmentation models. Significant excesses of p over $\bar{\text{p}}$ production rates and excess of Λ's over their antibaryon production rates in light quark jets for scaled particle momentum range $x_p > 0.2$ have been observed. These baryon excesses at high x_p are direct evidence of leading particle effects. There are many more high momentum K^-'s than K^+'s in light quark jets. This K^- excess result is good evidence of leading particle effects and also indicates that high momentum K's are mainly produced in $s\bar{s}$ quark events. The JETSET model and the SLD MC simulation describe the scaled momentum x_p distributions of the normalized difference in production rates between hadrons and antihadrons in light quark jets qualitatively very well. The UCLA model also describes the normalized difference well except for p and Λ distributions at high x_p. The prediction of the HERWIG model is inconsistent with the data for p's and Λ's throughout the entire x_p region.

A pure gluon jet sample, and a mixture sample of light quark and gluon jets have been selected from three jet events again using topological vertex finding. By comparing these two jet samples, the hypothesis that the relative production of different hadron species in gluon and light quark jets are the same has been tested. Differences in charged hadron multiplicity and momentum spectrum predicted by perturbative QCD have been observed by several experiments (OPAL, DELPHI, ALEPH), and been confirmed by our measurement. Also, differences in identified pions, kaons and protons have been observed. By comparing π, K and p fractions in gluon and light quark jets, hadron species dependence of these differences can be studied. The results of the gluon tagged jet and $uds-$jet mixture comparison, Fig. 6.24, show deviations from unity of each hadron fraction. However, the deviation features are reproduced by the SLD MC simulation, in which no difference in quark and gluon jets is predicted. This indicates that the deviation features come from jet tagging biases. We conclude that, within context of the SLD MC simulation, differences between gluon jets and light quark jets are hadron species independent at the level of $\sim$0.06 of the hadron fractions in any momentum region.

The data and SLD MC ratios averaged over $1 < p < 15$ GeV/c are consistent with each other, and can limit any overall deviations from equality to $\pm 2\%$ for $\pi^{\pm}$, $\pm 8\%$ for $K^{\pm}$ and $\pm 18\%$ for p/$\bar{\text{p}}$ at the 95% confidence level.

The result of relative hadron fractions in gluon and light quark jets is more precise than any other previous measurements. The best measurement so far for $\pi^{\pm}$, $\text{K}^{\pm}$, p/$\bar{\text{p}}$ fractions are from DELPHI. The measurement from DELPHI with a precision comparable to our measurement is highly model dependent due to inclusion of c and b quark jets in their quark jet sample.

Appendix A

Electroweak Asymmetries

In order to extract the coupling asymmetry parameters A_f, several asymmetries have been measured. These asymmetries can be represented with ratios of cross-sections which do not depend on the details of detector efficiencies and absolute luminosity measurements.

A.1 The Left-Right Asymmetry A_{LR}

An asymmetry can be measured at the SLD by exploiting the polarized electron beam is the Left-Right Asymmetry, A_{LR}. The longitudinal polarization of the electron beams allows to measure the parity violating asymmetry at the Z^0 pole.

$$A_{LR} = \frac{\sigma(e^+e^-_L \to Z^0 \to f\bar{f}) - \sigma(e^+e^-_R \to Z^0 \to f\bar{f})}{\sigma(e^+e^-_L \to Z^0 \to f\bar{f}) + \sigma(e^+e^-_R \to Z^0 \to f\bar{f})}. \tag{A.1}$$

where L and R refer to left-handed (negative) and right-handed (positive) incident electron beam polarization respevtively. This asymmetry is defined as a normalized difference of cross sections to cancel systematic uncertainties. This quantity depends on vector (v_e) and axial-vector (a_e) couplings of the Z^0 bosons to the electrons as from the SM prediction.

$$A_{LR} = A_e = \frac{2v_e a_e}{v_e^2 + a_e^2} = \frac{2[1 - 4\sin^2\theta_W^{eff}(M_Z^2)]}{1 + [1 - 4\sin^2\theta_W^{eff}(M_Z^2)]}. \tag{A.2}$$

A_{LR} is a sensitive function of the effective Weinberg angle $\sin^2\theta_W^{eff}(M_Z^2)$ and depends on virtual electroweak radiation corrections. A_{LR} is a convenient asymmetry to measure experimentally since is no dependence on the final state fermion couplings and flavor identification or angular distribution. The definition of A_{LR} using the electron beam polarization,P_e is

$$A_{LR}^{meas} = \frac{\sigma_L - \sigma_R}{\sigma_L + \sigma_R} = |P_e| A_e \tag{A.3}$$

where σ_L and σ_R are the $e^+e^0 \rightarrow Z^0$ production cross section at the Z^0 pole with a left- or right-handed electron beam, respectively. These cross sections are integrated over the detector acceptance. The final state electrons are excluded due to their t-channel scattering contaminations. From A_{LR} measurement, $\sin^2\theta_W^{eff}(M_Z^2)$ can be isolated. The latest SLD result of the average Weinberg angle [131] is

$$sin^2\theta_W^{eff}(M_Z^2) \quad = \quad 0.23102 \pm 0.00031, \tag{A.4}$$

A.2 The Forward-Backward Asymmetries A_{FB}^f and $\tilde{A}_{FB}^f$

The Forward-Backward Asymmetry A_{FB}^f is formed using both the initial state coupling to electrons, A_e and the final state couplings to fermions f, A_f as well as P_e. A_{FB}^f is defined using the sign of $\cos\theta_f$, where θ_f is the polar angle of the outgoing fermion to the electron beam direction.

$$A_{FB}^f(x) = \frac{\sigma^f(x>0) - \sigma^f(x<0)}{\sigma^f(x>0) + \sigma^f(x<0)} = 2A_f \frac{A_e - P_e}{1 - A_e P_e} \frac{x}{1+x^2} \tag{A.5}$$

where $x = \cos\theta_f$ and σ^f is the cross section in the forward $(x > 0)$ or backward $(x < 0)$ hemispheres.

This asymmetry can be measured at both SLC and LEP since is can be formed for an unpolarized beam. For the $P_e = 0$ case (LEP), A_{FB}^f integrated over $\cos\theta$ is simply

$$A_{FB}^f = \frac{3}{4} A_e A_f \tag{A.6}$$

The initial- and final-state asymmetries cannot be individually extracted from this asymmetry.

With the known polarization of electron beams, the left-right-forward-backward asymmetry $\tilde{A}_{FB}^f$ is formed with inclusion of the beam polarization sign and the sign of $\cos\theta_f$.

$\tilde{A}^f_{FB}$ is defined as

$$\tilde{A}^f_{FB}(x) = \frac{[\sigma^f_L(x>0) - \sigma^f_R(x>0)] - [\sigma^f_L(x<0) - \sigma^f_R(x<0)]}{[\sigma^f_L(x>0) + \sigma^f_R(x>0)] + [\sigma^f_L(x<0) + \sigma^f_R(x<0)]} = 2|P_e|A_f \frac{x}{1+x^2} \quad \text{(A.7)}$$

where L and R refer to left-handed and right-handed electron beams and $x = \cos\theta_f$. Unlike A^f_{FB}, this quantity allows to isolate the final state coupling of the Z^0 boson A_f independently from the value of A_e.

Since the beam polarization $|P_e| \approx 74\%$ at SLC is much larger than $A_e \approx 0.15$, this asymmetry is significantely larger compared to $A^f_{FB}(P_e = 0)$.

Appendix B

Tables of Charged Hadron Fractions

	Hadron Fractions: Liquid Analysis		
p range	f_π	f_K	f_{p}
0.35–0.45	0.9629±0.0035±0.0136	–	–
0.45–0.55	0.9245±0.0036±0.0065	–	–
0.55–0.65	0.9208±0.0034±0.0063	–	–
0.65–0.75	0.9062±0.0036±0.0064	–	–
0.75–1.00	0.8857±0.0022±0.0062	0.0674±0.0014±0.0016	0.0289±0.0047±0.0131
1.00–1.25	0.8646±0.0012±0.0107	0.0818±0.0008±0.0078	0.0449±0.0012±0.0095
1.25–1.50	0.8492±0.0013±0.0108	0.0891±0.0009±0.0064	0.0559±0.0009±0.0087
1.50–1.75	0.8358±0.0015±0.0113	0.0993±0.0010±0.0066	0.0570±0.0008±0.0066
1.75–2.00	0.8148±0.0019±0.0194	0.1122±0.0012±0.0075	0.0601±0.0009±0.0066
2.00–2.25	0.8080±0.0024±0.0207	0.1165±0.0014±0.0036	0.0608±0.0009±0.0071
2.25–2.50	0.7966±0.0031±0.0170	0.1243±0.0017±0.0201	0.0630±0.0010±0.0082
	Hadron Fractions: Combined Analysis		
p range	f_π	f_K	f_{p}
2.50–2.75	0.8056±0.0026±0.0351	0.1270±0.0019±0.0150	0.0689±0.0012±0.0070
2.75–3.00	0.7721±0.0025±0.0102	0.1443±0.0021±0.0141	0.0680±0.0013±0.0070
3.00–3.25	0.7763±0.0027±0.0136	0.1502±0.0023±0.0178	0.0695±0.0014±0.0077
3.25–3.50	0.7649±0.0028±0.0124	0.1611±0.0026±0.0206	0.0716±0.0015±0.0085
3.50–3.75	0.7558±0.0029±0.0116	0.1739±0.0029±0.0237	0.0672±0.0017±0.0093
3.75–4.00	0.7500±0.0031±0.0114	0.1760±0.0032±0.0260	0.0727±0.0019±0.0109
4.00–4.50	0.7356±0.0023±0.0112	0.1818±0.0026±0.0238	0.0741±0.0016±0.0134
4.50–5.00	0.7253±0.0025±0.0116	0.1917±0.0033±0.0288	0.0742±0.0020±0.0127
5.00–5.50	0.7081±0.0028±0.0133	0.2000±0.0042±0.0308	0.0766±0.0027±0.0127
5.50–6.50	0.7124±0.0023±0.0388	0.2057±0.0043±0.0359	0.0727±0.0028±0.0178
6.50–7.50	0.7019±0.0026±0.0539	0.2029±0.0077±0.0426	0.0713±0.0052±0.0246

Table B.1: Measured hadron fractions for the liquid and combined analyses. The second term in each column is statistical errors, and the third term in each column is systematic errors from particl identification. The systematic errors are completely positively correlated between all momentum bins in a given analysis.

	Hadron Fractions: Gas Analysis		
p range	f_π	f_K	f_p
2.50–3.00	0.7670±0.0031±0.0737	–	–
3.00–3.50	0.7542±0.0024±0.0173	–	–
3.50–4.00	0.7452±0.0025±0.0117	–	–
4.00–4.50	0.7243±0.0027±0.0094	–	–
4.50–5.00	0.7120±0.0030±0.0085	–	–
5.00–5.50	0.6998±0.0032±0.0088	–	–
5.50–6.00	0.6944±0.0035±0.0090	–	–
6.00–6.50	0.6839±0.0038±0.0100	–	–
6.50–7.00	0.6788±0.0042±0.0108	–	–
7.00–7.50	0.6709±0.0045±0.0119	–	–
7.50–8.50	0.6573±0.0035±0.0127	–	–
8.50–9.50	0.6331±0.0040±0.0121	–	–
9.50–10.50	0.6251±0.0046±0.0124	0.2008±0.0043±0.0261	
10.50–11.50	0.6290±0.0050±0.0137	0.2703±0.0048±0.0145	0.0841±0.0042±0.0143
11.50–12.50	0.6170±0.0058±0.0142	0.2840±0.0054±0.0114	0.0829±0.0045±0.0146
12.50–13.50	0.6054±0.0064±0.0141	0.2937±0.0059±0.0114	0.0810±0.0048±0.0138
13.50–14.50	0.5967±0.0071±0.0148	0.2907±0.0064±0.0113	0.0818±0.0051±0.0131
14.50–16.00	0.5744±0.0068±0.0162	0.3048±0.0061±0.0121	0.0930±0.0048±0.0128
16.00–17.50	0.5670±0.0082±0.0192	0.3071±0.0072±0.0131	0.0954±0.0054±0.0128
17.50–19.00	0.5391±0.0099±0.0201	0.3380±0.0087±0.0150	0.1043±0.0055±0.0092
19.00–20.50	0.5487±0.0123±0.0229	0.3331±0.0105±0.0166	0.0987±0.0062±0.0102
20.50–22.00	0.5041±0.0126±0.0366	0.3555±0.0108±0.0267	0.0973±0.0057±0.0164
22.00–24.00	0.4871±0.0140±0.0418	0.3576±0.0118±0.0304	0.0925±0.0056±0.0180
24.00–26.00	0.4891±0.0197±0.0528	0.3753±0.0168±0.0403	0.0977±0.0067±0.0214
26.00–30.00	0.5154±0.0222±0.0799	0.3842±0.0190±0.0631	0.0604±0.0055±0.0299
30.00–35.00	0.5536±0.0461±0.1086	0.4046±0.0450±0.0741	0.0668±0.0087±0.0230
35.00–45.00	–	–	0.0328±0.0273±0.0231

Table B.2: Measured hadron fractions for the gas analysis. The second term in each column is statistical errors, and the third term in each column is systematic errors from particl identification. The systematic errors are completely positively correlated between all momentum bins in a given analysis.

p	Pion Fraction in $Z^0 \to$ $u\bar{u}$, $d\bar{d}$, $s\bar{s}$	$c\bar{c}$	$b\bar{b}$
0.35–0.45	0.9771±0.0061±0.0005	0.9830±0.0250±0.0012	0.9645±0.0086±0.0007
0.45–0.55	0.9335±0.0058±0.0011	0.9490±0.0260±0.0018	0.9415±0.0079±0.0009
0.55–0.65	0.9318±0.0063±0.0011	0.8994±0.0239±0.0027	0.9434±0.0092±0.0010
0.65–0.75	0.9089±0.0062±0.0012	0.9374±0.0258±0.0027	0.9043±0.0085±0.0013
0.75–1.00	0.8983±0.0051±0.0012	0.8902±0.0192±0.0020	0.9159±0.0061±0.0010
1.00–1.25	0.8720±0.0027±0.0014	0.8683±0.0062±0.0016	0.8877±0.0031±0.0008
1.25–1.50	0.8545±0.0021±0.0015	0.8633±0.0050±0.0022	0.8632±0.0027±0.0009
1.50–1.75	0.8480±0.0022±0.0014	0.8500±0.0053±0.0022	0.8536±0.0027±0.0016
1.75–2.00	0.8314±0.0025±0.0015	0.8275±0.0059±0.0025	0.8272±0.0032±0.0011
2.00–2.25	0.8247±0.0029±0.0014	0.8239±0.0069±0.0026	0.8207±0.0038±0.0011
2.25–2.50	0.8207±0.0034±0.0013	0.8177±0.0082±0.0023	0.8149±0.0045±0.0010
2.50–3.00	0.8040±0.0027±0.0013	0.7946±0.0064±0.0023	0.7905±0.0035±0.0010
3.00–3.50	0.7890±0.0031±0.0013	0.7862±0.0077±0.0036	0.7686±0.0041±0.0010
3.50–4.00	0.7735±0.0037±0.0010	0.7703±0.0092±0.0035	0.7371±0.0049±0.0010
4.00–4.50	0.7705±0.0044±0.0008	0.7235±0.0107±0.0030	0.7295±0.0060±0.0010
4.50–5.00	0.7484±0.0043±0.0006	0.6775±0.0104±0.0025	0.6757±0.0059±0.0013
5.00–6.00	0.7287±0.0034±0.0005	0.6782±0.0081±0.0020	0.6584±0.0048±0.0015
6.00–7.50	0.7170±0.0033±0.0021	0.6446±0.0076±0.0025	0.6235±0.0050±0.0020
7.50–8.50	0.6941±0.0047±0.0005	0.6003±0.0110±0.0031	0.5955±0.0076±0.0025
8.50–9.50	0.6604±0.0051±0.0005	0.5586±0.0124±0.0034	0.5624±0.0089±0.0030
9.50–10.50	0.7077±0.0848±0.0007	0.6274±0.1378±0.0057	0.6551±0.0903±0.0029
10.50–12.50	0.6581±0.0054±0.0008	0.5972±0.0143±0.0043	0.6171±0.0110±0.0036
12.50–14.50	0.6413±0.0062±0.0008	0.5087±0.0176±0.0067	0.6572±0.0138±0.0044
14.50–17.50	0.6088±0.0063±0.0011	0.4764±0.0192±0.0064	0.6605±0.0163±0.0060
17.50–21.50	0.5668±0.0074±0.0013	0.4561±0.0268±0.0064	0.6662±0.0222±0.0075
21.50–27.50	0.5099±0.0096±0.0005	0.4837±0.0367±0.0059	0.6952±0.0369±0.0092
27.50–35.00	0.5384±0.0261±0.0012	0.6887±0.1445±0.0299	0.9555±0.0875±0.0053

Table B.3: Pion fractions in events of different flavors. The first error is statistical, the second is the unfolding systematic. The relative systematic uncertainty given in tables B.1–B.2 is common to all flavors.

p	Kaon Fraction in $Z^0 \rightarrow$ $u\bar{u}$, $d\bar{d}$, $s\bar{s}$	$c\bar{c}$	$b\bar{b}$
0.35–0.45	0.0229±0.0061±0.0005	0.0170±0.0250±0.0012	0.0355±0.0086±0.0007
0.45–0.55	0.0665±0.0058±0.0011	0.0510±0.0260±0.0018	0.0585±0.0079±0.0009
0.55–0.65	0.0682±0.0063±0.0011	0.1006±0.0239±0.0027	0.0566±0.0092±0.0010
0.65–0.75	0.0911±0.0062±0.0012	0.0626±0.0258±0.0027	0.0957±0.0085±0.0013
0.75–1.00	0.0737±0.0035±0.0009	0.0577±0.0135±0.0016	0.0667±0.0043±0.0008
1.00–1.25	0.0806±0.0015±0.0008	0.0856±0.0035±0.0007	0.0773±0.0018±0.0005
1.25–1.50	0.0869±0.0016±0.0007	0.0899±0.0037±0.0006	0.0855±0.0020±0.0005
1.50–1.75	0.0943±0.0018±0.0007	0.0909±0.0042±0.0009	0.1014±0.0023±0.0011
1.75–2.00	0.1076±0.0021±0.0008	0.1039±0.0050±0.0013	0.1198±0.0027±0.0006
2.00–2.25	0.1135±0.0025±0.0007	0.1123±0.0060±0.0013	0.1262±0.0034±0.0007
2.25–2.50	0.1088±0.0030±0.0006	0.1276±0.0074±0.0010	0.1358±0.0041±0.0006
2.50–3.00	0.1214±0.0024±0.0006	0.1300±0.0058±0.0008	0.1557±0.0033±0.0006
3.00–3.50	0.1344±0.0028±0.0006	0.1482±0.0070±0.0020	0.1755±0.0038±0.0007
3.50–4.00	0.1490±0.0034±0.0005	0.1653±0.0084±0.0020	0.2118±0.0046±0.0009
4.00–4.50	0.1505±0.0041±0.0005	0.2016±0.0098±0.0025	0.2146±0.0056±0.0009
4.50–5.00	0.1638±0.0049±0.0004	0.1992±0.0124±0.0021	0.2443±0.0069±0.0011
5.00–6.00	0.1697±0.0049±0.0004	0.2220±0.0117±0.0022	0.2460±0.0069±0.0012
6.00–7.50	0.1923±0.0077±0.0015	0.2285±0.0186±0.0019	0.2555±0.0117±0.0015
9.50–10.50	0.1841±0.0229±0.0003	0.2288±0.0524±0.0030	0.2124±0.0313±0.0021
10.50–12.50	0.2588±0.0047±0.0005	0.3084±0.0121±0.0040	0.3159±0.0097±0.0032
12.50–14.50	0.2761±0.0055±0.0004	0.3616±0.0161±0.0057	0.2844±0.0121±0.0037
14.50–17.50	0.2780±0.0057±0.0004	0.4302±0.0186±0.0093	0.3132±0.0148±0.0055
17.50–21.50	0.3253±0.0071±0.0006	0.4545±0.0263±0.0103	0.3074±0.0209±0.0069
21.50–27.50	0.3777±0.0095±0.0006	0.4611±0.0360±0.0097	0.2806±0.0352±0.0083
27.50–35.00	0.4195±0.0261±0.0012	0.2047±0.1451±0.0372	0.0466±0.0821±0.0039

Table B.4: Pion fractions in events of different flavors. The first error is statistical, the second is the unfolding systematic. The relative systematic uncertainty given in tables B.1–B.2 is common to all flavors.

p	Proton Fraction in $Z^0 \rightarrow$ $u\bar{u}$, $d\bar{d}$, $s\bar{s}$	$c\bar{c}$	$b\bar{b}$
0.75–1.00	0.0280±0.0041±0.0004	0.0521±0.0153±0.0019	0.0174±0.0048±0.0004
1.00–1.25	0.0474±0.0025±0.0007	0.0461±0.0058±0.0013	0.0350±0.0028±0.0003
1.25–1.50	0.0586±0.0017±0.0009	0.0469±0.0039±0.0019	0.0513±0.0021±0.0004
1.50–1.75	0.0577±0.0016±0.0008	0.0591±0.0037±0.0014	0.0450±0.0018±0.0006
1.75–2.00	0.0609±0.0017±0.0008	0.0687±0.0041±0.0014	0.0530±0.0020±0.0008
2.00–2.25	0.0618±0.0019±0.0008	0.0638±0.0045±0.0015	0.0531±0.0023±0.0008
2.25–2.50	0.0704±0.0020±0.0008	0.0547±0.0048±0.0024	0.0493±0.0023±0.0007
2.50–3.00	0.0747±0.0017±0.0008	0.0754±0.0041±0.0019	0.0538±0.0019±0.0007
3.00–3.50	0.0766±0.0019±0.0008	0.0656±0.0048±0.0026	0.0559±0.0024±0.0008
3.50–4.00	0.0775±0.0023±0.0006	0.0644±0.0059±0.0028	0.0511±0.0029±0.0008
4.00–4.50	0.0789±0.0029±0.0005	0.0749±0.0074±0.0026	0.0558±0.0037±0.0009
4.50–5.00	0.0780±0.0036±0.0004	0.0711±0.0096±0.0027	0.0566±0.0048±0.0009
5.00–6.00	0.0761±0.0037±0.0003	0.0764±0.0097±0.0026	0.0610±0.0053±0.0010
6.00–7.50	0.0677±0.0060±0.0006	0.0718±0.0167±0.0026	0.0626±0.0096±0.0010
10.50–12.50	0.0831±0.0047±0.0004	0.0944±0.0146±0.0050	0.0669±0.0097±0.0009
12.50–14.50	0.0827±0.0052±0.0005	0.1297±0.0185±0.0077	0.0583±0.0114±0.0009
14.50–17.50	0.1132±0.0053±0.0009	0.0935±0.0195±0.0075	0.0263±0.0118±0.0006
17.50–21.50	0.1079±0.0052±0.0008	0.0895±0.0217±0.0072	0.0265±0.0125±0.0008
21.50–27.50	0.1124±0.0053±0.0003	0.0552±0.0215±0.0077	0.0242±0.0170±0.0009
27.50–35.00	0.0421±0.0076±0.0001	0.1066±0.0609±0.0098	-0.0022±0.0312±0.0020

Table B.5: Pion fractions in events of different flavors. The first error is statistical, the second is the unfolding systematic. The relative systematic uncertainty given in tables B.1–B.2 is common to all flavors.

Fraction of Tracks in uds Quark Jets		
p	Positive Pions	Negative Pions
1.00–1.25	0.4354±0.0042±0.0020	0.4384±0.0042±0.0020
1.25–1.50	0.4298±0.0043±0.0019	0.4260±0.0043±0.0020
1.50–1.75	0.4154±0.0048±0.0018	0.4241±0.0048±0.0019
1.75–2.00	0.4070±0.0055±0.0017	0.4127±0.0055±0.0018
2.00–2.25	0.4101±0.0065±0.0018	0.4033±0.0065±0.0018
2.25–2.50	0.4064±0.0079±0.0018	0.4030±0.0078±0.0019
2.50–3.00	0.3917±0.0052±0.0019	0.4041±0.0053±0.0021
3.00–3.50	0.3960±0.0057±0.0021	0.3763±0.0057±0.0021
3.50–4.00	0.3579±0.0063±0.0021	0.3915±0.0064±0.0023
4.00–4.50	0.3748±0.0073±0.0020	0.3746±0.0073±0.0021
4.50–5.00	0.3774±0.0084±0.0021	0.3699±0.0084±0.0022
5.00–6.00	0.3690±0.0075±0.0022	0.3850±0.0077±0.0024
6.00–7.50	0.3647±0.0105±0.0023	0.3585±0.0104±0.0024
7.50–8.50	0.3454±0.0086±0.0025	0.3202±0.0086±0.0025
8.50–9.50	0.3146±0.0095±0.0023	0.3306±0.0095±0.0026
9.50–10.50	0.3811±0.0121±0.0032	0.3866±0.0122±0.0034
10.50–12.50	0.3179±0.0096±0.0026	0.3444±0.0098±0.0029
12.50–14.50	0.2935±0.0113±0.0029	0.3546±0.0118±0.0034
14.50–17.50	0.2862±0.0120±0.0033	0.3281±0.0124±0.0038
17.50–21.50	0.2710±0.0139±0.0026	0.2811±0.0141±0.0030
21.50–27.50	0.2396±0.0190±0.0037	0.2843±0.0196±0.0046
27.50–35.00	0.2148±0.0458±0.0043	0.3326±0.0495±0.0050

Table B.6: Measured positive and negative pion fractions in light quark (u, d and s) jets. The first error is statistical, the second is the total systematic due to uncertainties in the heavy-flavor backgrounds and quark-tag purity.

Fraction of Tracks in uds Quark Jets		
p	Positive Kaons	Negative Kaons
1.00–1.25	0.0441±0.0021±0.0003	0.0393±0.0021±0.0002
1.25–1.50	0.0446±0.0024±0.0003	0.0458±0.0024±0.0002
1.50–1.75	0.0517±0.0027±0.0003	0.0540±0.0027±0.0003
1.75–2.00	0.0554±0.0032±0.0004	0.0628±0.0032±0.0004
2.00–2.25	0.0633±0.0039±0.0004	0.0623±0.0039±0.0004
2.25–2.50	0.0560±0.0046±0.0005	0.0667±0.0047±0.0005
2.50–3.00	0.0627±0.0037±0.0005	0.0633±0.0037±0.0003
3.00–3.50	0.0691±0.0044±0.0007	0.0837±0.0044±0.0007
3.50–4.00	0.0928±0.0054±0.0009	0.0818±0.0054±0.0006
4.00–4.50	0.0843±0.0065±0.0008	0.0945±0.0066±0.0007
4.50–5.00	0.0857±0.0081±0.0009	0.1001±0.0082±0.0008
5.00–6.00	0.0962±0.0082±0.0009	0.0982±0.0082±0.0006
6.00–7.50	0.0907±0.0133±0.0015	0.1322±0.0135±0.0015
9.50–10.50	0.0598±0.0112±0.0036	0.1725±0.0117±0.0034
10.50–12.50	0.0944±0.0078±0.0022	0.1596±0.0083±0.0022
12.50–14.50	0.1090±0.0095±0.0023	0.1725±0.0101±0.0023
14.50–17.50	0.0830±0.0100±0.0045	0.2230±0.0109±0.0043
17.50–21.50	0.1168±0.0121±0.0034	0.2191±0.0128±0.0034
21.50–27.50	0.0768±0.0164±0.0076	0.3160±0.0189±0.0069
27.50–35.00	0.1559±0.0432±0.0031	0.2356±0.0464±0.0039

Table B.7: Measured positive and negative kaon fractions in light quark (u, d and s) jets. The first error is statistical, the second is the total systematic due to uncertainties in the heavy-flavor backgrounds and quark-tag purity.

Fraction of Tracks in uds Quark Jets		
p	Positive Protons	Negative Protons
1.00–1.25	0.0169±0.0031±0.0002	0.0214±0.0031±0.0002
1.25–1.50	0.0222±0.0022±0.0002	0.0269±0.0022±0.0003
1.50–1.75	0.0302±0.0022±0.0003	0.0274±0.0022±0.0002
1.75–2.00	0.0329±0.0025±0.0003	0.0310±0.0025±0.0003
2.00–2.25	0.0353±0.0027±0.0003	0.0305±0.0027±0.0003
2.25–2.50	0.0400±0.0030±0.0004	0.0339±0.0030±0.0003
2.50–3.00	0.0400±0.0026±0.0004	0.0391±0.0026±0.0004
3.00–3.50	0.0423±0.0030±0.0004	0.0374±0.0029±0.0004
3.50–4.00	0.0374±0.0035±0.0003	0.0380±0.0035±0.0003
4.00–4.50	0.0457±0.0045±0.0006	0.0359±0.0045±0.0004
4.50–5.00	0.0456±0.0057±0.0006	0.0335±0.0056±0.0005
5.00–6.00	0.0484±0.0059±0.0009	0.0258±0.0057±0.0008
6.00–7.50	0.0455±0.0101±0.0008	0.0269±0.0101±0.0007
10.50–12.50	0.0744±0.0077±0.0014	0.0419±0.0077±0.0012
12.50–14.50	0.0820±0.0087±0.0018	0.0352±0.0085±0.0016
14.50–17.50	0.1160±0.0092±0.0028	0.0399±0.0088±0.0025
17.50–21.50	0.0796±0.0084±0.0013	0.0560±0.0083±0.0011
21.50–27.50	0.1185±0.0098±0.0031	0.0416±0.0085±0.0026
27.50–35.00	0.0349±0.0112±0.0003	0.0305±0.0121±0.0003

Table B.8: Measured proton and antiproton fractions in light quark (u, d and s) jets. The first error is statistical, the second is the total systematic due to uncertainties in the heavy-flavor backgrounds and quark-tag purity.

Normalized Production Differences			
p	D_{π^-}	D_{K^-}	D_{p}
1.00–1.25	0.004±0.010±0.000	-0.058±0.047±0.004	-0.117±0.151±0.008
1.25–1.50	-0.004±0.011±0.001	0.013±0.049±0.001	-0.096±0.084±0.007
1.50–1.75	0.010±0.013±0.001	0.022±0.048±0.002	0.049±0.071±0.003
1.75–2.00	0.007±0.015±0.001	0.062±0.051±0.004	0.029±0.072±0.002
2.00–2.25	-0.008±0.018±0.001	-0.008±0.059±0.001	0.072±0.076±0.005
2.25–2.50	-0.004±0.022±0.001	0.087±0.072±0.006	0.083±0.075±0.006
2.50–3.00	0.015±0.014±0.001	0.004±0.057±0.002	0.011±0.061±0.001
3.00–3.50	-0.025±0.016±0.002	0.095±0.056±0.007	0.061±0.069±0.004
3.50–4.00	0.045±0.018±0.003	-0.063±0.060±0.005	-0.008±0.088±0.001
4.00–4.50	0.000±0.019±0.001	0.057±0.072±0.004	0.120±0.104±0.008
4.50–5.00	-0.010±0.021±0.001	0.078±0.086±0.006	0.153±0.134±0.010
5.00–6.00	0.021±0.017±0.002	0.010±0.084±0.003	0.305±0.148±0.021
6.00–7.50	-0.009±0.017±0.001	0.186±0.121±0.013	0.257±0.264±0.017
7.50–8.50	-0.038±0.027±0.003	–	–
8.50–9.50	0.025±0.031±0.002	–	–
9.50–10.50	0.007±0.033±0.001	0.485±0.098±0.033	–
10.50–12.50	0.040±0.029±0.003	0.257±0.062±0.017	0.279±0.127±0.019
12.50–14.50	0.094±0.036±0.007	0.226±0.069±0.015	0.399±0.141±0.027
14.50–17.50	0.068±0.041±0.005	0.458±0.067±0.031	0.488±0.111±0.033
17.50–21.50	0.018±0.053±0.002	0.305±0.074±0.021	0.174±0.117±0.012
21.50–27.50	0.085±0.079±0.006	0.609±0.088±0.041	0.481±0.105±0.032
27.50–35.00	0.215±0.184±0.015	0.202±0.233±0.014	0.060±0.328±0.004

Table B.9: Normalized difference D_{π^-}, D_{K^-} and D_{p} in light quark jets. The first error is statistical, the second is the total systematic due to uncertainties in the heavy-flavor backgrounds and quark-tag purity.

The pion fractions in gluons and light quarks		
p range	$f_\pi \pm$ stat. $\pm$ syst. in gluons	$f_\pi \pm$ stat. $\pm$ syst. in light quarks
1.00–1.25	0.8341±0.0085±0.0234	0.8701±0.0035±0.0242
1.25–1.50	0.8038±0.0101±0.0225	0.8579±0.0039±0.0240
1.50–1.75	0.8098±0.0119±0.0230	0.8393±0.0046±0.0240
1.75–2.00	0.7843±0.0143±0.0268	0.8160±0.0057±0.0280
2.00–2.25	0.7930±0.0182±0.0285	0.8217±0.0072±0.0296
2.25–2.50	0.8051±0.0244±0.0264	0.8180±0.0095±0.0267
2.50–3.00	0.7197±0.0153±0.0300	0.7723±0.0056±0.0320
3.00–3.50	0.7453±0.0170±0.0310	0.7616±0.0061±0.0314
3.50–4.00	0.6957±0.0198±0.0287	0.7426±0.0067±0.0301
4.00–5.00	0.6469±0.0171±0.0280	0.7241±0.0055±0.0294
5.00–6.00	0.6084±0.0228±0.0313	0.6934±0.0068±0.0306
6.00–7.00	0.6559±0.0298±0.0500	0.6837±0.0083±0.0528
10.00–15.00	0.5746±0.0439±0.0346	0.6116±0.0082±0.0280
15.00–25.00	–	0.5257±0.0152±0.0288

Table B.10: Measured pion fractions in the gluon tagged jet sample and in the $uds-$jet mixture sample. The first error is statistical, and the second error is systematic from particl identification.

The kaon fractions in gluons and light quarks		
p range	$f_K \pm$ stat. $\pm$ syst. in gluons	$f_K \pm$ stat. $\pm$ syst. in light quarks
1.00–1.25	0.1131±0.0062±0.0085	0.0844±0.0024±0.0076
1.25–1.50	0.1281±0.0073±0.0064	0.0930±0.0026±0.0063
1.50–1.75	0.1230±0.0081±0.0066	0.1101±0.0031±0.0066
1.75–2.00	0.1615±0.0101±0.0081	0.1247±0.0037±0.0076
2.00–2.25	0.1690±0.0124±0.0097	0.1307±0.0045±0.0093
2.25–2.50	0.1872±0.0162±0.0129	0.1416±0.0057±0.0126
2.50–3.00	0.2023±0.0136±0.0171	0.1577±0.0046±0.0153
3.00–3.50	0.2034±0.0165±0.0220	0.1706±0.0056±0.0198
3.50–4.00	0.2129±0.0209±0.0277	0.1887±0.0070±0.0257
4.00–5.00	0.3028±0.0233±0.0481	0.2052±0.0068±0.0348
5.00–6.00	0.3168±0.0421±0.0738	0.2389±0.0117±0.0563
6.00–7.00	0.2003±0.0699±0.0864	0.2564±0.0213±0.0889
10.00–15.00	0.3186±0.0408±0.0173	0.2984±0.0078±0.0159
15.00–25.00	–	0.3600±0.0137±0.0203

Table B.11: Measured kaon fractions in the gluon tagged jet sample and in the $uds-$jet mixture sample. The first error is statistical, and the second error is systematic from particl identification.

The proton fractions in gluons and light quarks		
p range	$f_p\pm$ stat.$\pm$ syst. in gluons	$f_p\pm$ stat.$\pm$ syst. in light quarks
1.00–1.25	0.0604±0.0093±0.0185	0.0430±0.0036±0.0184
1.25–1.50	0.0902±0.0076±0.0087	0.0574±0.0026±0.0085
1.50–1.75	0.0820±0.0070±0.0065	0.0600±0.0025±0.0064
1.75–2.00	0.0953±0.0079±0.0067	0.0661±0.0027±0.0065
2.00–2.25	0.0883±0.0084±0.0072	0.0692±0.0030±0.0072
2.25–2.50	0.0949±0.0096±0.0086	0.0766±0.0034±0.0085
2.50–3.00	0.1124±0.0088±0.0080	0.0842±0.0029±0.0072
3.00–3.50	0.1018±0.0104±0.0095	0.0857±0.0035±0.0087
3.50–4.00	0.1433±0.0152±0.0153	0.0929±0.0045±0.0115
4.00–5.00	0.1021±0.0141±0.0203	0.0989±0.0045±0.0178
5.00–6.00	0.1609±0.0307±0.0482	0.0927±0.0077±0.0344
6.00–7.00	0.1475±0.0572±0.0753	0.0991±0.0146±0.0829
10.00–15.00	0.0764±0.0366±0.0266	0.0849±0.0071±0.0226
15.00–25.00	–	0.0932±0.0088±0.0134

Table B.12: Measured proton fractions in the gluon tagged jet sample and in the $uds-$jet mixture sample. The first error is statistical, and the second error is systematic from particl identification.

The relative ratio of the pion fractions		
p range	data $r_{f_\pi} \pm$ stat.$\pm$ syst.	MC $r_{f_K} \pm$ stat.
1.00–1.25	0.9586±0.0105±0.0002	0.9795±0.0047
1.25–1.50	0.9369±0.0125±0.0000	0.9657±0.0055
1.50–1.75	0.9649±0.0151±0.0002	0.9613±0.0066
1.75–2.00	0.9612±0.0188±0.0001	0.9641±0.0081
2.00–2.25	0.9651±0.0237±0.0001	0.9723±0.0106
2.25–2.50	0.9842±0.0319±0.0001	0.9956±0.0145
2.50–3.00	0.9319±0.0209±0.0002	0.9351±0.0095
3.00–3.50	0.9786±0.0237±0.0004	0.9293±0.0106
3.50–4.00	0.9368±0.0280±0.0007	0.9168±0.0121
4.00–5.00	0.8934±0.0246±0.0024	0.9354±0.0142
5.00–6.00	0.8774±0.0340±0.0064	0.9745±0.0165
6.00–7.00	0.9593±0.0451±0.0010	0.9263±0.0149
10.00–15.00	0.9395±0.0729±0.0136	0.9140±0.0176
15.00–25.00	–	0.9988±0.0470

Table B.13: The ratio of the measured pion fraction in the gluon tagged jet sample to that in the $uds-$jet mixture sample. The first error is statistical, and the second error is systematic from particl identification.

The relative ratio of the kaon fractions		
p range	data $r_{f_\pi} \pm$ stat.$\pm$ syst.	MC $r_{f_K} \pm$ stat.
1.00–1.25	1.3400±0.0828±0.0200	1.1917±0.0355
1.25–1.50	1.3774±0.0874±0.0245	1.2012±0.0355
1.50–1.75	1.1172±0.0800±0.0070	1.2039±0.0370
1.75–2.00	1.2951±0.0896±0.0140	1.1186±0.0381
2.00–2.25	1.2930±0.1048±0.0178	1.1730±0.0457
2.25–2.50	1.3220±0.1262±0.0265	1.1000±0.0547
2.50–3.00	1.2828±0.0940±0.0160	1.2256±0.0435
3.00–3.50	1.1923±0.1043±0.0094	1.2365±0.0475
3.50–4.00	1.1282±0.1184±0.0069	1.3296±0.0577
4.00–5.00	1.4756±0.1236±0.0158	1.1230±0.0637
5.00–6.00	1.3261±0.1878±0.0036	1.0889±0.0825
6.00–7.00	0.7812±0.2802±0.0661	1.1552±0.0845
10.00–15.00	1.0677±0.1395±0.0011	1.0524±0.1415
15.00–25.00	–	0.9758±0.1072

Table B.14: The ratio of the measured kaon fraction in the gluon tagged jet sample to that in the $uds-$jet mixture sample. The first error is statistical, and the second error is systematic from particl identification.

The relative ratio of the proton fractions		
p range	data $r_{f_\pi} \pm$ stat. $\pm$ syst.	MC $r_{f_K} \pm$ stat.
1.00–1.25	1.4047±0.2462±0.1788	1.2348±0.0901
1.25–1.50	1.5714±0.1503±0.0906	1.2734±0.0564
1.50–1.75	1.3667±0.1298±0.0435	1.3647±0.0537
1.75–2.00	1.4418±0.1332±0.0499	1.3188±0.0527
2.00–2.25	1.2760±0.1334±0.0287	1.2799±0.0559
2.25–2.50	1.2389±0.1369±0.0315	1.3289±0.0608
2.50–3.00	1.3349±0.1142±0.0504	1.2470±0.0462
3.00–3.50	1.1879±0.1307±0.0484	1.3900±0.0569
3.50–4.00	1.5425±0.1799±0.1277	1.2505±0.0643
4.00–5.00	1.0324±0.1501±0.0989	1.2370±0.0819
5.00–6.00	1.7357±0.3612±0.4552	1.2967±0.1076
6.00–7.00	1.4884±0.6174±0.2109	1.3822±0.1250
10.00–15.00	0.8999±0.4376±0.1674	1.6504±0.2456
15.00–25.00	–	1.2188±0.2258

Table B.15: The ratio of the measured proton fraction in the gluon tagged jet sample to that in the $uds-$jet mixture sample. The first error is statistical, and the second error is systematic from particl identification.

References

[1] H. Fritzsch, M. Gell-Mann, and H. Leutwyler, “ADVANTAGES OF THE COLOR OCTET GLUON PICTURE,” *Phys. Lett.* **B47** (1973) 365–368.

[2] H. D. Politzer, “RELIABLE PERTURBATIVE RESULTS FOR STRONG INTERACTIONS?,” *Phys. Rev. Lett.* **30** (1973) 1346–1349.

[3] D. J. Gross and F. Wilczek, “ULTRAVIOLET BEHAVIOR OF NONABELIAN GAUGE THEORIES,” *Phys. Rev. Lett.* **30** (1973) 1343–1346.

[4] T. Sjostrand, “High-energy physics event generation with PYTHIA 5.7 and JETSET 7.4,” *Comput. Phys. Commun.* **82** (1994) 74–90.

[5] G. Marchesini *et al.*, “HERWIG: A Monte Carlo event generator for simulating hadron emission reactions with interfering gluons. Version 5.1 - April 1991,” *Comput. Phys. Commun.* **67** (1992) 465–508.

[6] S. Chun and C. Buchanan, “A simple plausible path from QCD to successful prediction of $e^+e^- \to$ hadronization data,” *Phys. Rept.* **292** (1998) 239–317.

[7] **SLD** Collaboration, J.-c. Zhou, “Multiplicity moments in e^+e^- annihilation into hadrons at the Z0 resonance,”. Presented at 1994 Meeting of the American Physical Society, Division of Particles and Fields (DPF 94), Albuquerque, NM, 2-6 Aug 1994.

[8] **OPAL** Collaboration, R. Akers *et al.*, “Multiplicity and transverse momentum correlations in multi - hadronic final states in e^+e^- interactions at S**(1/2) = 91.2-GeV,” *Phys. Lett.* **B320** (1994) 417–430.

[9] **ALEPH** Collaboration, D. Decamp *et al.*, “Measurement of the charged particle multiplicity distribution in hadronic Z decays,” *Phys. Lett.* **B273** (1991) 181–192.

[10] **DELPHI** Collaboration, P. Abreu *et al.*, “Charged particle multiplicity distributions in Z0 hadronic decays,” *Z. Phys.* **C50** (1991) 185–194.

[11] **ALEPH** Collaboration, “Topology dependence of event properties in hadronic Z decays,”. Prepared for International Europhysics Conference on High- energy Physics (HEP 95), Brussels, Belgium, 27 Jul - 2 Aug 1995.

[12] **ALEPH** Collaboration, I. G. Knowles, “Evidence for topology dependence in three jet event multiplicities,”. Prepared for 12th International Workshop on High-energy Physics (HADRONS 96), Novy Svet, Ukraine, 9-16 Jun 1996.

[13] F. Halzen and A. D. Martin, *Quarks and Leptons: an introductory course in modern particle physics.* Wiley, 1984.

[14] S. L. Glashow, “PARTIAL SYMMETRIES OF WEAK INTERACTIONS,” *Nucl. Phys.* **22** (1961) 579–588.

[15] S. Weinberg, "A MODEL OF LEPTONS," *Phys. Rev. Lett.* **19** (1967) 1264–1266.

[16] A. Salam in *Elementary Particle Theory*, N. Svartholm, ed., p. 367. Almqvist and Wiksell, Stockholm, 1968.

[17] P. W. Higgs, "Broken symmetries, massless particles and gauge fields," *Phys. Lett.* **12** (1964) 132–133.

[18] P. W. Higgs, "BROKEN SYMMETRIES AND THE MASSES OF GAUGE BOSONS," *Phys. Rev. Lett.* **13** (1964) 508–509.

[19] P. Clarke, "An Introduction to cross-sections and asymmetries measurable using polarized beams in high-energy e^+e^- colliders," Tech. Rep. RAL-90-055, 1990.

[20] M. Luscher, S. Sint, R. Sommer, and P. Weisz, "Chiral symmetry and O(a) improvement in lattice QCD," *Nucl. Phys.* **B478** (1996) 365–400, `arXiv:hep-lat/9605038`.

[21] M. Luscher, S. Sint, R. Sommer, P. Weisz, and U. Wolff, "Non-perturbative O(a) improvement of lattice QCD," *Nucl. Phys.* **B491** (1997) 323–343, `arXiv:hep-lat/9609035`.

[22] J. R. Ellis, M. K. Gaillard, and G. G. Ross, "SEARCH FOR GLUONS IN e^+e^- ANNIHILATION," *Nucl. Phys.* **B111** (1976) 253.

[23] L. R. Surguladze and M. A. Samuel, "Total hadronic cross-section in e^+e^- annihilation at the four loop level of perturbative QCD," *Phys. Rev. Lett.* **66** (1991) 560–563.

[24] K. G. Chetyrkin, J. H. Kuhn, and A. Kwiatkowski, "QCD corrections to the e^+e^- cross-section and the Z boson decay rate: Concepts and results," *Phys. Rept.* **277** (1996) 189–281.

[25] A. Ali *et al.*, "QCD PREDICTIONS FOR FOUR JET FINAL STATES IN e^+e^- ANNIHILATION," *Nucl. Phys.* **B167** (1980) 454.

[26] K. J. F. Gaemers and J. A. M. Vermaseren, "FOUR JET EVENTS IN e^+e^- COLLISIONS AND THE NONABELIAN NATURE OF QCD," *Zeit. Phys.* **C7** (1980) 81.

[27] A. Signer and L. J. Dixon, "Electron positron annihilation into four jets at next-to-leading order in alpha(s)," *Phys. Rev. Lett.* **78** (1997) 811–814, `arXiv:hep-ph/9609460`.

[28] V. N. Gribov and L. N. Lipatov, "Deep inelastic e p scattering in perturbation theory," *Yad. Fiz.* **15** (1972) 781–807.

[29] V. N. Gribov and L. N. Lipatov, "e^+e^- pair annihilation and deep inelastic e p scattering in perturbation theory," *Yad. Fiz.* **15** (1972) 1218–1237.

[30] G. Altarelli and G. Parisi, "ASYMPTOTIC FREEDOM IN PARTON LANGUAGE," *Nucl. Phys.* **B126** (1977) 298.

[31] Y. L. Dokshitzer, V. A. Khoze, S. I. Troian, and A. H. Mueller, "QCD COHERENCE IN HIGH-ENERGY REACTIONS," *Rev. Mod. Phys.* **60** (1988) 373.

[32] K. Kato and T. Munehisa, "MONTE CARLO APPROACH TO QCD JETS IN THE NEXT-TO-LEADING LOGARITHMIC APPROXIMATION," *Phys. Rev.* **D36** (1987) 61.

[33] C. Peterson, D. Schlatter, I. Schmitt, and P. M. Zerwas, "SCALING VIOLATIONS IN INCLUSIVE e^+e^- ANNIHILATION SPECTRA," *Phys. Rev.* **D27** (1983) 105.

[34] D. Dong, "Measurement of the b quark fragmentation function in Z0 decays,". SLAC-R-550.

[35] "SLAC LINEAR COLLIDER CONCEPTUAL DESIGN REPORT," Tech. Rep. SLAC-R-229, 1980.

[36] **SLD and SLC** Collaboration, M. Breidenbach, "SLC and SLD: Experimental experience with a linear collider,". Presented at 2nd International Workshop on Physics and Experiments with Linear e^+e^- Colliders, Waikoloa, HI, 26- 30 Apr 1993.

[37] J. Seeman, "The Stanford Linear Collider," *Ann. Rev. Nucl. Part. Sci.* **41** (1990) 389.

[38] J. T. Seeman, "Status of the Stanford Linear Collider,". Talk given at ECFA Workshop on e^+e^- Linear Colliders (LC 92), Garmisch Partenkirchen, Germany, 25 Jul - 2 Aug 1992.

[39] T. Limberg, P. Emma, and R. Rossmanith, "The North Arc of the SLC as a spin rotator." Presented at 1993 Particle Accelerator Conference (PAC 93), Washington, DC, 17-20 May 1993.

[40] M. Woods, "The polarized electron beam for the SLAC Linear Collider," `arXiv:hep-ex/9611006`.

[41] **SLD** Collaboration, M. J. Fero, "The Compton polarimeter for SLC,". Presented at 10th International Symposium on High Energy Spin Physics (SPIN 92 - 35th Yamada Conference), Nagoya, Japan, 9-14 Nov 1992.

[42] A. Lath, "A Precise measurement of the left-right cross-section asymmetry in Z boson production,". SLAC-0454.

[43] **SLD** Collaboration, P. L. Reinertsen, "Precise measurement of the weak mixing angle from leptonic polarization asymmetries at the SLD experiment," *Nucl. Phys. Proc. Suppl.* **76** (1999) 45–54.

[44] J. Kent *et al.*, "PRECISION MEASUREMENTS OF THE SLC BEAM ENERGY,". Presented at IEEE Particle Accelerator Conf., Chicago, Ill., Mar 20-23, 1989.

[45] **SLD** Collaboration, "SLD DESIGN REPORT," Tech. Rep. SLAC-R-273, 1984.

[46] K. Abe *et al.*, "Design and performance of the SLD vertex detector, a 307 Mpixel tracking system," *Nucl. Instrum. Meth.* **A400** (1997) 287–343.

[47] A. S. Chou, "B decay charm counting via topological vertexing,". SLAC-R-578.

[48] M. D. Hildreth *et al.*, "Performance of the SLD central drift chamber," *IEEE Trans. Nucl. Sci.* **42** (1995) 451.

[49] M. J. Fero *et al.*, "Performance of the SLD central drift chamber," *Nucl. Instrum. Meth.* **A367** (1995) 111–114.

[50] D. C. Williams, "The Left-right forward - backward asymmetry for B quarks at the SLD,". SLAC-0445.

[51] M. D. Hildreth *et al.*, "Performance of the SLD central drift chamber," *IEEE Trans. Nucl. Sci.* **42** (1995) 451–458.

[52] **SLD** Collaboration, K. Abe *et al.*, "Measurements of R(b) with impact parameters and displaced vertices," *Phys. Rev.* **D53** (1996) 1023–1038.

[53] M. Cavalli-Sforza *et al.*, "CONSTRUCTION AND TESTING OF THE SLD CERENKOV RING IMAGING DETECTOR," *IEEE Trans. Nucl. Sci.* **37** (1990) 1132–1141.

[54] K. Abe *et al.*, "Performance of the CRID at SLD," *Nucl. Instrum. Meth.* **A343** (1994) 74–86.

[55] J. Seguinot and T. Ypsilantis, "A Historical survey of ring imaging Cerenkov counters," *Nucl. Instrum. Meth.* **A343** (1994) 1–29.

[56] **SLD-CRID** Collaboration, K. Abe *et al.*, "Production of 400 mirrors with high VUV reflectivity for use in the SLD Cerenkov ring imaging detector," *Nucl. Instrum. Meth.* **A300** (1991) 501–510.

[57] **SLD-CRID** Collaboration, H.Kawahara and J.Va'vra Tech. Rep. SLD CRID internal note 78, 1993.

[58] T. J. Pavel, "Measurement of charged hadron spectra at the Z0 with Cherenkov ring imaging,". SLAC-R-0491.

[59] K. Abe *et al.*, "Performance of the SLD barrel CRID during the 1992 physics data run," *IEEE Trans. Nucl. Sci.* **40** (1993) 589–592.

[60] H. Stangle, "Measurement of the Z0 $\rightarrow$ s anti-s coupling at the SLD,". SLAC-R-549.

[61] **SLD** Collaboration, K. Abe *et al.*, "The performance of the Barrel CRID at the SLD: Long-term operational experience," *IEEE Trans. Nucl. Sci.* **45** (1998) 648–656.

[62] **SLD** Collaboration, E. Vella, "SLD liquid argon calorimeter,". Presented at 3rd International Conference on Calorimetry in High Energy Physics (Note: dates changed from Oct 6-9), Corpus Christi, TX, 29 Sep - 2 Oct 1992.

[63] D. Axen *et al.*, "The Lead liquid argon sampling calorimeter of the SLD detector," *Nucl. Instrum. Meth.* **A328** (1993) 472–494.

[64] B. Andersson, G. Gustafson, G. Ingelman, and T. Sjostrand, “PARTON FRAGMENTATION AND STRING DYNAMICS,” *Phys. Rept.* **97** (1983) 31.

[65] **CLEO** Collaboration, “QQ - The CLEO Event Generator,” Tech. Rep. http://www.lns.cornell.edu/public/CLEO/soft/QQ.

[66] R. Brun, F. Bruyant, M. Maire, A. C. McPherson, and P. Zanarini, “GEANT: Detector description and simulation tool,” Tech. Rep. CERN-DD/EE/84-1, 1987.

[67] P. N. Burrows, H. Park, K. T. Pitts, and J. M. Yamartino, “Estimate of combined triggering and selection efficiency for hadronic events,” Tech. Rep. SLD Note 229, 1993.

[68] **SLD** Collaboration, K. Abe *et al.*, “Measurement of alpha-s (M(Z)**2) from hadronic event observables at the Z0 resonance,” *Phys. Rev.* **D51** (1995) 962–984, `hep-ex/9501003`.

[69] D. M. D. Aston and T. Pavel, “PRODUCTION OF π^+, π^-, K^+, K^-, p and $\bar{\mathbf{p}}$ IN HADRONIC Z^0 DECAYS,” Tech. Rep. SLD Physics Note 58, 1997.

[70] J. Neal, Homer Alfred, “Measurement of the gamma (Z0 $\rightarrow$ b b) / gamma (Z0 $\rightarrow$ hadrons) using the SLD,”. SLAC-R-0473.

[71] D. J. Jackson, “A topological vertex reconstruction algorithm for hadronic jets,” *Nucl. Instrum. Meth.* **A388** (1997) 247–253.

[72] T. R. Wright, *Parity Violation in Decays of Z Bosons into Heavy Quarks at SLD.* PhD thesis, University of Wisconsin, 2001.

[73] **JADE** Collaboration, W. Bartel *et al.*, “EXPERIMENTAL STUDIES ON MULTI - JET PRODUCTION IN e^+e^- ANNIHILATION AT PETRA ENERGIES,” *Z. Phys.* **C33** (1986) 23.

[74] **JADE** Collaboration, S. Bethke *et al.*, “EXPERIMENTAL INVESTIGATION OF THE ENERGY DEPENDENCE OF THE STRONG COUPLING STRENGTH,” *Phys. Lett.* **B213** (1988) 235.

[75] S. Catani, Y. L. Dokshitzer, M. Olsson, G. Turnock, and B. R. Webber, “New clustering algorithm for multi-jet cross-sections in e^+e^- annihilation,” *Phys. Lett.* **B269** (1991) 432–438.

[76] S. Bethke, Z. Kunszt, D. E. Soper, and W. J. Stirling, “New jet cluster algorithms: Next-to-leading order QCD and hadronization corrections,” *Nucl. Phys.* **B370** (1992) 310–334.

[77] **SLD** Collaboration, K. Abe *et al.*, “Production of pi+, K+, K0, K*0, Phi, p and Lambda0 in hadronic Z0 decays,” *Phys. Rev.* **D59** (1999) 052001, `hep-ex/9805029`.

[78] I. Baird, Kenneth G., “Strange particle production in hadronic Z0 decays,”. SLAC-R-0483.

[79] **ALEPH** Collaboration, D. Buskulic *et al.*, “Inclusive pi+-, K+- and (p, anti-p) differential cross- sections at the Z resonance,” *Z. Phys.* **C66** (1995) 355–366.

[80] **DELPHI** Collaboration, P. Abreu *et al.*, "Production characteristics of K0 and light meson resonances in hadronic decays of the Z0," *Z. Phys.* **C65** (1995) 587–602.

[81] **OPAL** Collaboration, R. Akers *et al.*, "Inclusive strange vector and tensor meson production in hadronic Z0 decays," *Z. Phys.* **C68** (1995) 1–12.

[82] P. Burrows and H. Masuda, "An Optimised QCD Parameter Set For The JETSET 7.4 Monte Carlo Program," Tech. Rep. SLD Physics Note 36, 1995.

[83] K. Baird, P. Burrows, M. Dima, P. Jacques, M. Kalelkar, *et al.*, "RESULTS ON IDENTIFIED HADRON PRODUCTION IN HADRONIC Z^0 DECAYS," Tech. Rep. SLD Physics Note 60, 1998.

[84] **Particle Data Group** Collaboration, D. E. Groom *et al.*, "Review of particle physics," *Eur. Phys. J.* **C15** (2000) 1.

[85] **DELPHI** Collaboration, P. Abreu *et al.*, "pi+-, K+-, p and anti-p production in Z0 → q anti-q, Z0 → b anti-b, Z0 → u anti-u, d anti-d, s anti-s," *Eur. Phys. J.* **C5** (1998) 585–620.

[86] **SLD** Collaboration, K. Abe *et al.*, "Measurement of A_c with charmed mesons at SLD," *Phys. Rev.* **D63** (2001) 032005.

[87] **OPAL** Collaboration, G. Abbiendi *et al.*, "Leading particle production in light flavour jets," *Eur. Phys. J.* **C16** (2000) 407–421, `hep-ex/0001054`.

[88] S. J. Brodsky and J. F. Gunion, "HADRON MULTIPLICITY IN COLOR GAUGE THEORY MODELS," *Phys. Rev. Lett.* **37** (1976) 402–405.

[89] K. Konishi, A. Ukawa, and G. Veneziano, "A SIMPLE ALGORITHM FOR QCD JETS," *Phys. Lett.* **B78** (1978) 243.

[90] M. B. Einhorn and B. G. Weeks, "JET PRODUCTION BY A GLUON SOURCE IN QCD," *Nucl. Phys.* **B146** (1978) 445.

[91] I. G. Knowles *et al.*, "QCD Event Generators," `arXiv:hep-ph/9601212`.

[92] A. Bassetto, M. Ciafaloni, G. Marchesini, and A. H. Mueller, "JET MULTIPLICITY AND SOFT GLUON FACTORIZATION," *Nucl. Phys.* **B207** (1982) 189.

[93] G. Marchesini and B. R. Webber, "SIMULATION OF QCD JETS INCLUDING SOFT GLUON INTERFERENCE," *Nucl. Phys.* **B238** (1984) 1.

[94] Y. I. Azimov, Y. L. Dokshitzer, V. A. Khoze, and S. I. Troian, "THE STRING EFFECT AND QCD COHERENCE," *Phys. Lett.* **B165** (1985) 147–150.

[95] K. Sugano, "PROPERTIES OF GLUON JETS: A REVIEW," *Int. J. Mod. Phys.* **A3** (1988) 2249.

[96] **HRS** Collaboration, M.Derrick *et al.*, "COMPARISION OF CHARGED PARTICLE MULTIPLICITIES IN QUARK JETS AND GLUON JETS PRODUCED IN e^+e^- ANNIHILATION AT 29 GEV," *Phys. Lett.* **B165** (1985) 449.

[97] **MARK II** Collaboration, A.Petersen. *et al.*, "Inclusive Charged-Particle Distribution in Nearly Threefold-Symmetric Three-Jet Events at $E_{c.m.} = 29$ GeV," *Phys. Rev. Lett.* **55** (1985) 1954.

[98] **UA2** Collaboration, P. Bagnaia *et al.*, "MEASUREMENT OF PRODUCTION AND PROPERTIES OF JETS AT THE CERN anti-p p COLLIDER," *Z. Phys.* **C20** (1983) 117.

[99] **UA1** Collaboration, G. Arnison *et al.*, "HADRONIC JET PRODUCTION AT THE CERN PROTON - ANTI-PROTON COLLIDER," *Phys. Lett.* **B132** (1983) 214.

[100] **PLUTO** Collaboration, C. Berger *et al.*, "MULTIPLICITY DISTRIBUTIONS IN e^+e^- ANNIHILATIONS AT PETRA ENERGIES," *Phys. Lett.* **B95** (1980) 313.

[101] **AMY** Collaboration, Y. K. Kim *et al.*, "A COMPARISON OF QUARK AND GLUON JETS PRODUCED IN HIGH- ENERGY e^+e^- ANNIHILATIONS," *Phys. Rev. Lett.* **63** (1989) 1772.

[102] **TASSO** Collaboration, W. Braunschweig *et al.*, "COMPARISON OF INCLUSIVE FRACTIONAL MOMENTUM DISTRIBUTIONS OF QUARK AND GLUON JETS PRODUCED IN e^+e^- ANNIHILATION," *Z. Phys.* **C45** (1989) 1.

[103] **JADE** Collaboration, W. Bartel *et al.*, "EXPERIMENTAL EVIDENCE FOR DIFFERENCES IN P(T) BETWEEN QUARK JETS AND GLUON JETS," *Phys. Lett.* **B123** (1983) 460.

[104] **CELLO** Collaboration, H. J. Behrend *et al.*, "TOPOLOGY OF HADRONIC e^+e^- ANNIHILATION EVENTS AT 22-GeV AND 34-GeV center-of-mass ENERGY," *Phys. Lett.* **B110** (1982) 329.

[105] Y. Iwasaki, "A Measurement of quark and gluon jet differences at the Z0 resonance,". SLAC-R-0460.

[106] J. W. Gary, "Tests of QCD using differences between gluon and quark jets," `arXiv:hep-ex/9909024`.

[107] **OPAL** Collaboration, P. D. Acton *et al.*, "A Study of differences between quark and gluon jets using vertex tagging of quark jets," *Z. Phys.* **C58** (1993) 387–404.

[108] **OPAL** Collaboration, R. Akers *et al.*, "A Model independent measurement of quark and gluon jet properties and differences," *Z. Phys.* **C68** (1995) 179–202.

[109] **DELPHI** Collaboration, P. Abreu *et al.*, "Energy dependence of the differences between the quark and gluon jet fragmentation," *Z. Phys.* **C70** (1996) 179–196.

[110] **ALEPH** Collaboration, D. Buskulic *et al.*, "Quark and gluon jet properties in symmetric three jet events," *Phys. Lett.* **B384** (1996) 353–364.

[111] **OPAL** Collaboration, K. Ackerstaff *et al.*, "Multiplicity distributions of gluon and quark jets and tests of QCD analytic predictions," *Eur. Phys. J.* **C1** (1998) 479–494, `hep-ex/9708029`.

[112] **OPAL** Collaboration, "Experimental properties of gluon and quark jets produced from a point source." OPAL Physics Note PN344, Contribution paper to the XXIX ICHEP, Vancouver, 1998.

[113] A. Capella, I. M. Dremin, J. W. Gary, V. A. Nechitailo, and J. Tran Thanh Van, "Evolution of average multiplicities of quark and gluon jets," *Phys. Rev.* **D61** (2000) 074009, `arXiv:hep-ph/9910226`.

[114] S. Lupia and W. Ochs, "Unified QCD description of hadron and jet multiplicities," *Phys. Lett.* **B418** (1998) 214–222, `arXiv:hep-ph/9707393`.

[115] **DELPHI** Collaboration, P. Abreu *et al.*, "Investigation of the splitting of quark and gluon jets," *Eur. Phys. J.* **C4** (1998) 1–17.

[116] **DELPHI** Collaboration, P. Abreu *et al.*, "Measurement of the gluon fragmentation function and a comparison of the scaling violation in gluon and quark jets," *Eur. Phys. J.* **C13** (2000) 573–589.

[117] **DELPHI** Collaboration, K. Hamacher, O. Klapp, P. Langefeld, and M. Siebel, "Precise measurement of the gluon fragmentation function and a comparison of the scaling violation in gluon and quark jets,". CERN-OPEN-99-435.

[118] **DELPHI** Collaboration, P. Abreu *et al.*, "The scale dependence of the hadron multiplicity in quark and gluon jets and a precise determination of C(A)/C(F)," *Phys. Lett.* **B449** (1999) 383–400, `arXiv:hep-ex/9903073`.

[119] V. A. Khoze, S. Lupia, and W. Ochs, "Perturbative universality in soft particle production," *Eur. Phys. J.* **C5** (1998) 77–90, `arXiv:hep-ph/9711392`.

[120] **OPAL** Collaboration, G. Abbiendi *et al.*, "Experimental properties of gluon and quark jets from a point source," *Eur. Phys. J.* **C11** (1999) 217–238, `arXiv:hep-ex/9903027`.

[121] C. Peterson and T. F. Walsh, "MODEL OF A NONPERTURBATIVE GLUON JET," *Phys. Lett.* **B91** (1980) 455.

[122] **OPAL** Collaboration, S. Baumann, "Identified particles in quark and gluon jets,". Prepared for 7th International Conference on Hadron Spectroscopy (Hadron 97), Upton, NY, 25-30 Aug 1997.

[123] **OPAL** Collaboration, J. H. Vossebeld, "Recent results on particle production from OPAL," `arXiv:hep-ex/0101009`.

[124] **OPAL** Collaboration, G. Abbiendi *et al.*, "Multiplicities of pi0, eta, K0 and of charged particles in quark and gluon jets," *Eur. Phys. J.* **C17** (2000) 373–387, `arXiv:hep-ex/0007017`.

[125] **ALEPH** Collaboration, G. V. M *et al.*, "Inclusive Production of π^0, η, $\eta'(958)$, K_s and Λ^0 in Two- and Three-jet Events from hadronic Z Decays,". ALEPH 99-006, CONF. 99-040.

[126] **DELPHI** Collaboration, P. Abreu *et al.*, "Identified Charged Particles in Quark and Gluon Jets," *Eur. Phys. J.* **C17** (2000) 207–222, `arXiv:hep-ex/0106063`.

[127] **L3** Collaboration, M. Acciarri *et al.*, "Measurement of eta production in two and three jet events from hadronic Z decays at LEP," *Phys. Lett.* **B371** (1996) 126–136.

[128] **L3** Collaboration, M. Acciarri *et al.*, "K0(S) and Lambda production in quark and gluon jets at LEP," *Phys. Lett.* **B407** (1997) 389–401.

[129] **OPAL** Collaboration, "Identified Charged Particle Production in Quark and Gluon Jets." OPAL Physics Note PN299, Contribution paper to the XXIX ICHEP, Vancouver, 1998.

[130] **ARGUS** Collaboration, H. Albrecht *et al.*, "Physics with ARGUS," *Phys. Rept.* **276** (1996) 223–405.

[131] **SLD** Collaboration, J. P. Fernandez, "Measurements of A(LR), A(lepton) and A(b) from SLD," `hep-ex/9903040`.